Phonon-induced dephasing of quantum dot excitons and microcavity-embedded quantum dot polaritons

Amy Morreau

Cardiff University

A thesis submitted for the degree of Doctor of Philosophy

December 31, 2018

Abstract

Central to the present work is the interaction between a semiconductor quantum dot (QD) exciton and its phonon environment. In the spectral domain, phonon assisted dephasing of the QD exciton presents as a phonon broadband, which is superimposed upon a narrow zero-phonon line (ZPL). The phonon broadband exhibits a high degree of thermal sensitivity, which we exploit in order to measure the temperature of semiconductor QD samples from their respective photoluminescence (PL) spectra. Temperature measurement is achieved through an automated fit procedure based upon the independent boson (IB) model with additional Gaussian and Lorentzian broadening. We find there to be very good agreement between fit temperature and nominal (cryostat-measured) temperature. Further, the fit procedure enables extraction of other key parameters such as the material deformation potential and the QD confinement lengths.

Also presented is a semi-analytical exact solution to the problem of phonon decoherence in a QD embedded in an optical microcavity. The approach is based on Trotter's decomposition theorem and takes into account the effects of the exciton-cavity and exciton-phonon coupling on equal footing, thereby providing access to regimes of comparable polaron and polariton timescales. We show that the emission spectrum consists of two polariton lines, with optical decoherence determined by acoustic phonon-induced transitions between the polariton states. When viewed in the polariton frame, we find the dependence of the polariton line broadening on the exciton-cavity coupling strength to be well described by Fermi's Golden Rule for real phonon-assisted transitions.

For comparison, we additionally calculate the QD-microcavity absorption spectra according to well-known master equation approaches and examine the agreement between the differing methods. We show that there is good agreement between the approaches if the polariton dynamics are slow in comparison to the polaron timescale, but significant deviation at comparable polaron and polariton timescales. We attribute the observed discrepancies to a break-down in the master equation approach within the latter regime.

Phonon-induced dephasing of quantum dot excitons and microcavity-embedded quantum dot polaritons

Amy Morreau

Cardiff University

A thesis submitted for the degree of

Doctor of Philosophy

December 31, 2018

For Kevin, my everything.

Acknowledgements

Firstly, I would like to express my deep gratitude to my supervisor, Dr Egor Muljarov, who has provided invaluable support and guidance. Egor's willingness to give his time and wisdom so generously, coupled with his contagious enthusiasm for the subject, has gifted me the perfect environment in which to learn and develop as a researcher.

I would like to thank Professor Wolfgang Langbein and Dr Francesco Masia, both of whom have encouraged me to consider the practical implementation of ideas that I had previously thought of in a purely theoretical context. I am also grateful to my fellow PhD student Lorenzo Scarpelli, who has been an enthusiastic and patient guide on my journey to develop my understanding of the experimental aspects of this work.

I gratefully acknowledge the funding received towards my PhD from the Engineering and Physical Sciences Research Council (ESPRC).

I would like to thank my mother for patiently nurturing my sense of curiosity and for providing me with unbounded encouragement and counsel over the years.

I would also like to thank my father, who has dedicated his working life to research and has inspired me to do the same.

I extend my gratitude to my wider family, particularly my grandfather Patrick and my aunt Alison for their generous financial contributions to my academic journey.

Finally, I would like to thank Kevin for being there when I needed him. Always.

Abstract

Central to the present work is the interaction between a semiconductor quantum dot (QD) exciton and its phonon environment. In the spectral domain, phonon assisted dephasing of the QD exciton presents as a phonon broadband, which is superimposed upon a narrow zero-phonon line (ZPL). The phonon broadband exhibits a high degree of thermal sensitivity, which we exploit in order to measure the temperature of semiconductor QD samples from their respective photoluminescence (PL) spectra. Temperature measurement is achieved through an automated fit procedure based upon the independent boson (IB) model with additional Gaussian and Lorentzian broadening. We find there to be very good agreement between fit temperature and nominal (cryostat-measured) temperature. Further, the fit procedure enables extraction of other key parameters such as the material deformation potential and the QD confinement lengths.

Also presented is a semi-analytical exact solution to the problem of phonon decoherence in a QD embedded in an optical microcavity. The approach is based on Trotter's decomposition theorem and takes into account the effects of the exciton-cavity and exciton-phonon coupling on equal footing, thereby providing access to regimes of comparable polaron and polariton timescales. We show that the emission spectrum consists of two polariton lines, with optical decoherence determined by acoustic phonon-induced transitions between the polariton states. When viewed in the polariton frame, we find the dependence of the polariton line broadening on the exciton-cavity coupling strength to be well described by Fermi's Golden Rule for real phonon-assisted transitions.

For comparison, we additionally calculate the QD-microcavity absorption spectra according to well-known master equation approaches and examine the agreement between the differing methods. We show that there is good agreement between the approaches if the polariton dynamics are slow in comparison to the polaron timescale, but significant deviation at comparable polaron and polariton timescales. We attribute the observed discrepancies to a break-down in the master equation approach within the latter regime.

Contents

List of Publications

1. A. Morreau and E. A. Muljarov. Phonon-Induced Dephasing in Quantum Dot-Cavity QED (2018). arXiv: http://arxiv.org/abs/1807.10977v1, *submitted to Phys. Rev. Lett.*

2. C. X. Zheng, J. Tersoff, W. X. Tang, A. Morreau, and D. E. Jesson. Novel GaAs surface phases via direct control of chemical potential. *Phys. Rev. B* **93** (2016), 195314.

3. L. Scarpelli, A. Morreau, S. Moroni, F. Masia, E. Pelucchi, E. A. Muljarov and W. Langbein (2018). Fit of phonon assisted sidebands allows extraction of the Lorentzian dephasing and localization length of quantum dot excitonic transitions. *Unpublished manuscript, to be submitted to Phys. Rev. Lett.*

Oral presentations

1. A. Morreau and E. A. Muljarov. Phonon induced dephasing in a quantum dot-microcavity system. *Photon 2018*, Birmingham, UK (September 2018).

2. E. A. Muljarov and A. Morreau. Phonon-induced dephasing in quantum dots coupled to an optical microcavity. *Metanano 2018*, Sochi, Russia (September 2018).

Poster presentations

1. A. Morreau and E. A. Muljarov. Exciton-photon-phonon dynamics in a quantum dot-microcavity system. *International Conference on Optics of Excitons in Confined Systems (OECS)*, Bath, UK (September 2017).

2. A. Morreau and E. A. Muljarov. Phonon induced dephasing in a quantum dot cavity-QED. *ECR poster competition*, Cardiff, UK (June 2018).

List of Abbreviations

CWE . . . . . Continuous wave excitation

FSS . . . . . Fine structure splitting

IB (model) . . Independent boson (model)

JC (model) . . Jaynes-Cummings (model)

PL . . . . . Photoluminescence

PQD . . . . . Pyramidal quantum dot

QD . . . . . Quantum dot

TCL . . . . . Time convolutionless

ZPL . . . . . Zero-phonon line

List of Commonly Used Symbols

$a^\dagger$ (a)	Cavity photon creation (annihilation) operator.
$d^\dagger$ (d)	Exciton creation (annihilation) operator.
$b_q^\dagger$ (b_q)	Phonon creation (annihilation) operator of the phonon mode with wave vector q.
$\mathcal{F}$	Inverse Fourier transform $\mathcal{F}\{g(t)\} = \int_{-\infty}^{\infty} dt\, g(t) e^{i\omega t}$.
$J(\omega)$	Phonon spectral density.
$N_{\mathbf{q}}$	Bose distribution function: $N_q = 1/[e^{\beta\omega_q} - 1]$.
ω_X	Complex exciton frequency: $\omega_X = \Omega_X - i\gamma_X$.
ω_C	Complex cavity frequency: $\omega_C = \Omega_C - i\gamma_C$.
Ω_p	Polaron shift.
$\theta(t)$	Heaviside step function.
$\otimes$	Tensor product.
$\mathcal{T}$	Time-ordering operator – places operators acting at later times to the right.

1 Introduction

A quantum dot (QD) defines a three-dimensional region of electronic confinement. In the field of semiconductors, this confinement is achieved through the layering of two or more semiconductor materials, each with a distinct bandgap energy. Typical material choices include gallium arsenide (GaAs), aluminium gallium arsenide (AlGaAs) and indium gallium arsenide (InGaAs).

The confinement associated with a QD has a profound impact on the properties of the material, primarily due to band energy quantisation. In bulk semiconductors, the promotion of an electron from the valence band to the conduction band creates a void, or *hole* in the former, which may be treated as a positively charged particle. The electron and hole form a bound pair, known as an *exciton* [1]. The same is true within low-dimensional semiconductor structures, such as QDs, but quantisation of the electron and hole energies ensures that the exciton transition energy Ω_X is a discrete, well-defined value. In a simplistic model, the creation (or recombination) of an exciton may only occur upon absorption (or emission) of a photon of energy equal to the exciton transition energy Ω_X. In reality, however, one cannot neglect the influence of the phonon environment on the QD dynamics, even at zero temperature [2–6]. Physically, phonons are quasiparticles that provide a quantum description of lattice deformation [7]. When an exciton is created, the negative electron and positive hole interact with the surrounding lattice through

the Coulomb interaction, surrounding the exciton with a phonon cloud. We treat this phonon-dressed exciton as a quasi-particle known as a *polaron* [8, 9]. A consequence of the exciton-phonon interaction is that light is not only emitted (or absorbed) at the exciton transition energy Ω_X, but also across a broad range of frequencies through phonon mediated transitions. If we consider the absorption (or emission) spectra, we observe a sharp peak at Ω_X, which we refer to as the *zero phonon line* (ZPL), alongside a broad spectrum, which we term the *phonon broadband* [2–5]. This behaviour is well-described by the exactly-solvable independent boson (IB) model [10], which is discussed in detail in Sec. 1.3 below. Within the IB model, one may account for various parameters of the QD and its environment such as the QD confinement lengths, the deformation potential of the material and the temperature. As part of the present work (detailed in Chapter 2), we apply the IB model to calculate theoretical emission spectra, which we compare to experimental photoluminescence (PL) emission data. Through an automated fit procedure, we determine the QD parameters that provide the best description of the observed PL emission spectra. Of particular interest is the temperature, upon which the phonon broadband is strongly dependent. This leads us to consider the concept and feasibility of exploiting the thermal properties of phonons to produce a so-called *phonon thermometer*.

Another branch of the present work is the phonon-induced dephasing of a QD-microcavity system. Whilst superficially similar to the phonon-induced dephasing of an exciton QD described above, the additional coupling between the cavity mode and the excitonic state has a profound impact of the behaviour of the system as a whole. With no known exact solution, phonon-induced decoherence in a qubit-cavity system represents a long-standing fundamental problem within quantum electrodynamics (QED). In order to investigate this problem further, it is instructive to consider the QD-microcavity system without phonons, which is well-described by the exactly-solvable Jaynes-Cummings (JC) model [11] (see Sec. 1.2 below). A distinction is made between the so-called weak coupling regime and the strong coupling regime, according to the coupling strength between the

exciton and cavity [12, 13]. For the case of strong coupling, there is a partly reversible exchange of energy, which gives rise to a superposition and light and matter, known as a "dressed state" or *polariton* [14]. Whilst the JC model provides a good basis for understanding the QD-cavity system, there is significant theoretical and experimental evidence [15–27] to suggest that the phonons play a crucial role in the optical decoherence and hence the overall dynamics of the system. Various approaches to the problem of incorporating phonon-induced dephasing within a model for the QD-microcavity system have been suggested in the literature, ranging from Born-Markov approximations [15, 16, 28] to path-integral methods [19, 21] and non-equilibrium Green's function techniques [22]. We provide, in Chapter 3, a brief discussion on the merits and deficiencies of such approaches, alongside details of a new method that aims to address the shortcomings in existing techniques. Our method, which we will refer to herein as the *Trotter decomposition method*, provides an asymptotically exact solution to the problem of phonon-induced decoherence in a qubit-cavity system. This solution allows us not only to rigorously prove results already known in the literature, but also to predict new important physical phenomena which have not been previously observed, discussed or calculated. We conclude with a comparison of polarisation and emission spectra obtained from the Trotter decomposition method against those obtained from the established master equation approaches [15, 16, 28, 29] (see Chapter 4). We show that there is, in general, good agreement between the various approaches for small to moderate exciton-cavity coupling strengths ($g < 0.2$ meV), which provides an additional confirmation of the validity and accuracy of the Trotter decomposition approach. There is, however, significant deviation at higher coupling strengths, which we attribute to the break-down of the master equation approaches.

In anticipation of the above, the present chapter introduces the two aforementioned models: the Independent Boson (IB) model and the Jaynes-Cummings (JC) model. We also present a formalism for calculating the polarisation and absorption from the density matrix of the system, which may be applied to both the IB and JC models.

1.1 Polarisation and absorption calculations

Throughout this work, we focus on linear polarisation and associated absorption/emission spectra. It is therefore natural to initially outline the formalism through which these quantities are determined. We take, as our starting point, the standard definition of optical polarisation,

$$P(t) = \mathrm{Tr}\left\{\rho(t)c\right\}, \tag{1.1}$$

where Tr denotes the trace operation, $\rho(t)$ is the density matrix and the annihilation operator c is associated with the observation mode. If we consider the QD-cavity system, observation may be undertaken in the excitonic mode (in which case c represents the excitonic annihilation operator d) or the cavity mode (with c representing the cavity annihilation operator a).

For non-trivial polarisation, we must provide external excitation to the system. We consider a pulsed excitation of the form,

$$H_{\mathrm{ext}} = \delta(t - t_0)\mathcal{V}, \tag{1.2}$$

$$\mathcal{V} = \mu(\tilde{c}^{\dagger} + \tilde{c}), \tag{1.3}$$

where μ is a constant and $\tilde{c}^{\dagger}$ is the creation operator associated with the excitation mode. Without loss of generality, we may assume that the excitation is applied at time $t_0 = 0$. The density matrix immediately after this time has the form

$$\rho(0_+) = e^{-i\mathcal{V}}\rho(-\infty)e^{i\mathcal{V}}, \tag{1.4}$$

where $\rho(-\infty)$ is the density matrix of the fully unexcited system.

Subsequent time-evolution of the density matrix is determined by the standard Schrödinger representation time evolution,

$$\rho(t > 0) = e^{-iHt}\rho(0_+)e^{iHt}, \tag{1.5}$$

$$= e^{-iHt}e^{-i\mathcal{V}}\rho(-\infty)e^{i\mathcal{V}}e^{iHt} \tag{1.6}$$

where H is the full system Hamiltonian (not including the external pulsed excitation H_{ext}). If we consider only linear polarisation we may neglect all terms higher than first order in μ. Thus, substituting for $\rho(t)$ in Eq. (1.1),

$$P_L(t) = \text{Tr}\{e^{-iHt}\,\mathcal{V}\,\rho(-\infty)\,e^{iHt}\,c\}, \tag{1.7}$$

where we have dropped the factor of $-i$. It should be noted that this polarisation defined in Eq. (1.7) describes the linear response of a pulsed excitation in the channel associated with operators $\tilde{c}$ and $\tilde{c}^\dagger$ (through $\mathcal{V}$ defined in Eq. (1.3)) and measured in the channel associated with operator c.

To find the absorption, we apply the basic principle of conservation of probability. In terms of formal scattering theory, the absorption $A(\omega)$ is the rate for transitions into all states other than the initial state. We employ Fermi's golden rule for a periodic harmonic potential $\mathcal{V}\,e^{-i\omega t}$, which states that the probability of a transition from initial state i to final state f occurring per unit time, $R_{i\to f}$, is given by[1],

$$R_{i\to f}(\omega) = 2\pi|\,\langle i|\,\mathcal{V}\,|f\rangle\,|^2\delta(E_f - E_i - \omega), \tag{1.8}$$

where H_{ext} is the external excitation, given by Eq. (1.2), and $E_{i(f)}$ is the energy of the initial (final) state $|i\rangle$ ($|f\rangle$).

The absorption is given by the transition rate between all initial and final states, with each contribution weighted by the probability that the system is found in the associated initial state w_i

$$A(\omega) = \sum_{i,f} w_i\,R_{i\to f}(\omega) \tag{1.9}$$

$$= 2\pi \sum_{i,f} w_i|\,\langle i|\,\mathcal{V}\,|f\rangle\,|^2\delta(E_f - E_i - \omega). \tag{1.10}$$

Noting that a general delta-function in the frequency domain $\delta(\omega)$ may be written as,

$$\delta(\omega) = \frac{1}{2\pi}\int_{-\infty}^{\infty} dt\,e^{-i\omega t}, \tag{1.11}$$

[1]Throughout this work we take $\hbar = 1$.

we recast Eq. (1.10) as,

$$A(\omega) = \int_{-\infty}^{\infty} dt \sum_{i,f} w_i |\langle i| \mathcal{V} |f\rangle|^2 e^{-i(E_f - E_i)t} e^{i\omega t} \tag{1.12}$$

$$= \int_{-\infty}^{\infty} dt \sum_{i,f} w_i \langle i| e^{iHt} \mathcal{V} e^{-iHt} |f\rangle \langle f| \mathcal{V} |i\rangle e^{i\omega t} \tag{1.13}$$

$$= \int_{-\infty}^{\infty} dt \sum_{i} w_i \langle i| e^{iHt} \mathcal{V} e^{-iHt} \mathcal{V} |i\rangle e^{i\omega t}. \tag{1.14}$$

We now note that w_i is the probability of finding the system in initial state i before the pulse is applied: $w_i = \langle i| \rho(-\infty) |i\rangle$. Further noting that $\sum_i \langle i| \ldots |i\rangle$ describes the trace operation, Eq. (1.14) becomes,

$$A(\omega) = \int_{-\infty}^{\infty} dt\, e^{i\omega t} \,\mathrm{Tr}\left\{ e^{-iHt} \mathcal{V} \rho(-\infty) e^{iHt} \mathcal{V} \right\}, \tag{1.15}$$

where we have used the cyclic property of the trace operation. Taking the form of $\mathcal{V}$ given in Eq. (1.3) we have,

$$A(\omega) = \mu \int_{-\infty}^{\infty} dt\, e^{i\omega t} \left(\mathrm{Tr}\left\{ e^{-iHt} \mathcal{V} \rho(-\infty) e^{iHt} \tilde{c} \right\} + \mathrm{Tr}\left\{ \tilde{c}^\dagger (e^{-iHt} \rho(-\infty) \mathcal{V} e^{iHt})^\dagger \right\} \right) \tag{1.16}$$

$$= \mu \int_{-\infty}^{\infty} dt\, e^{i\omega t} \left(\mathrm{Tr}\left\{ e^{-iHt} \mathcal{V} \rho(-\infty) e^{iHt} \tilde{c} \right\} + \text{c.c.} \right), \tag{1.17}$$

where c.c. indicates the complex conjugate. Noting that the trace within Eq. (1.17) is in fact the linear polarisation given in Eq. (1.7) (providing the condition $c = \tilde{c}$ is satisfied), we arrive at the following expression for the absorption[2],

$$A(\omega) = \mathrm{Re} \int_{-\infty}^{\infty} dt\, P_L(t) e^{i\omega t} = \mathrm{Re}\, \mathcal{F}\left\{ P_L(t) \right\}. \tag{1.18}$$

where we have dropped the unimportant factor of μ. Accordingly, Eq. (1.18) demonstrates that the inverse Fourier transform ($\mathcal{F}\{\ldots\}$) of the linear response $P_L(t)$[3] in the pulsed excitation regime is equivalent, in the lowest perturbation order, to absorption in the continuous wave excitation (CWE) regime. All references to absorption within this work relate to this CWE regime, but are found from the Fourier transform of polarisation in the pulsed excitation regime, as described above.

[2] If we had not dropped the factor of $-i$ within the expression for polarisation given in Eq. (1.7), the absorption would instead be given by the *imaginary* part of the inverse Fourier transform

[3] We consider only *linear* polarisation in this work and will herein drop the subscript L for simplicity of notation.

1.2 The Jaynes-Cummings (JC) model

The interaction of a single fermionic two-level system with a bosonic photon mode is well-described by the JC model. In this work, we apply the JC model to an excitonic system coupled to a cavity photon. We consider only the absolute ground state, the excitonic ground state (neglecting excited states of the exciton) and a single cavity mode.

The Hamiltonian H of the exciton-cavity system is given by:

$$H = \omega_X d^\dagger d + \omega_C a^\dagger a + g(a^\dagger d + d^\dagger a)\,, \tag{1.19}$$

where $d^\dagger$ ($a^\dagger$) is the exciton (cavity photon) creation operator, g is the exciton-cavity coupling strength, and ω_X (ω_C) is the *complex* exciton (cavity photon) frequency,

$$\omega_{X,C} = \Omega_{X,C} - i\gamma_{X,C}\,, \qquad \Omega_{X,C}, \gamma_{X,C} \in \mathbb{R}\,. \tag{1.20}$$

Physically, the imaginary part γ_X of the complex exciton frequency ω_X represents the ZPL dephasing, whilst γ_C corresponds to the radiative decay rate. Note that due to the inclusion of $\gamma_{X,C}$ within Eq. (1.19), the Hamiltonian is in fact not a Hamiltonian in the traditional sense: it is not Hermitian and therefore its eigenvalues are potentially complex and do not correspond to energy.

Focusing on *linear* polarisation enables reduction of the basis to just three states: the absolute ground state $|0\rangle$, the excitonic mode $|X\rangle$ and the cavity mode $|C\rangle$. In this reduced basis, the excitonic and cavity operators may be expressed explicitly as:

$$d^\dagger = |X\rangle\langle 0|\,, \qquad d = |0\rangle\langle X|\,, \tag{1.21}$$

$$a^\dagger = |C\rangle\langle 0|\,, \qquad a = |0\rangle\langle C|\,. \tag{1.22}$$

Evaluating the polarisation $P(t)$ according to Eq. (1.7) (see Sec. B.1.1 of the Appendix for full derivation), we arrive at the following expression,

$$P_{jk}(t) = \theta(t)\ \langle j|\, e^{-iHt}\, |k\rangle\,. \tag{1.23}$$

where the index j denotes the mode of excitation ($\tilde{c} = |0\rangle\langle j|$) and k denotes the mode of observation ($c = |0\rangle\langle k|$). Note that we have neglected the unimportant

factor of $i\mu$. The Heaviside step function within Eq. (1.23) arises as a result of applying the excitation at $t = 0$. Eq. (1.23) may be expressed as a 2×2 matrix product in the $\{|X\rangle, |C\rangle\}$, compactly accounting for all four possible combinations of excitation and measurement conditions,

$$\hat{P}(t) = \theta(t) \begin{pmatrix} P_{XX}(t) & P_{XC}(t) \\ P_{CX}(t) & P_{CC}(t) \end{pmatrix} = \theta(t) \underbrace{\begin{pmatrix} \alpha & \beta \\ -\beta & \alpha \end{pmatrix}}_{\hat{Y}} \begin{pmatrix} e^{-i\omega_1 t} & 0 \\ 0 & e^{-i\omega_2 t} \end{pmatrix} \underbrace{\begin{pmatrix} \alpha & -\beta \\ \beta & \alpha \end{pmatrix}}_{\hat{Y}^{-1}} . \tag{1.24}$$

The coefficients α, β of eigenvector matrices $\hat{Y}$, $\hat{Y}^{-1}$ and the eigenvalues $\omega_{1,2}$ have the following forms:

$$\alpha = \frac{\Delta}{\sqrt{\Delta^2 + g^2}}, \tag{1.25}$$

$$\beta = \frac{g}{\sqrt{\Delta^2 + g^2}}, \tag{1.26}$$

$$\omega_{1,2} = \frac{\omega_X + \omega_C}{2} \pm \sqrt{g^2 + \delta^2}, \tag{1.27}$$

with $\Delta = \sqrt{\delta^2 + g^2} - \delta$ and $\delta = 1/2\,(\omega_X - \omega_C)$. It should be noted that the eigenvalues $\omega_{1,2}$ are, in general, *complex*,

$$\omega_{1,2} = \Omega_{1,2} - i\gamma_{1,2}\,, \tag{1.28}$$

where $\Omega_{1,2}$ are the real energies and $\gamma_{1,2}$ are the associated linewidths.

1.2.1 Weak and strong coupling regimes

It is interesting to explore the influence of the term $\pm\sqrt{g^2 + \delta^2}$ within the eigenvalue expression, Eq. (1.27). Considering, for simplicity, the case of zero detuning between exciton and cavity $\Omega_X = \Omega_C$, we may re-express Eq. (1.27) as,

$$\omega_{1,2} = \Omega_C - \frac{i}{2}(\gamma_X + \gamma_c) \pm \frac{1}{2}\sqrt{4g^2 - (\gamma_X - \gamma_C)^2}\,. \tag{1.29}$$

If the exciton-cavity coupling strength g is smaller than $1/2|\gamma_X - \gamma_C|$ then the term $\pm\sqrt{g^2 + \delta^2}$ provides a purely imaginary contribution to the eigenvalues $\omega_{1,2}$ and hence the real energies are degenerate ($\Omega_{1,2} = \Omega_C$). This is known as the *weak coupling regime* and is classified spectrally by a single peak in the emission or

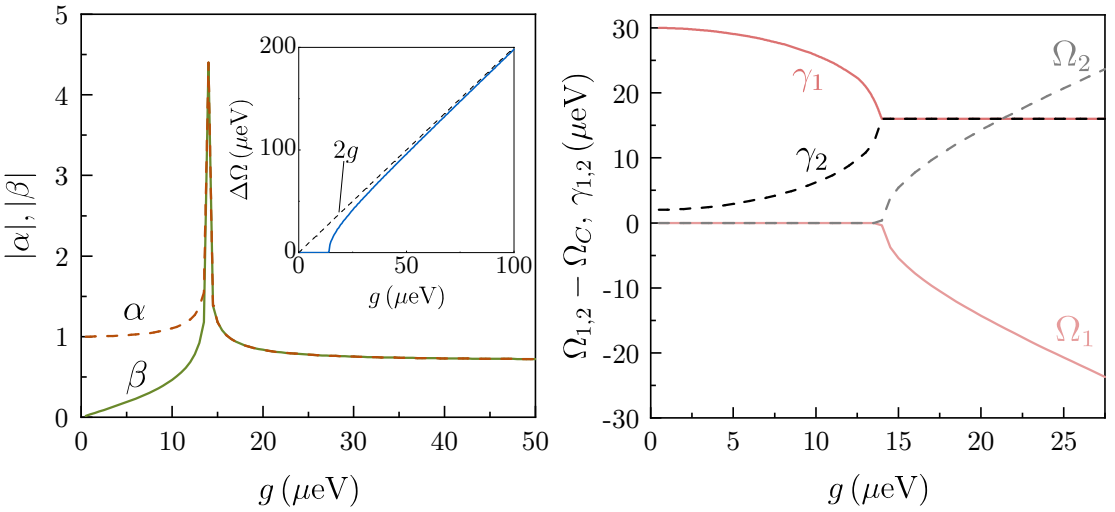

Figure 1.1: Left: absolute values of eigenvector coefficients α and β, shown as a function of the exciton-cavity coupling strength g. The sharp peak in both $|\alpha|$ and $|\beta|$ at approximately $14\,\mu$eV is a consequence of the finite long-time ZPL dephasing γ_X and radiative decay γ_C: the denominator of α and β is minimised for $\delta \approx g$, which, for the case of zero detuning, occurs at $g = \delta = {}^1\!/_2(\gamma_X - \gamma_C) = 14\,\mu$eV. Left inset: polariton line separation $\Delta\Omega = \Omega_2 - \Omega_1$ as a function of exciton-cavity coupling strength g, with dashed line showing $\Delta\Omega = 2g$. Right: real and imaginary parts of lower (1) and upper (2) polariton eigenfrequencies. For both panels, we have considered the case of zero detuning ($\Omega_X = \Omega_C$), $\gamma_X = 2\,\mu$eV and $\gamma_C = 30\,\mu$eV.

absorption spectrum. Within the weak coupling regime, there is a notable Purcell effect (modification of the QD exciton radiative lifetime) [30, 31].

If, on the other hand, $g > {}^1\!/_2\,|\gamma_X - \gamma_C|$, the real energies $\Omega_{1,2}$ are non-degenerate[4] and two spectral peaks are observed. The peaks are located at the real eigenenergies $\Omega_{1,2}$ with respective linewidths $\gamma_{1,2}$, as determined by Eq. (1.27).

Fig. 1.1 illustrates the real eigenenergies $\Omega_{1,2}$, linewidths $\gamma_{1,2}$ and eigenvector coefficients $\alpha\,\beta$ across a range of exciton-cavity coupling strengths $0 < g < 50\,\mu$eV. The figure shows the case of zero detuning $\Omega_X = \Omega_C$, with realistic values of $\gamma_X = 2\,\mu$eV and $\gamma_C = 30\,\mu$eV [11]. The transition from weak to strong coupling can be clearly seen at $g = (\gamma_C - \gamma_X)/2 = 14\,\mu$eV. Note that the weak-coupling regime dependence of the exciton decay rate on the electromagnetic field density (and hence the coupling strength g) [30–32] has been neglected.

[4] Considering, again, the case of zero detuning $\Omega_X = \Omega_C$

The remainder of this work (including consideration of the phonon environment within the QD-cavity system outlined in Chapters 3 and 4) focuses only on the strong coupling regime. Herein, any references to "small g" should be interpreted as small relative to the confines of the strong coupling regime.

1.2.2 Absorption

Calculating the absorption in this regime according to Eq. (1.18), we obtain spectra formed of two Lorentzian broadened lines,

$$A_{XX}(\omega) = \mathrm{Re}\left\{\frac{i\alpha^2}{\omega-\omega_1} + \frac{i\beta^2}{\omega-\omega_2}\right\}, \tag{1.30}$$

$$A_{CC}(\omega) = \mathrm{Re}\left\{\frac{i\beta^2}{\omega-\omega_1} + \frac{i\alpha^2}{\omega-\omega_2}\right\}. \tag{1.31}$$

Note that physically, only $A_{XX}(\omega)$ (absorption in the exciton mode under exciton feeding) and $A_{CC}(\omega)$ (absorption in the cavity mode under cavity feeding) are truly absorption spectra (see Sec. 1.1), and therefore the off-diagonal elements of $\mathcal{F}\{P(t)\}$ will not be considered.

Fig. 1.2 shows absorption spectra $A_{XX}(\omega)$ and $A_{CC}(\omega)$ calculated according to Eqs. (1.30) and (1.31) for exciton-cavity coupling strengths $g = 0.05$, 0.10 and 0.50 meV. Each spectrum consists of two peaks, located at respective real eigenenergies $\Omega_{1,2}$ with linewidths $\gamma_{1,2}$. We interpret these peaks as polariton states, each composed of a superposition of exciton and cavity states.

1.2.3 Rabi splitting and polariton timescale

With reference to Fig. 1.2, it is clear that the splitting between the two polariton lines, $\Delta\Omega = \Omega_1 - \Omega_2$, is strongly dependent upon the exciton-cavity coupling strength g. This separation, known as the *Rabi splitting*, is straightforwardly obtained from Eq. (1.29) for the case of zero detuning and strong coupling,

$$\Delta\Omega = \Omega_1 - \Omega_2 \approx 2g\,, \tag{1.32}$$

This approximation is illustrated by the dashed black line in the inset of Fig. 1.1.

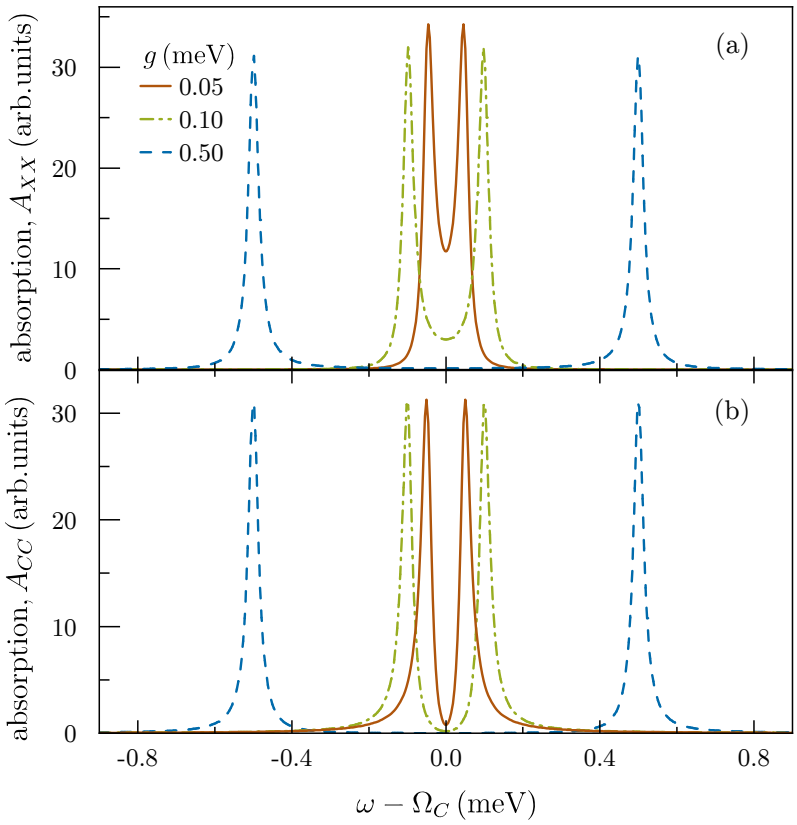

Figure 1.2: Absorption spectra (a) $A_{XX}(\omega)$ and (b) $A_{CC}(\omega)$ calculated according to the Jaynes-Cummings model, shown for various exciton-cavity coupling strengths g. We have taken the case of zero detuning between cavity and exciton modes $\Omega_X = \Omega_C$ and set $\gamma_X = 2\,\mu$eV and $\gamma_C = 30\,\mu$eV.

The Rabi splitting $\Delta\Omega$ is related to characteristic polariton timescale τ_{JC}, the latter describing the period of Rabi oscillations in the time domain:

$$\tau_{\mathrm{JC}} = \frac{2\pi}{\Delta\Omega} \approx \frac{\pi}{g}\,. \tag{1.33}$$

We will return to the Jaynes-Cummings model in Chapter 3, where we take the model as just one part of a more sophisticated description that includes the influence of the phonon environment on the exciton-cavity dynamics.

1.3 The independent boson (IB) model

The general phenomenon of phonon-induced dephasing in semiconductor QDs (in the absence of a confining cavity) has been successfully explained and quantified by the exactly solvable IB model [10]. This model describes a *polaron*, formed from a QD exciton coupled to bulk acoustic phonons [3], with a characteristic polaron formation time τ_{IB}. The IB model accounts for the major effect of the non-Markovian pure dephasing, although is known to fail treating the exciton ZPL broadening [5].

The Hamiltonian for the exciton-phonon system has the form

$$H = H_{\mathrm{ph}} + (\omega_X + V)\, d^\dagger d\,, \tag{1.34}$$

where $d^\dagger$ (d) is the exciton creation (annihilation) operator and ω_X is the *complex* exciton frequency, including the long-time ZPL dephasing γ_X.

The contribution to the Hamiltonian from the phonon continuum H_{ph} and the exciton-phonon coupling V are respectively given by

$$H_{\mathrm{ph}} = \sum_q \omega_q b_q^\dagger b_q\,, \tag{1.35}$$

$$V = \sum_q \lambda_q^* (b_q + b_{-q}^\dagger)\,, \tag{1.36}$$

where $b_q^\dagger$ (ω_q) is the creation operator (frequency) of the phonon mode with wave vector q, and λ_q is the matrix element of the exciton-phonon coupling for this mode, discussed further in Sec. 1.3.2. Noting that $\lambda_q^* = \lambda_q$, we may re-express Eq. (1.36) as,

$$V = \sum_q \lambda_q^* b_q + \lambda_q b_q^\dagger\,. \tag{1.37}$$

It is convenient at this point to adopt the formalism of open quantum systems [33], treating the exciton as the *system* and the phonons as the *environment*. We assume that the combined evolution of the system and environment is closed (neglecting the ZPL dephasing γ_X), and therefore follows unitary Hamiltonian dynamics. However, due to interactions between the system and the environment, neither will necessarily follow a unitary evolution individually.

The combination of the system and environment has a Hilbert space $\mathcal{H}$ composed of the tensor product ($\otimes$) of the excitonic Hilbert space $\mathcal{H}^{(X)}$ and the phononic Hilbert space $\mathcal{H}^{(\mathrm{ph})}$,

$$\mathcal{H} = \mathcal{H}^{(X)} \otimes \mathcal{H}^{(\mathrm{ph})} . \tag{1.38}$$

Similarly, the density matrix $\rho(t)$ for the combined system is given by the tensor product of the density matrices pertaining to the excitonic system and the phonon environment,

$$\rho(t) = \rho_X(t) \otimes \rho_{\mathrm{ph}}(t) . \tag{1.39}$$

As discussed in the previous section, we must apply an excitation to the system in order to obtain a non-trivial polarisation. We again assume a pulsed excitation of the form of Eq. (1.2), but in this case demand that $\tilde{c}^\dagger = d$ since we do not have a cavity mode within the system. Again assuming that the excitation is applied at time $t = 0$, the density matrix immediately after this time has the form of Eq. (1.4), where $\rho(-\infty)$ is the density matrix of the fully unexcited system. In this case, $\rho(-\infty)$ comprises an exciton part in the absolute ground state $|0\rangle$ and a phonon part in thermal equilibrium,

$$\rho(-\infty) = |0\rangle \langle 0| \otimes \rho_{\mathrm{ph}} . \tag{1.40}$$

Here, the density matrix of the phonon subspace, ρ_{ph}, is given by

$$\rho_{\mathrm{ph}} = \frac{e^{-\beta H_{\mathrm{ph}}}}{\mathrm{Tr}\left\{e^{-\beta H_{\mathrm{ph}}}\right\}_{\mathrm{ph}}} , \tag{1.41}$$

with $\beta = (k_B T)^{-1}$ and the trace being taken over all possible phonon states.

Subsequent time-evolution of the density matrix is determined by the standard Schrödinger representation time evolution, described by Eq. (1.5). Inserting Eqs. (1.2), (1.5) and (1.40) into Eq. (1.1), for the polarisation, we obtain the following expression for polarisation (full derivation in Sec. B.2.1 of the Appendix):

$$P(t) = \theta(t)\, e^{-i\omega_X t} \langle e^{-iVt} \rangle_{\mathrm{ph}} , \tag{1.42}$$

where $\langle \ldots \rangle_{\rm ph}$ denotes the trace over all phonon states. As for the JC case, the Heaviside step function $\theta(t)$ is a consequence of applying the excitation at $t = 0$, and we have omitted the factor of $i\mu$.

We note that e^{-iVt} is the time-evolution operator $\hat{U}(t)$ (see Section A.3.4 of the Appendix for discussion), which may be expressed as,

$$e^{-iVt} = \hat{U}(t) = \mathcal{T}\left[\exp\left(-i\int_0^t \mathrm{d}t'\,\tilde{V}(t')\right)\right], \tag{1.43}$$

where $\mathcal{T}$ is the time ordering operator, and the tilde notation denotes the interaction representation,

$$\tilde{V}(t) = e^{iH_{\rm ph}t}\,V\,e^{-iH_{\rm ph}t} = \sum_q \lambda_q^* b_q e^{-i\omega_q t} + \lambda_q b_q^\dagger e^{i\omega_q t}\,. \tag{1.44}$$

Using the linked cluster expansion [5, 6, 10], we may express Eq. (1.43) in terms of the *cumulant* $K(t)$ (full derivation in Sec. B.2.2 of the Appendix),

$$\langle e^{-iVt}\rangle = \left\langle \mathcal{T}\left[\exp\left(-i\int_0^t \mathrm{d}t_1 \tilde{V}(t_1)\right)\right]\right\rangle = e^{K(t)}\,. \tag{1.45}$$

Inserting Eq. (1.45) into Eq. (1.42), we find an expression for the linear polarisation in terms of the cumulant $K(t)$,

$$P(t) = \theta(t)\,e^{-i\omega_X t}e^{K(t)}\,. \tag{1.46}$$

As shown in Sec. B.2.2 of the Appendix, the cumulant $K(t)$ is given by

$$K(t) = -\frac{1}{2}\int_0^t \mathrm{d}t_1 \int_0^t \mathrm{d}t_2 \left\langle \mathcal{T}\tilde{V}(t_1)\tilde{V}(t_2)\right\rangle\,. \tag{1.47}$$

In brief, the cumulant has this form due to the requirement of the linked cluster theorem [10] to take only connected diagrams in the exponent. In the linear interaction, the only connected diagram is that given in Eq. (1.47). In all higher orders, the time integrals of the phonon propagators may be separated and hence such orders may be factorised.

1.3.1 Calculation of the cumulant $K(t)$

Returning to Eq. (1.47) and inserting the expression for $\tilde{V}(t)$ from Eq. (1.44),

$$K(t) = -\frac{1}{2}\sum_{\mathbf{q}}\int_0^t \mathrm{d}t_1 \int_0^t \mathrm{d}t_2\, |\lambda_q|^2 \left([N_{\mathbf{q}}+1]e^{-i\omega_q|t_1-t_2|} + N_{\mathbf{q}} e^{i\omega_q|t_1-t_2|} \right), \quad (1.48)$$

where N_q is the Bose distribution function $N_q = 1/[e^{\beta\omega_q}-1]$, and we have used $\langle b_q^\dagger b_q\rangle = N_q$ and $\langle b_q b_q^\dagger\rangle = N_q + 1$. Noting that λ_q is independent of time, we may perform the double integration to give,

$$K(t) = \sum_q |\lambda_q|^2 \left(\frac{N_q}{\omega_q^2}\left[e^{i\omega_q t}-1\right] + \frac{N_q+1}{\omega_q^2}\left[e^{-i\omega_q t}-1\right] + \frac{it}{\omega_q}\right). \quad (1.49)$$

The phonon spectral density $J(\omega)$ is defined as

$$J(\omega) = \sum_q |\lambda_{\mathbf{q}}|^2 \delta(\omega-\omega_{\mathbf{q}}). \quad (1.50)$$

This is equivalent to taking the product of $|\lambda_{\mathbf{q}}|^2$ with the density of states in ω-space. Converting the summation over q to an integration $\sum_q \to \frac{\mathbb{V}}{(2\pi)^3 v_s^3}\int d^3\omega$, where $\mathbb{V}$ is the sample volume and v_s is the speed of sound in the sample material, the spectral density becomes

$$J(\omega) = |\lambda_q|^2 \frac{2\mathbb{V}}{(2\pi)^2 v_s^3}\omega^2, \quad (1.51)$$

The cumulant $K(t)$ therefore has the form

$$K(t) = \frac{1}{4\pi}\int d^3\omega\, \frac{J(\omega)}{\omega^2}\left(\frac{N(\omega)}{\omega^2}\left[e^{i\omega t}-1\right] + \frac{N(\omega)+1}{\omega^2}\left[e^{-i\omega t}-1\right] + \frac{it}{\omega}\right), \quad (1.52)$$

where $N(\omega) = 1/[e^{\beta\omega}-1]$. This may be expressed in terms of the rapid initial decay $K_{BB}(t)$ (which forms the phonon broadband in frequency space) and the long-time asymptotics $K_\infty(t)$ (which forms the zero-phonon line in frequency space),

$$K(t) = \underbrace{\frac{1}{4\pi}\int d^3\omega\, \frac{J(\omega)}{\omega^4}\left(N(\omega)e^{i\omega t} + [N(\omega)+1]e^{-i\omega t}\right)}_{K_{BB}(t)} + \underbrace{(-i\Omega_p t - S)}_{K_\infty(t)}, \quad (1.53)$$

where the polaron shift Ω_p has the form

$$\Omega_p = -\frac{1}{4\pi}\int d^3\omega\, \frac{J(\omega)}{\omega^3} \quad (1.54)$$

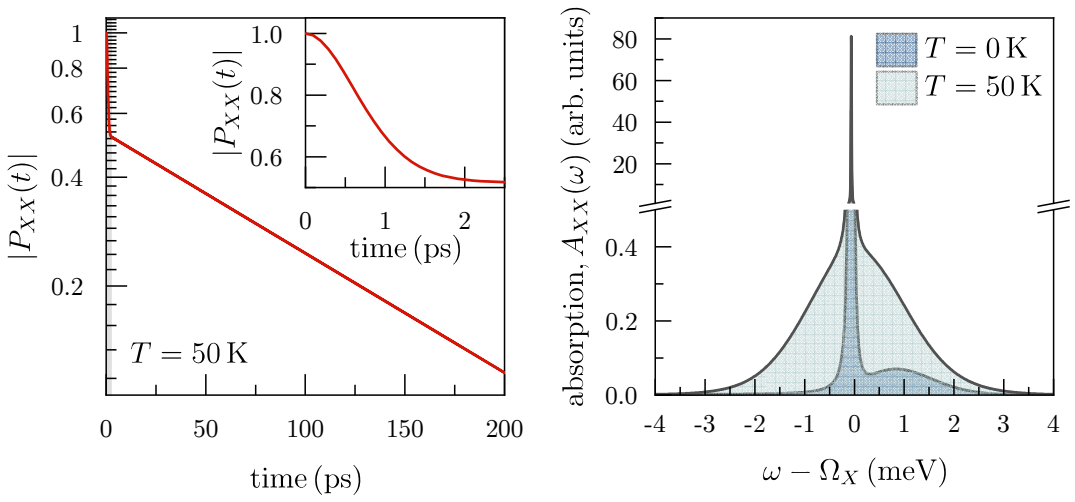

Figure 1.3: Left: absolute value of the IB polarisation shown at $T = 50$ K. Left inset: magnification of the initial 2.5 ps shown in the primary figure. Right: IB absorption spectra for temperatures $T = 0$ K and $T = 50$ K. Full calculation for both panels carried out according to Eqs. (1.68) to (1.70) with $a = 3.3\,\mathrm{nm}$, $D_c - D_v = -6.5\,\mathrm{eV}$, $v_s = 4.6 \times 10^3\,\mathrm{m/s}$, and $\rho_m = 5.65\,\mathrm{g/cm^3}$.

and the Huang-Rhys factor S is given by

$$S = \frac{1}{4\pi} \int d^3\omega \, \frac{J(\omega)}{\omega^4} \coth\left(\frac{\omega}{2k_B T}\right). \tag{1.55}$$

Inserting Eq. (1.53) into Eq. (1.46), we see that the polarisation may be expressed as

$$P(t) = \theta(t)\, e^{-S} e^{-i(\omega_X + \Omega_p)t} e^{K_{BB}(t)}\,. \tag{1.56}$$

The left panel of Fig. 1.3 shows the magnitude of the polarisation, which is related to the cumulant $K(t)$ according to Eq. (1.46). The initial rapid decay associated with $K_{BB}(t)$, magnified in the inset, occurs within approximately two picoseconds at $T = 50$ K. The time taken for this decay is, in general, a function of temperature as shown in Fig. 1.4.

It is interesting at this point to also consider the absorption, which is calculated from the polarisation according to Eq. (1.18). The right panel of Fig. 1.3 shows the absorption spectra for two temperatures: $T = 0$ K and $T = 50$ K. If we neglect the broadband contribution K_{BB}, we are left with the zero-phonon line, for which

we are able to obtain a simple analytic expression:

$$A_{\mathrm{ZPL}}(\omega) = \frac{e^{-S}\gamma_X}{(\omega - \bar{\Omega}_X)^2 + \gamma_X^2}\,, \tag{1.57}$$

where we have expressed ω_X in terms of its real and imaginary parts and have defined $\bar{\Omega}_X = \Omega_X + \Omega_p$. This is a Lorentzian broadened line centred upon frequency $\bar{\Omega}_X$ with full width at half maximum (FWHM) of $2\gamma_X$.

Note that if we consider the very simple case of the system *without* phonons, it is straightforward to calculate the absorption as $A(\omega) = \gamma_X / \left[(\omega - \Omega_X)^2 + \gamma_X^2\right]$. Comparison of this expression with Eqns. (1.56) and (1.57) clearly shows certain effects associated with the phonon interaction:

1. The ZPL intensity is suppressed by a factor of e^{-S};

2. The ZPL is displaced from the exciton frequency Ω_X by the polaron shift Ω_p.

3. There is an additional contribution to the polarisation of $e^{K_{BB}(t)}$, which is simply absent in the case with no phonons. This contribution produces, in the time domain, a rapid initial decay in $P(t)$, as shown in Fig. 1.3. In the frequency domain, this corresponds to a spectrally broad absorption feature known as the *phonon broadband*. At zero temperature, the broadband is highly asymmetric due to the absence of environmental phonons to assist the exciton in absorption a photon of lower energy than the ZPL. At higher temperature, the broadband becomes more symmetric and increases in magnitude as more phonons become available to assist exciton transitions.

1.3.2 Matrix element λ_q

At low temperatures, the exciton-phonon interaction is dominated by the deformation potential coupling to longitudinal acoustic (LA) phonons [3]. Assuming that (i) the phonon parameters in the confined QD do not differ significantly from those in the surrounding material, and (ii) the acoustic phonons have linear

dispersion $\omega_q = v_s|\mathbf{q}|$, where v_s is the sound velocity in the material, the matrix coupling element λ_q is given by

$$\lambda_q = \frac{q\mathcal{D}(\mathbf{q})}{\sqrt{2\rho_m\omega_q\mathbb{V}}}\,, \tag{1.58}$$

where ρ_m is the mass density of the material and $\mathcal{D}(\mathbf{q})$ is the form-factor [5, 6],

$$\mathcal{D}(\mathbf{q}) = \int \mathrm{d}\mathbf{r}_e \int \mathrm{d}\mathbf{r}_h |\psi_X(\mathbf{r}_e, \mathbf{r}_h)|^2 \left(D_c e^{-i\mathbf{q}\cdot\mathbf{r}_e} - D_v e^{-i\mathbf{q}\cdot\mathbf{r}_h}\right) . \tag{1.59}$$

We assume a factorisable form of the exciton wave function,

$$\Psi_X(\mathbf{r}_e, \mathbf{r}_h) = \psi_e(\mathbf{r}_e)\psi_h(\mathbf{r}_h)\,, \tag{1.60}$$

where $\psi_{e(h)}(\mathbf{r})$ is the confined electron (hole) ground state wave function. This assumption enables us to express the form-factor $\mathcal{D}(q)$ as

$$\mathcal{D}(\mathbf{q}) = -\int \mathrm{d}\mathbf{r} \left[D_v|\psi_h(\mathbf{r})|^2 - D_c|\psi_e(\mathbf{r})|^2\right] e^{-i\mathbf{q}\cdot\mathbf{r}}\,, \tag{1.61}$$

with $D_{c(v)}$ being the material-dependent deformation potential constant for the conduction (valence) band.

The most straightforward case is that of a spherically symmetric parabolic confinement potential[5], producing Gaussian ground state wave functions:

$$\psi_{e(h)}(\mathbf{r}) = \frac{1}{\sqrt{\pi^{3/2}a_{e(h)}^3}} \exp\left(-\frac{r^2}{2a_{e(h)}^2}\right), \tag{1.62}$$

Taking the case of equal exciton and hole confinement lengths $a_e = a_h = a$ and inserting Eq. (1.62) into Eq. (1.61) we have,

$$\mathcal{D}(q) = (D_c - D_v)e^{-\frac{a^2q^2}{4}}\,, \tag{1.63}$$

and thus, from Eq. (1.58), the matrix coupling element $\lambda_{\mathbf{q}}$ is given by

$$\lambda_q = \sqrt{\frac{q}{2\rho_m v_s \mathbb{V}}}(D_v - D_c)\exp\left(-\frac{a^2q^2}{4}\right). \tag{1.64}$$

Inserting this expression for λ_q into Eq. (1.51) for the spectral density,

$$J(\omega) = J_0\,\omega^3 e^{-\frac{\omega^2}{\omega_0^2}}\,, \tag{1.65}$$

[5] A more sophisticated model for anisotropic QDs is considered in Chapter 2

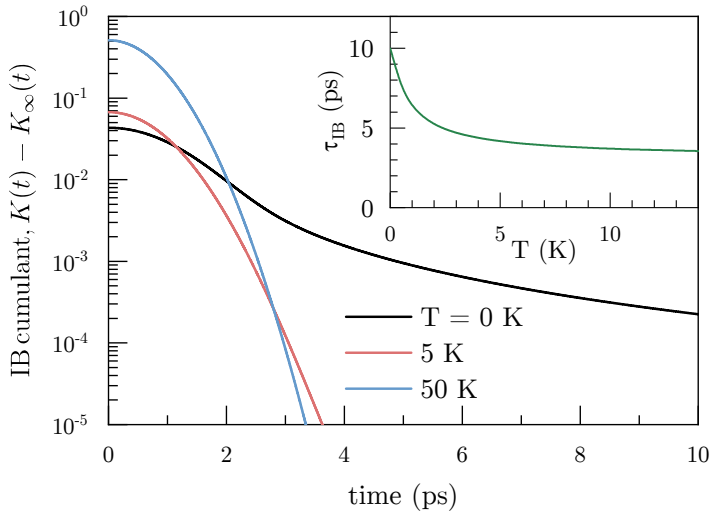

Figure 1.4: Broadband contribution $K_{BB}(t)$ to the IB cumulant $K(t)$ shown at varyious temperatures. Inset: phonon memory time τ_{IB} calculated according to the time taken for $K_{BB}(t)$ to drop below a threshold value. As for Fig. 1.3, the cumulant calculation is carried out according to Eqs. (1.68) to (1.70) with $a = 3.3\,\mathrm{nm}$, $D_c - D_v = -6.5\,\mathrm{eV}$, $v_s = 4.6 \times 10^3\,\mathrm{m/s}$, and $\rho_m = 5.65\,\mathrm{g/cm^3}$.

with

$$J_0 = \frac{(D_v - D_c)^2}{(2\pi)^2 \rho_m v_s^5}\,. \tag{1.66}$$

$$\omega_0 = \frac{\sqrt{2} v_s}{a}\,. \tag{1.67}$$

Exploiting the spherical symmetry of this spectral density allows us to replace $\int d^3\omega$ with $4\pi \int_0^\infty d\omega\, \omega^2$ in Eq. (1.53) for $K(t)$,

$$K_{BB}(t) = J_0 \int_0^\infty d\omega\, \omega\, e^{-\frac{\omega^2}{\omega_0^2}} \left(N(\omega) e^{i\omega t} + [N(\omega) + 1] e^{-i\omega t} \right)\,, \tag{1.68}$$

$$\Omega_p = J_0 \sqrt{\frac{\pi}{2}} \frac{v_s^3}{a^3}\,, \tag{1.69}$$

$$S = J_0 \int_0^\infty d\omega\, \omega\, e^{-\frac{\omega^2}{\omega_0^2}} \coth\left(\frac{\omega}{2 k_B T} \right)\,, \tag{1.70}$$

where, in Eq. (1.69), we have performed the analytic integration over ω. We note from Eqs. (1.68) to (1.70) that we arrive at a fully analytic expression for the polaron shift Ω_p, but evaluation of $K_{BB}(t)$ and S require numeric integration. A note on optimising the computation of $K_{BB}(t)$ through use of fast Fourier transform (FFT) algorithms is provided in Sec. B.2.3 of the Appendix.

As a final remark, the frequency ω_0 is known as the *cut-off frequency*, and defines a characteristic time scale of the phonon system τ_{IB},

$$\tau_{\mathrm{IB}} \approx \frac{2\pi}{\omega_0} \approx \frac{\sqrt{2}\pi}{v_s}\,. \tag{1.71}$$

For typical parameters $a = 3.3\,\mathrm{nm}$, $v_s = 4.6\times10^3$ m/s, this equates to approximately 3.2 ps. We refer to this characteristic timescale τ_{IB} as the phonon memory time. Physically, it is the time required for the lattice atoms or ions to return to their equilibrium positions (i.e. for the phonon cloud surrounding an exciton to dissipate) once the exciton has recombined. A more accurate estimation of the phonon memory time τ_{IB} may be obtained by performing the above-described full cumulant calculation. Fig. 1.4 illustrates the broadband contribution to the cumulant $K_{BB}(t)$ for various temperatures. An alternative, and more accurate, definition of the phonon memory time τ_{IB} is the time taken for $K_{BB}(t)$ to drop below a threshold value, which we take to be 10^{-3}. At low temperature (< 5 K), τ_{IB} is strongly temperature dependent, but becomes approximately constant beyond ~ 5 K.

2
The phonon thermometer

In this chapter, we focus on the phonon-induced dephasing of semiconductor quantum dots. We seek to exploit the temperature sensitivity of the phonon broadband to create a “phonon thermometer". To do so, we apply an optical excitation to the semiconductor QD sample and measure the spontaneous emission of light - the *photoluminescence* (PL). Initially, we consider the concept of a *thermal ratio* [34], which we define as the PL intensity, $I(\omega)$, relative to its reflection about the ZPL, $I(-\omega)$. Providing that the ZPL broadening is minimal, this simple ratio constitutes a straightforward method to extract the sample temperature from the influence of the phonon environment. We find, however, that the ZPL width of the measured samples is sufficiently large to cause problems with the thermal ratio. In view of this, we move on to a full theoretical fit of the experimental PL emission spectra. We employ the IB model to calculate theoretical emission spectra for a given set of QD parameters such as the QD dimensions and sample temperature. We then compare these spectra to experimental emission data, adjusting the model parameters through an automated fit procedure in order to optimise the agreement between theory and experiment. There are a number of parameters of particular interest, including the fit temperature and the confinement dimensions. The former is clearly central to our desire to create a phonon thermometer, but will also

enable us to verify the accuracy of the theoretical fit through comparison of the fit temperature and the nominal (cryostat-measured) temperature of the system.

2.1 Quantum dot samples

We measure the spontaneous emission spectra from three samples, all of which are InGaAs/GaAs pyramidal quantum dots (PQDs). PQDs are of particular academic and industrial interest due to their inherent site-control capability [35] and their high degree of crystal symmetry. Moreover, it is possible to vertically stack multiple QDs within the same pyramidal recess, effectively creating QD molecules [36]. A schematic diagram of two vertically stacked QDs is shown in Fig. 2.1; we will refer to this structure herein as a *double pyramidal quantum dot* (double PDQ). Control over the kinetic parameters during fabrication allows tuning of the distance between the two adjacent QDs, from ~ 0.1 nm to ~ 1000 nm, which in turn changes the nature of the interaction between the QDs.

2.1.1 Sample fabrication

The samples were fabricated by Dr. E. Pelucchi at University College Cork. A detailed description of the fabrication process is beyond the scope of this work, but an overview will be provided in this section. For further details, we refer the reader to references [36–38].

In brief, low-pressure organo-metallic chemical vapour deposition (OMCVD) is applied to a pre-patterned GaAs substrate along the (111) crystallographic orientation. After growth, the GaAs substrate is removed through selective wet etching, yielding an array of uprightstanding pyramids, each with a single QD located near its apex. The QD is formed by an InGaAs layer deposited between GaAs inner barriers and AlGaAs outer barriers[36]. Other quantum confinement features arise during this fabrication process, such as lateral quantum wires (LQWRs) and lateral quantum wells (LQWs) [37, 39, 40], but such features are unimportant in the context of the present work and will not be discussed further.

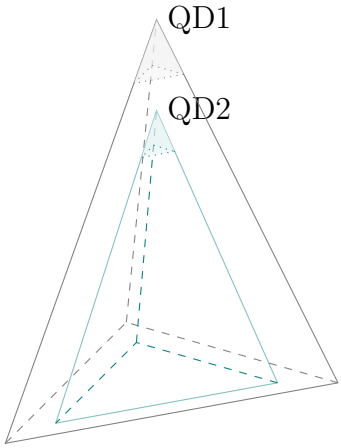

Figure 2.1: Schematic of a double quantum dot sample, containing two vertically stacked quantum dots.

Of the three PQD samples under consideration, two are double PQDs (such as those illustrated schematically in Fig. 2.1) and one is a single PQD. In relation to the two double PQDs, which we will refer to herein as samples (A) and (B), the QD separation is ~ 2 nm. Investigation of prior samples by B. Van Hattem [39] indicates that the QDs are ellipsoidal ("pancake") in shape.

2.2 Data acquisition and peak characterisation

The steps of data collection and peak characterisation were undertaken by L. Scarpelli at Cardiff University – the reader is directed to reference [37] for further details.

2.2.1 Data acquisition: PL emission spectra

Samples are mounted in a closed cycle cryostat and non-resonantly excited by a low intensity Helium-Neon laser pulse at $\lambda = 633$ nm. A microscope objective is mounted inside the cryostat on the cold shield, having a temperature of approximately 30 K. A long-pass colour filter with a cutoff wavelength of 680 nm removes the input laser pulse from the detection path. The QD spontaneous emission is spectrally resolved by a spectrometer and detected by a CCD of 1340×100 square pixels of length $20\,\mu$m. In order to create circularly polarised transitions, a permanent Neodymium magnet is placed proximal to the rear surface of the sample in the Faraday configuration (i.e.

aligned along the growth direction). The resultant magnetic field is $B_z = 0.45$ T (where z defines the direction orthogonal to the sample plane). A quarter waveplate projects the right and left-handed circularly polarised emission into the linear polarisation basis. To improve the signal-to-noise ratio (SNR), and hence enhance the resolution of the phonon sidebands, N acquisitions are summed per spectrum (with N between 20 and 200, depending on the signal strength).

PL emission spectra are captured at nominal (cryostat-measured) temperatures $T = 5$, 10, 15, 20, 30 K for each sample. Additional measurements at $T = 50$ and 100 K are taken in relation to the two double PQD samples. Accordingly, a total of 19 PL spectra are available for analysis.

2.2.2 Peak characterisation

Prior to any substantive analysis of the collected emission spectra, it is important to establish the origin of the observed spectral peaks. Peak characterisation is performed using polarisation resolved measurements of power dependence and fine structure splitting (FSS) [37].

Power dependence measurements look at the peak area (characterised with a Voigt profile) as a function of the excitation power L. We expect a L^k dependence, where a value of $k \sim 1$ implies an exciton (X) transition [41, 42] and $k \sim 2$ suggests a bi-exciton (XX) transition [43].

FSS measurements are undertaken in the absence of an external magnetic field (the above-mentioned permanent Neodymium magnet is removed). A $\lambda/2$ waveplate is located in the detection path at an angle of $\theta_{\lambda/2}$ relative to the horizontal axis of the laboratory reference frame. Variation of the angle $\theta_{\lambda/2}$ alters the projection of the linearly polarised $|L_1\rangle$ and $|L_2\rangle$ states onto the horizontal and vertical (H-V) axes of the laboratory reference frame. The vertical (π_V) and horizontal (π_H) PL components are each directed to spatially separated regions of the CCD camera by a polarisation displacer. Oscillation of the peak energy as a function of the waveplate angle $\theta_{\lambda/2}$ is a clear indication of FSS. We expect FSS in exciton (X) and biexciton (XX) states, but not in trion (X*) states – for further information see Sec. 2.5.2 below.

We observe two peaks in the double PQD samples. We characterise the lower energy peak as a trion (X*) and the higher energy peak as an exciton (X). In relation to the exciton state, we observe a FSS of $27.31 \pm 0.14\,\mu$eV. In the single PQD sample, we observe a single peak that we characterise as a trion (X*).

2.2.3 Experimental noise

We assume three primary contributions to the experimental noise within the PL spectra:

1. *Read noise* σ_r: electronic noise generated by the CCD during the detection of the photo-generated electrons. In broad terms, this noise depends on the number of pixels utilised in signal measurement and the number of data acquisitions but is independent of the PL intensity $I(\omega)$.

2. *Camera sensitivity noise* α: noise due to variation in the detection sensitivity of pixels in different regions of the CCD. A signal of intensity $I(\omega)$ has associated camera sensitivity noise $\alpha I(\omega)$.

3. *Shot noise*: noise associated with the Poisson statistics of light proportional to $\sqrt{I(\omega)}$.

Accounting for all three contributions, we arrive at the following expression for the total experimental noise:

$$\sigma_D(\omega) = \sqrt{\sigma_r^2 + (\alpha I(\omega))^2 + I(\omega)}\,. \tag{2.1}$$

Measurements of the read noise σ_r and the camera sensitivity noise α are taken for each PL spectrum during the data acquisition process.

2.3 Equilibration timescales

The primary assumption associated with the concept of a PL phonon thermometer is that the exciton and associated polaron cloud are in thermal equilibrium at the point of radiative exciton recombination. If this were not true then non-equilibrium

effects would strongly influence the PL spectra and the latter would not characterise the true sample temperature.

Thermal equilibrium is reached via a two-step process. The above-bandgap excitation (λ = 633 nm) promotes electrons to energies above the conduction band minimum (and holes to energies below the valence band maximum). These photoexcited electrons (holes) are not Boltzmann-distributed; the first step in achieving equilibrium is for the electrons (holes) to interact separately with one another through electron-electron (hole-hole) collisions and intervalley scattering to form a Boltzmann distribution [44]. This process is often termed *carrier thermalisation* and occurs very rapidly ($<$ 100 fs [44, 45]).

The excitation applied by the Helium-Neon laser is approximately 0.5 eV above the bandgap, which far exceeds k_BT (the latter ranging between 0.4 meV and 8.6 meV for the temperatures under consideration). Accordingly, the electron and hole temperatures (as defined the respective Boltzmann distributions) are elevated relative to the lattice temperature. A second stage is therefore required in order to reach equilibrium: *carrier cooling* [44]. Here, the carriers interact with longitudinal optical (LO) phonons to dissipate excess energy, heating the lattice and cooling the charge carriers until thermal equilibrium is achieved. Hot electrons and hot holes cool at different rates due to differences in effective mass; the lighter electrons cool more slowly and therefore dictate the total carrier cooling time [44]. In bulk GaAs, the electron cooling time is $\sim$ 1 ps [44], although is altered by various factors including excitation power and temperature. The timescale of electron cooling in QDs is subject to ongoing investigation, with significant debate regarding the influence of the QD confinement. There are many proponents of a *phonon bottleneck* theory [46–54]: a slowing of electron cooling due to the requirement of multiphonon processes to facilitate transitions between the discretised conduction band energy levels. There are, however, a significant number of reports that contradict the prediction of a phonon bottleneck [55–62] so further investigation into the matter is undoubtedly required.

2.4 Thermal ratio

Before we look at a full theoretical fit procedure, it is instructive to initially consider an alternative "phonon thermometer" technique, which we term the *thermal ratio*. This technique is elegant in its simplicity, giving an insight into the broadening of the ZPL as well as the phonon temperature.

Returning to Eq. (1.53), we note that the rapidly decaying part of the cumulant K_{BB} has the form $K_{BB}(t) \propto N_q e^{i\omega t} + [N_q + 1]e^{-i\omega t}$, where N_q is the Bose distribution function $N_q = 1/[e^{\beta\omega_q} - 1]$. Physically, K_{BB} contains both phonon absorption ($\propto N_q$) and phonon emission ($\propto N_q + 1$) terms. When the PL emission spectrum is considered, the phonon emission (absorption) term in the cumulant generates the low (high) energy phonon sideband. At $T = 0$ K, the PL emission spectrum is highly asymmetric – phonon absorption cannot occur at this temperature ($N_q = 0$) and hence only the phonon emission (low energy) sideband is present. As the temperature is increased, phonon absorption becomes increasingly probable and hence the high energy sideband gains prominence. At $T = 50$ K, phonon absorption and emission rates are approximately equal ($N_q \sim N_q + 1$), and hence the phonon broadband is highly symmetric about the ZPL.

The form of the rapidly decaying part of the cumulant $K_{BB}(t)$ enables us to define a thermal ratio R_T [34],

$$R_T = \ln\left(\frac{I(-\omega)}{I(\omega)}\right) = \frac{\omega}{k_B T}\,, \tag{2.2}$$

where $I(\omega)$ is the PL intensity. Note that Eq. (2.2) is valid providing we take the ZPL as the zero of frequency (which we may do without any loss of generality) and we assume no long-time ZPL dephasing.

Fig. 2.2 shows the PL intensity and the corresponding thermal ratio for the trion peak of sample (A) measured at nominal temperature $T = 5$ K. The thermal ratio follows the expected linear dependence on photon frequency ω (where we have taken the zero of frequency at the centre of the ZPL). The gradient of this line indicates a temperature of approximately 12.8 K. We note, however, there is a significant offset of the thermal ratio at the ZPL location. This offset is a consequence of finite ZPL

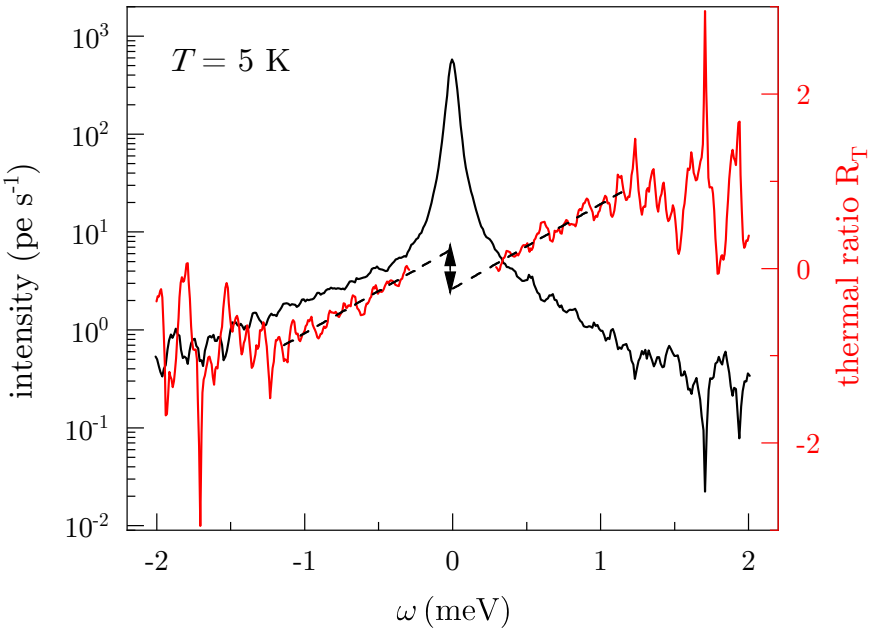

Figure 2.2: PL emission intensity and thermal ratio calculated according to Eq. (2.2) for the trion (X*) peak of double PQD sample (A) at nominal temperature $T = 5$ K. The centre of the thermal ratio (corresponding to the location of the ZPL) has been masked.

broadening. We assume that the ZPL broadening may be approximated by a Voigt profile: a convolution of a Lorentzian function and a Gaussian function. Such a function is invariant under reflection about its centre, breaking the thermal ratio defined in Eq. (2.2) (the derivation of which assumed a delta-function ZPL).

Fig. 2.3 explores the origin of the offset within the thermal ratio R_T further, looking at the thermal ratio calculated from theoretical emission spectra. The advantage of considering theoretical spectra is that Lorentzian and Gaussian broadening of the ZPL may be considered separately. It is clear from Fig. 2.3 that the Gaussian broadening does not cause a noticeable offset, but the offset associated with the Lorentzian-broadened ZPL is significant. This is due to the Lorentzian function having more pronounced tails that the corresponding Gaussian, causing the break-down of the thermal ratio for an extended frequency range surrounding the ZPL. Our findings in relation to the thermal ratio R_T guide our full theoretical fit procedure. In particular, we attribute separate Gaussian and Lorentzian broadening parameters to each spectral peak.

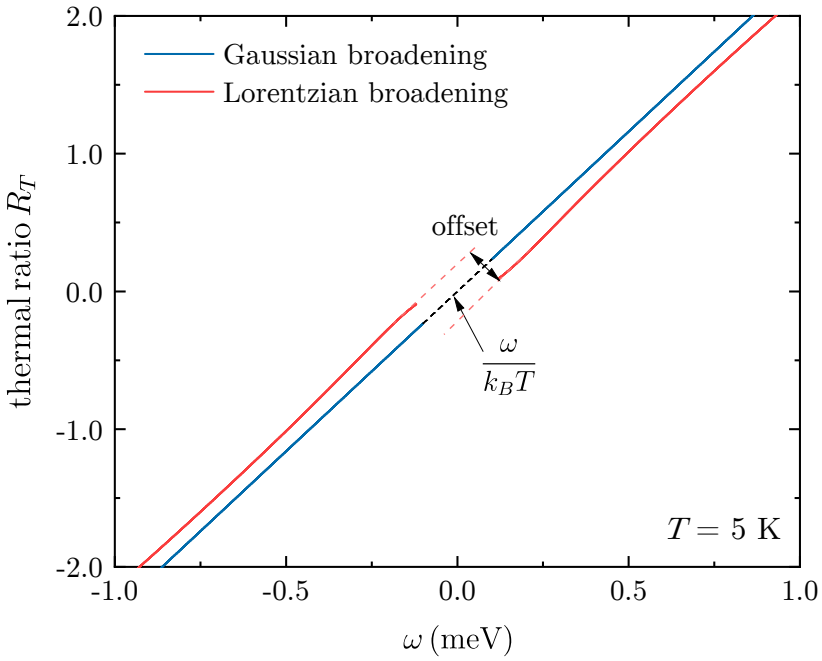

Figure 2.3: Thermal ratio calculated according to Eq. (2.2) from theoretical emission spectrum at $T = 5$ K. Polarisation $P(t)$ calculated according to the IB model, Eq. (1.56), and emission spectrum given by the real part of the Fourier transform of $P(t)$: $I(\omega) = \mathrm{Re} \int_{-\infty}^{\infty} dt\, P(t)\, e^{-i\omega t}$. ZPL modified to include Lorentzian broadening (red) and Gaussian broadening (blue), each with a FWHM of $4\,\mu$eV.

2.5 Emission spectrum: theory

Having in mind the nature of the QDs used experimentally, we must extend our IB model theory to include the case of ellipsoidal confinement potentials. This requires modification of the matrix element λ_q, but all other elements of Sec. 1.3 (Eq. (1.61) and all prior equations) apply to this more generalised case.

An ellipsoidal confinement potential produces ground state wave functions of the form,

$$\psi_{e(h)}(\mathbf{r}) = \frac{1}{\sqrt{\pi^{3/2} a_{\parallel}^2 a_{\perp}}} \exp\left(-\frac{x^2+z^2}{2a_{\parallel}^2}\right) \exp\left(-\frac{y^2}{2a_{\perp}^2}\right), \tag{2.3}$$

where, for simplicity, we have taken the case of $a_{\parallel,e} = a_{\parallel,h} = a_{\parallel}$ and $a_{\perp,e} = a_{\perp,h} = a_{\perp}$. Physically, $a_{\parallel}$ is the in-plane QD confinement length and $a_{\perp}$ is the confinement length normal to the plane. We expect our "pancake" QDs to have $a_{\parallel} > a_{\perp}$. From

Eqns. (1.51), (1.58) and (1.61), we have,

$$J(\omega) = J_0\,\omega^3 \exp\left(-\frac{a_\parallel^2 q_\parallel^2}{4}\right)\exp\left(-\frac{a_\perp^2 q_\perp^2}{4}\right), \tag{2.4}$$

where J_0 is defined in Eq. (1.66), $q_\parallel^2 = q_x^2 + q_z^2$ and $q_\perp^2 = q_y^2$. Inserting Eq. (2.4) into Eq. (1.52), noting that $q_\parallel = \omega\sin(\theta)/v_s$ and $q_\perp = \omega\cos(\theta)/v_s$,

$$K(t) = \frac{J_0}{2}\int_0^\infty d\omega \int_0^\pi d\theta \sin(\theta)\,\omega^3 \exp\left(-\frac{a_\parallel^2\omega^2\sin^2(\theta)}{2v_s^2}\right)\exp\left(-\frac{a_\perp^2\omega^2\cos^2(\theta)}{2v_s^2}\right)\alpha(\omega)\,, \tag{2.5}$$

where $\alpha(\omega) = \frac{N(\omega)}{\omega^2}\left[e^{i\omega t}-1\right] + \frac{N(\omega)+1}{\omega^2}\left[e^{-i\omega t}-1\right] + \frac{it}{\omega}$. Integrating over θ,

$$K(t) = \frac{J_0 v_s\sqrt{\pi}}{\sqrt{2}\sqrt{a_\parallel^2 - a_\perp^2}}\int_0^\infty d\omega\,\omega^2\,\mathrm{erfi}\left(\frac{\omega}{\sqrt{2}v_s}\sqrt{a_\parallel^2 - a_\perp^2}\right)\exp\left(-\frac{a_\parallel^2\omega^2}{2v_s^2}\right)\alpha(\omega)\,, \tag{2.6}$$

where erfi is the imaginary error function $\mathrm{erfi}\,(z) = -i\,\mathrm{erf}\,(iz)$. Analogously to the case of spherically symmetric confinement potential, we may separate the cumulant $K(t)$ into the rapidly decaying part $K_{BB}(t)$ and the long-time asymptotics: $K(t) = K_{BB}(t) - i\Omega_p t - S$. We arrive at an analytic function for the polaron shift Ω_p, but the Huang-Rhys factor S and $K_{BB}(t)$ require numerical integration,

$$K_{BB}(t) = \mathcal{F}\left\{\frac{J_0 v_s\sqrt{\pi}}{\sqrt{2}\sqrt{a_\parallel^2 - a_\perp^2}}N(\omega)\,\mathrm{erfi}\left(\frac{\omega}{\sqrt{2}v_s}\sqrt{a_\parallel^2 - a_\perp^2}\right)\exp\left(-\frac{a_\parallel^2\omega^2}{2v_s^2}\right)\right\}, \tag{2.7}$$

$$\Omega_p = J_0\sqrt{\frac{\pi}{2}}\frac{v_s^3}{a_\parallel^2 a_\perp}\,, \tag{2.8}$$

$$S = \frac{J_0 v_s\sqrt{\pi}}{\sqrt{2}\sqrt{a_\parallel^2 - a_\perp^2}}\int_0^\infty d\omega\,\mathrm{erfi}\left(\frac{\omega}{\sqrt{2}v_s}\sqrt{a_\parallel^2 - a_\perp^2}\right)\exp\left(-\frac{a_\parallel^2\omega^2}{2v_s^2}\right)\coth\left(\frac{\omega}{2k_BT}\right), \tag{2.9}$$

where $\mathcal{F}$ is the inverse Fourier transform. A note on the derivation of Eq. (2.7) is provided in Sec. C.1 of the Appendix.

As a final remark, it should be noted that the computational implementation of Eqns. (2.7) and (2.9) is problematic for the case $a_\parallel > a_\perp$. This is due to the behaviour of the erfi function: $\mathrm{erfi}\left(\frac{\omega}{\sqrt{2}v_s}\sqrt{a_\parallel^2 - a_\perp^2}\right) \to \infty$ as $\omega \to \infty$. This is, in fact, compensated by the factor $\exp\left(-\frac{a_\parallel^2\omega^2}{2v_s^2}\right)$, but we have found that the computational algorithm is unable to recognise this. Accordingly, we re-express Eqns. (2.7) and (2.9) in terms of the Faddeeva function $W(z)$, which is defined as,

$$W(z) = e^{-z^2}(1 + \mathrm{erfi}(z))\,. \tag{2.10}$$

We may therefore re-express Eqns. (2.7) and (2.9) as,

$$K_{BB}(t) = \mathcal{F}\left\{\frac{J_0 v_s\sqrt{\pi}}{\sqrt{2}\sqrt{a_\parallel^2 - a_\perp^2}} N_q\,\eta(\omega)\right\}, \tag{2.11}$$

$$S = \frac{J_0 v_s\sqrt{\pi}}{\sqrt{2}\sqrt{a_\parallel^2 - a_\perp^2}} \int_0^\infty d\omega\,\eta(\omega)\,\coth\left(\frac{\omega}{2k_B T}\right), \tag{2.12}$$

where

$$\eta(\omega) = W\left(\frac{\omega}{\sqrt{2}v_s}\sqrt{a_\parallel^2 - a_\perp^2}\right)\exp\left(-\frac{a_\perp^2\omega^2}{2v_s^2}\right) - \exp\left(-\frac{a_\parallel^2\omega^2}{2v_s^2}\right). \tag{2.13}$$

2.5.1 Gaussian and Lorentzian broadening

From the IB model, we know that the polarisation $P(t)$ is related to the cumulant $K(t)$ by,

$$P_{\mathrm{IBM}}(t) = \theta(t)\,e^{-i\Omega_X t}e^{K(t)}. \tag{2.14}$$

This is equivalent to Eq. (1.46) but for the case of a purely real excitation (exciton or trion) frequency Ω_X. Guided by Sec. 2.4, we now explicitly include both Gaussian and Lorentzian broadening terms. In the time domain, these terms appear as a product,

$$P(t) = P_{\mathrm{IBM}}(t)\exp\left(-\frac{\gamma_L t}{2}\right)\exp\left(-\left[\frac{\gamma_G t}{4\sqrt{\ln(2)}}\right]^2\right). \tag{2.15}$$

Note that we have defined $\gamma_{G,L}$ such that, in the frequency domain, the FWHM of a purely Gaussian (Lorentzian) broadened ZPL is equal to γ_G (γ_L). Within Eq. (2.15), we fix parameters $\rho_m = 5.67\times10^3$ kg m^3 and $v_s = 4.6\times10^3$ m/s, leaving the following free parameters: temperature T; in plane QD confinement length $a_\parallel$ and out of plane QD confinement length $a_\perp$; deformation potential $|D_c - D_v|$; Gaussian broadening FWHM γ_G; Lorentzian broadening FWHM γ_L; and, real excitation frequency Ω_X.

2.5.2 FSS adjustment

FSS occurs as a result of the electron-hole (e-h) exchange interaction, which couples the electron and hole spins of an exciton state. This coupling can be described in

terms of an effective magnetic field generated by the holes (electrons), which causes the electron (hole) spins to precess [63]. The general form of the spin Hamiltonian for the e-h exchange interaction is given by [64–66],

$$H_{\text{exch}} = -\sum_{i=x,y,z} \left(a_i J_{h,i} S_{e,i} + b_i J_{h,i}^3 S_{e,i}\right), \tag{2.16}$$

where $J_{h,i}$ ($S_{e,i}$) is the hole (electron) spin in the i-direction. Neglecting heavy-hole and light-hole mixing, the exciton is composed of a heavy hole with $J_h = 3/2$, $J_{h,z} = \pm 3/2$ and an electron with $S_e = 1/2$, $S_{e,z} = \pm 1/2$, where z labels the growth direction [64]. The z-projection of the angular momentum of the exciton $M = J_{h,z} + S_{e,z}$ may therefore take four possible values: $M = \pm 1, \pm 2$. Exciton states with $|M| = 2$ are dark (do not couple to the light field), whilst states with $|M| = 1$ are bright (optically active). The $|M| = 1$ and $|M| = 2$ states do not mix with one another [64] regardless of the crystallographic symmetry of the sample. However, for ellipsoidal QDs there is mixing between the two $|M| = 1$ states, giving eigenstates

$$|FSS_1\rangle = \frac{1}{\sqrt{2}} \left(|+1\rangle + |-1\rangle\right), \tag{2.17}$$

$$|FSS_2\rangle = \frac{1}{\sqrt{2}} \left(|+1\rangle - |-1\rangle\right), \tag{2.18}$$

where $|\pm 1\rangle$ are exciton states labelled by quantum number M. The corresponding eigenenergies are,

$$E_{FSS_1} = \frac{1}{2} \left(\delta_0 + \delta_1\right), \tag{2.19}$$

$$E_{FSS_2} = \frac{1}{2} \left(\delta_0 - \delta_1\right), \tag{2.20}$$

where δ_0 and δ_1 are parameters that depend on the shape and symmetry of the QD. We therefore expect an exciton to exhibit two linearly polarised transitions aligned with the principal axis of the QD, separated in energy by the FSS δ_1. FSS measurements performed by L. Scarpelli (described briefly in Sec. 2.2.2 above), indicate an exciton FSS of $\delta_1 = 27.31 \pm 0.14\,\mu$eV. Note that the trion (X*) transition does not exhibit any FSS: the two electrons (holes) of the trion state pair together to form a spin singlet, and the resulting exchange interaction with the hole spin is quenched.

In collecting the PL emission spectra, we measure circularly polarised σ_+ polarisation. The external magnetic field $B_z = 0.45$ T induces Zeeman splitting, generating two circularly polarised eigenstates $|+1\rangle$ and $|-1\rangle$ separated by energy δ_Z, measured by L. Scarpelli to be $28.84 \pm 1.99\,\mu$eV and $30.20 \pm 0.90\,\mu$eV for the exciton (X) and trion (X*) respectively. The trion (X*) transition therefore appears in the PL spectrum as a single peak at the energy of the $|+1\rangle$ Zeeman eigenstate. For the exciton (X) transition, however, there is competition between the linearly polarised FSS states and circularly polarised Zeeman states, giving rise to elliptical polarisation. The eigenstates of the Hamiltonian $H = H_{Zeeman} + H_{exch}$ are the following [64],

$$|L_1\rangle = \frac{1}{\sqrt{1+C_+^2}} \left(|+1\rangle + C_+ |-1\rangle\right) , \tag{2.21}$$

$$|L_2\rangle = \frac{1}{\sqrt{1+C_-^2}} \left(|+1\rangle + C_- |-1\rangle\right) , \tag{2.22}$$

where $C_\pm = \kappa \pm \sqrt{1+\kappa^2}$ and κ is the ratio of the Zeeman and fine structure splittings: $\kappa = \delta_Z/\delta_1$. The corresponding eigenenergies are [64]:

$$E_{L_1} = \frac{1}{2}\left(\delta_0 + \sqrt{\delta_1^2 + \delta_Z^2}\right) \tag{2.23}$$

$$E_{L_1} = \frac{1}{2}\left(\delta_0 - \sqrt{\delta_1^2 + \delta_Z^2}\right) \tag{2.24}$$

In the PL spectrum (measured in the σ_+ channel), this equates to two exciton (X) peaks separated in frequency by $\sqrt{\delta_1^2 + \delta_Z^2} = 39.7\,\mu$eV, the higher energy exciton peak having an intensity of $[1 + C_+^2]/[1 + C_-^2] = 6.35$ times that of the lower energy exciton peak.

2.5.3 Full PL emission spectrum

As previously discussion, the double PQD samples show a low energy trion (X*) peak and a higher energy exciton (X) peak. These peaks are separated by ~ 4 meV, which is of the same order as the frequency width of the phonon broadband. We must therefore fit both peaks together, summing the contribution from each excitation in the frequency domain to give the total PL emission. The single PQD

sample, however, shows only a trion (X*) peak,

$$I(\omega) = \begin{cases} \alpha_{X^*} I_{X^*}(\omega) + \alpha_X I_X(\omega) & \text{double PQD,} \\ \alpha_{X^*} I_{X^*}(\omega) & \text{single PQD,} \end{cases} \tag{2.25}$$

where α_{X,X^*} are the transition intensities, and $I_{X,X^*}(\omega) = \mathrm{Re} \int_{-\infty}^{\infty} dt\, P_{X,X^*}(t)\, e^{-i\omega t}$ with P_{X,X^*} calculated according to Eq. (2.15). The peak intensities α_{X,X^*} depend upon the excitation efficiency including the carrier relaxation from excited states down to the band edges of the QD and are a free parameter of the fit. Finally, taking into account the FSS of the exciton (X) transition, we arrive at the following expression:

$$I(\omega) = \begin{cases} \alpha_{X^*} I_{X^*}(\omega) + \alpha_X \left[I_X(\omega) + 6.35\, I_X(\omega + 39.7\,\mu\mathrm{eV}) \right] & \text{double PQD,} \\ \alpha_{X^*} I_{X^*}(\omega) & \text{single PQD.} \end{cases} \tag{2.26}$$

Eq. (2.26) contains 12 free parameters (or 8 for the single PQD sample) to be determined by the fit procedure: each excitation peak has associated confinement lengths $a_\parallel$, $a_\perp$, Gaussian and Lorentzian broadening parameters $\gamma_{G,L}$, excitation transition frequency Ω_X and intensity scaling factor $\alpha_X(\alpha_{X^*})$.

2.6 Fit procedure

As previously discussed, we have a total of 19 PL spectra originating from measurements of three different samples (two double PQDs and one single PQD). At the low temperatures under consideration, $T \leq 100$ K, we anticipate minimal thermal expansion of the QD structure and therefore expect the QD confinement potentials $a_\parallel$, $a_\perp$ to be constant for each sample. Furthermore, all samples are of the same basic construction and therefore we expect the material-dependent deformation potential $|D_c - D_v|$ to be consistent across all measured PL spectra. Guided by these principles, we implement a two-fold fit procedure.

We initially fit all 19 measured PL spectra according to the method outlined in Sec. 2.6.1 below, with each double PQD spectrum providing 12 parameter values and associated σ (68%) confidence intervals, and each single PQD spectrum providing 8 parameter values and associated σ confidence intervals.

Parameter		Fit Value (with σ confidence bound)	
		X*	X
$\lvert D_c - D_v \rvert$	(eV)	7.48 (0.07)	
$a_\perp$	(nm)	1.76 (0.02)	1.78 (0.06)
$a_\parallel$	(nm)	5.74 (0.04)	5.81 (0.12)

Table 2.1: $1/\sigma^2$ weighted average of deformation potential $|D_c - D_v|$, trion (X*) and exciton (X) confinement lengths $a_\perp$, $a_\parallel$ for double PQD sample (A).

For the single PQD sample, we take the $1/\sigma^2$ weighted average of the fit-determined trion confinement length parameters $a_\perp$ and $a_\parallel$ across all measured temperatures $T = 5$, 10, 15, 20 and 30. Similarly, for each double PQD sample we take the $1/\sigma^2$ weighted average of the fit-determined trion and exciton confinement length parameters $a_\perp$, $a_\parallel$ across all measured temperatures $T = 5$, 10, 15, 20, 30, 50 and 100 K. To fix the deformation potential $|D_c - D_v|$, we take the $1/\sigma^2$ weighted average over all 19 PL spectra. The resulting parameter values for double PQD sample (A) are given in Table 2.1, with those for double PQD sample (B) and the single PQD sample given in Secs. C.3 and C.4 of the Appendix respectively. In relation to the confinement lengths, it is interesting to compare our results to the dimensions calculated from diamagnetic shift measurements undertaken on a similar sample [39]. This comparison was carried out by E. A. Muljarov, applying the exciton and hole wavefunctions of Eq. (2.3) to the measured diamagnetic shifts in order to ensure consistency with our theoretical model. The diamagnetic shift measurements suggest $a_\parallel = 7$ nm and $a_\perp = 5$ nm, which is in reasonable agreement with our findings of $a_\parallel = 5.8$, 6.2, 5.3 nm and $a_\perp = 1.8$, 1.8, 3.1 nm for double PQD samples (A) & (B) and the single PQD sample respectively[1].

We are now in a position to constrain the deformation potential and the QD confinement parameters according to calculated $1/\sigma^2$ weighted averages. We apply the procedure outlined in Sec. 2.6.1 again to all PL spectra, fixing the deformation potential and QD confinement lengths appropriately. It is the output of this second, constrained, fitting cycle that provides our final results.

[1]For double PQD samples, the average of trion (X*) and exciton (X) parameter values are quoted here.

2.6.1 Procedure per measured PL spectrum

This section outlines the procedure applied to each measured PL spectrum in both the initial fitting cycle (no constraints) and the subsequent fitting cycle (deformation potential and QD confinement parameters fixed). Initially, the measured PL data is plotted and clearly erroneous data or peaks that are not to be included in the fit are manually masked from the fit procedure. The noise associated with each data point σ_i is calculated according to Eq. (2.1) of Sec. 2.2.3 and provides a weighting to the least squares fit procedure. We seek to minimise the quantity

$$\sum_i \left(\frac{y_i - Y_i}{\sigma_i} \right)^2 , \tag{2.27}$$

for measured PL intensity y_i and fit PL intensity Y_i. From this minimisation procedure, we find the set of fit parameters that maximise agreement between the theoretical spectrum of Eq. (2.26) and the experimentally observed PL data. We also calculate σ (68%) confidence intervals for each fit parameter using the inverse R-factor from QR decomposition of the Jacobian, the degrees of freedom for error, and the root mean squared error (RMSE).

2.7 Results and analysis

Figs. 2.4 and 2.5 show the experimental and fitted PL spectra for double PQD sample (A) at nominal temperatures $T = 20$ K and $T = 30$ K respectively. Also shown are tabulated fit values and associated σ confidence bounds. All other spectra and tabulated fit values are provided in Secs. C.2, C.3 and C.4 of the Appendix.

The figures show very good agreement between the experimental PL spectra and the respective theoretical fit. This is a good indication that our model provides sufficient degrees of freedom to accurately capture the true physical picture. On the other hand, the σ confidence intervals associated with the fit parameters are, in general, a small fraction of the respective parameter itself. This suggests that we have no redundant degrees of freedom. These findings are particularly relevant in relation to the broadening parameters, suggesting that a Voigt profile (convolution of Lorentzian and Gaussian) provides a good approximation of the true lineshape.

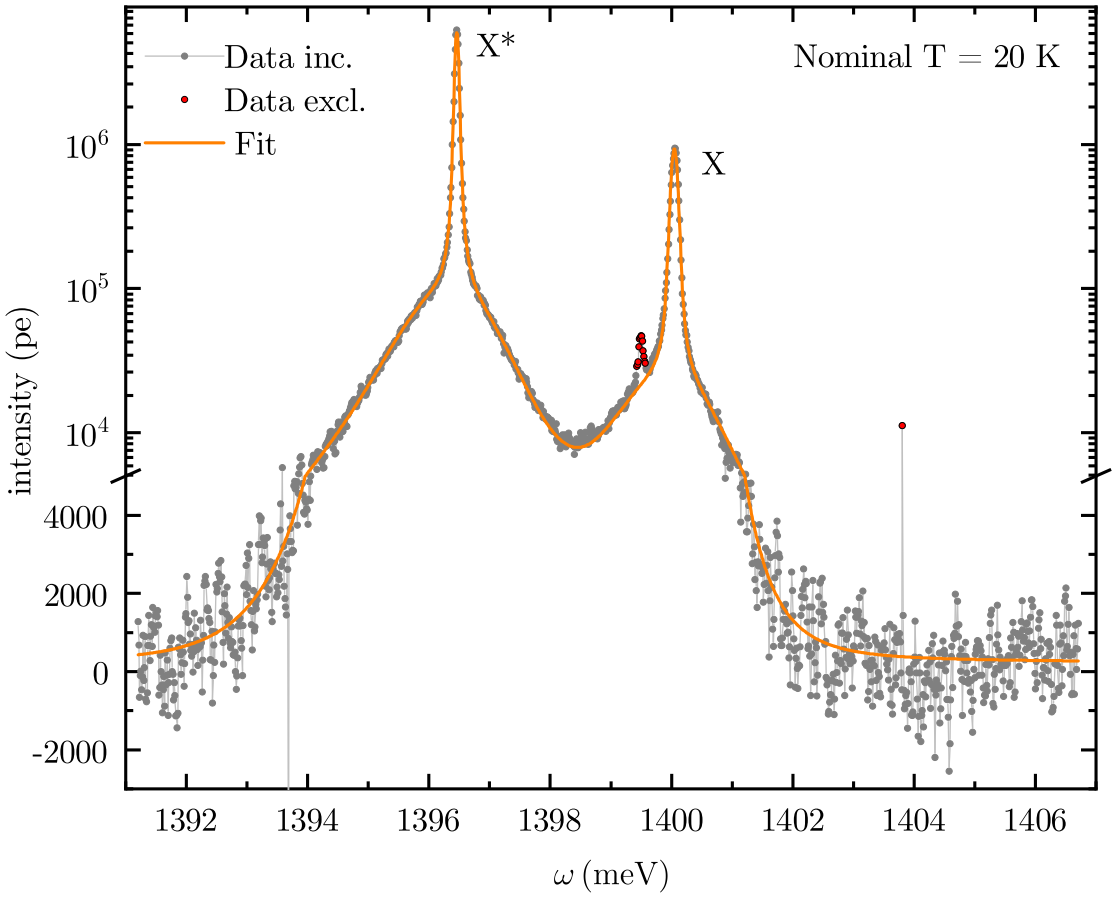

(a) Experimental and fitted PL emission spectra, showing data manually excluded from fit in red.

Parameter		Fit Value (with σ confidence bound)	
		X*	X
T	(K)	19.73 (0.33)	
γ_L	(μeV)	31.74 (1.57)	41.16 (2.60)
γ_G	(μeV)	57.48 (3.12)	96.24 (4.08)
$\omega_X - \omega_{\text{ref}}$	(meV)	-0.22 (8.85E-04)	3.27 (1.16E-03)
α		5.99E+06 (2.16E+05)	8.29E+05 (2.78E+04)

(b) Tabulated fit values, with deformation potential and QD confinement lengths fixed to the values detailed in Table 2.1. Reference frequency $\omega_{\text{ref}} = 1,396.64$ meV

Figure 2.4: PL spectrum and fit for double PQD sample (A) with nominal temperature $T = 20$ K.

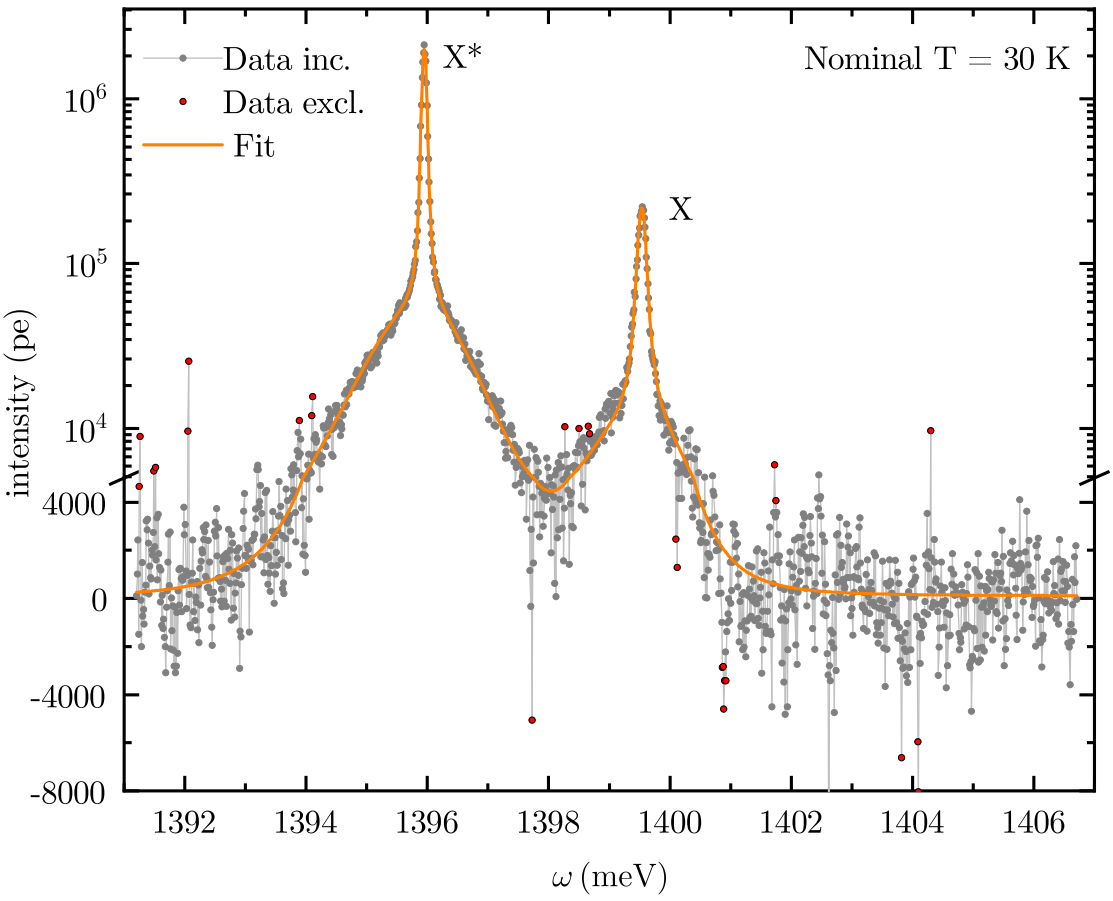

(a) Experimental and fitted emission PL spectra, showing data manually excluded from fit in red.

Parameter		Fit Value (with σ confidence bound)	
		X*	X
T	(K)	29.23 (0.34)	
γ_L	(μeV)	36.19 (0.94)	91.28 (3.17)
γ_G	(μeV)	62.58 (1.55)	83.00 (5.01)
$\omega_X - \omega_{\text{ref}}$	(meV)	-0.73 (3.78E-04)	2.86 (7.55E-04)
α		1.99E+06 (3.62E+04)	1.92E+05 (3.30E+03)

(b) Tabulated fit values, with deformation potential and QD confinement lengths fixed to the values detailed in Table 2.1. Reference frequency $\omega_{\text{ref}} = 1,396.64$ meV

Figure 2.5: PL spectrum and fit for double PQD sample (A) with nominal temperature $T = 30$ K.

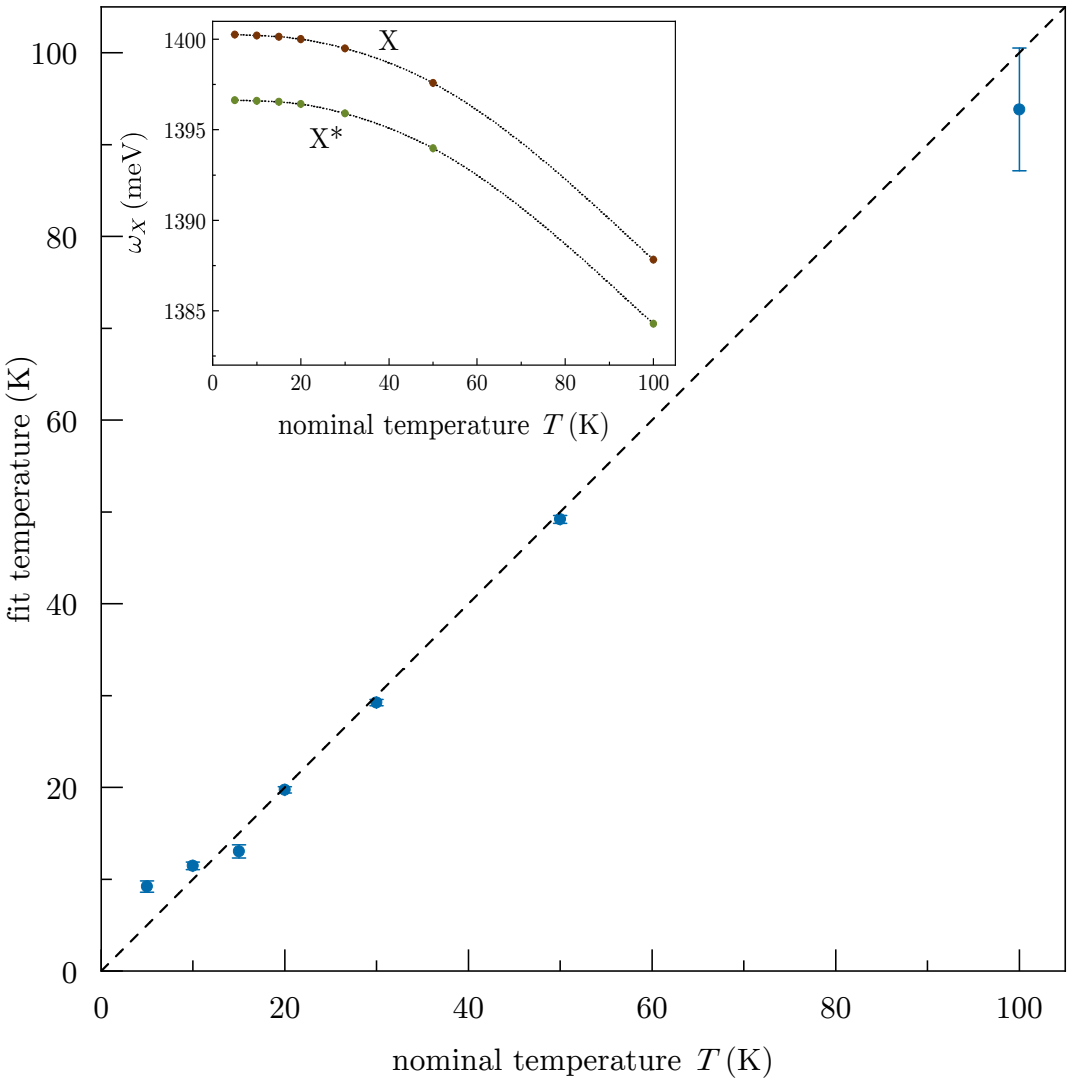

Figure 2.6: Fit temperature (with σ error bars) as a function of nominal temperature, shown for double PQD sample (A). Inset: excitation (exciton/trion) transition frequency as a function of nominal temperature, shown for double PQD sample (A).

Recalling our original goal of creating a "phonon thermometer", we now examine whether the temperatures determined by the fit procedure are commensurate to the nominal (cryostat-measured) temperatures of the system. Fig. 2.6 shows the relationship between the fit temperature and the nominal temperature for double PQD sample (A). Equivalent plots for double PQD sample (B) and the single PQD sample can be respectively found in Secs. C.3 and C.4 of the Appendix. We see from Fig. 2.6 that there is generally very good agreement between the fit temperature and the nominal (cryostat-measured) temperature. This is particularly true within

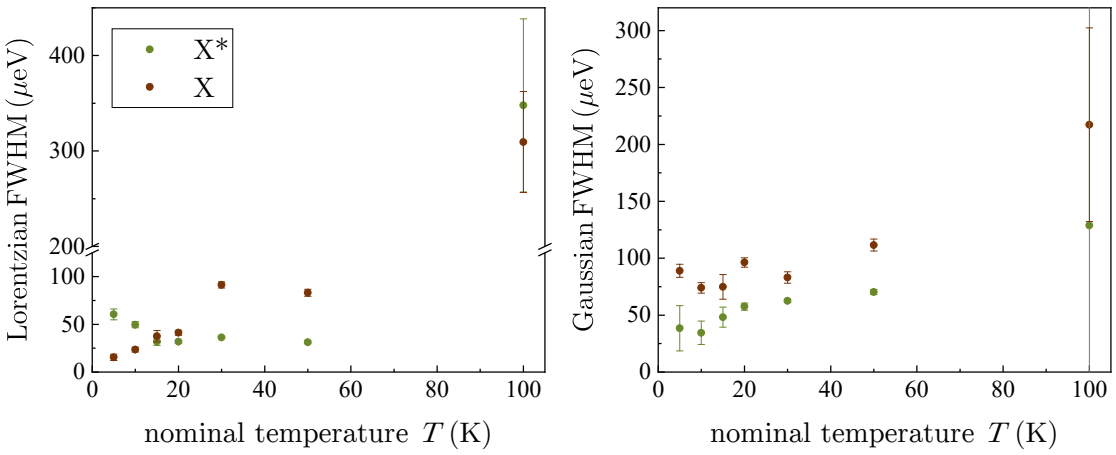

Figure 2.7: Lorentzian γ_L and Gaussian γ_G broadening parameters (with σ error bars) as a function of nominal temperature, shown for double PQD sample (A).

the temperature range $20 \leq T \leq 50$ K. For $T < 10$ K, however, the fit procedure suggests higher temperatures than those measured by the cryostat. The picture is similar in relation to the other samples, shown in Secs. C.3 and C.4 of the Appendix.

Clearly the low temperature discrepancies could be indicative of a flaw within the fit procedure. One potential explanation is that the phonon broadband weight (which carries the temperature-dependence) constitutes only a small proportion of the total PL spectrum at such low temperatures. Non-equilibrium effects not taken into account in the theoretical model may also influence the measured PL spectrum. Alternatively, it is feasible that the fit temperature provides a more accurate indication of the true sample temperature than the cryostat measurement. Further investigation is required in order to attribute the origin of this low temperature deviation with any degree of certainty.

Focusing now on the inset of Fig. 2.6, we see that the trion (X*) and exciton (X) transition frequencies exhibit approximately equivalent temperature-dependent behaviour. This behaviour is well-understood in bulk semiconductors [67], with dot-specific influences in GaAs/InGaAs QDs expected to be small [68]. We attribute the observed temperature-dependent bandgap reduction to (i) scattering of electrons by phonons, and (ii) thermal expansion of the lattice [68].

Fig. 2.7 shows the behaviour of the Lorentzian and Gaussian broadening parameters $\gamma_{L,G}$ for double PQD sample (A). Equivalent plots for double PQD sample (B) and the single PQD sample can be respectively found in Secs. C.3 and C.4 of the Appendix. With reference to Fig. 2.7, we see a weak dependence of the broadening parameters with temperature. In general, there is an increase in broadening with temperature, although this is not the case for the Lorentzian broadening of the exciton transition in double PQD sample (A). We note that the error bars, denoting the σ confidence intervals, are very large at $T = 100$ K. This is understandable: the phonon broadband is significant at high temperature, which diminishes the prominence of the Lorentzian tails, making it difficult to separate the total broadening into Gaussian and Lorentzian components.

We tentatively attribute the Lorentzian broadening to the radiative lifetime of the excited state (exciton or trion) and pure dephasing mechanisms, and the Gaussian broadening to spectral diffusion due to charging and trap states. However, the exact physical origin of the Lorentzian and Gaussian broadening profiles is not clear and further investigation is required in order to gain a full understanding of the temperature-dependent behaviour.

2.8 Chapter conclusion

To conclude this chapter, we have shown that the influence of the phonon environment on QD PL emission spectra can be successfully exploited as a "phonon thermometer". A simple thermal ratio provides a good indication of temperature, but this is improved by a full fit procedure. Moreover, the fit procedure enables straightforward determination of other QD parameters that are traditionally difficult to measure. Measurement of QD confinement lengths, for example, is typically performed through diamagnetic shift experiments [39], whilst deformation potential measurements require the application of hydrostatic pressure generated through use of a diamond anvil cell [69, 70].

In order to progress this research direction further, it would be beneficial to examine the PL spectra under resonant excitation so as to target the excitonic

ground state and mitigate the effect of higher energy states. It would also be prudent to perform time-resolved spectroscopy in order to gain a better understanding of the equilibration timescales and establish whether non-equilibrium effects significantly influence the PL spectra and hence the fit parameters. It is our vision that the fit procedure outlined in this chapter will not only provide a phonon-based temperature measurement but also constitute a simple method for determining key QD parameters.

3

Phonon-induced dephasing in a QD-cavity system

As discussed in the introductory chapter, the task of rigorously accounting for phonon-induced decoherence in a qubit-cavity system is a long-standing fundamental problem within cavity quantum electrodynamics (cavity-QED). It is natural to draw upon the JC and IB models when addressing this problem, but the combination of the two models presents a significant challenge. Various approaches to the QD-cavity problem have been suggested in the literature, ranging from Born-Markov approximations [15, 16, 28] to path-integral methods [19, 21] and non-equilibrium Green's function techniques [22]. These approaches can be broadly divided into perturbative and non-perturbative methods.

The weak coupling master equation is commonly employed in the regime of weak exciton-phonon interactions. This approach relies upon a perturbative treatment of the exciton-phonon interaction and has been applied in the Markovian [20, 71] and non-Markovian [72, 73] regimes. For stronger exciton-phonon interactions, the polaron master equation is more appropriate. Here, the exciton-phonon coupling is assumed to be the dominant interaction, modifying the exciton state to a polaron (phonon-dressed exciton) state. Formally, this modification is made through a polaron transformation of the system Hamiltonian, with the polaron-

cavity interaction treated perturbatively to the second order Born approximation [15, 16, 28, 29] or beyond [20, 22]. These perturbative master-equation approaches work well if the polaron formation time is much quicker than the polariton dynamics, but fail when these timescales become comparable [28].

Non-perturbative techniques based on a quasi-adiabatic Feynman path-integral scheme [74] enable accurate numerical solutions but are computationally expensive and provide little insight into the underlying physics. Nahri *et al.* [21] apply a tensor multiplication scheme [74] to the case of a QD-cavity system with super-ohmic spectral density. This technique requires a complex algorithm with an "on-the-fly path selection" optimization [75]. Glassl *et al.* [19] present a real-time path-integral scheme [76] adapted for a QD in a loss-less cavity. Cavity and QD dampings are included in later work [77], but in this case the exciton-phonon coupling is added phenomenologically.

We present, in this Chapter, a new method that has been developed in response to the problem of incorporating phonon-induced dephasing within a model for the QD-microcavity system. Our method provides an asympotically exact solution to this longstanding problem, alongside simple analytic approximations. Central to our approach is a Trotter decomposition of the full system Hamiltonian into two exactly solvable parts: (i) a phonon-free JC model part and (ii) an independent boson model part. Crucially, our approach is valid for all exciton-phonon coupling strengths. Further, it takes the effects of the exciton-photon and exciton-phonon coupling on equal footing, thereby providing access to regimes of comparable polaron and polariton timescales.

3.1 Hamiltonian and linear polarisation

When phonon interactions are taken into account, the JC Hamiltonian of Eq. (1.19) gains two extra terms, $H_{\rm ph}$ and $d^\dagger dV$:

$$H = \omega_X d^\dagger d + \omega_C a^\dagger a + g(a^\dagger d + d^\dagger a) + H_{\rm ph} + d^\dagger dV\,, \tag{3.1}$$

In analogy to Sec. 1.3, H_{ph} characterises the contribution from the phonon continuum and V characterises the exciton-phonon coupling,

$$H_{\mathrm{ph}} = \sum_q \omega_q b_q^\dagger b_q \,, \tag{3.2}$$

$$V = \sum_q \lambda_q^* b_q + \lambda_q b_q^\dagger \,, \tag{3.3}$$

where, as in Sec. 1.3, $b_{\mathbf{q}}^\dagger$ ($\omega_{\mathbf{q}}$) is the creation operator (frequency) of the q-th phonon mode, and $\lambda_{\mathbf{q}}$ is the matrix element of the exciton-phonon coupling for this mode. Note that Eqs. (3.2) and (3.3) are identical to the terms of the IB model given in Eqs. (1.35) and (1.37) respectively.

A key principle of the present method is a separation of the system Hamiltonian H into two exactly solvable parts, $H = H_{\mathrm{JC}} + H_{\mathrm{IB}}$, described by the JC and IB models respectively:

$$H = \underbrace{\omega_X d^\dagger d + \omega_C a^\dagger a + g(a^\dagger d + d^\dagger a)}_{H_{\mathrm{JC}}} + \underbrace{H_{\mathrm{ph}} + d^\dagger d V}_{H_{\mathrm{IB}}} \,, \tag{3.4}$$

where H_{JC} is identical to the Jaynes-Cummings Hamiltonian given in Eq. (1.19), and H_{IB} is equal to the independent boson model Hamiltonian Eq. (1.34) without the term $\omega_X d^\dagger d$ (which is taken into account through the JC component).

While our approach is general and suited for describing the dynamics of any elements of the reduced density matrix of the JC sub-system, we will concentrate on the most simple and intuitively clear quantities: the linear optical polarisation and associated absorption. For this purpose, it is sufficient to reduce the basis of the exciton-cavity system to the three states outlined in Sec. 1.1: the absolute ground state $|0\rangle$, the excitonic excitation $|X\rangle$, and the cavity excitation $|C\rangle$. In this basis, $d^\dagger = |X\rangle\langle 0|$ and $a^\dagger = |C\rangle\langle 0|$.

In analogy with our treatment of the JC and IB systems, we take as our starting point the standard definition of polarisation, given by Eq. (1.1). We consider the case of a pulsed excitation of the form

$$\mathcal{V} = \mu(\tilde{c}^\dagger + \tilde{c}) \,, \tag{3.5}$$

where μ is the dipole moment and the creation operator $\tilde{c}^\dagger$ may be either the exciton creation operator $d^\dagger$ or the cavity creation operator $a^\dagger$, depending on the mode of excitation. We apply the excitation at time $t = 0$ to a fully unexcited system described by density matrix $\rho(-\infty)$:

$$\rho(-\infty) = |0\rangle\langle 0| \otimes \rho_0\,, \qquad \rho_0 = \frac{e^{-\beta H_{\mathrm{ph}}}}{\mathrm{Tr}\left\{e^{-\beta H_{\mathrm{ph}}}\right\}_{\mathrm{ph}}}\,. \tag{3.6}$$

Here, $\beta = (k_B T)^{-1}$, and the trace is taken over all possible phonon states. The density matrix immediately after excitation is therefore given by

$$\rho(0_+) = e^{-i\mathcal{V}}\rho(-\infty)e^{i\mathcal{V}}, \tag{3.7}$$

To evaluate Eq. (3.7), we expand the exponential terms $e^{\pm i\mathcal{V}}$ as Taylor series and, considering the linear polarisation, take only the terms that are linear in μ. Subsequent temporal evolution is described by the standard Lindblad master equation,

$$i\dot{\rho} = [\mathcal{H}, \rho] + i\gamma_X\left(2d\rho d^\dagger - d^\dagger d\rho - \rho d^\dagger d\right) + i\gamma_C\left(2a\rho a^\dagger - a^\dagger a\rho - \rho a^\dagger a\right)\,, \tag{3.8}$$

where $\mathcal{H}$ is the Hermitian counterpart to the full Hamiltonian given by Eq. (3.4):

$$\mathcal{H} = \Omega_X d^\dagger d + \Omega_C a^\dagger a + g(a^\dagger d + d^\dagger a) + H_{\mathrm{ph}} + d^\dagger d V\,. \tag{3.9}$$

Note that complex frequencies $\omega_{X,C}$ of Eq. (3.4) have been replaced with their respective real components $\Omega_{X,C}$; the dissipative (imaginary) components $gamma_{X,C}$ are accounted for separately within the Lindblad master equation. We focus on the strong coupling regime, in which γ_X and γ_C may be treated as approximately constant parameters.

Formally solving Eq. (3.8) (see Sec. D.1 for details) gives the linear polarisation in terms of a 2×2 matrix $\hat{P}(t)$ with the matrix elements $P_{jk}(t)$

$$P_{jk}(t) = \langle\langle j|\,\hat{U}(t)\,|k\rangle\rangle_{\mathrm{ph}}\,, \tag{3.10}$$

where $\langle\ldots\rangle_{\mathrm{ph}}$ denotes the expectation value over all phonon degrees of freedom in thermal equilibrium, $j, k = X, C$, and $\hat{U}(t)$ is the time evolution operator,

$$\hat{U}(t) = e^{iH_{\mathrm{ph}}t}e^{-iHt}\,. \tag{3.11}$$

In Eq. (3.10), j indicates the feeding channel and k indicates the mode in which the polarisation is measured. For example, P_{XX} (P_{CC}) denotes the excitonic (photonic) polarisation under a pulsed exciton (cavity) excitation.

3.2 Trotter's decomposition approach

Using Trotter's decomposition theorem, the time evolution operator $\hat{U}(t)$ of Eq. (3.11) can be re-expressed as

$$\hat{U}(t) = \lim_{\Delta t \to 0} e^{iH_{\rm ph}t} \left(e^{-iH_{\rm IB}\Delta t} e^{-iH_{\rm JC}\Delta t} \right)^N , \tag{3.12}$$

where $\Delta t = t/N$. We introduce two new operators, $\hat{M}$ and $\hat{W}$, associated with the JC and IB Hamiltonians, respectively,

$$\hat{M}(t_n - t_{n-1}) = \hat{M}(\Delta t) = e^{-iH_{\rm JC}\Delta t}, \tag{3.13}$$

$$\hat{W}(t_n, t_{n-1}) = e^{iH_{\rm ph}t_n} e^{-iH_{\rm IB}\Delta t} e^{-iH_{\rm ph}t_{n-1}}, \tag{3.14}$$

where $t_n = n\Delta t$. Exploiting the commutivity of $H_{\rm JC}$ and $H_{\rm ph}$ enables us to express the time evolution operator as a time-ordered product of pairs $\hat{W}\hat{M}$ (see Sec. D.2 of the Appendix for details):

$$\hat{U}(t) = \mathcal{T} \prod_{n=1}^{N} \hat{W}(t_n, t_{n-1}) \hat{M}(t_n - t_{n-1}), \tag{3.15}$$

where $\mathcal{T}$ is the time ordering operator. Noting that both $\hat{W}$ and $\hat{M}$ are 2×2 matrices in the $|X\rangle$, $|C\rangle$ basis and that $\hat{W}$ is diagonal (with diagonal elements W_i), the polarisation Eq. (3.10) takes the form

$$\begin{aligned} P_{jk}(t) = \sum_{i_{N-1}=X,C} \cdots \sum_{i_1=X,C} & M_{i_N i_{N-1}} \dots M_{i_2 i_1} M_{i_1 i_0} \\ & \times \langle W_{i_N}(t, t_{N-1}) \dots W_{i_2}(t_2, t_1) W_{i_1}(t_1, 0) \rangle_{\rm ph} , \end{aligned} \tag{3.16}$$

where $i_N = j$, $i_0 = k$, $M_{i_n i_m} = [\hat{M}(\Delta t)]_{i_n i_m}$, and

$$W_{i_n}(t_n, t_{n-1}) = \mathcal{T} \exp\left\{ -i\delta_{i_n X} \int_{t_{n-1}}^{t_n} V(\tau) d\tau \right\} \tag{3.17}$$

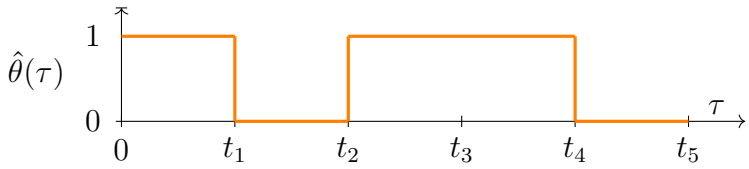

Figure 3.1: Example realisation with $N = 5$. In this realisation, $i_1 = X$, $i_2 = C$, $i_3 = X$, $i_4 = X$, $i_5 = C$, as is clear from the step function $\hat{\theta}(t)$.

with δ_{ij} the Kronecker delta and $V(\tau) = e^{iH_{\rm ph}\tau}Ve^{-iH_{\rm ph}\tau}$ is the interaction representation of the exciton-phonon coupling V given by Eq. (3.3). Further details of the derivation of Eq. (3.16) are given in Sec. D.2 of the Appendix.

It is instructive at this point to introduce the concept of a "realisation" of the system as a particular combination of indices i_n within the full summation of Eq. (3.16). We associate with each realisation a step-function $\hat{\theta}(\tau)$ being equal to 0 over the time interval $t_n - t_{n-1}$ if the system is in state $|C\rangle$ ($i_n = C$) or equal to 1 if the system is in state $|X\rangle$ ($i_n = X$). An example realisation and associated step function $\hat{\theta}(\tau)$ is illustrated in Fig. 3.1. The product of W-operators for a particular realisation may be written as

$$W_{i_N}(t, t_{N-1}) \dots W_{i_1}(t_1, 0) = \mathcal{T} \exp\left\{-i \int_0^t \bar{V}(\tau) d\tau\right\}, \tag{3.18}$$

where $\bar{V}(\tau) = \hat{\theta}(\tau)V(\tau)$. Now, applying the linked cluster theorem [5, 6, 10], described in Sec. 1.3, for calculating the trace of Eq. (3.18) over all phonon states, we obtain

$$\langle W_{i_N}(t, t_{N-1}) \dots W_{i_2}(t_2, t_1) W_{i_1}(t_1, 0)\rangle_{\rm ph} = e^{\bar{K}(t)}, \tag{3.19}$$

where

$$\bar{K}(t) = -\frac{1}{2} \int_0^t d\tau_1 \int_0^t d\tau_2 \langle \mathcal{T} \bar{V}(\tau_1) \bar{V}(\tau_2)\rangle \tag{3.20}$$

is the linear cumulant for the particular realisation. The explicit dependence of Eq. (3.20) on the specific indices i_n of the realisation is given by

$$\bar{K}(t) = \sum_{n=1}^{N} \sum_{m=1}^{N} \delta_{i_n X} \delta_{i_m X} K_{|n-m|}, \tag{3.21}$$

where

$$K_{|n-m|} = -\frac{1}{2} \int_{t_{n-1}}^{t_n} d\tau_1 \int_{t_{m-1}}^{t_m} d\tau_2 \langle \mathcal{T} V(\tau_1) V(\tau_2)\rangle. \tag{3.22}$$

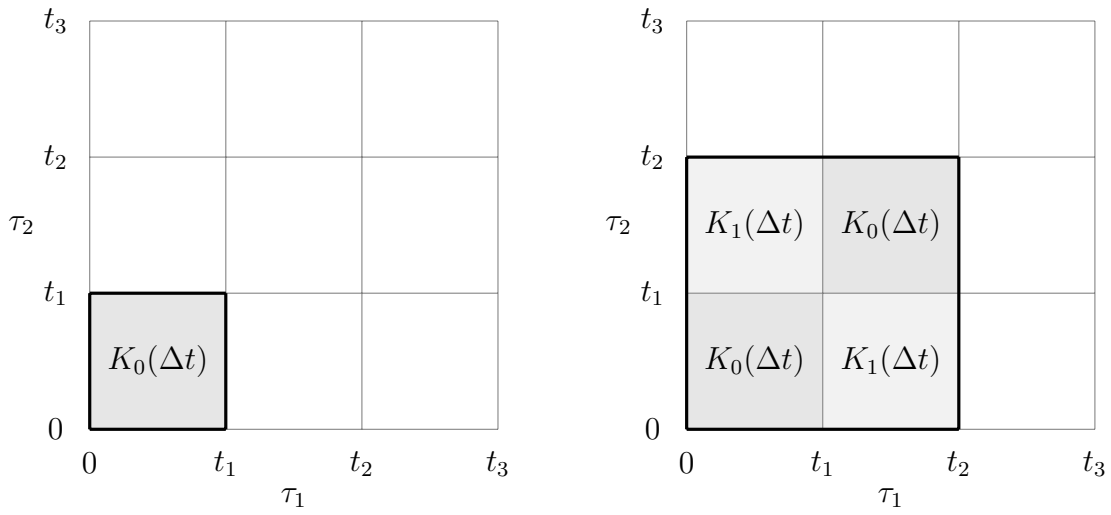

Figure 3.2: Graphical representation of the use of the IB model cumulant $K(t)$ for finding $K_{|n-m|}$, which provides examples of calculating K_0 (left) and K_1 (right).

Note that $K_{|n-m|}$ depends only on the time difference $|t_n - t_m| = \Delta t|n-m|$. Furthermore, all $K_{|n-m|}$ can be efficiently calculated from the standard IB model cumulant $K(t)$, described in Sec. 1.3. For example, inserting $m = n$ into Eq. (3.22), we find K_0 is given by

$$K_0 = -\frac{1}{2}\int_0^{t_1} \mathrm{d}\tau_1 \int_0^{t_1} \mathrm{d}\tau_2 \langle \mathcal{T} V(\tau_1) V(\tau_2)\rangle = K(\Delta t)\,, \tag{3.23}$$

where $K(t)$ is the IB cumulant calculated in Sec. 1.3.1. Calculation of K_0 therefore simply requires evaluation of the IB cumulant $K(t)$ at time $t = \Delta t$.

Analogously, to find K_1 we may set $m = 1$ and $n = 2$ which gives

$$K_1 = -\frac{1}{2}\int_{t_1}^{t_2} \mathrm{d}\tau_1 \int_0^{t_1} \mathrm{d}\tau_2 \langle \mathcal{T} V(\tau_1) V(\tau_2)\rangle\,, \tag{3.24}$$

or, by setting $m = 2$ and $n = 1$ instead, we obtain the same result:

$$K_1 = -\frac{1}{2}\int_0^{t_1} \mathrm{d}\tau_1 \int_{t_1}^{t_2} \mathrm{d}\tau_2 \langle \mathcal{T} V(\tau_1) V(\tau_2)\rangle\,. \tag{3.25}$$

Eqs. (3.24) and (3.25) correspond to the squares labeled as K_1 in Fig. 3.2. In order to calculate K_1 from the IB cumulant, we note that

$$K(2\Delta t) = 2K_0 + 2K_1. \tag{3.26}$$

Therefore,

$$K_1 = \frac{1}{2}\left[K(2\Delta t) - 2K_0\right]. \tag{3.27}$$

In general, all the integrals K_p can be found recursively:

$$K_{p>0} = \frac{1}{2}\left[K((p+1)\Delta t) - (p+1)K_0 - \sum_{q=1}^{p-1} 2(p+1-q)K_q\right] . \tag{3.28}$$

Having in mind an application of this theory to semiconductor QDs coupled to bulk acoustic phonons, we use the conditions of the super-Ohmic coupling spectral density and a finite phonon memory time [76]. This finite phonon memory time is exactly τ_{IB} calculated in Sec. 1.3.2. Having a finite phonon memory time allows us to reduce dramatically the number of terms in the double summation of Eq. (3.21). Indeed, we need to take into account only instances in which $|t_m - t_n| \leqslant \tau_{\mathrm{IB}}$. When selecting Δt, we must also be mindful of the requirement imposed by the Trotter decomposition method: $\Delta t \to 0$, which in reality corresponds to the condition $\Delta t \ll \tau_{\mathrm{JC}}$. Here, τ_{JC} characterises the timescale of energy exchange between the exciton and cavity states, and, as discussed in Sec. 1.2, is related to the polariton splitting $\Delta\Omega$ by $\tau_{\mathrm{JC}} \approx 2\pi/\Delta\Omega$.

We initially consider the most straightforward application of the technique, which will be referred to as the nearest neighbour regime.

3.2.1 Nearest neighbour (NN) regime

In the NN approach, we limit our consideration to $|n - m| \leqslant 1$, selecting $\Delta t \approx \tau_{\mathrm{IB}}$ so as to best satisfy both aforementioned conditions on Δt. This approach is therefore only valid if the polariton timescale τ_{JC} is much longer than the phonon memory time τ_{IB}.

In the NN case, the summation over n and m in Eq. (3.21) is simplified to

$$\bar{K}(t) = \delta_{i_N X} K_0 + \sum_{n=1}^{N-1} \delta_{i_n X}\left(K_0 + 2\delta_{i_{n+1} X} K_1\right) . \tag{3.29}$$

Crucially, this reduction to a single summation allows us to re-express Eq. (3.16) as

$$P_{jk}(t) = e^{\delta_{jX} K_0} \sum_{i_{N-1}} \cdots \sum_{i_1} G_{i_N i_{N-1}} \ldots G_{i_2 i_1} M_{i_1 k} , \tag{3.30}$$

where

$$G_{i_n i_{n-1}} = M_{i_n i_{n-1}} e^{\delta_{i_n X}(K_0 + 2\delta_{i_{n-1} X} K_1)} . \tag{3.31}$$

See Sec. D.3 of the Appendix for further details in relation to Eq. (3.30), including its application to the example realisation shown in Fig. 3.1.

Equation (3.30) can be compactly written in 2×2 matrix form in the $|X\rangle$, $|C\rangle$ basis:

$$\hat{P}(t) = \begin{pmatrix} P_{XX} & P_{XC} \\ P_{CX} & P_{CC} \end{pmatrix} = \begin{pmatrix} e^{K_0} & 0 \\ 0 & 1 \end{pmatrix} \hat{G}^{N-1} \hat{M} \tag{3.32}$$

with $\hat{G}$ given by

$$\hat{G} = \begin{pmatrix} M_{XX} e^{K_0+2K_1} & M_{XC} \\ M_{CX} e^{K_0} & M_{CC} \end{pmatrix}. \tag{3.33}$$

It should be noted that our time step $\Delta t \approx \tau_{\mathrm{IB}}$ is too large to capture the initial rapid phonon-induced decay of the polarisation associated with the phonon broadband [3, 5]. There is, however, a simple solution to this problem: For all $t < \tau_{\mathrm{IB}}$, replace our fixed Δt with a variable $\Delta t' = t/2$ as illustrated in Fig. 3.3. Crucially, this ensures that no portions of the $K(t)$ grid are neglected. We therefore may allow $\Delta t'$ to become arbitrarily small whilst always exactly calculating $K(t)$. Note that this is only valid for $t < \tau_{\mathrm{IB}}$: If we were to extend this approach to $t > \tau_{\mathrm{IB}}$ then for some values of t our time interval $\Delta t'$ would become too large, and the accuracy of the calculation would be degraded.

3.2.2 L-neighbour (LN) regime

We now address a general case in which the polaron and polariton time scales can be comparable, $\tau_{\mathrm{IB}} \sim \tau_{\mathrm{JC}}$, for example, in the case of very-strong exciton-cavity coupling g. This implies that we must find a way to reduce the time-step Δt in the Trotter decomposition. We achieve this by going beyond the NN regime to the LN regime, where L indicates the number of "neighbours" that we consider, corresponding to the condition $|n - m| \leqslant L$ in Eq. (3.21). The aforementioned condition $\Delta t \ll \tau_{\mathrm{JC}}$ applies equally to the LN regime, and therefore in this regime we are bound by the constraint $L\Delta t \gtrsim \tau_{\mathrm{IB}}$. Importantly, this allows us to treat comparable polaron and polariton timescales providing we choose L such that the condition $\tau_{\mathrm{IB}}/L \ll \tau_{\mathrm{JC}}$ is satisfied.

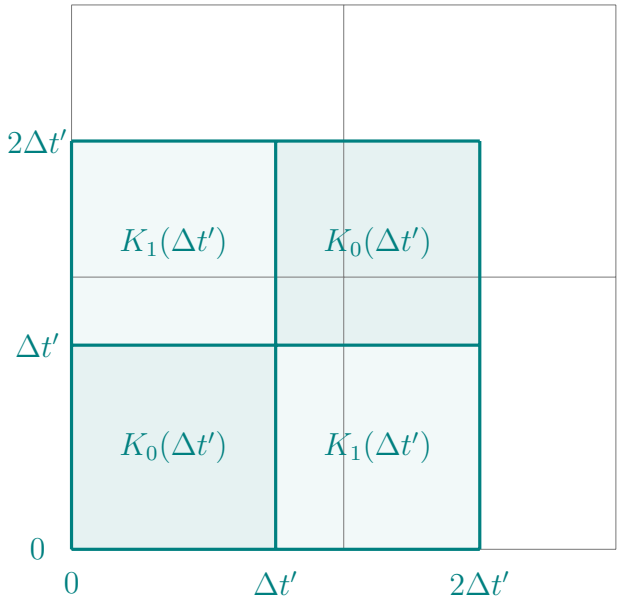

Figure 3.3: The adaptation of the grid of Fig. 3.2 for small time: $t < \tau_{\mathrm{IB}}$. The grey grid illustrates the Δt discretisation used for $t > \tau_{\mathrm{IB}}$ (as for Fig. 3.2), whilst the green grid illustrates the adapted discretisation for $t < \tau_{\mathrm{IB}}$. In this small time regime, the time t is always split into a 2×2 grid, giving $\Delta t' = t/2$.

In the LN approach we define a quantity $F^{(n)}_{i_L \ldots i_1}$ which is generated via a recursive relation

$$F^{(n+1)}_{i_L \ldots i_1} = \sum_{l=X,C} G_{i_L \ldots i_1 l} F^{(n)}_{i_{L-1} \ldots i_1 l} \,, \tag{3.34}$$

using $F^{(1)}_{i_L \ldots i_1} = M_{i_1 k}$ as the initial value, where $\hat{M}$ is defined as before by Eq. (3.13), while $G_{i_L \ldots i_1 l}$ is the LN analog of Eq. (3.31):

$$G_{i_L \ldots i_1 l} = M_{i_1 l} e^{\delta_{lX}(K_0 + 2\delta_{i_1 X} K_1 \ldots + 2\delta_{i_L X} K_L)} \,. \tag{3.35}$$

The polarisation matrix elements are then given by

$$P_{jk}(t) = e^{\delta_{jX} K_0} F^{(N)}_{C \ldots C j} \,. \tag{3.36}$$

Eqs. (3.34) – (3.36) present an asymptotically exact solution for the linear polarisation. By extending the matrix size of the operators involved, it is straightforward to generalise this result to other correlators, such as the photon indistinguishability [22, 78, 79] or to other elements of the density matrix, such as the four-wave mixing polarisation [11, 80].

3.2.3 Analytic approximation

From the NN result Eq. (3.32), one can extract a simple analytic expression that describes the long-time behaviour of the linear optical response. We use the asymptotic behaviour of the standard IB model cumulant $K(t)$ in the long time regime (see Sec. 1.3),

$$K(t) \approx -i\Omega_p t - S\,, \tag{3.37}$$

where Ω_p is the polaron shift and S is the Huang-Rhys factor (the explicit forms of which are provided in Sec. 1.3). This allows us to approximate $K_0 \approx -i\Omega_p \Delta t - S$ and $K_1 \approx S/2$. In the limit $\Delta t \approx \tau_{\mathrm{IB}} \ll \tau_{\mathrm{JC}}$ this results in a fully analytic long-time dependence of the polarisation (see Sec. D.4 of the Appendix for details):

$$P(t) \approx e^{-\hat{S}/2} e^{-i\tilde{H}t} e^{-\hat{S}/2} \quad (t > \tau_{\mathrm{IB}}), \tag{3.38}$$

where

$$\tilde{H} = \begin{pmatrix} \omega_X + \Omega_p & g e^{-S/2} \\ g e^{-S/2} & \omega_C \end{pmatrix}, \quad \hat{S} = \begin{pmatrix} S & 0 \\ 0 & 0 \end{pmatrix}. \tag{3.39}$$

Comparing Eq. (3.39) with the JC Hamiltonian Eq. (**??**), we see that the effect of acoustic phonons in this limit ($\tau_{\mathrm{IB}} \ll \tau_{\mathrm{JC}}$) is a reduction of the exciton-cavity coupling strength g by a factor of $e^{S/2}$ and a polaron shift of the bare exciton frequency: $\omega_X \to \omega_X + \Omega_p$. We also note that the ZPL weight of the excitonic polarisation is surpressed by a factor of e^S. These facts are consistent with the analytic results of the IB model and are in agreement with previous experimental and theoretical works [15, 81]. Also, the form of the modified Hamiltonian $\tilde{H}$ given by Eq. (3.39) is exactly the same as obtained after making the polaron transformation of the full Hamiltonian H and then neglecting any interactions which appear in the polaron frame [15, 20].

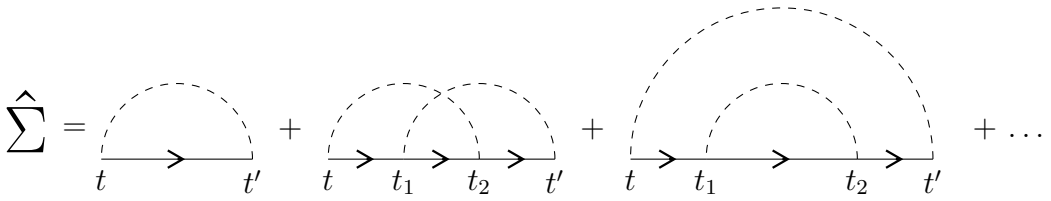

Figure 3.4: Second and fourth order diagrams contributing to the full self energy. Solid lines with arrows (dashes lines) represent the polariton (phonon) non-interacting Green's functions.

3.2.4 Refined analytic approximation

The analytic solution described in Sec. 3.2.3 is suited only for describing the optical polarisation at long times $t \gtrsim \tau_{\mathrm{IB}}$, so that any information on the evolution at short times, which is responsible for the phonon broadband observed in the optical spectra of quantum dots, is missing. To improve upon this, we additionally provide a refined purely analytic approach which properly takes into account both the short and long time dynamics, providing a smooth transition between the two regimes.

The refined analytic approach is based on a self-energy formalism. It requires calculation of the full phonon-dressed polariton Green's function $\hat{G}(t)$, which is related to the polarisation matrix via

$$\hat{P}(t) = \hat{Y}\hat{G}(t)\hat{Y}^{-1}\,, \tag{3.40}$$

where $\hat{Y}$ and $\hat{Y}^{-1}$ are the matrices that diagonalise the JC Hamiltonian, defined in Eq. (1.24) – see Sec. D.5 of the Appendix for details. In order to obtain an expression for the full phonon-dressed polariton Green's function $\hat{G}(t)$, we must solve Dyson's equation,

$$\hat{G}(t) = \hat{G}^{(0)}(t) + \int_{-\infty}^{\infty} dt_1 \int_{-\infty}^{\infty} dt_2\, \hat{G}^{(0)}(t-t_1)\hat{\Sigma}(t_1-t_2)\hat{G}(t_2)\,, \tag{3.41}$$

where $\hat{\Sigma}(t)$ is self energy, and $\hat{G}^{(0)}(t)$ is the bare polariton Green's function,

$$\hat{G}^{(0)}(t) = \theta(t) \begin{pmatrix} e^{-i\omega_1 t} & 0 \\ 0 & e^{-i\omega_2 t} \end{pmatrix}, \tag{3.42}$$

with $\theta(t)$ being the Heaviside step function and $\omega_{1,2}$ being the eigenfrequencies of the JC Hamiltonian, defined in Eq. (1.27). The self energy $\hat{\Sigma}(t)$ is represented by all possible connected diagrams such as the second and fourth order diagrams

sketched in Fig. 3.4. In the regime $\tau_{\mathrm{JC}} \gg \tau_{\mathrm{IB}}$ (see Sec. D.5 of the Appendix for details), we obtain

$$\hat{\Sigma}(t) = \hat{Q} \begin{pmatrix} \Sigma_1(t) & 0 \\ 0 & \Sigma_2(t) \end{pmatrix}, \tag{3.43}$$

where $\Sigma_j(t)$ is the self energy of an isolated polariton state j, and $\hat{Q}$ is the polariton operator,

$$\hat{Q} = \hat{Y}^{-1} \begin{pmatrix} 1 & 0 \\ 0 & 0 \end{pmatrix} \hat{Y} = \begin{pmatrix} \alpha^2 & \alpha\beta \\ \alpha\beta & \beta^2 \end{pmatrix}, \tag{3.44}$$

where $\hat{Y}$ and $\hat{Y}^{-1}$ are the matrices that diagonalise the JC Hamiltonian (defined in Eq. (1.24)), and α and β are defined in Eqs. (1.25) and (1.25) respectively. The self energy of an isolated polariton state j contributes to the corresponding IB model problem

$$G_j^{\mathrm{IB}}(t) = G_j^{(0)}(t) + \int_{-\infty}^{\infty} dt_1 \int_{-\infty}^{\infty} dt_2\, G_j^{(0)}(t - t_1)\Sigma_j(t_1 - t_2)G_j^{\mathrm{IB}}(t_2)\,, \tag{3.45}$$

having the following exact solution:

$$G_j^{\mathrm{IB}}(t) = G_j^{(0)}(t)e^{K(t)}\,, \tag{3.46}$$

where $K(t)$ is the IB cumulant, calculated in Sec. 1.3 and, from Eq. (3.42), $G_j^{(0)}$ is $\theta(t)e^{-i\omega_j t}$. We know from the IB model that its exact solution in the form of a cumulant includes a nonvanishing contribution of all higher-order diagrams of the self energy series (for realistic phonon parameters of semiconductor quantum dots). From Eq. (3.45), we may find the self energies in frequency domain:

$$\Sigma_j(\omega) = \frac{1}{G_j^{(0)}(\omega)} - \frac{1}{G_j^{\mathrm{IB}}(\omega)}\,, \tag{3.47}$$

where $\Sigma_j(\omega)$, $G_j^{(0)}(\omega)$, and $G_j^{\mathrm{IB}}(\omega)$ are the Fourier transforms of $\Sigma_j(t)$, $G_j^{(0)}(t)$, and $G_j^{\mathrm{IB}}(t)$, respectively. The full matrix Green's function (and hence the polarisation) is then obtained by solving Dyson's equation (Eq. (3.41)) in the frequency domain:

$$\hat{G}(\omega) = \left[\mathbb{1} - \hat{G}^{(0)}(\omega)\hat{\Sigma}(\omega)\right]^{-1} \hat{G}^{(0)}(\omega)\,, \tag{3.48}$$

where $\hat{G}^{(0)}$ and $\hat{\Sigma}$ are given in the time domain by Eqs. (3.42) and (3.43) respectively, with self energy components provided via Eq. (3.47) by the IB model solution Eq. (3.46).

An obvious drawback of the above analytic model is that it does not shows any phonon-induced renormalisation of the exciton-cavity coupling due to the interaction with the phonon bath. This is a consequence of the present approach not properly taking into account the cumulative effect of self-energy diagrams of higher order, for which the approximate commutation of matrices $\hat{Q}$ and $\hat{G}^{(0)}(t)$ (used in the derivation of Eq. (3.43)) is not valid. This problem can, however, be easily remedied through use of the large time asymptotics obtained in Sec. 3.2.3. We introduce *by hand* one minor correction: we replace the exciton-cavity coupling g in the bare JC Hamiltonian by the renormalised coupling strength $ge^{-S/2}$ in the following way

$$H_{\mathrm{JC}} = \begin{pmatrix} \omega_X & g \\ g & \omega_C \end{pmatrix} \to \begin{pmatrix} \omega_X & ge^{-S} \\ g & \omega_C \end{pmatrix}. \tag{3.49}$$

As in Eq. (3.40), we may express the Fourier transform of the polarisation as

$$\hat{P}(\omega) = \begin{pmatrix} e^{-S/2} & 0 \\ 0 & 1 \end{pmatrix} \begin{pmatrix} \bar{\alpha} & \bar{\beta} \\ -\bar{\beta} & \bar{\alpha} \end{pmatrix} \hat{\bar{G}}(\omega) \begin{pmatrix} \bar{\alpha} & -\bar{\beta} \\ \bar{\beta} & \bar{\alpha} \end{pmatrix} \begin{pmatrix} e^{S/2} & 0 \\ 0 & 1 \end{pmatrix}, \tag{3.50}$$

where the matrices containing $\bar{\alpha}$ and $\bar{\beta}$ diagonalise a symmetrised Hamiltonian $\bar{H}_{\mathrm{JC}}$:

$$\bar{H}_{\mathrm{JC}} = \begin{pmatrix} \omega_X & ge^{-S/2} \\ ge^{-S/2} & \omega_C \end{pmatrix} = \begin{pmatrix} \bar{\alpha} & \bar{\beta} \\ -\bar{\beta} & \bar{\alpha} \end{pmatrix} \begin{pmatrix} \bar{\omega}_1 & 0 \\ 0 & \bar{\omega}_2 \end{pmatrix} \begin{pmatrix} \bar{\alpha} & -\bar{\beta} \\ \bar{\beta} & \bar{\alpha} \end{pmatrix}. \tag{3.51}$$

Note that the first and last matrices of Eq. (3.50) arise as a result of the replacement of the adjusted Hamiltonian in Eq. (3.49) with its symmetrised version $\bar{H}_{\mathrm{JC}}$. We see that $\hat{\bar{G}}(\omega)$ in Eq. (3.50) is the analog of Eq. (3.48) with a replacement $\alpha \to \bar{\alpha}$, $\beta \to \bar{\beta}$, $\omega_{1,2} \to \bar{\omega}_{1,2}$.

For $P_{XX}(\omega)$ and $P_{CC}(\omega)$, Eq. (3.50) gives the following simple explicit expressions:

$$P_{XX}(\omega) = \frac{\bar{\alpha}^2 \bar{G}_1^{(0)}(\omega) + \bar{\beta}^2 \bar{G}_2^{(0)}(\omega)}{\bar{D}(\omega)}, \tag{3.52}$$

$$P_{CC}(\omega) = \left(\frac{\bar{\alpha}^2}{\bar{G}_1^{\mathrm{IB}}(\omega)} + \frac{\bar{\beta}^2}{\bar{G}_2^{\mathrm{IB}}(\omega)} \right) \frac{\bar{G}_1^{(0)}(\omega) \bar{G}_2^{(0)}(\omega)}{\bar{D}(\omega)}, \tag{3.53}$$

where

$$\bar{D}(\omega) = \bar{\alpha}^2 \frac{\bar{G}_1^{(0)}(\omega)}{\bar{G}_1^{\mathrm{IB}}(\omega)} + \bar{\beta}^2 \frac{\bar{G}_2^{(0)}(\omega)}{\bar{G}_2^{\mathrm{IB}}(\omega)} \tag{3.54}$$

and $\bar{G}_j^{(0)}(\omega)$ and $\bar{G}_j^{\mathrm{IB}}(\omega)$ are, respectively, the Fourier transform of $\bar{G}_j^{(0)}(t) = \theta(t)e^{-i\bar{\omega}_j t}$ and $\bar{G}_j^{\mathrm{IB}}(t) = \bar{G}_j^{(0)}(t)e^{K(t)}$.

Unlike the NN, LN and analytic approaches described above, the refined analytic approach calculates absorption directly. It is, however, straightforward to find the polarisation $P(t)$: we simply take the Fourier transform of Eqs. (3.52) and (3.53).

3.3 Results: polarisation and absorption

We consider, in this section, the polarisation as calculated by the various above-described approaches. We find that the long-time dynamics of the polarisation is bi-exponential,

$$\hat{P}(t) \approx \sum_{j=1}^{2} \hat{C}_j e^{-i(\Omega_j - i\Gamma_j)t} \quad (t > \tau_{\mathrm{IB}}), \tag{3.55}$$

where Ω_j (Γ_j) are the polariton frequencies (linewidths) and $\hat{C}_j$ are the amplitude matrices. This remains true even in the very strong coupling regime.

Fig. 3.5 shows the linear excitonic polarisation $|P_{XX}(t)|$ calculated according to the LN, NN and analytic approaches, Eqs. (3.32), (3.36) and (3.38) respectively. We take the case of relatively small exciton-cavity coupling $g = 50\,\mu$eV and consider temperatures $T = 0$ and $T = 50$ K. In relation to the LN approach, we take $L = 15$ as our most accurate solution – which we refer to herein as *exact*. The reader will appreciate that the true "exact" solution requires $L \to \infty$; however, within the range of exciton-cavity coupling strengths that we consider ($0 < g < 1.5$ meV), $L = 15$ is a very good approximation. We show in Sec. 3.6 that the relative error shows an exponential reduction with the number of neighbours L.

In this case of relatively small QD-cavity coupling, we may approximate the Rabi splitting $\Delta\Omega$ from the Hamiltonian in the analytic approximation Eq. (3.39). Diagonalisation of this Hamiltonian gives $\Delta\Omega = \Omega_2 - \Omega_1 = 2ge^{-S/2}$. The polariton timescale τ_{JC} is therefore given by $\tau_{\mathrm{JC}} = 2\pi/(2ge^{-S/2}) \sim 60$ ps. The phonon memory

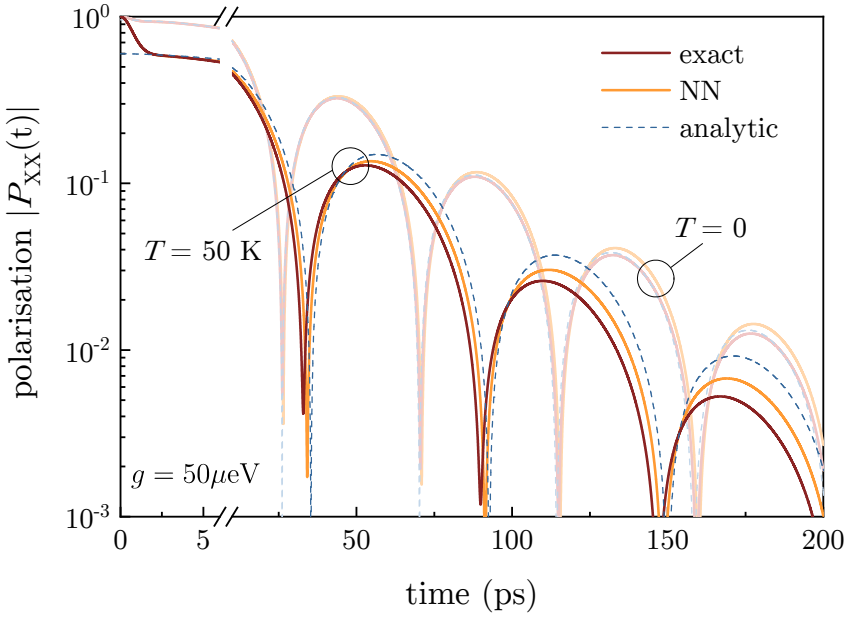

Figure 3.5: Excitonic linear polarisation for $T = 0$ and 50 K, calculated in the LN implementation Eq. (3.36) with $L = 15$, NN implementation Eq. (3.32), and analytic approximation Eq. (3.38). We use the realistic parameters of InGaAs QDs studied in [5, 6] and micropillars studied in [11, 80] including $g = 50\,\mu$eV, $\omega_X = \Omega_X - i\gamma_X$ with $\Omega_X = 1329.6$ meV and $\gamma_X = 2\,\mu$eV; $\omega_C = \Omega_C - i\gamma_C$ with $\Omega_C = \Omega_X + \Omega_p$, $\Omega_p = -49.8\,\mu$eV and $\gamma_C = 30\,\mu$eV.

time τ_{IB} is independent of exciton-cavity coupling strength g and is ~ 10 ps at $T = 0$ K and ~ 3.2 ps at $T = 50$ K (see Sec. 1.3.2 for details).

As described in Eq. (1.18), we may calculate the absorption spectra associated with the polarisations shown in Fig. 3.5 by taking the real part of the Fourier transform of $P(t)$. Fig. 3.6 illustrates the excitonic absorption spectra corresponding to the polarisations shown in Fig. 3.5. The absorption calculated according to the refined analytic approximation, Eq. (3.52), is additionally shown.

We see from Fig. 3.6 that the absorption spectra each consist of a well-resolved polariton doublet, described by the eigenvalues $\omega_j = \Omega_j - i\Gamma_j$ $(j = 1, 2)$ of the effective Hamiltonian Eq. (3.39), superimposed with a phonon broadband. At lower temperatures, the broadband is more asymmetric and the ZPL weight is increased, in agreement with the IB model. As expected, the analytic calculation Eq. (3.38) describes the long-time dynamics well but fails at short times, as it is

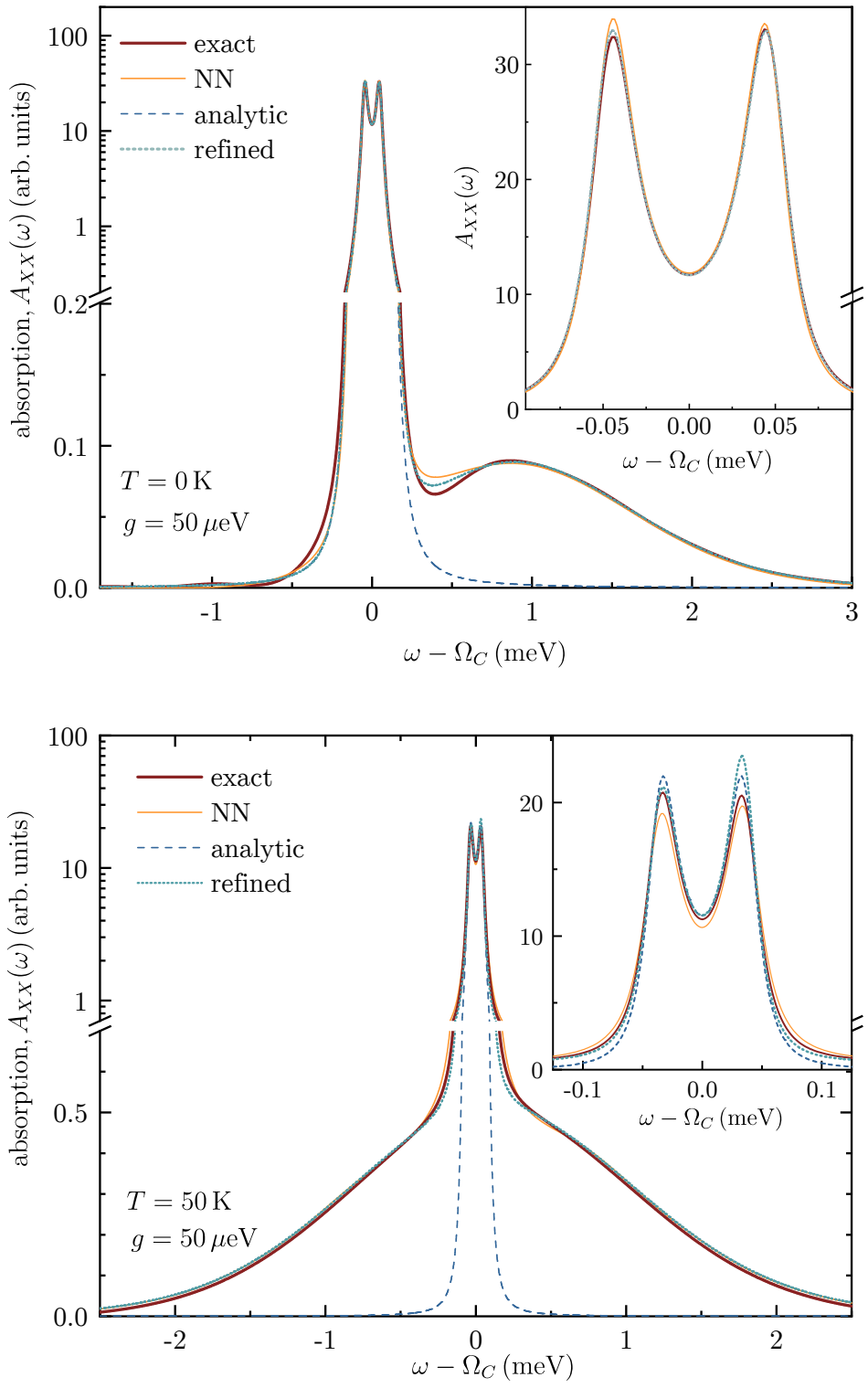

Figure 3.6: Absorption spectra corresponding to the excitonic linear polarisations shown in Fig. 3.5; spectra for temperature $T = 0$ K ($T = 50$ K) shown in the upper (lower) panel. Insets show the respective spectra within a limited frequency range, focusing on the polariton lines. All parameters as per Fig. 3.5.

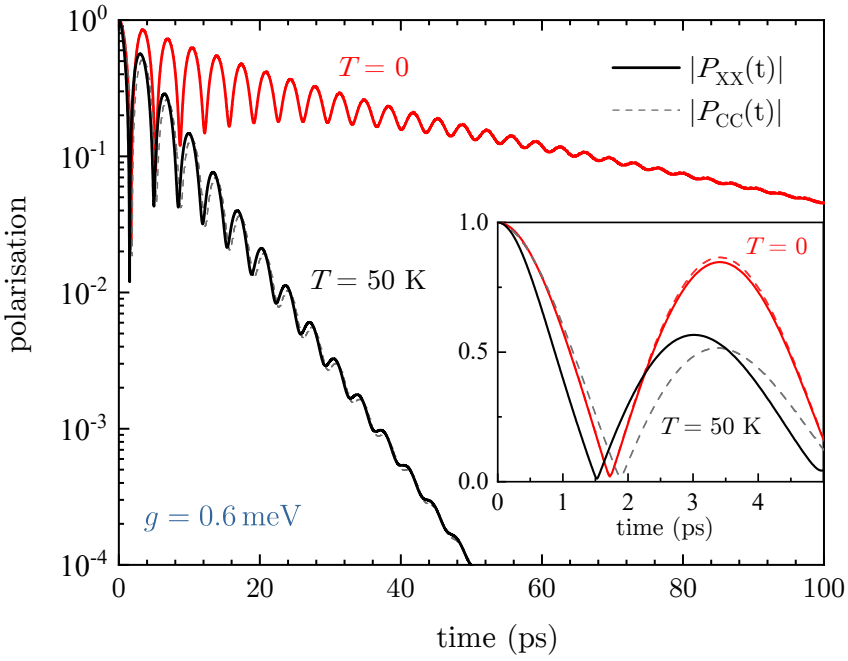

Figure 3.7: As Fig. 3.5, but for $g = 0.6$ meV and only exact (15-neighbour) result shown, for $T = 0$ (red lines) and 50 K (black lines). The cavity-photon polarisation and absorption are also shown (dashed lines). Inset: the initial polarisation dynamics.

clear from Fig. 3.5. This is manifested in the absorption spectra (Fig. 3.6) as an absence of the broadband. This, however, is not the case for the refined analytic approach, which accounts for the full temporal behaviour and hence reproduces the phonon broadband to good accuracy.

We now examine regimes of comparable polaron and polariton times $\tau_{\rm IB} \sim \tau_{\rm JC}$ (achieved by increasing the QD-cavity coupling constant to $g = 0.6$ meV while keeping all other parameters the same). In such regimes, the NN, analytic and refined analytic implementations all fail due to their reliance upon the assumption $\tau_{\rm IB} \ll \tau_{\rm JC}$. We will therefore consider only the exact (15-neighbour) results. Both polarisations, $|P_{XX}(t)|$ and $|P_{CC}(t)|$ are shown in Fig. 3.7. There is a clear damping of the beating of the two exponentials, even for zero detuning (shown). This implies that the lines of the polariton doublet now have quite different linewidths, as it is clear from Fig. 3.8.

We may understand the behaviour of the polariton linewidths in terms of real phonon assisted transitions between the lines of the polariton doublet. Indeed,

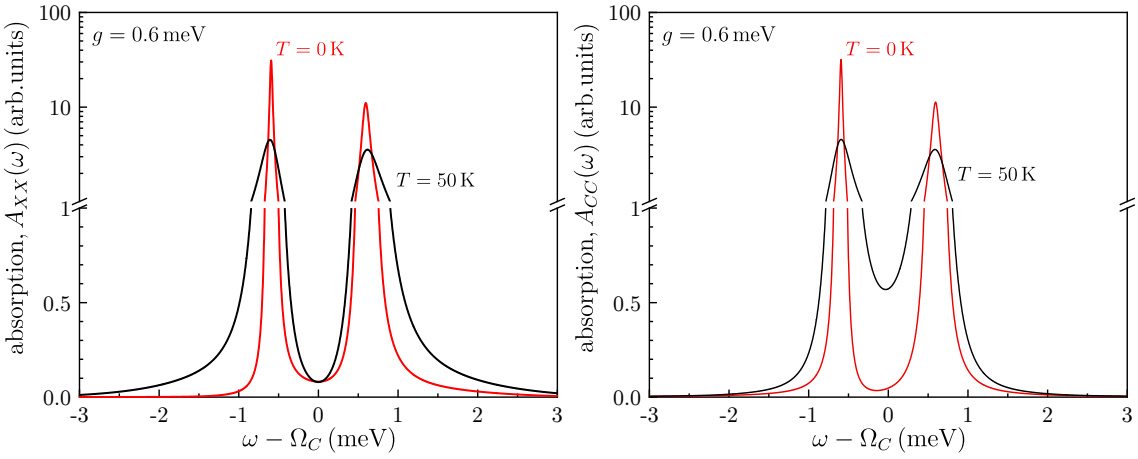

Figure 3.8: Absorption spectra corresponding to the linear polarisations shown in Fig. 3.7; exciton (photon) absorption shown in the left (right) panel.

at $T = 0$, the high-energy polariton state (2) is significantly broader than the low-energy state (1), due to the allowed transition $2 \to 1$, accompanied by emission of an acoustic phonon. The transition from the low-energy polariton state (1) to the higher energy state requires the absorption of an environmental phonon and is therefore forbidden at zero temperature; the finite width of the low energy polariton state at $T = 0$ is wholly due to the exciton dephasing γ_X and radiative decay γ_C inherent in the system. At elevated temperatures both transitions $2 \to 1$ and $1 \to 2$, with phonon emission and absorption respectively, are allowed, giving rise to more balanced linewidths. The phonon-induced line broadening is also strongly dependent on the exciton-cavity coupling strength g, which will be discussed further in Sec. 3.4

3.4 Analysis of polariton parameters

As discussed in the previous section, the long-time behaviour of the polarisation $P(t)$ is bi-exponential. Equivalently, in the frequency domain, the absorption spectrum comprises two polariton lines. With reference to Eq. (3.55), there are three key parameters that describe each polariton line: the (complex) amplitude C_j, the real frequency Ω_j and the Lorentzian line broadening Γ_j. We have seen in the previous section that the upper and lower polariton lines have approximately equal

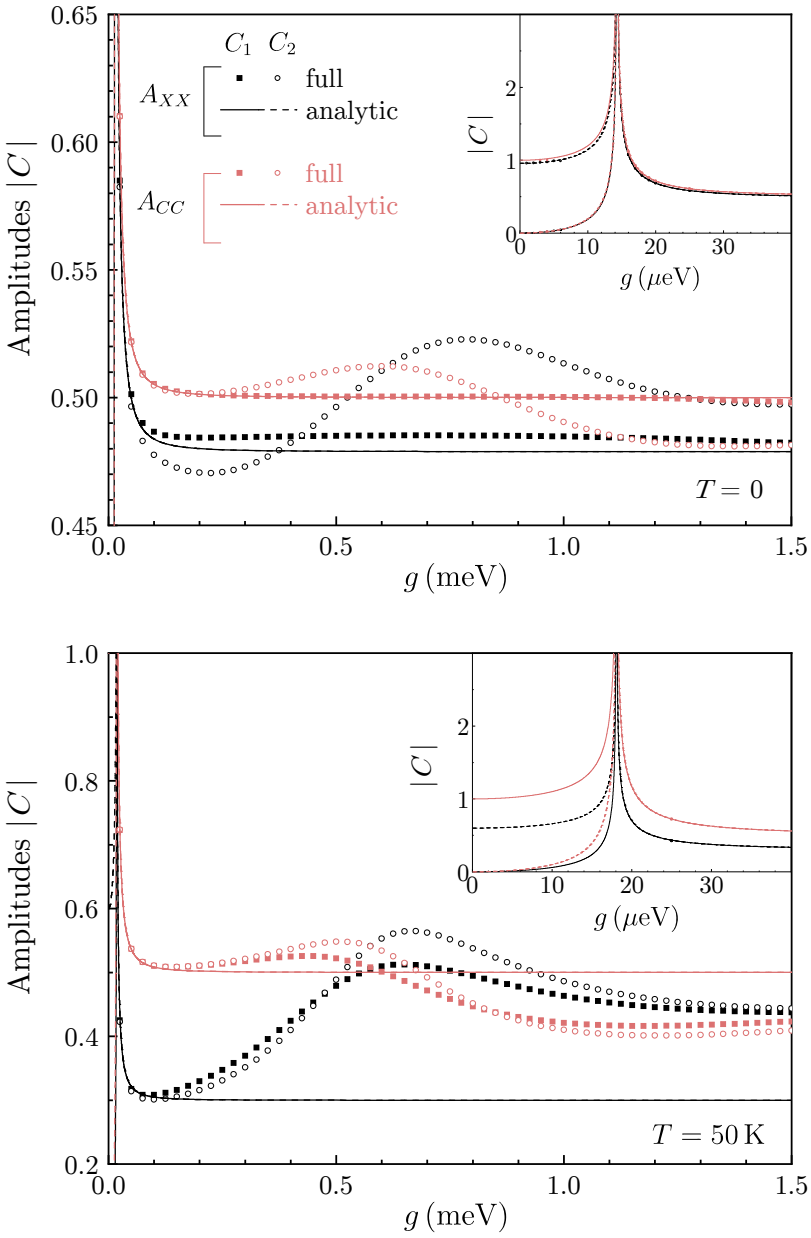

Figure 3.9: Polariton amplitude coefficients $C_{1,2}$ as a function of the QD-cavity coupling strength g for $T = 0$ (upper panel) and $T = 50$ K (lower panel). Coefficients for excitonic absorption $A_{XX}(\omega)$ (photonic absorption $A_{CC}(\omega)$) are shown in black (red). The amplitude coefficients corresponding to the lower polariton line C_1 (upper polariton line C_2) are shown for the exact (15-neighbour) calculation by full squares (open circles) and for the long-time analytic model by full (dashed) lines. Insets zoom in the region of small g, where there is significant amplitude variation with g. We take the case of zero effective detuning ($\Omega_C = \Omega_X + \Omega_p$), $\gamma_X = 2\,\mu$eV and $\gamma_C = 30\,\mu$eV.

broadening at $g = 50\,\mu$eV, but there is significant asymmetry between the lines at $g = 0.6$ meV. It is natural to investigate this behaviour further and to extend our analysis to all of the above-described key polariton parameters.

Fig. 3.9 illustrates the behaviour of the polariton amplitude coefficients $C_{1,2}$ as a function of exciton-cavity coupling strength g at zero temperature (upper panel) and $T = 50$ K (lower panel). The full squares and open circles denote the exact (15-neighbour) calculation, whilst the solid and dashed lines denote the analytic approximation. For both temperatures, there is good agreement between the two calculations at small exciton-cavity coupling strengths g (as expected) but significant divergence at larger g. The sharp peak in $|C_{1,2}|$ at small g is a consequence of the finite long-time ZPL dephasing γ_X and radiative decay γ_C. It is fully analogous to the peak shown in Fig. 1.1 in relation to the JC model.

We now consider the real polariton frequencies $\Omega_{1,2}$ and the associated linewidths $\Gamma_{1,2}$. Before we examine the results of the 15-neighbour calculation, it is instructive to consider the predictions of the analytic approximation, Eq. (3.38). Diagonalisation of the Hamiltonian, Eq. (3.39), gives eigenfrequencies

$$\omega_{1,2} = \frac{\bar{\omega}_X + \omega_C}{2} \pm \sqrt{(ge^{-S/2})^2 + 1/4(\bar{\omega}_X - \omega_C)^2}\,, \tag{3.56}$$

where $\bar{\omega}_X = \omega_X + \Omega_p$. For the case of zero effective detuning ($\Omega_C = \Omega_X + \Omega_p$), this simplifies to $\omega_{1,2} = \Omega_C + i/2(\gamma_X + \gamma_C) \pm ge^{-S/2}$ in the strong coupling regime $g \gg \gamma_X, \gamma_C$. Accordingly, the analytic model predicts constant polariton line broadening $\Gamma_{1,2} = i/2(\gamma_X + \gamma_C)$, and polariton line splitting $\Delta\Omega = 2ge^{-S/2}$ in agreement with the low g limit widely quoted in the literature [15, 20–22, 29, 77, 81].

The upper panel of Fig. 3.10 (Fig. 3.11) illustrates the deviation of the polariton splitting $\Delta\Omega$ (calculated in the 15-neighbour implementation) from the nominal JC splitting $2g$ as a function of exciton-cavity coupling strength g for temperature $T = 0$ ($T = 50$ K). The deviation of the analytic approximation, $2ge^{-S/2}$, from the nominal splitting, $2g$, is shown in dash. It is clear from this figure that the widely quoted suppression of the splitting by $e^{-S/2}$ is only a good approximation at small g. In fact, the polariton Rabi splitting $\Delta\Omega$ is, on average, approximately

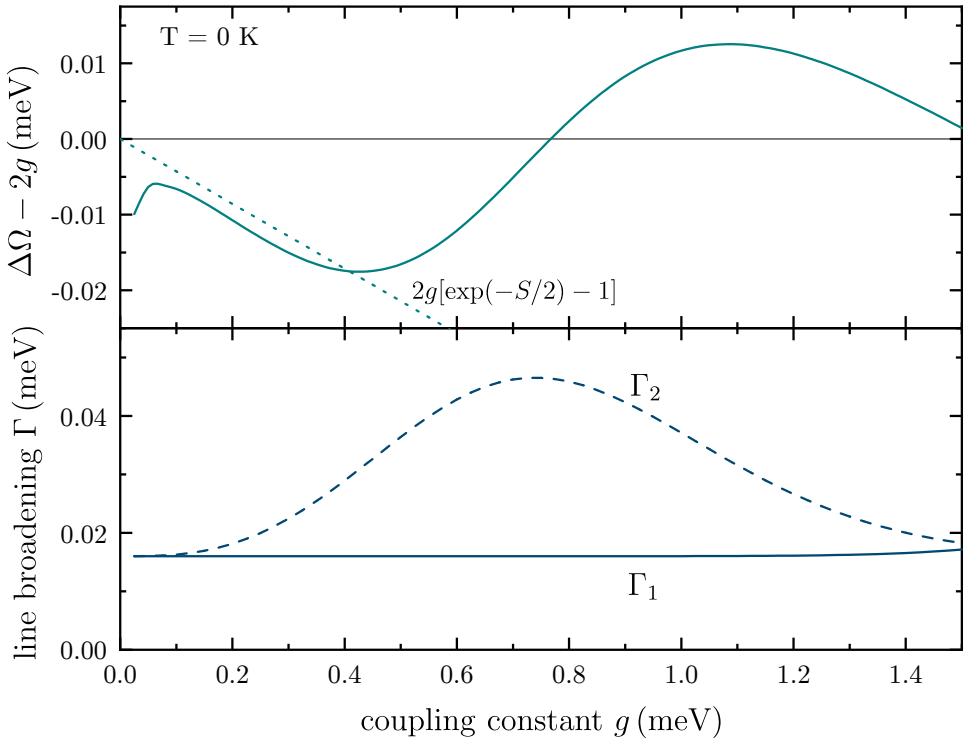

Figure 3.10: Variation of polariton line parameters with exciton-cavity coupling strength g at $T = 0$ K. Upper panel: Rabi splitting $\Delta\Omega$ as a function of g, with dotted line showing the analytic prediction of $\Delta\Omega = 2ge^{-S/2}$. Lower panel: broadening of lower (1) and upper (2) polariton lines as a function of g. As in Fig. 3.9, we take the case of zero effective detuning ($\Omega_C = \Omega_X + \Omega_p$), $\gamma_X = 2\,\mu$eV and $\gamma_C = 30\,\mu$eV.

equal to the phonon-free value of $2g$ across the full range of exciton-cavity coupling strength g, and is even enhanced at large g.

The lower panel of Fig. 3.10 shows the broadening of the lower (Γ_1) and upper (Γ_2) polariton lines at temperature $T = 0$, calculated in the 15-neighbour implementation. As expected, the lower polariton line has constant broadening equal to the average of the long-time ZPL dephasing γ_X and radiative decay γ_C. There are no phonon-mediated transitions from the lower to the upper polariton line (which would result in broadening of the former) due to an absence of environmental phonons at zero temperature. The analytic approximation of Sec. 3.2.3 does not account for phonon-mediated transitions and therefore correctly predicts Γ_1 at $T = 0$ K.

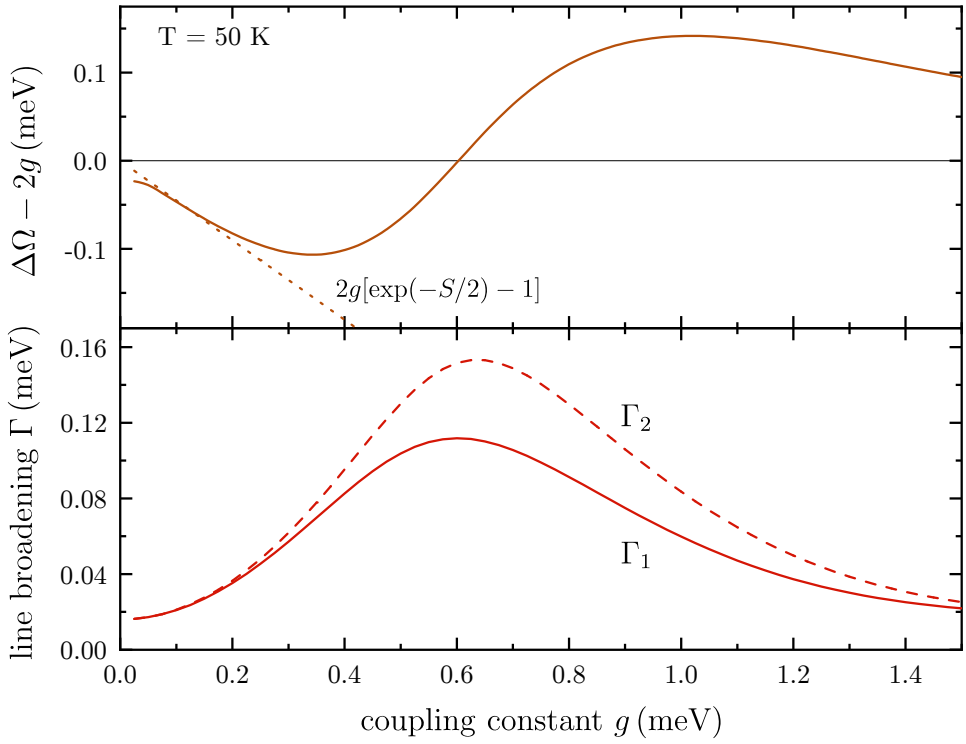

Figure 3.11: As Fig. 3.10, but for $T = 50$ K.

Conversely, transitions from the upper to the lower polariton line may occur via the emission of a phonon, which is permitted even at zero temperature. The maximum upper polariton line broadening occurs when the polariton splitting $\Delta\Omega = \Omega_2 - \Omega_1$ (shown in the upper panel) corresponds to the typical energy of acoustic phonons surrounding the QD [6], which is in the range $1-2$ meV for the QDs considered in this work. Fermi's golden rule (FGR) for real phonon-assisted transitions [6] in the polariton frame very closely reproduces the behaviour of the polariton line broadening $\Gamma_{1,2}$, as discussed in Sec. 3.5 below.

The lower panel of Fig. 3.11 shows the broadening of the polariton lines at $T = 50$ K. In this case, the transition from the lower to the upper polariton line may occur through the absorption of a phonon and thus both polariton lines show g-dependent broadening.

3.5 Interpretation: the polariton picture

In view of the foregoing, it is clear that the polarisation and absorption results can be best interpreted within the framework of the polariton model. We therefore make a polariton transformation defined by the matrices $\hat{Y}$ and $\hat{Y}^{-1}$ that together diagonalise the JC Hamiltonian $H_{\rm JC}$ (see Eq. (1.24)). Applying this transformation to the full Hamiltonian $H = H_{\rm JC} + H_{\rm IB}$, Eq. (3.1), we obtain

$$\begin{aligned} H \to H' &= \begin{pmatrix} \omega_1 & 0 \\ 0 & \omega_2 \end{pmatrix} + \begin{pmatrix} \alpha & \beta \\ -\beta & \alpha \end{pmatrix} \begin{pmatrix} V & 0 \\ 0 & 0 \end{pmatrix} \begin{pmatrix} \alpha & -\beta \\ \beta & \alpha \end{pmatrix} + H_{\rm ph}\mathbb{1} \\ &= \begin{pmatrix} \omega_1 + \alpha^2 V & \alpha\beta V \\ \alpha\beta V & \omega_2 + \beta^2 V \end{pmatrix} + H_{\rm ph}\mathbb{1}\,. \end{aligned} \tag{3.57}$$

We note that the Hamiltonian Eq. (3.57) can be also expressed in terms of polariton creation $p_{1,2}^\dagger$ and annihilation $p_{1,2}$ operators,

$$H' = (\omega_1 + \alpha^2 V)p_1^\dagger p_1 + (\omega_2 + \beta^2 V)p_2^\dagger p_2 + \alpha\beta V(p_1^\dagger p_2 + p_2^\dagger p_1) + H_{\rm ph}\mathbb{1}\,, \tag{3.58}$$

with $p_{1,2}$ being linear combinations of exciton and cavity photon annihilation operators,

$$p_1 = \alpha d - \beta a\,, \tag{3.59}$$

$$p_2 = \beta d + \alpha a\,. \tag{3.60}$$

The term $\alpha\beta V(p_1^\dagger p_2 + p_2^\dagger p_1)$ in Eq. (3.58) is of particular interest as it is responsible for phonon-assisted transitions between polariton states 1 and 2. Concentrating on this interaction term, the behaviour of the polariton broadening $\Gamma_{1,2}$ can be understood in terms of Fermi's golden rule [6],

$$\Gamma = \pi N_{\Delta E/v_s} \sum_q |\alpha\beta\lambda_q|^2 \delta(\Delta E - \omega_q)\,, \tag{3.61}$$

where $N_{\Delta E/v_s}$ is the Bose distribution function $N_q = 1/[e^{\beta\omega_q} - 1]$ evaluated at $q = \Delta E/v_s$, and $\Delta E = E_f - E_i$ is the energy difference between the initial (i) and final (f) polariton states. This energy difference is simply the polariton Rabi splitting $\Delta\Omega = \Omega_2 - \Omega_1$ for the $1 \to 2$ polariton transition, and $-\Delta\Omega$ for the $2 \to 1$ transition. The dependence of the polariton Rabi splitting on the exciton-cavity

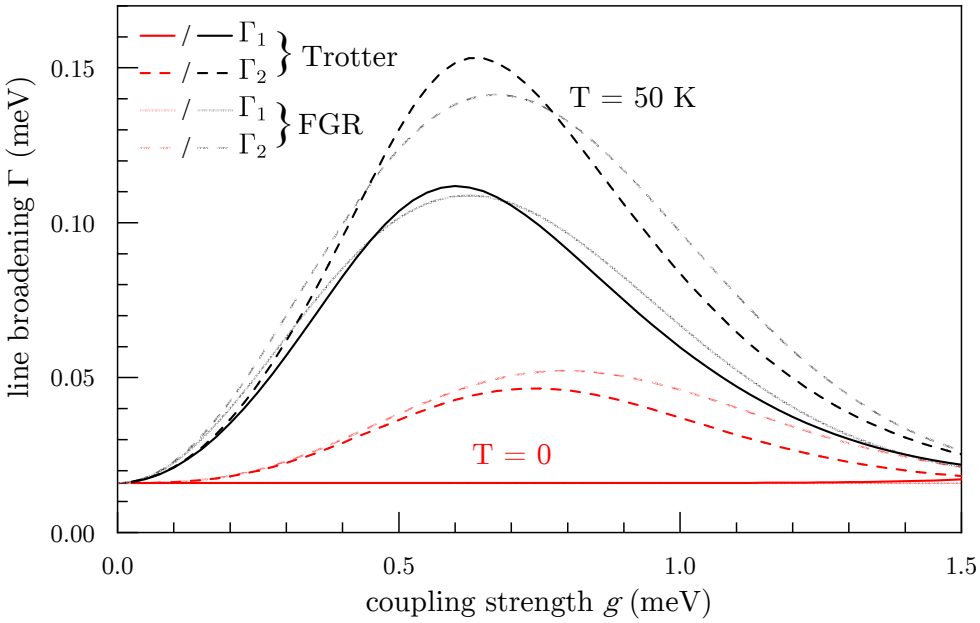

Figure 3.12: Polariton linewidths $\Gamma_{1,2}$ of the lower (solid lines) and upper (dashed lines) polariton states in Eq. (3.55) as functions of the QD-coupling strength g, calculated in the 15-neighbour approach (thick black and red lines) and estimated according to Fermi's golden rule (thin faded black and red lines).

coupling strength g is shown in Fig. 3.10 for $T = 0$ and Fig. 3.11 for $T = 50$ K. As discussed previously, we see from these figures that for zero effective detuning, the best approximation for the splitting $\Delta\Omega$ across the full range of exciton-cavity coupling strength g is the phonon-free value of $\Delta\Omega \approx 2g$. Noting that in the regime of $g \gg |\omega_X - \omega_C|$ we may approximate α and β for zero detuning as $\alpha \approx \beta \approx 1/\sqrt{2}$, and adding the intrinsic broadening Γ_0 due to the long-time ZPL dephasing γ_X and radiative decay γ_C, we obtain the following expressions for the lower (1) and upper (2) polariton line broadenings,

$$\Gamma_1 = \Gamma_0 + N_{2g/v_s}\Gamma_{\rm ph}\,, \qquad \Gamma_2 = \Gamma_0 + (N_{2g/v_s}+1)\Gamma_{\rm ph}\,, \tag{3.62}$$

with

$$\Gamma_0 = \frac{1}{2}(\gamma_X + \gamma_C)\,, \qquad \Gamma_{\rm ph} = \frac{g^3(D_c - D_v)^2}{2\pi\rho_m v_s^5}\exp\left(-\frac{2g^2l^2}{v_s^2}\right). \tag{3.63}$$

The linewidths $\Gamma_{1,2}$ calculated using Fermi's golden rule, Eqs. (3.62) and (3.63), are

shown in Fig. 3.12 alongside the Trotter decomposition results. This comparison demonstrates the remarkable accuracy to which Fermi's golden rule reproduces the behaviour of the polariton linewidth with exciton-cavity coupling strength g. The small discrepancies may be attributed to (i) multi-phonon transitions, which are not accounted for in FGR and (ii) approximation of the Rabi splitting as $\Delta\Omega \approx 2g$ within the FGR calculation.

3.6 Calculation accuracy

In this section we examine the accuracy of the 15-neighbour implementation of the Trotter decomposition method. To achieve this, calculate the polarisation in the LN implementation (Eq. (3.36)), taking L between 5 and 15. For each L, we extract the polariton line parameters from the long-time asymptotics of $P(t)$ and calculate the relative error in these parameters, taking $L = 15$ as the exact solution. Fig. 3.13 shows the relative error as a function of L for temperature $T = 50$ K and exciton-cavity coupling strength $g = 0.6$ meV. It can be seen from this figure that there is an exponential reduction of the calculation error with L. Deviation from this exponential reduction at $L \gtrsim 13$ is an artefact of taking the $L = 15$ calculation as exact when calculating the relative error; if we were to take the true exact solution, we would anticipate a continuation of this exponential trend. We may therefore estimate the error of the 15-neighbour calculation for each polariton line parameter by extrapolating the exponential portion of the plot (linear in the logarithmic scale shown) to $L = 15$ – giving a small relative error of $\sim 10^{-3}$ for the broadening parameters $\Gamma_{1,2}$ and even smaller relative errors for amplitude $A_{1,2}$ and real frequency $\Omega_{1,2}$ parameters. If we consider the situation at weaker exciton-cavity coupling strengths g, for example $g = 50\,\mu$eV (shown in Figs. 3.5 and 3.6), the relative error of the $L = 15$ approach will be yet lower still.

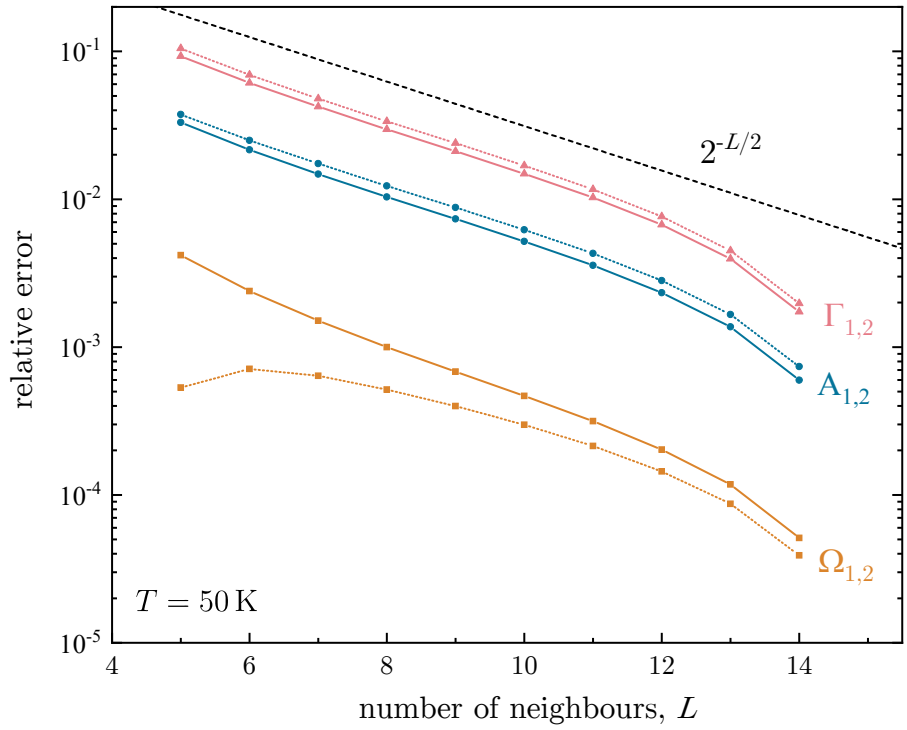

Figure 3.13: The relative error for the polariton line parameters at $T = 50$ K and $g = 0.6$ meV, as a function of the number of neighbours L, using $L = 15$ as the exact solution.

3.7 Chapter conclusion

In this chapter we have shown that the newly developed Trotter decomposition method accurately captures the dynamics of the QD-cavity system and associated phonon environment. We have focused on linear optical polarisation and absorption, but the approach is general and suited for describing the dynamics of any elements of the reduced density matrix of the JC sub-system.

Through the LN implementation of the Trotter method, we have accessed regimes of very strong exciton-cavity coupling (up to $g = 1.5$ meV), unveiling behaviour that has not been previously observed or predicted. To interpret the results of our calculations, we moved away from the conventional polaron transformation and instead performed an alternative transformation so as to move from an exciton-cavity basis to a polariton basis (a *polariton transformation*). Inspection of the transformed

Hamiltonian revealed that transitions between polariton lines are permitted through phonon interaction operator V suppressed by a transformation factor. Application of Fermi's golden rule within the polariton frame enabled derivation of simple analytic expressions for the polariton line broadenings $\Gamma_{1,2}$ that show remarkably close agreement to the exact results calculated via our Trotter decomposition method.

4

Master equation approach to phonon-induced dephasing

In this chapter we consider *master equation* based approaches to calculating the dynamics of the exciton-cavity system with phonon dephasing [15, 16, 20, 22, 28, 29]. Such approaches involve a unitary transformation, known as the *polaron transformation* [10, 15, 20, 22, 28]. The Hamiltonian in the transformed frame may be split into three parts, only one of which contains both phonon and exciton-cavity modes of freedom. It is assumed that this portion of the Hamiltonian is small and may be treated perturbatively.

In order to implement the master equation approach, we must first define a Hermitian Hamiltonian, which we denote by $\bar{H}$,

$$\bar{H} = \Omega_X d^\dagger d + \Omega_C a^\dagger a + g(a^\dagger d + d^\dagger a) + H_{\rm ph} + d^\dagger d V \,. \tag{4.1}$$

Note that this is equivalent to the Hermitian Hamiltonian defined in Eq. (3.1), but with complex frequencies $\omega_{X,C}$ replaced by their respective real components $\Omega_{X,C}$. Applying the polaron transformation to the Hamiltonian $\bar{H}$ we obtain,

$$\bar{H} \to H' = e^S H e^{-S} \,, \tag{4.2}$$

with transformation matrix S given by,

$$S = d^\dagger d \sum_q \left(\frac{\lambda_q}{\omega_q} b_q^\dagger - \frac{\lambda_q^*}{\omega_q} b_q \right) . \tag{4.3}$$

Note that the transformed Hamiltonian H' is also Hermitian, but we will omit the bar notation for clarity. The transformed Hamiltonian H' may be expressed as a sum of three parts,

$$H' = H_{\text{sys}} + H_{\text{bath}} + H_{\text{int}} \,, \tag{4.4}$$

respectively representing the *system* (the modified exciton-cavity part), the *bath* (phonon modes) and the *interaction* (coupling of the system to the phonon bath). The three parts of the full polaron-frame Hamiltonian Eq. (4.4) have the following forms (see Sec. E.1 of the Appendix for a detailed proof):

$$H_{\text{sys}} = (\Omega_X + \Omega_p) d^\dagger d + \Omega_C a^\dagger a + g\langle B\rangle (a^\dagger d + d^\dagger a) \,, \tag{4.5}$$

$$H_{\text{bath}} = H_{\text{ph}} = \sum_q \omega_q b_q^\dagger b_q \,, \tag{4.6}$$

$$H_{\text{int}} = \sum_{\alpha=g,u} X_\alpha \otimes B_\alpha \,, \tag{4.7}$$

where we have defined the following,

$$\Omega_p = -\sum_q \frac{|\lambda_q|^2}{\omega_q} \,, \tag{4.8}$$

$$B_\pm = \exp\left(\pm \sum_q \left(\frac{\lambda_q}{\omega_q} b_q^\dagger - \frac{\lambda_q^*}{\omega_q} b_q \right) \right) \,, \tag{4.9}$$

$$X_g = g(a^\dagger d + d^\dagger a) \,, \tag{4.10}$$

$$X_u = ig(d^\dagger a - a^\dagger d) \,, \tag{4.11}$$

$$B_g = {}^1\!/_2 \left(B_+ + B_- - 2\langle B\rangle \right) \,, \tag{4.12}$$

$$B_u = {}^i\!/_2 \left(B_- - B_+ \right) \,. \tag{4.13}$$

In Eq. (4.12), $\langle B\rangle = \langle B_-\rangle = \langle B_+\rangle$ characterises the expectation value of the phonon displacement in a thermal state [10],

$$\langle B_\pm\rangle = \langle B\rangle = \exp\left(-\frac{1}{2} \sum_q \left| \frac{\lambda_q}{\omega_q} \right|^2 \left(N_q + \frac{1}{2} \right) \right) \,, \tag{4.14}$$

where $N_q = 1/[e^{\beta\omega_q} - 1]$ and β is the inverse temperature $(k_B T)^{-1}$ (see Sec. E.1 of the Appendix for derivation of Eq. (4.14)). Converting the summation over q to an integration over ω $\left(\sum_q \to \frac{\mathbb{V}}{(2\pi)^3 v_s^3} \int d^3\omega\right)$, where $\mathbb{V}$ is the sample volume, and

expressing $|\lambda_q|^2$ in terms of the spectral density function $J(\omega) = \sum_q |\lambda_q|^2 \delta(\omega - \omega_q)$, the polaron shift Ω_p and $\langle B \rangle$ may be expressed respectively as,

$$\Omega_p = -\int_0^\infty d\omega \frac{J(\omega)}{\omega}\,, \tag{4.15}$$

$$\langle B \rangle = \exp\left(\frac{1}{2}\int_0^\infty d\omega \frac{J(\omega)}{\omega^2} \coth\left(\frac{\beta\omega}{2}\right)\right)\,. \tag{4.16}$$

Note that Eq. (4.15) for the polaron shift is identical to that given in relation to the linked-cluster expansion of the IB model in Eq. (1.54). Moreover, for superohmic spectral density $J(\omega) \propto \omega^3$, which is the case under consideration in this instance, $\langle B \rangle$ is related to the Huang-Rhys factor S defined in Eq. (1.55),

$$\langle B \rangle = e^{-S/2}\,. \tag{4.17}$$

In terms of Hilbert spaces, the total Hilbert space may be expressed as the direct product ($\otimes$) of the system and bath Hilbert spaces,

$$\mathcal{H} = \mathcal{H}^{(\mathrm{sys})} \otimes \mathcal{H}^{(\mathrm{bath})}\,. \tag{4.18}$$

The interaction Hamiltonian H_{int} is the only part of the full polaron-frame Hamiltonian H' to contain both system (exciton-cavity) and bath (phonon) degrees of freedom: the operators X_α act on the system, whilst the operators B_α act on the bath. A key principle of the master equation approach is to assume that the interaction Hamiltonian H_{int} may be treated as a perturbation. Accordingly, we define the interaction representation such that a generic operator O is given by

$$\tilde{O}(t) = e^{iH_0 t}\, O\, e^{-iH_0 t}\,, \tag{4.19}$$

where the tilde notation denotes the interaction representation and $H_0 = H_{\mathrm{bath}} + H_{\mathrm{sys}}$.

As in previous sections, we wish to calculate the temporal behaviour of the density matrix $\rho(t)$. In the master equation approach, this is achieved through use of the Lindblad master equation,

$$\frac{d\rho}{dt} = -i[H', \rho] + \mathcal{D}\,, \qquad t > 0 \tag{4.20}$$

where H' is the polaron-frame Hamiltonian, defined in Eq. (4.4), and $\mathcal{D}$ is the Lindblad dissipator. The latter characterises the dissipation due to the radiative decay rate of the cavity mode γ_C and the long-time ZPL dephasing γ_X,

$$\mathcal{D} = \gamma_C \left(2a\rho a^\dagger - a^\dagger a\rho - \rho a^\dagger a\right) + \gamma_X \left(2d\rho d^\dagger - d^\dagger d\rho - \rho d^\dagger d\right) . \tag{4.21}$$

This equation would be exactly solvable if we were to neglect the influence of phonons (giving the JC model). However, if phonon interactions are included, the best that we can achieve is an approximate solution. We apply several approximations that will limit the range of applicability of the equation but will assist in achieving a solution. In the first instance, it is convenient to express Eq. (4.20) in the interaction representation. Using $\rho(t) = e^{-iH_0 t}\tilde{\rho}(t)e^{iH_0 t}$ we obtain,

$$\frac{d\tilde{\rho}(t)}{dt} = -i[\tilde{H}_{\rm int}(t), \tilde{\rho}(t)] + \tilde{\mathcal{D}}(t) . \tag{4.22}$$

Eq. (4.22) has the formal solution

$$\tilde{\rho}(t) = \tilde{\rho}(0) + \int_0^t d\tau \left(-i[\tilde{H}_{\rm int}(\tau), \tilde{\rho}(\tau)] + \tilde{\mathcal{D}}(\tau)\right) . \tag{4.23}$$

Inserting Eq. (4.23) for $\tilde{\rho}(t)$ into Eq. (4.22) we find that,

$$\begin{aligned}\frac{d\tilde{\rho}(t)}{dt} = &-i\Big[\tilde{H}_{\rm int}(t), \rho(0)\Big] - i\left[\tilde{H}_{\rm int}(t), \int_0^t d\tau\ \tilde{\mathcal{D}}(\tau)\right] \\ &- \left[\tilde{H}_{\rm int}(t), \int_0^t d\tau\ [\tilde{H}_{\rm int}(\tau), \tilde{\rho}(\tau)]\right] + \tilde{\mathcal{D}}(t) .\end{aligned} \tag{4.24}$$

Note that this iterative procedure could therefore be repeated ad infinitum. We assume, however, that $H_{\rm int}$ is a small perturbation (the *weak coupling limit*), thereby rendering Eq. (4.24) sufficient. This is known as the *second-order Born approximation*. In the present form, we are able to make certain simplifying approximations to Eq. (4.24) that will enable us to find a solution for $\rho(t)$.

We are interested in the evolution of the exciton-cavity system, and thus require an equation that characterises the behaviour of the reduced density operator $\rho_{\rm S}(t)$. We therefore take the partial trace of Eq. (4.24) over all bath degrees of freedom,

$$\begin{aligned}\frac{d\tilde{\rho}_S(t)}{dt} = &\ {\rm tr}_B\left\{-i[\tilde{H}_{\rm int}(t), \tilde{\rho}(0)]\right\} - {\rm tr}_B\left\{i\left[\tilde{H}_{\rm int}(t), \int_0^t d\tau\ \tilde{\mathcal{D}}(\tau)\right]\right\} \\ &- \int_0^t d\tau\ \ {\rm tr}_B[\tilde{H}_{\rm int}(t), [\tilde{H}_{\rm int}(\tau), \tilde{\rho}(\tau)]] + \tilde{\mathcal{D}}_S(t) ,\end{aligned} \tag{4.25}$$

where $\tilde{\mathcal{D}}_S(t) = {\rm tr}_B\{\tilde{\mathcal{D}}(t)\}$ and we have used $\rho_{\rm S}(t) = {\rm tr}_B\{\rho(t)\}$.

4.1 Levels of approximation

In this section, we apply a number of assumptions and approximations that will allow us to recast Eq. (4.25) in a solvable form.

We now rely upon the weak coupling approximation, assuming that H_{int} is a small perturbation. Further, we assume that the bath is sufficiently large to be unaffected by the interaction with the system. These approximations allow us to factorise the density matrix $\tilde{\rho}(t)$ at all times,

$$\tilde{\rho}(t) = \tilde{\rho}_S(t) \otimes \tilde{\rho}_B \,, \tag{4.26}$$

where the bath density matrix $\tilde{\rho}_B$ is independent of time: $\tilde{\rho}_B = \tilde{\rho}_B(0)$. For reasons discussed in Sec. E.2 of the Appendix, this approximation causes the second term in Eq. (4.25) to vanish. Additionally, when applied at $t = 0$, this approximation removes the first term of Eq. (4.25).

We therefore arrive at the following form of the master equation:

$$\frac{d\tilde{\rho}_S(t)}{dt} = -\int_0^t d\tau \;\; \text{tr}_B[\tilde{H}_{\text{int}}(t), [\tilde{H}_{\text{int}}(\tau), \tilde{\rho}_S(\tau) \otimes \tilde{\rho}_B]] + \tilde{\mathcal{D}}_S(t) \,. \tag{4.27}$$

At this point, our approach differs according to the level of approximation, as outlined in Fig. 4.1. The different approximations are addressed separately in the following sections.

4.1.1 Time convolutionless (TCL) master equation

We note that Eq. (4.27) has memory: the future evolution of the system density matrix $\tilde{\rho}_S(t)$ depends upon the history of the density matrix through the integration of $\tilde{\rho}_S(\tau)$. We remove this memory through the *Markov approximation*, in which we make the replacement $\tilde{\rho}_S(\tau) \to \tilde{\rho}_S(t)$. This approximation is valid if the system evolution timescale τ_{JC} is large in comparison to the bath memory time τ_{IB}. This approximation gives a time-local form of the master equation,

$$\frac{d\tilde{\rho}_S(t)}{dt} = -\int_0^t d\tau \;\; \text{tr}_B[\tilde{H}'_{\text{int}}(t), [\tilde{H}'_{\text{int}}(\tau), \tilde{\rho}_S(t) \otimes \tilde{\rho}_B]] + \tilde{\mathcal{D}}_S(t) \,. \tag{4.28}$$

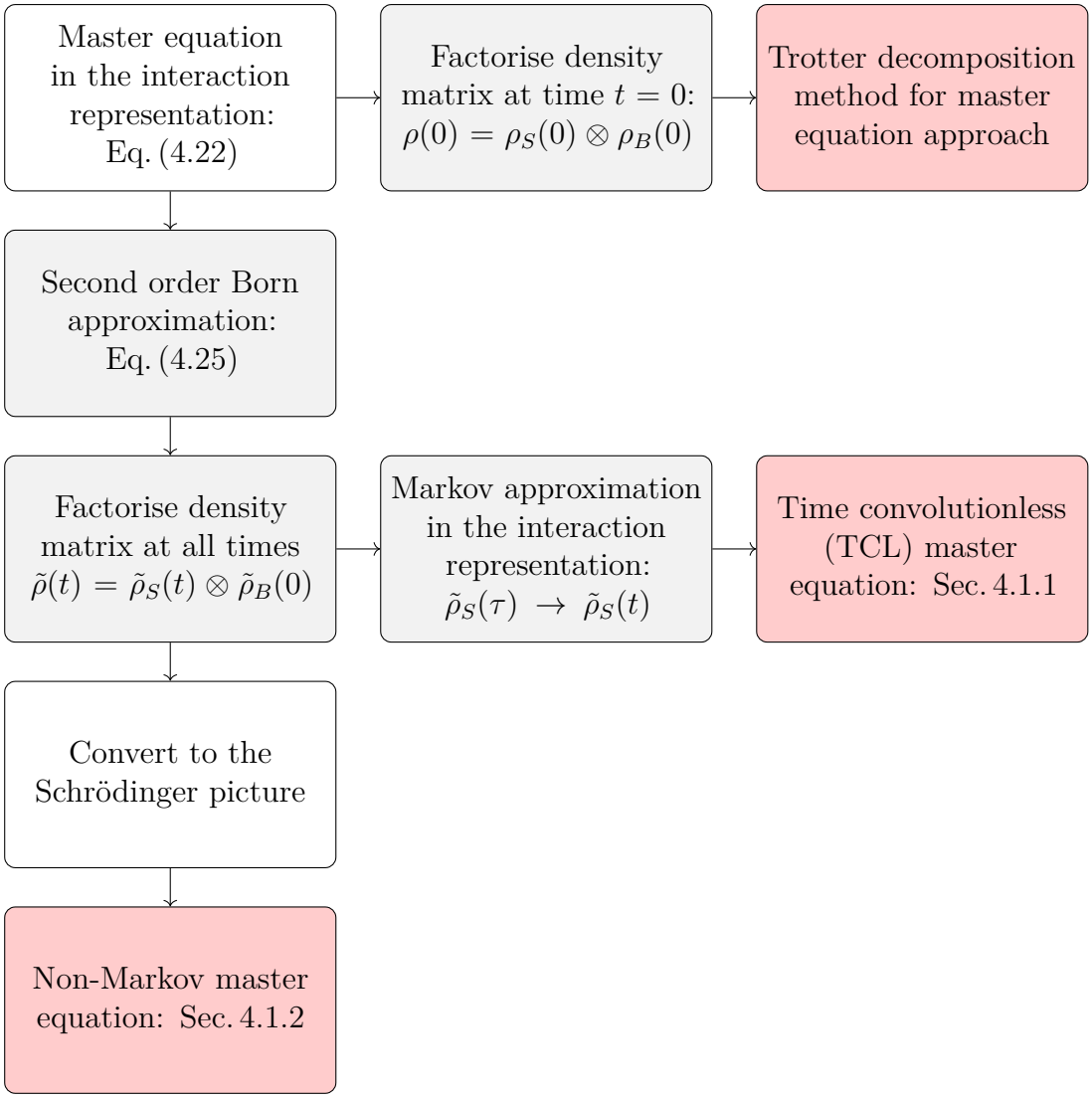

Figure 4.1: Diagrammatic representation of the different levels of approximation of the master equation that are considered in the present work. Grey boxes indicate approximations or assumptions. Also shown, for comparison, is the approximation required for the Trotter decomposition method. Whilst the description of the Trotter decomposition method given in Chapter 3 does not rely upon the master equation formalism, the method is equally applicable for the master equation approach.

We now convert Eq. (4.28) from the interaction representation to the Schrödinger representation and make the substitution $t' = t - \tau$, arriving at the following form of master equation (see Sec. E.2.1 of the Appendix for details):

$$\frac{d\rho_S(t)}{dt} = -i[H_{\text{sys}}, \rho_S(t)] + \mathcal{D}_S(t) - \int_0^t dt' \sum_{\alpha=g,u} \langle B_\alpha \tilde{B}_\alpha(-t')\rangle [X_\alpha, \tilde{X}_\alpha(-t')\rho_S(t)] + \text{H.c.} \tag{4.29}$$

Equations of motion

To derive the equations of motion from Eq. (4.29), we note from Eq. (**??**) that the system density matrix $\rho_S(t)$ may be expressed in the $\{|0\rangle, |X\rangle, |C\rangle\}$ basis. Equally, the excitonic and cavity operators may be expressed explicitly in this three-state basis as per Eqs. (1.21) and (1.22). Each term is considered individually in Sec. E.2.1 of the Appendix, but for the sake of brevity we will simply state the final equations of motion in this section. Whilst a general solution is possible, the following equations are valid only for the case of zero effective detuning ($\Omega_C = \Omega_X + \Omega_p$).

$$\frac{d\bar{\rho}}{dt} = Q(t)\bar{\rho}(t)\,, \tag{4.30}$$

where $\bar{\rho}$ is a vector made up of elements of the reduced system density matrix

$$\bar{\rho} = \begin{pmatrix} \rho_{X0} \\ \rho_{C0} \end{pmatrix}\,, \tag{4.31}$$

and $Q(t)$ is a 2x2 matrix of the form

$$Q(t) = -i \begin{pmatrix} \Omega_C - i\gamma_X & g\langle B\rangle \\ g\langle B\rangle & \Omega_C - i\gamma_C \end{pmatrix} + \int_0^t dt'\, I(t')\,, \tag{4.32}$$

with

$$I(t) = g^2 \begin{pmatrix} I_0(t) & I_1(t) \\ I_1(t) & I_0(t) \end{pmatrix}\,, \tag{4.33}$$

$$I_0(t) = G_g(t) + \cos(2g\langle B\rangle t)\, G_u(t)\,, \tag{4.34}$$

$$I_1(t) = i\sin(2g\langle B\rangle t)\, G_u(t)\,, \tag{4.35}$$

$$G_g(t) = \langle B_g \tilde{B}_g(-t)\rangle = \langle B\rangle^2 \left(\cosh(\phi(t)) - 1\right)\,, \tag{4.36}$$

$$G_u(t) = \langle B_u \tilde{B}_u(-t)\rangle = \langle B\rangle^2 \sinh(\phi(t))\,, \tag{4.37}$$

$$\phi(t) = \int_0^\infty d\omega \frac{J(\omega)}{\omega^2} \left(\coth\left(\frac{\beta\omega}{2}\right)\cos(\omega t) - i\sin(\omega t)\right)\,. \tag{4.38}$$

Note that $\phi(t)$ may be related to the IB cumulant $K(t)$: $\phi(t) = K(t) + i\Omega_p t + S$. Further, the matrix composed of $\Omega_C - i\gamma_{X,C}$ and $g\langle B\rangle$ in the expression for $Q(t)$ is identical to the Hamiltonian of the analytic Trotter decomposition solution Eq. (3.39). The additional integral term contained within the expression for $Q(t)$ is a perturbative correction to this Hamiltonian.

Polarisation and absorption

We solve Eq. (4.30) numerically to find $\bar{\rho}(t)$, paying close attention to the initial condition $\bar{\rho}(0+)$, which is dependent upon the feeding channel, as discussed in Secs. 1.2 and 3.1. The initial density matrix must be correctly transformed into the polaron frame, gaining a factor of B_- if under excitonic feeding.

Having found an expression for $\bar{\rho}$, we may then apply the standard definition of linear optical polarisation given in Eq. (1.1), noting that we must transform the density matrix back from the polaron frame (or equivalently transform the operator annihilation operator c into the polaron frame),

$$P(t) = \mathrm{Tr}\left\{\rho'(t) e^{S} c\, e^{-S}\right\}, \tag{4.39}$$

where $\rho'(t)$ is the density matrix in the polaron frame (denoted by $\rho(t)$ in all other instances in this Chapter for simplicity of notation). Relying on the prior approximation $\rho'(t) = \rho_S(t) \otimes \rho_B(t)$ allows us to reduce Eq. (4.39) to

$$P_{XX} = \langle B\rangle \rho_{X0}(t)\,, \qquad P_{CC} = \rho_{C0}(t)\,, \tag{4.40}$$

where we have used $c = d$ to give $P_{XX}(t)$, and $c = a$ to give $P_{CC}(t)$. As always, the absorption is found by taking the real part of the inverse Fourier transform of the polarisation, as described in Eq. (1.18).

4.1.2 Non-Markov master equation

In Sec. 4.1.1, we made the Markov approximation in the interaction picture and subsequently transformed into the Schrödinger representation. Another option available to us is to convert the master equation to the Schrödinger representation without the Markov approximation i.e. without modification of the argument of

the system density matrix $\rho_S(\tau)$. Such an approach leads us to the following form of the master equation (See Sec. E.2.2 of the Appendix for full derivation):

$$\frac{d\rho_S(t)}{dt} = -i[H_{\text{sys}}, \rho_S(t)] + \mathcal{D}_S(t) \\ - \int_0^t d\tau \sum_{\alpha=g,u} \langle B_\alpha \tilde{B}_\alpha(t-\tau)\rangle \left[X_\alpha, e^{-iH_{\text{sys}}(t-\tau)} X_\alpha \rho_S(\tau) e^{iH_{\text{sys}}(t-\tau)}\right] + \text{H.c.} \tag{4.41}$$

Note the similarities between Eq. (4.41) and Eq. (4.29).

Equations of motion

For zero effective detuning, Eq. (4.41) may be compactly expressed as

$$\frac{d\bar{\rho}}{dt} = -i \begin{pmatrix} \Omega_C - i\gamma_X & g\langle B\rangle \\ g\langle B\rangle & \Omega_C - i\gamma_C \end{pmatrix} \bar{\rho}(\tau) - \int_0^t d\tau\, \hat{W}(t-\tau)\bar{\rho}(\tau)\,, \tag{4.42}$$

where $\bar{\rho}$ is defined in Eq. (4.31) and $\hat{W}$ is given by

$$\hat{W}(t) = e^{-i\Omega_C t} g^2 \begin{pmatrix} \cos(g\langle B\rangle t)\, G_+(t) & -i\sin(g\langle B\rangle t)\, G_-(t) \\ -i\sin(g\langle B\rangle t')\, G_-(t) & \cos(g\langle B\rangle t)\, G_+(t) \end{pmatrix}, \tag{4.43}$$

with $G_\pm$ given by

$$G_\pm(t) = G_g(t) \pm G_u(t) = \langle B\rangle^2 \left(e^{\pm\phi(t)} - 1\right). \tag{4.44}$$

Importantly, the integral over $\hat{W}(t-\tau)\bar{\rho}(\tau)$ describes a convolution, which enables us to extract a simple solution to Eq. (4.41) in frequency space:

$$-\omega\bar{R}(\omega) = -i \underbrace{\begin{pmatrix} \Omega_C - i\gamma_X & g\langle B\rangle \\ g\langle B\rangle & \Omega_C - i\gamma_C \end{pmatrix}}_{(1)} \bar{R}(\omega) + \frac{g^2}{2} \underbrace{\begin{pmatrix} A(\omega) & B(\omega) \\ B(\omega) & A(\omega) \end{pmatrix}}_{(2)} \bar{R}(\omega) + \bar{\rho}(0)\,, \tag{4.45}$$

where $\bar{\rho}(0)$ contains the initial conditions, and

$$A(\omega) = G_+(\omega - \Omega_1) + G_+(\omega - \Omega_2) \tag{4.46}$$

$$B(\omega) = -G_-(\omega - \Omega_1) + G_-(\omega - \Omega_2)\,, \tag{4.47}$$

with $G_\pm(\omega)$ being the Fourier transform of $G_\pm(t)$. In deriving Eq. (4.45), we have used the fact that $e^{-i\Omega_C t}\cos(g\langle B\rangle t)$ may be expressed as $1/2(e^{-i\Omega_1 t} + e^{-i\Omega_2 t})$ where $\Omega_{1,2} = \Omega_C \pm g\langle B\rangle$ (and analogously for other elements of $\hat{W}(t)$). Noting the parallels

between matrix (1) in Eq. (4.45) and the JC Hamiltonian, Eq. (1.24), we denote matrices that diagonalise matrix (1) by $\tilde{\hat{Y}}$ and $\tilde{\hat{Y}}^{-1}$, with

$$\tilde{\hat{Y}} = \begin{pmatrix} \tilde{\alpha} & \tilde{\beta} \\ -\tilde{\beta} & \tilde{\alpha} \end{pmatrix}, \tag{4.48}$$

$$\tilde{\alpha} = \frac{\Delta}{\sqrt{\tilde{\Delta}^2 + (g\langle B\rangle)^2}}, \tag{4.49}$$

$$\tilde{\beta} = \frac{g\langle B\rangle}{\sqrt{\tilde{\Delta}^2 + (g\langle B\rangle)^2}}, \tag{4.50}$$

where $\tilde{\Delta} = \sqrt{\tilde{\delta}^2 + (g\langle B\rangle)^2} - \tilde{\delta}$ and $\tilde{\delta} = 1/2\,(\gamma_C - \gamma_X)$. Clearly, for $\gamma_X = \gamma_C$ we have the simple case of $\tilde{\alpha} = \tilde{\beta} = 1/\sqrt{2}$. This would allow simultaneous diagonalisation of matrices (1) and (2) within Eq. (4.45) and would provide an analytic solution for the linear absorption. For $\gamma_X \neq \gamma_C$, we make the replacement $\gamma_{X,C} \to \gamma_0$, where $\gamma_0 = 1/2(\gamma_X + \gamma_C)$. This is clearly an approximation; the validity of which increases with g (as the contribution of $\tilde{\delta}$ to $\tilde{\alpha}$ and $\tilde{\beta}$ decreases). With this approximation, we arrive at the following expressions for absorption:

$$A_{XX}(\omega) = \mathrm{Re}\left\{\frac{1}{2}\langle B\rangle^2\left(\frac{1}{\lambda_1(\omega)} + \frac{1}{\lambda_2(\omega)}\right)\right\}, \tag{4.51}$$

$$A_{CC}(\omega) = \mathrm{Re}\left\{\frac{1}{2}\left(\frac{1}{\lambda_1(\omega)} + \frac{1}{\lambda_2(\omega)}\right)\right\}, \tag{4.52}$$

where

$$\lambda_1(\omega) = -i[\omega - (\Omega_1 - i\gamma_0)] + g^2[G_g(\omega - \Omega_1) + G_u(\omega - \Omega_2)], \tag{4.53}$$

$$\lambda_2(\omega) = -i[\omega - (\Omega_2 - i\gamma_0)] + g^2[G_u(\omega - \Omega_1) + G_g(\omega - \Omega_2)]. \tag{4.54}$$

Note that the factor of $\langle B\rangle^2$ in Eq. (4.51) is due to the action of the polaron transformation matrix S on the excitonic excitation operator $d^\dagger$ and the observation operator d; S commutes with $c^\dagger$ and c so $A_{CC}(\omega)$ is unaffected.

4.2 Comparison of Trotter decomposition and master equation approaches

Having discussed various levels of approximation within the master equation approach, we now look to compare the absorption spectra calculated according to

(i) the Trotter decomposition method of Chapter 3, (ii) the TCL master equation of Sec. 4.1.1, and (iii) the Non-Markov master equation of Sec. 4.1.2. In relation to the Trotter approach, we take only the LN calculation with $L = 15$.

Fig. 4.2 shows the excitonic absorption spectra $A_{XX}(\omega)$ for relatively small exciton-cavity coupling strength $g = 50\,\mu$eV at $T = 0$ K (left panel) and $T = 50$ K (right panel). It is immediately clear that the master equation approaches (TCL and Non-Markov) do not reproduce the phonon broadband. This is an interesting consequence given that implementation of the master equation approaches requires calculation of $\phi(t)$, which is equivalent to the part of the IB cumulant responsible for the broadband, $K_{BB}(t)$. It is, however, understood to occur as a result of the density matrix factorisation employed within the master equation approaches: $\tilde{\rho}(t) = \tilde{\rho}_S(t) \otimes \tilde{\rho}_B$. Iles-Smith *et al.* [79, 82] adopt a variation of the above-described TCL master equation but calculate the emission spectrum under continuous wave excitation. Following the Wiener-Khinchin theorem, the steady state spectrum is expressed in terms of an electric field correlation function. Whilst the full form of this correlation function is intractable, approximate factorisation is possible if the polariton timescale is much longer than the polaron timescale (low g limit). This factorisation separates the emission spectrum into a contribution from the purely optical exciton recombination and a contribution from phonon-assisted transitions. The latter, responsible for the phonon broadband, has the form $\mathrm{Re}\int_0^\infty dt\, B^2 e^{-i\Omega_p t} g_0(t)(e^{\phi(t)} - 1)$ with $g_0(t) = \lim_{\tau\to\infty}\langle\tilde{d}^\dagger(\tau)\tilde{d}(\tau + t)\rangle$. Iles-Smith *et al.* make the approximation $g_0(t) \approx g_0(0)$, rendering the phonon contribution to the emission spectrum equivalent to the IB phonon broadband ($\mathrm{Re}\int_0^\infty dt\, e^{K(t)} - e^{K_\infty(t)}$) renormalised by $g_0(0)$. This approximation may be valid in the regime of small exciton-cavity coupling g. At high g, however, there is significant modification to the broadband (as can be seen from Figs. 4.3 and 4.4), which would not be accounted for in this approach.

Other than the above-described phonon broadband, there is very close agreement between the TCL master equation and the Trotter decomposition approach, particularly at $T = 0$. The results from the Non-Markov approach are poor at low

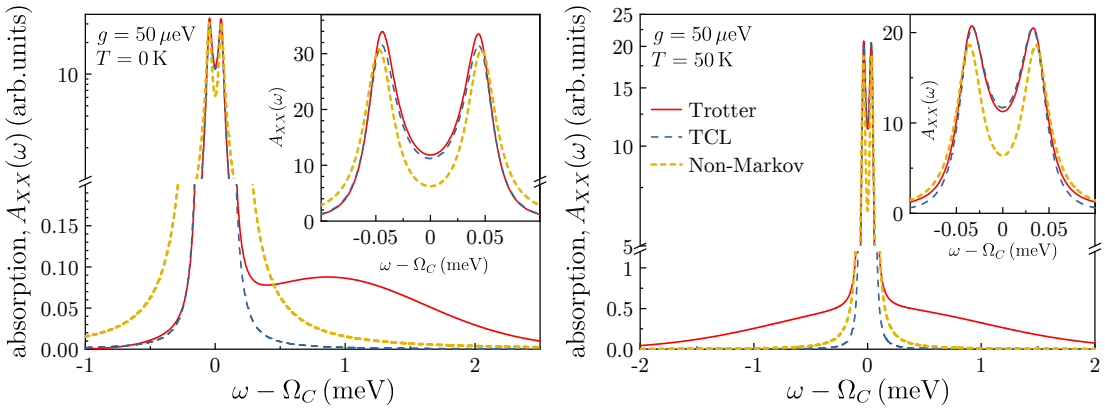

Figure 4.2: Comparison of excitonic absorption spectra calculated according to the Trotter decomposition method, the TCL master equation and the Non-Markov master equation for $g = 50\,\mu$eV, $\gamma_X = 2\,\mu$eV, $\gamma_C = 30\,\mu$eV. Other QD/phonon parameters as per Section 1.3: $a = 3.3\,$nm, $D_c - D_v = -6.5\,$eV, $v_s = 4.6 \times 10^3\,$m/s, and $\rho_m = 5.65\,$g/cm^3. Temperature $T = 0$ K ($T = 50$ K) is shown in the left (right) panel, with insets showing a reduced frequency range about the polariton peaks.

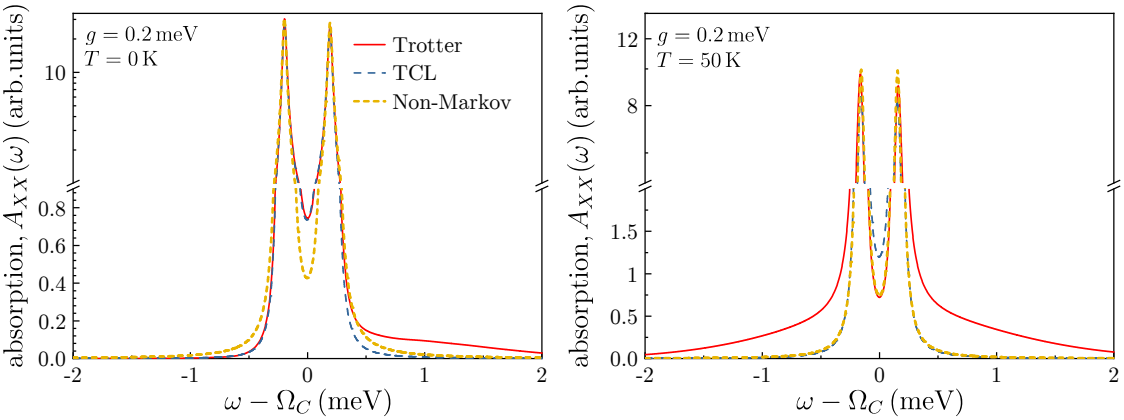

Figure 4.3: As Fig. 4.2 but with $g = 0.2$ meV.

exciton-cavity coupling g due to the assumption that $\tilde{\alpha} = \tilde{\beta} = 1/\sqrt{2}$ (equivalent to γ_X, $\gamma_C \to \gamma_0$) required in order to simultaneously diagonalise matrices (1) and (2) of Eq. (4.41). This accuracy of this approach would be significantly improved for similar exciton and cavity broadenings $\gamma_X \approx \gamma_C$.

We now consider the situation at increased exciton-cavity coupling strength g. Figs. 4.3 and 4.4 show the excitonic absorption spectra $A_{XX}(\omega)$ for $g = 0.2$ meV and $g = 0.6$ meV respectively. At $g = 0.2$ meV there is generally good agreement between

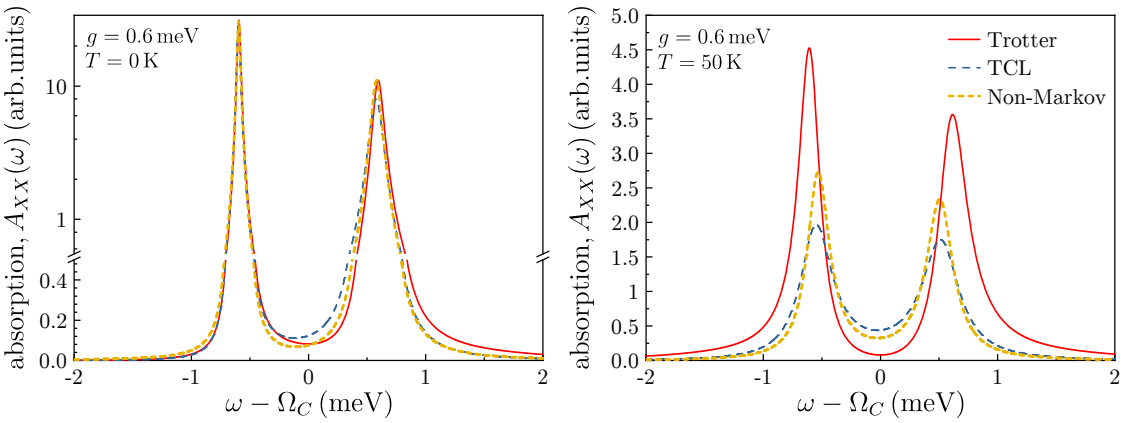

Figure 4.4: As Fig. 4.2 but with $g = 0.6$ meV.

all three models (again neglecting the differences due to the phonon broadband). The agreement is particularly close between the Trotter and TCL approaches at $T = 0$ K, and between the Trotter and Non-Markov approaches at $T = 50$ K. At $g = 0.6$ meV, there remains very good agreement for zero temperature, but we see significant discrepancies between the three approaches at $T = 50$ K.

To examine the situation further, it is instructive to consider the behaviour of the polariton linewidths $\Gamma_{1,2}$ with exciton-cavity coupling strength g. Fig. 4.5 shows the lower (1) and upper (2) polariton linewidths calculated at $T = 0$ K according to the three different approaches. All three approaches exactly capture the simple behaviour of the lower polariton linewidth Γ_1. As discussed in Sec. 3.4, the non-zero broadening of this line is a consequence of the finite long-time ZPL dephasing γ_X and radiative decay γ_C (set to $2\,\mu$eV and $30\,\mu$eV respectively); there is no contribution from phonon-mediated transitions and hence no dependence on the exciton-cavity coupling strength g. This is not the case for the upper polariton linewidth Γ_2: transitions from the upper polariton state (2) to the lower state (1) may proceed with the emission of a phonon, even at zero temperature. The upper polariton linewidths Γ_2 calculated according to the TCL and Non-Markov equations closely match those calculated from the Trotter decomposition method at low g and qualitatively agree thereafter. There is, however, a significant quantitative disparity, particularly at the broadening maxima (~ 0.75 meV).

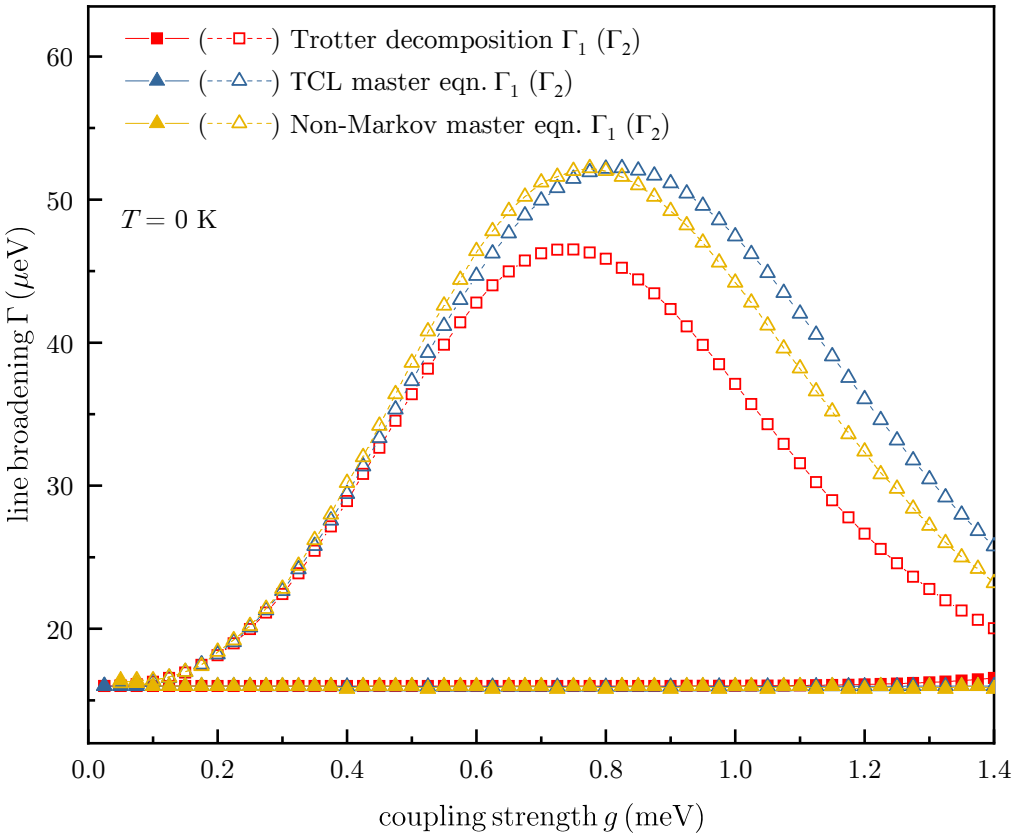

Figure 4.5: Linewidths $\Gamma_{1,2}$ of the lower (1) and upper (2) polariton states as calculated by the Trotter decomposition method (red), the TCL master equation (blue) and the Non-Markov master equation (yellow). Linewidths are shown as functions of the exciton-cavity coupling strength g for temperature $T = 0$ K.

Fig. 4.6 also shows the behaviour of the polariton linewidths $\Gamma_{1,2}$ with exciton-cavity coupling strength g, but at the increased temperature of $T = 50$ K. We see that the agreement between approaches is generally worse at this temperature, which is to be expected in view of the absorption spectra shown in Figs. 4.2 to 4.4. It is interesting to note that the ratio of the upper and lower polariton linewidths calculated according to the Non-Markov approach is approximately equal to that calculated by the Trotter decomposition method. The Non-Markov approach, however, does not exhibit the clear peak in linewidths that is shown at $g \sim 0.6$ meV by the Trotter decomposition results. As regards the TCL approach, there is good agreement at small exciton-cavity coupling strengths g but the results are clearly erroneous at large g. In particular, the TCL approach does not predict a

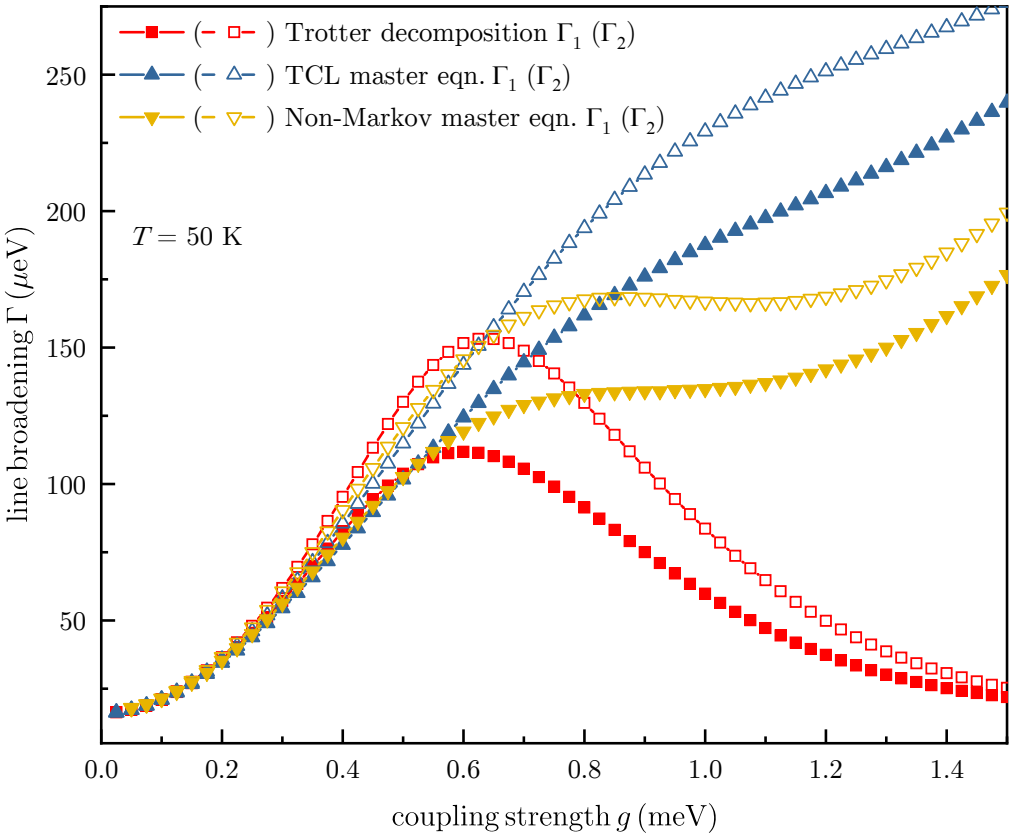

Figure 4.6: As Fig. 4.5 but for $T = 50$ K.

broadening maximum; instead indicating a general increase in broadening with coupling strength g.

Finally, we examine the behaviour of the Rabi splitting $\Delta\Omega = \Omega_2 - \Omega_1$ with exciton-cavity coupling strength g. Fig. 4.7 shows the polariton Rabi splitting $\Delta\Omega$ as a function of exciton-cavity strength g calculated at $T = 0$ K according to the three different approaches. The TCL and Non-Markov results are qualitatively similar to one-another across the full range of exciton-cavity coupling strengths, but at large g this behaviour is markedly different to that predicted by the Trotter decomposition method. Fig. 4.8 also shows the behaviour of the polariton Rabi splitting $\Delta\Omega$, but at the higher temperature of $T = 50$ K. Again, there is good agreement between all three approaches at small exciton-cavity coupling strengths g, but significant disparity at larger g.

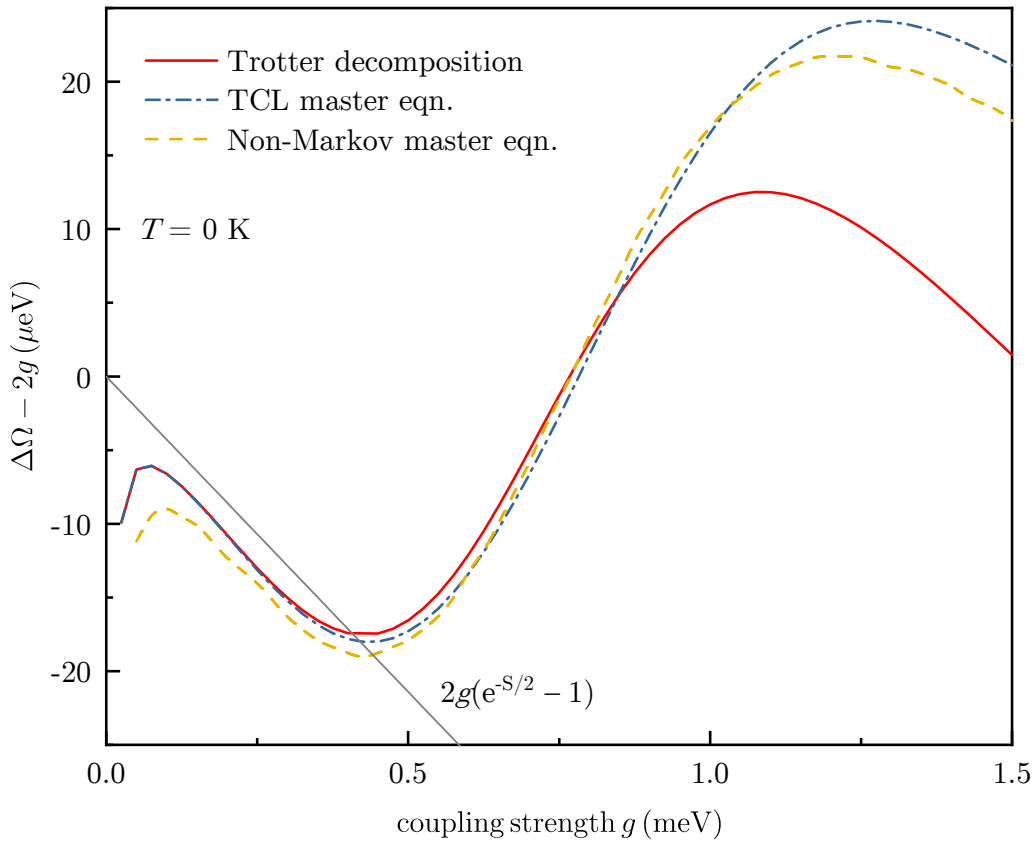

Figure 4.7: Deviation of the polariton Rabi splitting $\Delta\Omega$ from the nominal splitting $2g$ as a function of the exciton-cavity coupling strength g, shown for temperature $T = 0$ K. Also shown (black solid line) is the deviation of the phonon renormalised Rabi splitting $2ge^{-S/2}$ from the nominal Rabi splitting $2g$.

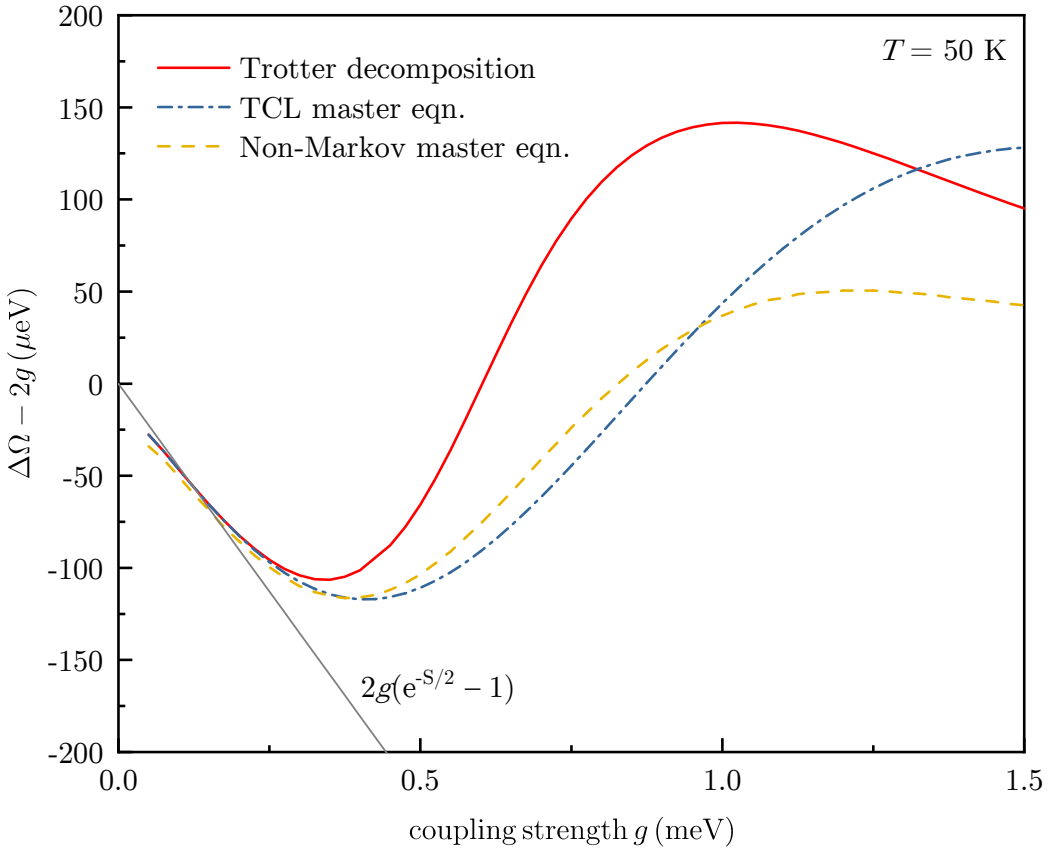

Figure 4.8: As Fig. 4.7 but for $T = 50$ K.

4.3 Chapter conclusion

To conclude this chapter, we have examined the origin of the above-described discrepancies between the Trotter decomposition method and the two master equation approaches (TCL and Non-Markov). One of the critical assumptions of the master equation is that the system evolution (characterised by τ_{JC} in Chapter 3) varies more slowly than the environmental relaxation timescale (characterised by τ_{IB} in Chapter 3). The Trotter decomposition method is not limited by this condition, and may access regimes of arbitrarily fast system evolution by increasing the number of neighbours L. The 15-neighbour Trotter decomposition approach, employed in all calculations in this chapter, is readily capable of accessing the full range of exciton-cavity coupling strengths shown in the figures, whilst the master equation approaches break down beyond $g \sim 0.2$ meV.

5 Conclusion

In this work we have studied many aspects of the interaction between a QD exciton and its phonon environment. We have exploited the thermally sensitive phonon broadband, often viewed as a unwanted feature within semiconductor QD applications, to measure the temperature of the QD sample. We have also analysed the role of phonons in a QD-microcavity system, developing a new method for exact calculation of the system dynamics.

5.1 Phonon thermometer

We have explored the concept of temperature measurement from QD PL spectra, looking at both a simple thermal ratio and a more complex fitting procedure. In relation to the fiting procedure, we have demonstrated very good agreement between the fit temperature and the nominal (cryostat-measured) temperature. There are, however, slight discrepancies at low temperature ($T \leq 10$ K) that merit further investigation. Moreover, we have shown that the fit procedure enables straightforward determination of other QD parameters such as confinement lengths and material deformation potential that are traditionally difficult to measure.

To further progress this avenue of research it would be prudent to conduct time-resolved spectroscopy with a view to determining the equilibration timescales,

particularly the carrier cooling timescale. It would also be instructive to investigate the Lorentzian and Gaussian broadening mechanisms further, which will require additional measurements under varying conditions such as resonant excitation and high dynamic range measurements for different excitation powers.

The general concept and associated fitting routine also has potential applications also in other physical systems such as colloidal QDs.

5.2 Phonon-induced dephasing of cavity-QD system

We have shown that our newly developed Trotter decomposition method enables calculation of the linear optical polarisation of the QD-cavity system through simple matrix product operations. In the L-neighbour implementation, the matrices are multidimensional (size 2^L), simplifying to 2×2 matrices for the NN ($L = 1$) approximation. Furthermore, each matrix element is easily calculable from the JC and IB models, with computation of the IB cumulant $K(t)$ being no more complex than the phonon propagator $\phi(t)$ required for the master equation based solutions.

Through the LN implementation of the Trotter method, we have accessed regimes of very strong exciton-cavity coupling (up to $g = 1.5$ meV), unveiling behaviour that has not been previously observed or predicted. In particular, we have found the absorption spectrum to consist of the phonon broadband alongside two Lorentzian broadened polariton lines. This holds true across the full range of exciton-cavity coupling strengths that we have considered. Guided by this observation, we have provided a physically intuitive interpretation of the above-described findings in terms of the polariton model. We have shown that within the polariton frame, Fermi's Golden Rule for real phonon-assisted transitions provides a very good description of the polariton line broadenings.

We have calculated, in Chapter 4, absorption spectra of the QD-microcavity system according to two levels of approximation of the well-known master equation approach. We have found the TCL master equation, in which the Markov approximation is made, provides a good description of the QD cavity system if the

polariton dynamics are slow (small exciton-cavity coupling strength g). However, this approach breaks down once the polariton and polaron timescales become comparable. The Non-Markov master equation shows slightly improved accuracy relative to the TCL approach in the regime of comparable polariton and polaron timescales, but nonetheless significant divergence from the Trotter decomposition predictions. We conclude that neither master equation approach is suited to exciton-cavity coupling strengths beyond $g \sim 0.2$ meV due to approximations made within their derivation. Moreover, even at small exciton-cavity coupling strengths the master equation approaches cannot capture the phonon broadband. This is in contrast to the Trotter decomposition approach, which can readily capture the phonon broadband and, through the LN implementation, is capable of accessing regimes of arbitrarily strong exciton-cavity coupling g.

As noted previously, the Trotter decomposition method may be easily adapted to determine the dynamics of any elements of the reduced density matrix of the JC sub-system. The calculation of photon indistinguishability would constitute an interesting extension to the current work.

Appendices

A
General derivations

A.1 Commutation relations

The exciton and cavity-photon operators obey the Fermi anticommutation relations,

$$\{a, a^\dagger\} = \{d, d^\dagger\} = 1\,, \tag{A.1}$$

$$\{a, a\} = \{d, d\} = 0\,, \tag{A.2}$$

$$\{a^\dagger, a^\dagger\} = \{d^\dagger, d^\dagger\} = 0\,. \tag{A.3}$$

The phonon operators obey the Bose commutation relations,

$$[b_q, b_{q'}^\dagger] = \delta_{qq'}\,, \tag{A.4}$$

$$[b_q, b_{q'}] = 0\,, \tag{A.5}$$

$$[b_q^\dagger, b_{q'}^\dagger] = 0\,. \tag{A.6}$$

A.2 Key identities

Baker-Hausdorff identity

$$e^S B e^{-S} = B + [S, B] + \frac{1}{2!}[S, [S, B]] + \ldots,, \tag{A.7}$$

for any two operators S and B.

A.3 Representations

A.3.1 Schrödinger representation

One of the foundations of Quantum Mechanics is the Schrödinger equation, which defines the relationship between wavefunction $\psi(t)$ and Hamiltonian H.

$$i\frac{\partial}{\partial t}\psi(t) = H\psi(t)\,. \tag{A.8}$$

This equation is expressed in the so-called *Schrödinger representation*, in which wave-functions are time-dependent and operators are independent of time.

A.3.2 Heisenberg representation

It is possible to change the representation so that the operators are time-dependent and the wavefunctions are independent of time. This is known as the *Heisenberg representation*. In this representation, a generic operator O obeys the following relation:

$$i\frac{\partial}{\partial t}O(t) = [O(t), H]\,. \tag{A.9}$$

This relation has the formal solution

$$O(t) = e^{iHt}O(0)e^{-iHt}\,. \tag{A.10}$$

The representations coincide at $t = 0$. Crucially, calculations of all physical observables are independent of the representation; the results are identical. Consider, for example, the matrix element of the operator O between states ψ_1 and ψ_2. In the Schrödinger representation, this is given by

$$\langle\psi_1(t)|\,\hat{O}\,|\psi_2(t)\rangle = \langle\psi_1|\,e^{iHt}\hat{O}e^{-iHt}\,|\psi_2\rangle\ . \tag{A.11}$$

Alternatively, in the Heisenberg representation, this is given by

$$\langle\psi_1|\,\hat{O}(t)\,|\psi_2\rangle = \langle\psi_1|\,e^{iHt}\hat{O}e^{-iHt}\,|\psi_2\rangle\ . \tag{A.12}$$

A.3.3 Interaction representation

This representation is generally employed when the Hamiltonian H may be separated into two parts

$$H = H_0 + V\,. \tag{A.13}$$

The separation is, in principle, arbitrary, but in order for the interaction representation to constitute a powerful tool, H_0 is typically chosen to be exactly solvable. For the purposes of this thesis, wavefunctions and operators in the Interaction representation will be denoted by a tilde ($\tilde{}$).

The time-dependence of the operators is governed by the unperturbed Hamiltonian H_0,

$$\tilde{O}(t) = e^{iH_0t}O(0)e^{-iH_0t}\,. \tag{A.14}$$

The time-dependence of the wavefunctions is, on the other hand, governed by the perturbation V,

$$\tilde{\psi}(t) = e^{iH_0t}\psi(t) = e^{iH_0t}e^{-iHt}\psi(0)\,, \tag{A.15}$$

hence,

$$\begin{aligned} i\frac{\partial\tilde{\psi}}{\partial t} &= e^{i\hat{H}_0t}(-H_0 + H)e^{-iHt}\phi(0) && \text{(A.16)}\\ &= \left(e^{iH_0t}V(t)e^{-iH_0t}\right)\left(e^{iH_0t}e^{-iHt}\psi(0)\right) && \text{(A.17)}\\ &= \tilde{V}\tilde{\psi}(t). && \text{(A.18)} \end{aligned}$$

Again, the wavefunctions and operators in the interaction representation coincide with those in the the Schrödinger and Heisenberg representations at $t = 0$, and calculation of any physical observable via the interaction representation yields identical results to calculations via the Schrödinger and Heisenberg representations. Returning to the example of the matrix element of the operator $\hat{O}$ between states ψ_1 and ψ_2,

$$\begin{aligned} \left\langle\tilde{\psi}_1(t)\right|\tilde{\hat{O}}(t)\left|\tilde{\psi}_2(t)\right\rangle &= \left(\langle\psi_1|\,e^{iHt}e^{-iH_0t}\right)\left(e^{iH_0t}\hat{O}e^{-iH_0t}\right)\left(e^{iH_0t}e^{-iHt}\,|\psi_2\rangle\right) && \text{(A.19)}\\ &= \langle\psi_1|\,e^{iHt}\hat{O}e^{-iHt}\,|\psi_2\rangle\ . && \text{(A.20)} \end{aligned}$$

A.3.4 The time evolution operator $\hat{U}(t)$

We define the time evolution operator $\hat{U}(t)$ such that its action produces the interaction representation wavefunction at time t from the wavefunction at time $t = 0$,

$$\tilde{\psi}(t) = \hat{U}(t)\psi(0)\,. \tag{A.21}$$

Thus, from Eq. (A.15),

$$\hat{U}(t) = e^{iH_0 t}e^{-iHt}\,. \tag{A.22}$$

Replacing $\tilde{\psi}(t)$ by $\hat{U}(t)\psi(0)$ in Eq. (A.18) gives an equivalent expression for $\hat{U}(t)$

$$i\frac{\partial \hat{U}(t)}{\partial t} = \tilde{V}(t)\hat{U}(t)\,. \tag{A.23}$$

Integrating Eq. (A.23) between 0 and t gives,

$$\hat{U}(t) - \hat{U}(0) = -i\int_0^t \mathrm{d}t_1 \tilde{V}(t_1)\hat{U}(t_1)\,, \tag{A.24}$$

where t_1 is a dummy variable of integration. We note that $\hat{U}(0) = 1$, and further note that this process may be repeated iteratively to give:

$$\hat{U}(t) = 1 - i\int_0^t \mathrm{d}t_1 \tilde{V}(t_1)\left(1 - i\int_0^{t_1} \mathrm{d}t_2 \tilde{V}(t_2)\hat{U}(t_2)\right)\text{etc.} \tag{A.25}$$

$$= 1 - i\int_0^t \mathrm{d}t_1 + (-i)^2\int_0^t \mathrm{d}t_1 \int_0^{t_1} \mathrm{d}t_2 \tilde{V}(t_1)\tilde{V}(t_2) + \ldots \tag{A.26}$$

$$= \sum_{n=0}^{\infty}(-i)^n \int_0^t \mathrm{d}t_1 \int_0^{t_1} \mathrm{d}t_2 \ldots \int_0^{t_{n-1}} \mathrm{d}t_n \tilde{V}(t_1)\tilde{V}(t_2)\ldots\tilde{V}(t_n)\,. \tag{A.27}$$

We now introduce the time-ordering operator $\mathcal{T}$, which acts upon a group of time-dependent operators to arrange the group such that the earliest times are furthest right. We note that in Eq. (A.27) we have $t_n < t_{n-1} \ldots < t_1 < t$ and thus the operators are ordered in accordance with the time-ordering operation. We are therefore able to re-express Eq. (A.27) in a form that includes the time-ordering operator $\mathcal{T}$. We use the following identity:

$$\int_0^t \mathrm{d}t_1 \int_0^{t_1} \mathrm{d}t_2 \ldots \int_0^{t_{n-1}} \mathrm{d}t_n \tilde{V}(t_1)\tilde{V}(t_2)\ldots\tilde{V}(t_n) = \frac{1}{n!}\int_0^t \mathrm{d}t_1 \int_0^t \mathrm{d}t_2 \ldots \int_0^t \mathrm{d}t_n \tilde{V}(t_1)\tilde{V}(t_2)\ldots\tilde{V}(t_n)\,. \tag{A.28}$$

This factor of $n!$ simply accounts for the change in integration limits. If we take the example of $n = 2$ then on the left hand side of equation A.28 we are integrating within a triangle defined by the lines $t_2 = 1$, $t_2 = t_1$ and $t_1 = t$, whereas on the right hand side we are integrating within a rectangle defined by the lines $t_2 = 0$, $t_2 = t$, $t_1 = 0$ and $t_1 = t$ i.e. twice the area of the left hand side. Applying Eq. (A.28) to Eq. (A.27) gives:

$$\hat{U}(t) = \sum_{n=0}^{\infty}(-i)^n \int_0^t \mathrm{d}t_1 \int_0^t \mathrm{d}t_2 \ldots \int_0^t \mathrm{d}t_n \mathcal{T}[\tilde{\hat{V}}(t_1)\tilde{\hat{V}}(t_2)\ldots\tilde{\hat{V}}(t_n)]\,, \tag{A.29}$$

which may be compactly expressed as

$$\hat{U}(t) = \mathcal{T}\left[\exp\left(-i\int_0^t \mathrm{d}t_1 \tilde{V}(t_1)\right)\right]\,. \tag{A.30}$$

B
JC and IB models

B.1 JC model

B.1.1 Derivation of Eq. (1.23) for the JC polarisation

Taking as our starting point Eq. (1.7), with $\mathcal{V}$ given by Eq. (1.3),

$$P_L(t) = i\mu \,\mathrm{Tr}\{e^{-iHt}\,(\tilde{c} + \tilde{c}^\dagger)\,\rho(-\infty)\,e^{iHt}\,c\}, \tag{B.1}$$

We now express $\tilde{c}$ explicitly as $|0\rangle\langle j|$ and c as $|0\rangle\langle k|$,

$$P_{jk}(t) = i\mu \,\mathrm{Tr}\left\{e^{-iHt}\,|j\rangle\langle 0|\,e^{iHt}\,|0\rangle\langle k|\right\}, \tag{B.2}$$

where we have used $\rho(-\infty) = |0\rangle\langle 0|$. Exploiting the cyclic properties of the trace operation and neglecting the unimportant factor of $i\mu$,

$$P_{jk}(t) = \mathrm{Tr}\left\{\langle j|\,e^{-iHt}\,|k\rangle\langle 0|\,e^{iHt}\,|0\rangle\right\}. \tag{B.3}$$

Noting that $\langle 0|\,e^{iHt}\,|0\rangle = 1$, we may simplify Eq. (B.3) to give Eq. (1.23).

B.2 IB model

B.2.1 Derivation of Eq. (1.42)

From Eqs. (1.1) and (1.39)

$$P(t) = \theta(t)\,\mathrm{Tr}\left\{e^{-iHt}e^{-i\mathcal{V}}\,(|0\rangle\langle 0|\otimes\rho_{\mathrm{ph}})\,e^{i\mathcal{V}}e^{iHt}d\right\}, \tag{B.4}$$

where, as for the JC case, the Heaviside step function $\theta(t)$ is a consequence of the pulsed excitation at $t = 0$. We may simplify Eq. (B.4) to

$$P(t) = \theta(t)\,\mathrm{Tr}\left\{e^{-iHt}e^{-i\mathcal{V}}\left|0\right\rangle\left\langle 0\right|\rho_{\mathrm{ph}}e^{i\mathcal{V}}e^{iHt}d\right\}. \tag{B.5}$$

We now express $e^{\pm i\mathcal{V}}$ as a Taylor series with $\mathcal{V}$ given by Eq. (1.2),

$$P(t) = \theta(t)\,\mathrm{Tr}\left\{e^{-iHt}\left(1 - i\mu(d^{\dagger}+d) + \ldots\right)\left|0\right\rangle\left\langle 0\right|\rho_{\mathrm{ph}}\left(1 + i\mu(d^{\dagger}+d) + \ldots\right)e^{iHt}d\right\}. \tag{B.6}$$

Expressing d and $d^{\dagger}$ explicitly in the $\{\left|0\right\rangle, \left|X\right\rangle\}$ basis and taking only the terms that are linear in μ (hence considering only linear polarisation), Eq. (B.6) becomes

$$P(t) = -i\mu\theta(t)\,\mathrm{Tr}\left\{e^{-iHt}\left|X\right\rangle\left\langle 0\right|\rho_{\mathrm{ph}}e^{iHt}\left|0\right\rangle\left\langle X\right|\right\}. \tag{B.7}$$

Using the cyclic properties of the trace operation, this may be re-expressed as

$$P(t) = -i\mu\theta(t)\left\langle \left\langle X\right|e^{-iHt}\left|X\right\rangle\rho_{\mathrm{ph}}\left\langle 0\right|e^{iHt}\left|0\right\rangle\right\rangle_{\mathrm{ph}}, \tag{B.8}$$

where $\langle\ldots\rangle_{\mathrm{ph}}$ indicates the trace over all phonon states.

With reference to the form of the Hamiltonian H given in Eq. (1.34), we note that $\left\langle 0\right|e^{iHt}\left|0\right\rangle = \left\langle X\right|e^{iH_{\mathrm{ph}}t}\left|X\right\rangle$. We may therefore re-express Eq. (B.8) as

$$P(t) = -i\mu\theta(t)\left\langle \left\langle X\right|e^{-iHt}e^{iH_{\mathrm{ph}}t}\left|X\right\rangle\right\rangle_{\mathrm{ph}}. \tag{B.9}$$

Omitting the unimportant factor of $i\mu$ gives Eq. (1.42).

B.2.2 Solution to Eq. (1.43) via the linked cluster expansion

Expanding Eq. (1.43),

$$\left\langle\mathcal{T}\left[\exp\left(-i\int_0^t \mathrm{d}t_1\tilde{V}(t_1)\right)\right]\right\rangle = \sum_{n=0}^{\infty}\frac{(-i)^n}{n!}\int_0^t \mathrm{d}t_1\int_0^t \mathrm{d}t_2\ldots\int_0^t \mathrm{d}t_n\left\langle\mathcal{T}\,\tilde{V}(t_1)\tilde{V}(t_2)\ldots\tilde{V}(t_n)\right\rangle, \tag{B.10}$$

where $\langle\ldots\rangle$ denotes the expectation value over all phonon states. We wish to consider V of the form of Eq. (1.37). We will initially derive the result for a single

phonon state of wave vector q and will subsequently sum over all wave vectors. We define our V for a single phonon state as V_q:

$$V_q = \lambda_q^* b_q + \lambda_q b_q^\dagger \,. \tag{B.11}$$

Since $\tilde{V}_q$ consists of phonon creation and destruction operators $b_q^\dagger$ and b_q, there must be an even number of $\tilde{V}$ operators acting on state $|\,\rangle$ in order to give a non-zero result. Also, Wick's theorem [10] states that when making all of the possible pairings between creation and destruction operators, each pairing should be time ordered, and the time ordering of each pair gives the proper time ordering of the full result. Upon application of these principles, equation (B.10) becomes

$$\begin{aligned}
&\left\langle \mathcal{T}\left[\exp\left(-i\int_0^t \mathrm{d}t_1 \tilde{V}(t_1)\right)\right]\right\rangle_{\text{single } q} \\
&\quad = 1 - \frac{1}{2}\int_0^t \mathrm{d}t_1 \int_0^t \mathrm{d}t_2 \left\langle \mathcal{T}\tilde{V}_q(t_1)\tilde{V}_q(t_2)\right\rangle + \frac{1}{24}\int_0^t \mathrm{d}t_1 \int_0^t \mathrm{d}t_2 \int_0^t \mathrm{d}t_3 \int_0^t \mathrm{d}t_4 \\
&\qquad \Big(\left\langle \mathcal{T}\tilde{V}_q(t_1)\tilde{V}_q(t_2)\right\rangle \left\langle \mathcal{T}\tilde{V}_q(t_3)\tilde{V}_q(t_4)\right\rangle + \left\langle \mathcal{T}\tilde{V}_q(t_1)\tilde{V}_q(t_3)\right\rangle \left\langle \mathcal{T}\tilde{V}_q(t_2)\tilde{V}_q(t_4)\right\rangle \\
&\qquad + \left\langle \mathcal{T}\tilde{V}_q(t_1)\tilde{V}_q(t_4)\right\rangle \left\langle \mathcal{T}\tilde{V}_q(t_2)\tilde{V}_q(t_3)\right\rangle \Big) + \ldots
\end{aligned} \tag{B.12}$$

We define a function $K_q(t)$:

$$K_q(t) = -\frac{1}{2}\int_0^t \mathrm{d}t_1 \int_0^t \mathrm{d}t_2 \left\langle \mathcal{T}\tilde{V}_q(t_1)\tilde{V}_q(t_2)\right\rangle . \tag{B.13}$$

Noting that K_q is a function of t only, we can write

$$\left\langle \mathcal{T}\left[\exp\left(-i\int_0^t \mathrm{d}t_1 \tilde{V}(t_1)\right)\right]\right\rangle_{\text{single } q} = 1 + K_q(t) + \frac{1}{2}K_q^2(t) + \ldots \tag{B.14}$$

We now sum over all q, giving the cumulant $K(t)$,

$$K(t) = -\frac{1}{2}\int_0^t \mathrm{d}t_1 \int_0^t \mathrm{d}t_2 \left\langle \mathcal{T}\tilde{V}(t_1)\tilde{V}(t_2)\right\rangle \tag{B.15}$$

We therefore have

$$\left\langle \mathcal{T}\left[\exp\left(-i\int_0^t \mathrm{d}t_1 \tilde{V}(t_1)\right)\right]\right\rangle = 1 + K(t) + \frac{1}{2}K(t)^2 + \ldots \tag{B.16}$$

Considering the $(2n)^{th}$ order term of Eq. (B.12):

$$\begin{aligned}
&\frac{(-i)^{2n}}{(2n)!}\int_0^t \mathrm{d}t_1 \int_0^t \mathrm{d}t_2 \ldots \int_0^t \mathrm{d}t_{2n} \left\langle \mathcal{T}\tilde{V}(t_1)\tilde{V}(t_2)\tilde{V}(t_{2n})\right\rangle = \\
&\frac{(-i)^{2n}}{(2n)!}\int_0^t \mathrm{d}t_1 \int_0^t \mathrm{d}t_2 \ldots \int_0^t \mathrm{d}t_{2n} \left\langle \mathcal{T}\tilde{V}(t_1)\tilde{V}(t_2)\right\rangle \left\langle \mathcal{T}\tilde{V}(t_3)\tilde{V}(t_4)\right\rangle \ldots \left\langle \mathcal{T}\tilde{V}(t_{2n-1})\tilde{V}(t_{2n})\right\rangle \\
&\quad + \text{all other permutations}
\end{aligned} \tag{B.17}$$

If we always place $\tilde{V}(t_1)$ first then we have a choice of $(2n-1)$ variables to place second i.e. to pair with $\tilde{V}(t_1)$. Whichever variable we choose to place third, we will have a choice of $(2n-3)$ variables to pair it with. Continuing in this vein, the total number of permutations is given by

$$\begin{aligned}(2n-1)(2n-3)(2n-5)\dots(3)(1) &= \frac{(2n)(2n-1)(2n-2)(2n-3)\dots(2)(1)}{(2n)(2n-2)(2n-4)\dots(4)(2)} \\ &= \frac{(2n)!}{(2[n])(2[n-1])(2[n-2])\dots(2[2])(2[1])} \\ &= \frac{(2n)!}{2^n n!}. \end{aligned} \tag{B.18}$$

We therefore have the following expression for the $(2n)^{th}$ order term:

$$\frac{(-i)^{2n}}{(2n)!}\frac{(2n)!}{2^n n!}\left[-2K(t)\right]^n = \frac{[K(t)]^n}{n!}. \tag{B.19}$$

This is the n^{th} order term in the expansion of $e^{K(t)}$. Hence,

$$\left\langle \mathcal{T}\left[\exp\left(-i\int_0^t \mathrm{d}t_1 \tilde{V}(t_1)\right)\right]\right\rangle = e^{K(t)}\,. \tag{B.20}$$

B.2.3 Note on computing the rapidly decaying part of the cumulant $K_{BB}(t)$

Returning to our definition $N(\omega) = 1/[e^{\beta\omega}-1]$, we note that

$$N(-\omega) = \frac{1}{e^{-\beta\omega}-1} = -[N(\omega)+1]\,. \tag{B.21}$$

We now define function $g(\omega)$,

$$g(\omega) = \omega\, e^{-\frac{\omega^2}{\omega_0^2}} N(\omega) e^{i\omega t}\,. \tag{B.22}$$

Noting that $g(-\omega) = \omega\, e^{-\frac{\omega^2}{\omega_0^2}}[N(\omega)+1]e^{-i\omega t}$, we may express Eq. (1.68) as

$$K_{BB}(t) = J_0 \int_0^\infty d\omega\, g(\omega) + g(-\omega) \tag{B.23}$$

$$= J_0 \int_{-\infty}^\infty d\omega\, g(\omega) \tag{B.24}$$

$$= \mathcal{F}\left\{ J_0\, \omega\, N(\omega)\, e^{-\frac{\omega^2}{\omega_0^2}} \right\}, \tag{B.25}$$

where $\mathcal{F}$ denotes the inverse Fourier transform. Expressing $K_{BB}(t)$ in this way is of particular value when numerical calculation is required since calculation may be achieved through fast Fourier transform (FFT) algorithms.

C
Phonon thermometer

C.1 IB cumulant for ellipsoidal confinement potential: calculation of $K_{BB}(t)$

Returning to our definition $N(\omega) = 1/[e^{\beta\omega} - 1]$, we note that

$$N(-\omega) = \frac{1}{e^{-\beta\omega} - 1} = -[N(\omega) + 1]\,. \tag{C.1}$$

We now define function $g(\omega)$,

$$g(\omega) = N(\omega)\, e^{-\frac{a_\parallel^2 \omega^2}{2v_s^2}}\, \mathrm{erfi}\left(\frac{\omega}{\sqrt{2}v_s}\sqrt{a_\parallel^2 - a_\perp^2}\right) e^{i\omega t}\,. \tag{C.2}$$

We may express the rapidly decaying part of Eq. (2.6) as

$$K_{BB}(t) = \frac{J_0 v_s \sqrt{\pi}}{\sqrt{2}\sqrt{a_\parallel^2 - a_\perp^2}} \int_0^\infty d\omega\, [g(\omega) + g(-\omega)] \tag{C.3}$$

$$= \mathcal{F}\left\{ \frac{J_0 v_s \sqrt{\pi}}{\sqrt{2}\sqrt{a_\parallel^2 - a_\perp^2}}\, N(\omega)\, e^{-\frac{a_\parallel^2 \omega^2}{2v_s^2}}\, \mathrm{erfi}\left(\frac{\omega}{\sqrt{2}v_s}\sqrt{a_\parallel^2 - a_\perp^2}\right)\right\}, \tag{C.4}$$

where $\mathcal{F}$ denotes the inverse Fourier transform. Expressing $K_{BB}(t)$ in this way is of particular value as it allows the use of Fourier transform (FFT) algorithms.

C.2 Double PQD - sample (A)

In addition to Figs. 2.4 and 2.5, experimental and fit PL spectra are shown in Figs. C.1 to C.5.

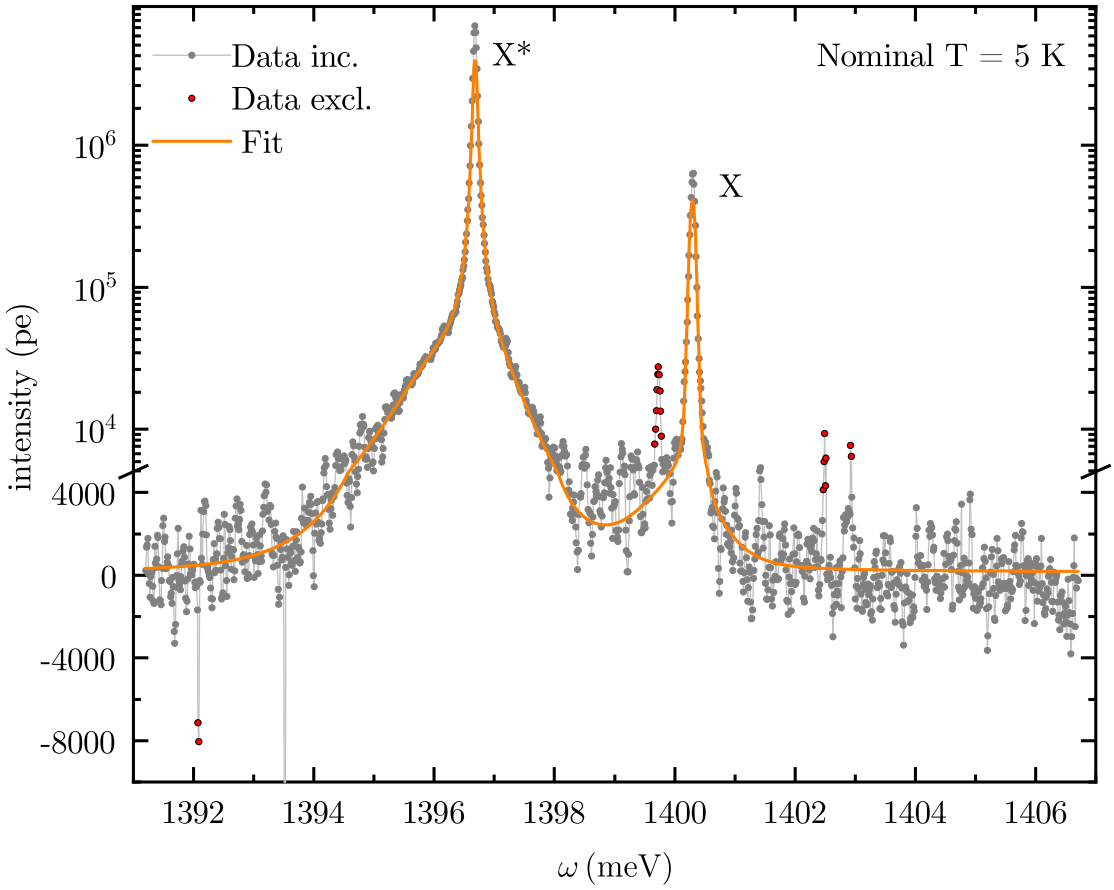

(a) Experimental and fitted PL emission spectra, showing data manually excluded from fit in red.

Parameter		Fit Value (with σ confidence bound)	
		X*	X
T	(K)	9.19 (0.61)	
γ_L	(μeV)	60.44 (5.73)	15.49 (3.30)
γ_G	(μeV)	38.48 (19.85)	88.97 (7.73)
$\omega_X - \omega_{\text{ref}}$	(meV)	0.00 (3.08E-03)	3.62 (2.31E-03)
α		3.96E+06 (5.80E+05)	3.69E+05 (3.69E+04)

(b) Tabulated fit values, with deformation potential and QD confinement lengths fixed to the values detailed in Table 2.1. Reference frequency $\omega_{\text{ref}} = 1,396.64$ meV

Figure C.1: PL spectrum and fit for double PQD sample (A) with nominal temperature $T = 5$ K.

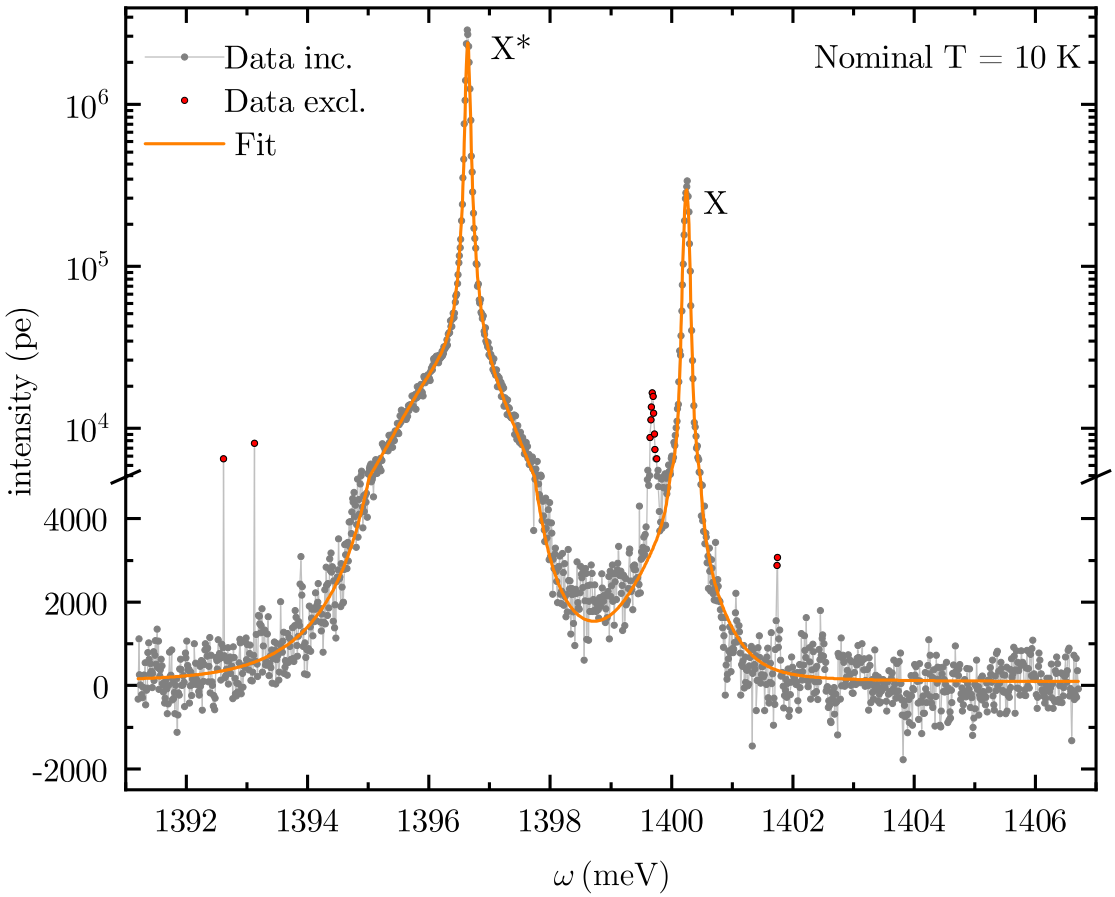

(a) Experimental and fitted PL emission spectra, showing data manually excluded from fit in red.

Parameter		Fit Value (with σ confidence bound)	
		X*	X
T	(K)	11.46 (0.40)	
γ_L	(μeV)	49.63 (3.20)	23.56 (2.51)
γ_G	(μeV)	34.46 (10.24)	73.98 (4.61)
$\omega_X - \omega_{\text{ref}}$	(meV)	-0.04 (1.73E-03)	3.57 (1.57E-03)
α		2.41E+06 (2.15E+05)	2.71E+05 (1.75E+04)

(b) Tabulated fit values, with deformation potential and QD confinement lengths fixed to the values detailed in Table 2.1. Reference frequency $\omega_{\text{ref}} = 1,396.64$ meV

Figure C.2: PL spectrum and fit for double PQD sample (A) with nominal temperature $T = 10$ K.

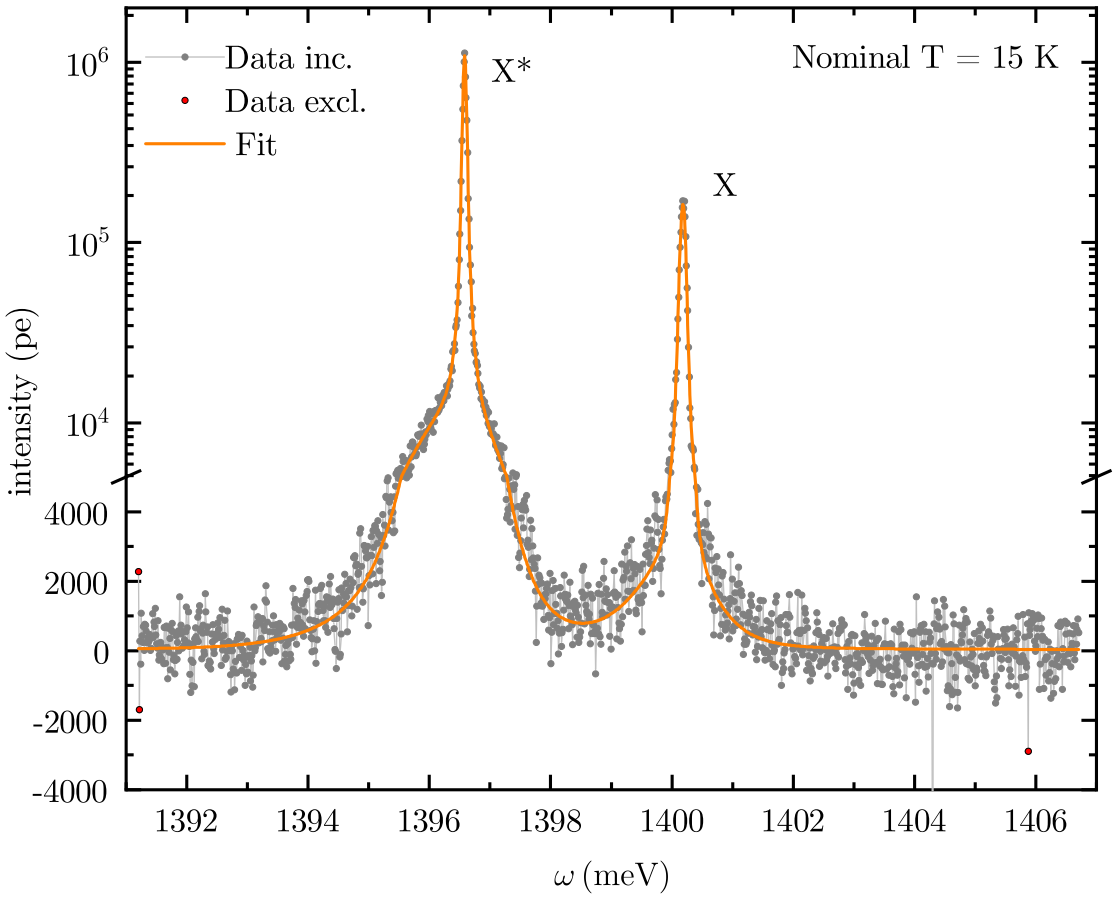

(a) Experimental and fitted PL emission spectra, showing data manually excluded from fit in red.

Parameter		Fit Value (with σ confidence bound)	
		X*	X
T	(K)	13.03 (0.73)	
γ_L	(μeV)	31.77 (3.84)	37.57 (5.91)
γ_G	(μeV)	48.24 (8.74)	74.87 (10.83)
$\omega_X - \omega_{\text{ref}}$	(meV)	-0.10 (2.34E-03)	3.51 (3.06E-03)
α		1.09E+06 (1.20E+05)	1.46E+05 (1.62E+04)

(b) Tabulated fit values, with deformation potential and QD confinement lengths fixed to the values detailed in Table 2.1. Reference frequency $\omega_{\text{ref}} = 1,396.64$ meV

Figure C.3: PL spectrum and fit for double PQD sample (A) with nominal temperature $T = 15$ K.

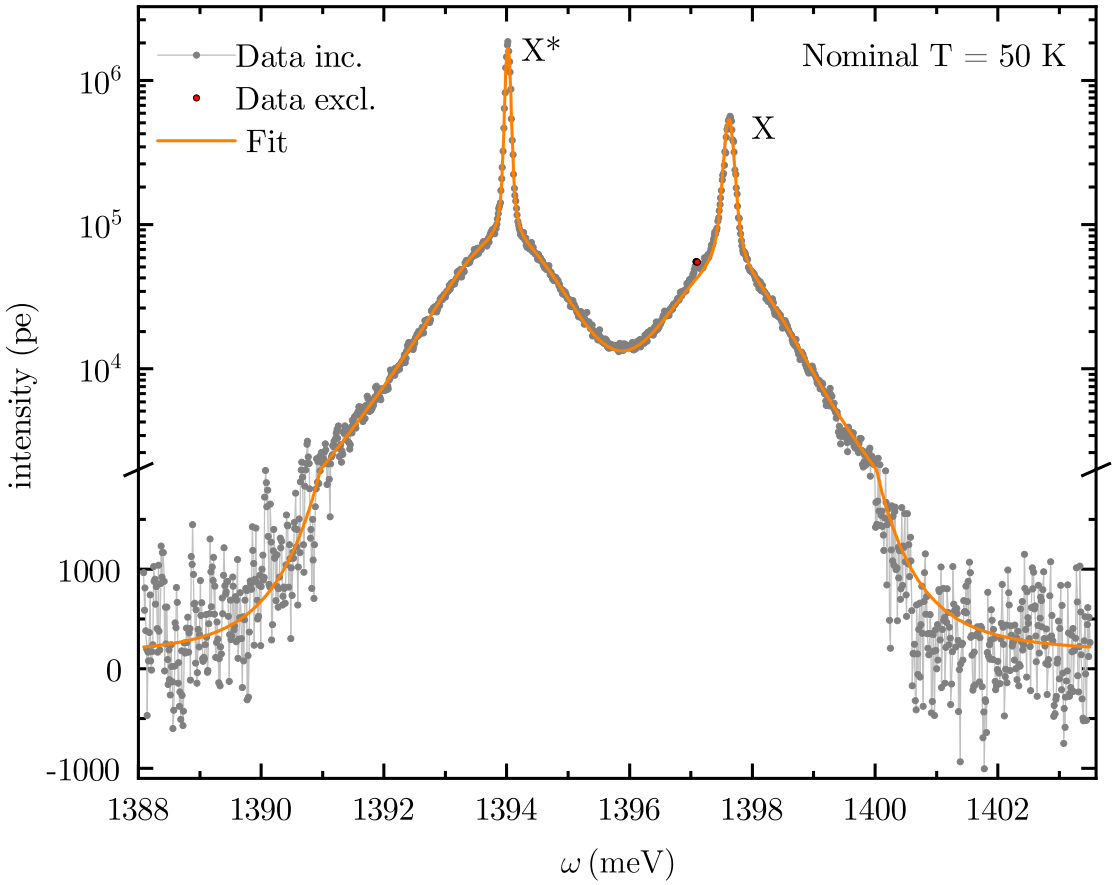

(a) Experimental and fitted PL emission spectra, showing data manually excluded from fit in red.

Parameter		Fit Value (with σ confidence bound)	
		X*	X
T	(K)	49.19 (0.43)	
γ_L	(μeV)	31.21 (1.54)	83.06 (3.71)
γ_G	(μeV)	70.26 (2.24)	111.55 (5.23)
$\omega_X - \omega_{\text{ref}}$	(meV)	-2.66 (5.95E-04)	0.95 (9.65E-04)
α		1.66E+06 (3.51E+04)	4.66E+05 (8.94E+03)

(b) Tabulated fit values, with deformation potential and QD confinement lengths fixed to the values detailed in Table 2.1. Reference frequency $\omega_{\text{ref}} = 1,396.64$ meV

Figure C.4: PL spectrum and fit for double PQD sample (A) with nominal temperature $T = 50$ K.

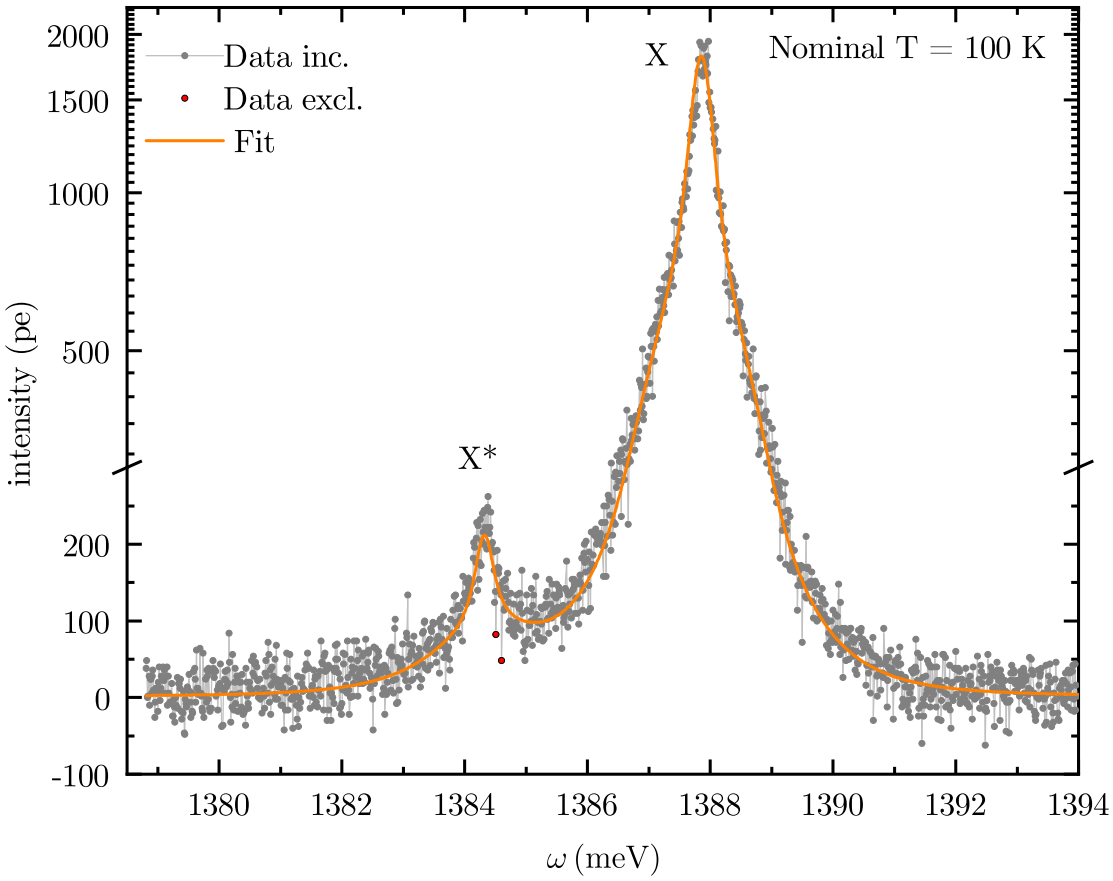

(a) Experimental and fitted PL emission spectra, showing data manually excluded from fit in red.

Parameter		Fit Value (with σ confidence bound)	
		X*	X
T	(K)	93.83 (6.67)	
γ_L	(μeV)	347.80 (90.68)	309.39 (52.82)
γ_G	(μeV)	128.87(222.71)	217.25 (85.05)
$\omega_X - \omega_{\text{ref}}$	(meV)	-12.36 (1.91E-02)	-8.72 (1.08E-02)
α		1.89E+02 (1.94E+01)	1.56E+03 (1.14E+02)

(b) Tabulated fit values, with deformation potential and QD confinement lengths fixed to the values detailed in Table 2.1. Reference frequency $\omega_{\text{ref}} = 1,396.64$ meV

Figure C.5: PL spectrum and fit for double PQD sample (A) with nominal temperature $T = 100$ K.

C.3 Double PQD - sample (B)

Table C.1 provides the deformation potential $|D_c - D_v|$ and QD confinement lengths $a_{\parallel}$, $a_{\perp}$ calculated from the first fitting cycle and fixed for the second fitting cycle. Experimental and fit PL spectra are shown in Figs. C.6 to C.12, alongside tabulated fit values and associated σ confidence bounds.

Fig. C.13 shows the relationship between the fit temperature and the nominal temperature, as well as the behaviour of the exciton and trion transition frequencies with temperature. Finally, Fig. C.14 illustrates the temperature-dependence of the Gaussian and Lorentzian broadening parameters.

Parameter		Fit Value (with σ confidence bound)	
		X*	X
$\lvert D_c - D_v \rvert$	(eV)	7.48 (0.07)	
$a_{\perp}$	(nm)	1.75 (0.03)	2.25 (0.15)
$a_{\parallel}$	(nm)	6.13 (0.06)	6.261 (0.23)

Table C.1: $1/\sigma^2$ weighted average of deformation potential $|D_c - D_v|$, trion (X*) and exciton (X) confinement lengths $a_{\perp}$, $a_{\parallel}$ for double PQD sample (B).

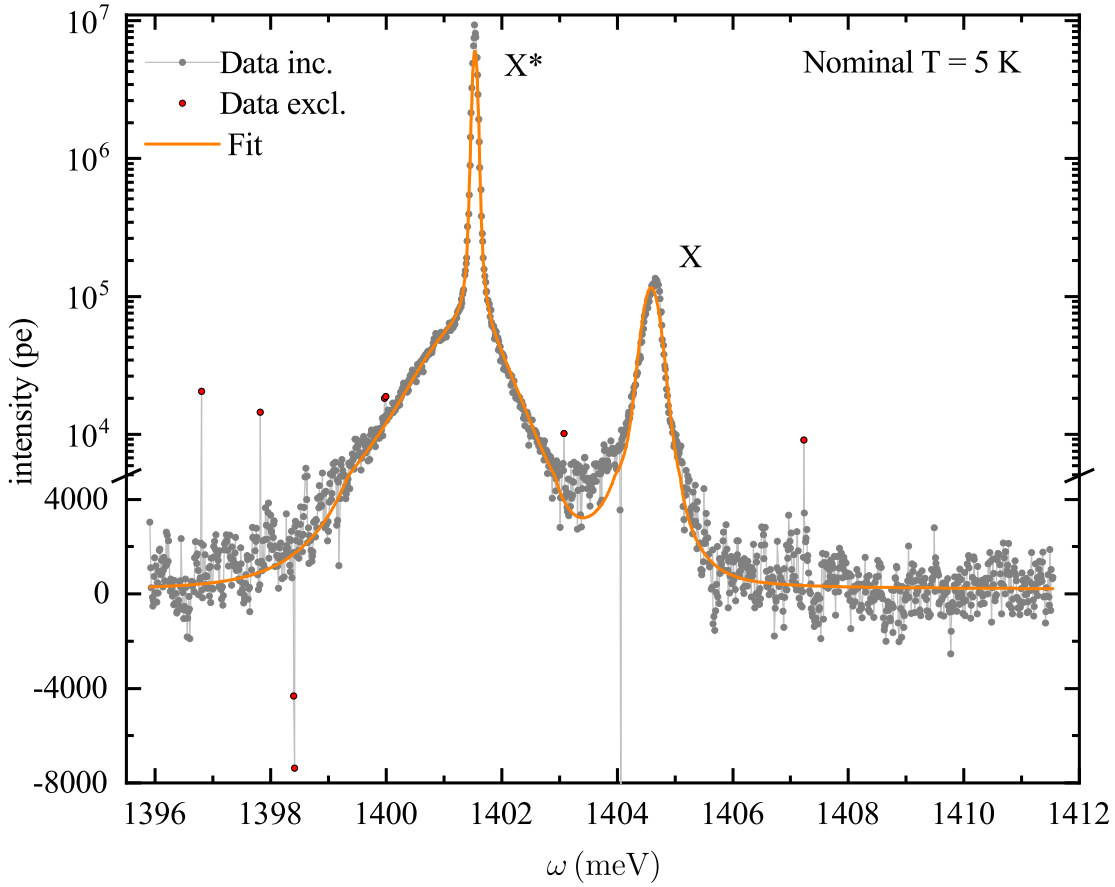

(a) Experimental and fitted PL emission spectra, showing data manually excluded from fit in red.

Parameter		Fit Value (with σ confidence bound)	
		X*	X
T	(K)	10.14 (0.52)	
γ_L	(μeV)	19.62 (3.61)	76.11 (11.58)
γ_G	(μeV)	86.88 (10.24)	295.35 (24.61)
$\omega_X - \omega_{\text{ref}}$	(meV)	0.00 (3.16E-03)	3.07 (6.56E-03)
α		6.00E+06 (4.74E+05)	9.91E+04 (8.20E+03)

(b) Tabulated fit values, with deformation potential and QD confinement lengths fixed to the values detailed in Table C.1. Reference frequency $\omega_{\text{ref}} = 1,401.5$ meV

Figure C.6: PL spectrum and fit for double PQD sample (B) with nominal temperature $T = 5$ K.

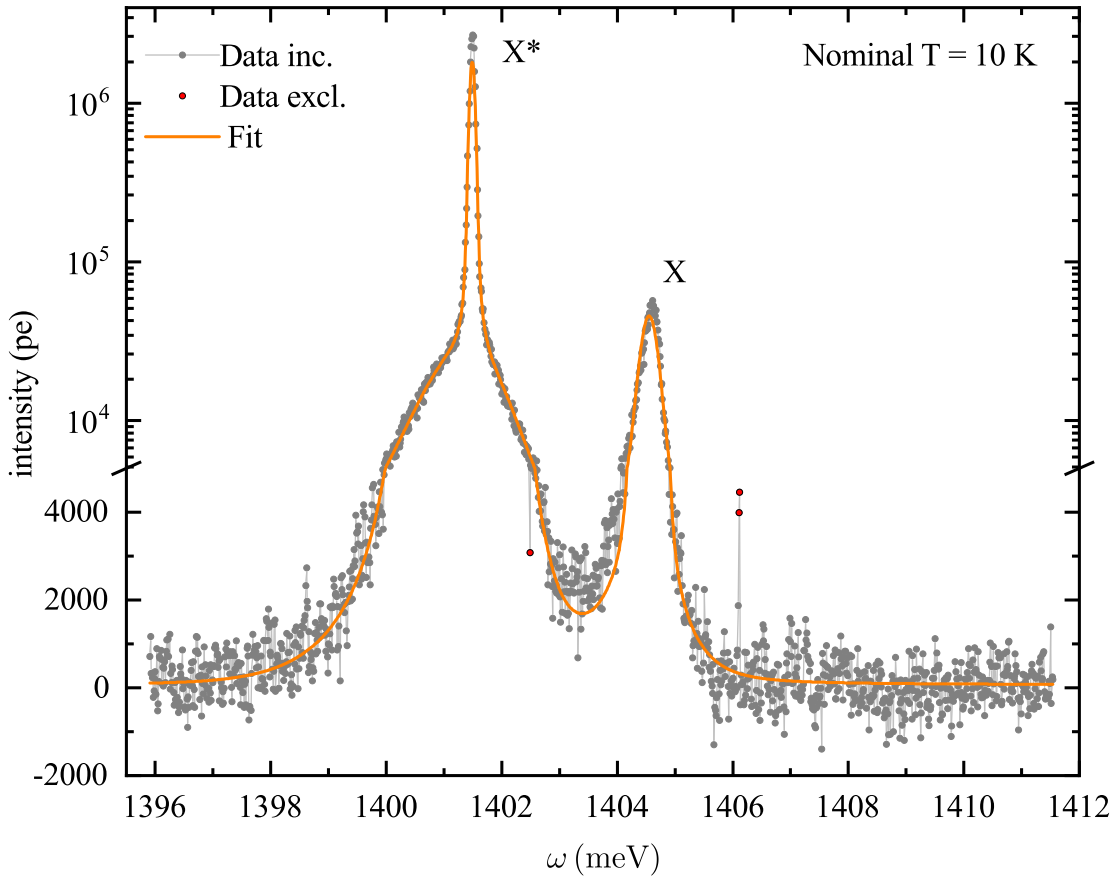

(a) Experimental and fitted PL emission spectra, showing data manually excluded from fit in red.

Parameter		Fit Value (with σ confidence bound)	
		X*	X
T	(K)	14.75 (0.68)	
γ_L	(μeV)	20.43 (3.30)	98.31 (13.00)
γ_G	(μeV)	91.43 (5.96)	277.83 (16.98)
$\omega_X - \omega_{\text{ref}}$	(meV)	-0.05 (2.36E-03)	3.03 (5.14E-03)
α		1.84E+06 (1.29E+05)	3.91E+04 (2.36E+03)

(b) Tabulated fit values, with deformation potential and QD confinement lengths fixed to the values detailed in Table C.1. Reference frequency $\omega_{\text{ref}} = 1,401.5$ meV

Figure C.7: PL spectrum and fit for double PQD sample (B) with nominal temperature $T = 10$ K.

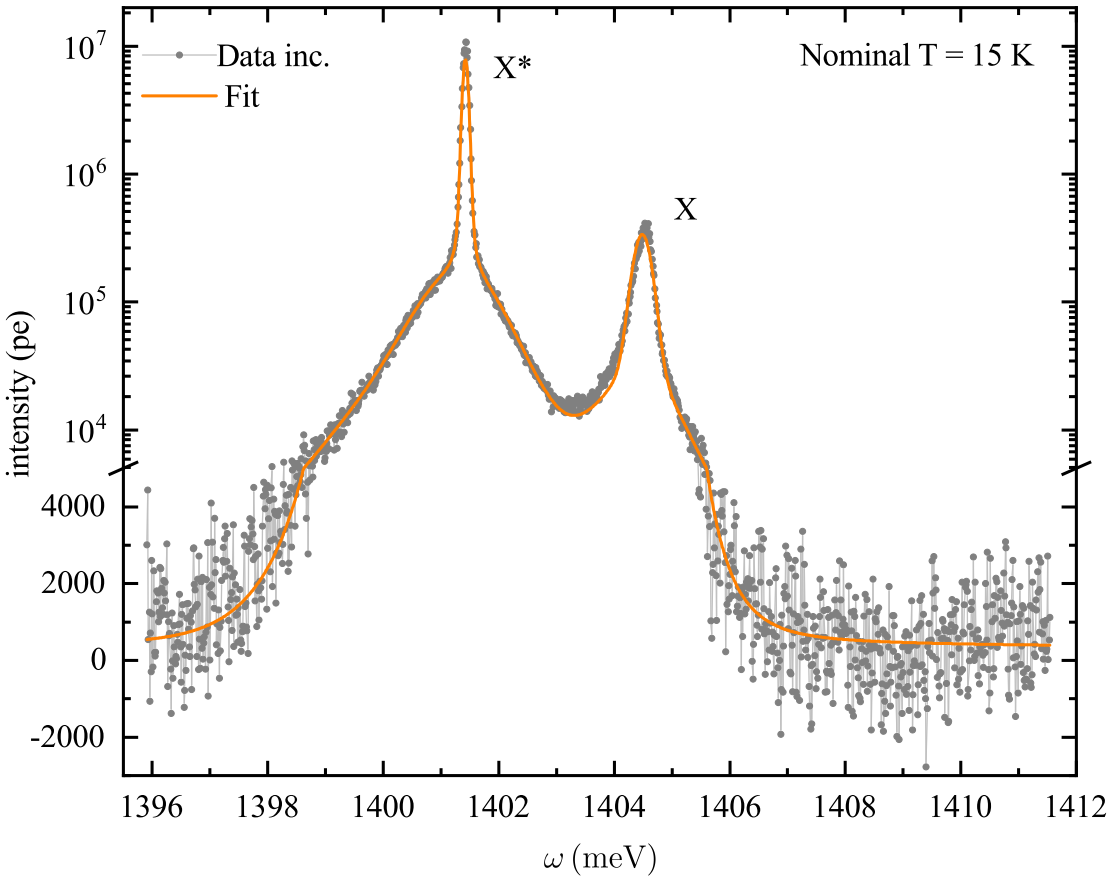

(a) Experimental and fitted PL emission spectra. No data manually excluded from this fit.

Parameter		Fit Value (with σ confidence bound)	
		X*	X
T	(K)	20.40 (0.68)	
γ_L	(μeV)	19.15 (3.13)	53.90 (8.76)
γ_G	(μeV)	102.24 (6.93)	315.45 (15.01)
$\omega_X - \omega_{\text{ref}}$	(meV)	-0.11 (2.07E-03)	2.96 (3.92E-03)
α		7.93E+06 (4.34E+05)	2.89E+05 (1.31E+04)

(b) Tabulated fit values, with deformation potential and QD confinement lengths fixed to the values detailed in Table C.1. Reference frequency $\omega_{\text{ref}} = 1,401.5$ meV

Figure C.8: PL spectrum and fit for double PQD sample (B) with nominal temperature $T = 15$ K.

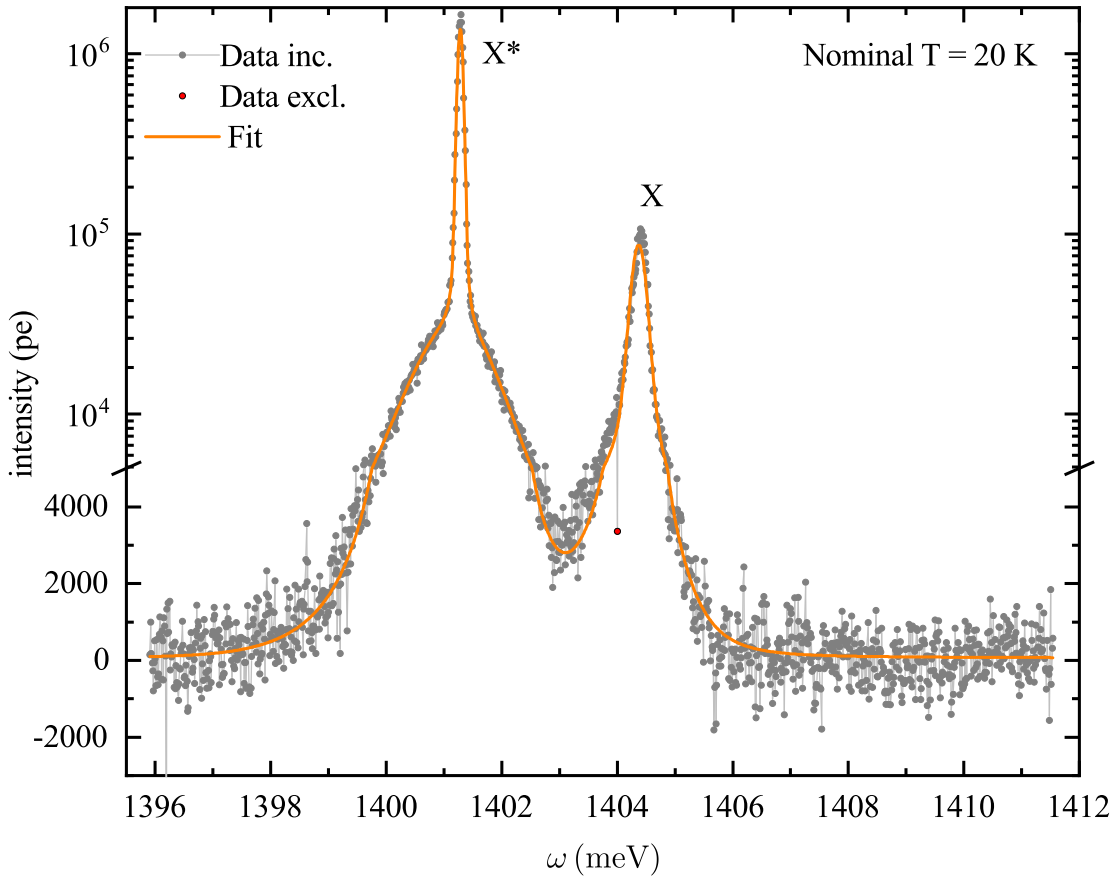

(a) Experimental and fitted PL emission spectra, showing data manually excluded from fit in red.

Parameter		Fit Value (with σ confidence bound)	
		X*	X
T	(K)	22.73 (0.92)	
γ_L	(μeV)	17.29 (3.00)	86.57 (11.87)
γ_G	(μeV)	96.53 (4.91)	232.02 (13.72)
$\omega_X - \omega_{\text{ref}}$	(meV)	-0.25 (1.81E-03)	2.85 (3.71E-03)
α		1.37E+06 (8.48E+04)	7.47E+04 (3.69E+03)

(b) Tabulated fit values, with deformation potential and QD confinement lengths fixed to the values detailed in Table C.1. Reference frequency $\omega_{\text{ref}} = 1,401.5$ meV

Figure C.9: PL spectrum and fit for double PQD sample (B) with nominal temperature $T = 20$ K.

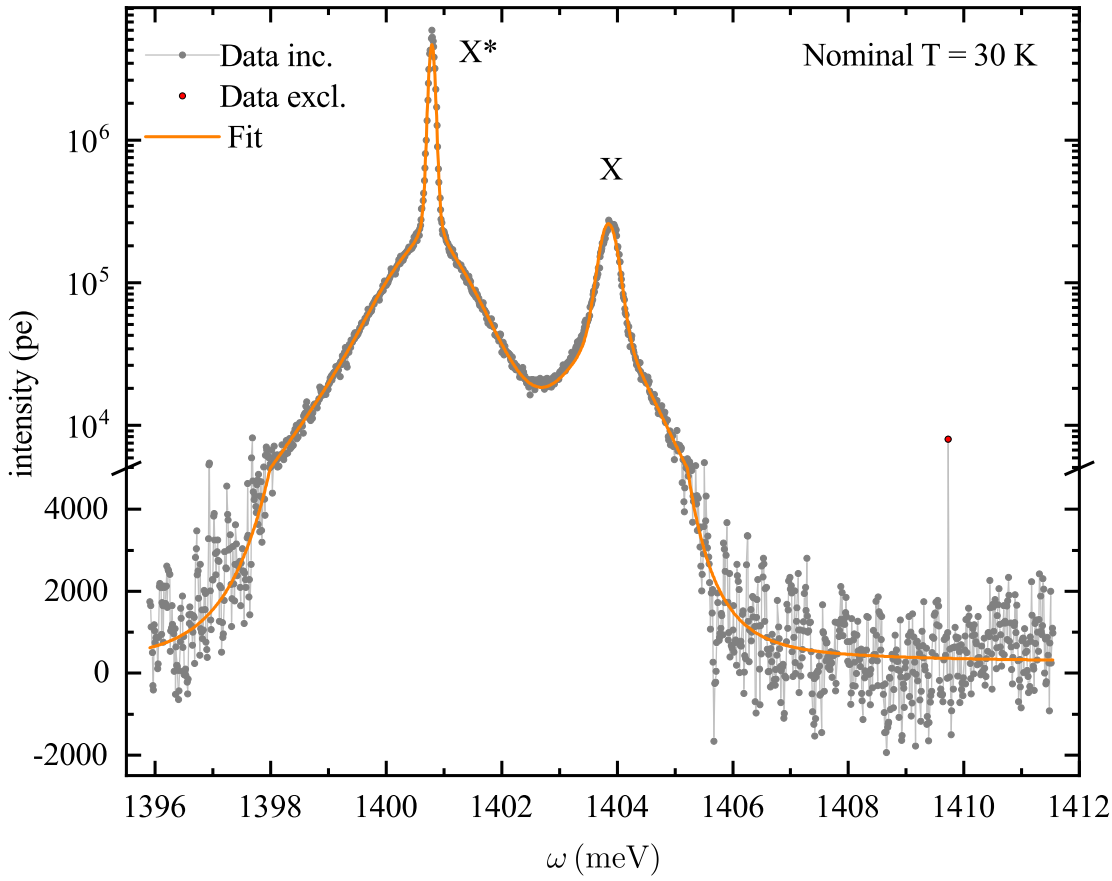

(a) Experimental and fitted PL emission spectra, showing data manually excluded from fit in red.

Parameter		Fit Value (with σ confidence bound)	
		X*	X
T	(K)	34.51 (0.89)	
γ_L	(μeV)	23.07 (3.25)	97.95 (10.14)
γ_G	(μeV)	106.48 (4.56)	303.19 (11.68)
$\omega_X - \omega_{\text{ref}}$	(meV)	-0.75 (1.58E-03)	2.33 (3.34E-03)
α		4.68E+06 (2.21E+05)	2.22E+05 (7.20E+03)

(b) Tabulated fit values, with deformation potential and QD confinement lengths fixed to the values detailed in Table C.1. Reference frequency $\omega_{\text{ref}} = 1,401.5$ meV

Figure C.10: PL spectrum and fit for double PQD sample (B) with nominal temperature $T = 30$ K.

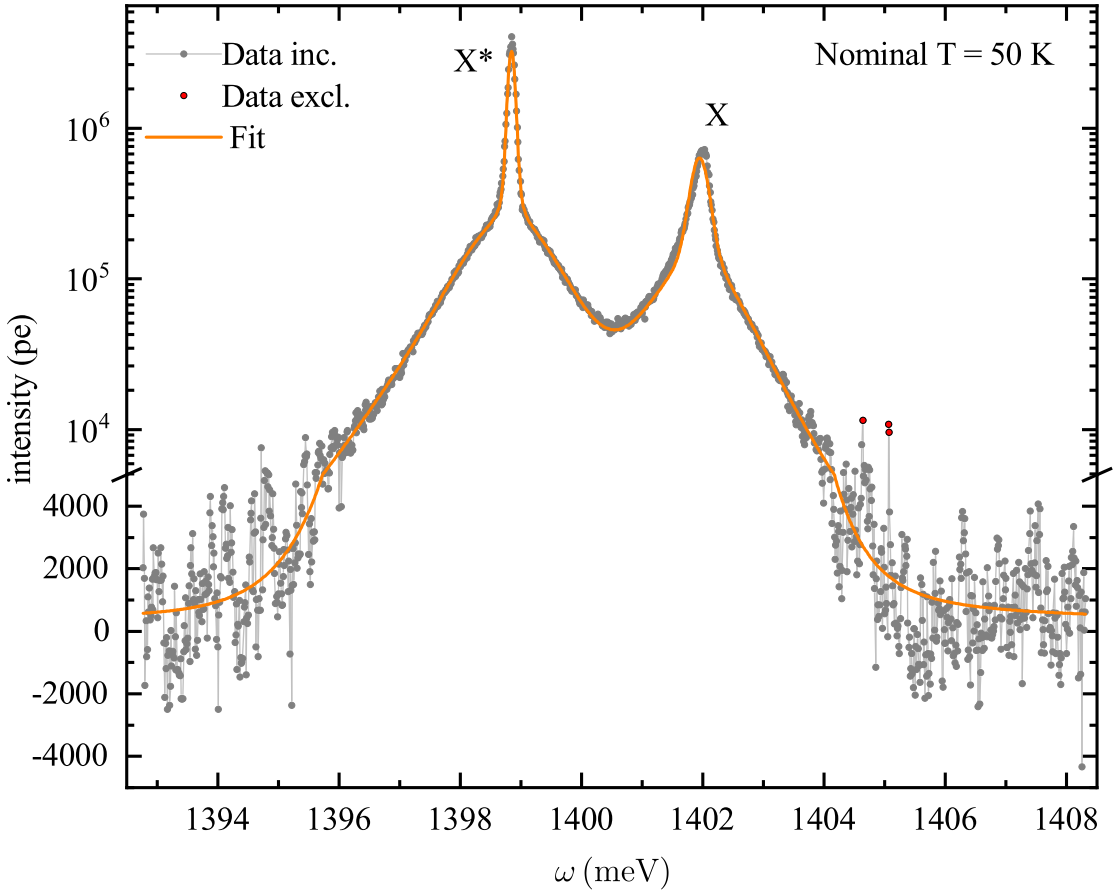

(a) Experimental and fitted PL emission spectra, showing data manually excluded from fit in red.

Parameter		Fit Value (with σ confidence bound)	
		X*	X
T	(K)	56.17 (0.98)	
γ_L	(μeV)	32.72 (4.09)	119.13 (9.23)
γ_G	(μeV)	111.10 (5.09)	255.41 (10.94)
$\omega_X - \omega_{\text{ref}}$	(meV)	-2.69 (1.37E-03)	0.42 (2.66E-03)
α		3.24E+06 (1.17E+05)	5.43E+05 (1.39E+04)

(b) Tabulated fit values, with deformation potential and QD confinement lengths fixed to the values detailed in Table C.1. Reference frequency $\omega_{\text{ref}} = 1,401.5$ meV

Figure C.11: PL spectrum and fit for double PQD sample (B) with nominal temperature $T = 50$ K.

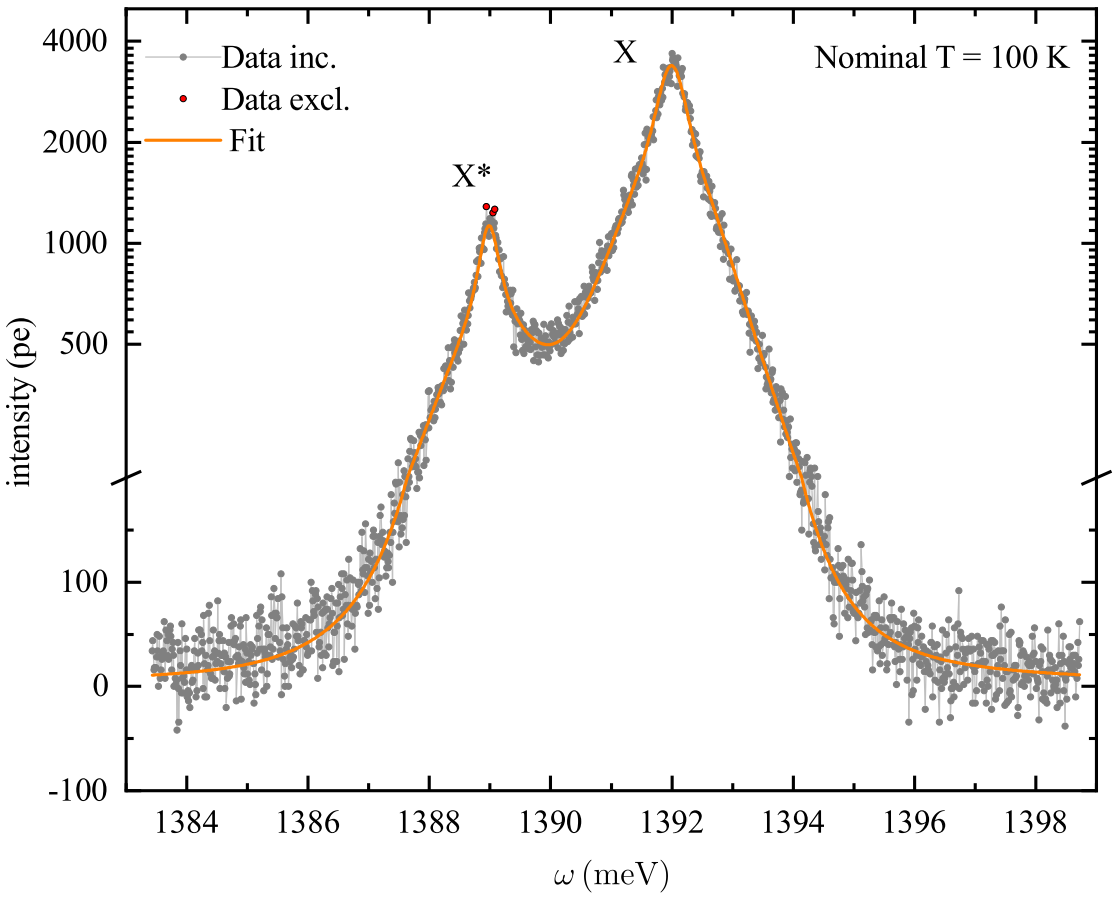

(a) Experimental and fitted PL emission spectra, showing data manually excluded from fit in red.

Parameter		Fit Value (with σ confidence bound)	
		X*	X
T	(K)	113.97 (3.08)	
γ_L	(μeV)	397.63 (30.84)	439.12 (19.92)
γ_G	(μeV)	25.08 (365.47)	236.88 (42.34)
$\omega_X - \omega_{\text{ref}}$	(meV)	-12.55 (6.48E-03)	-9.52 (4.50E-03)
α		1.05E+03 (3.65E+01)	2.88E+03 (6.04E+01)

(b) $\omega_{\text{ref}} = 1,401.5$ meV

Figure C.12: PL spectrum and fit for double PQD sample (B) with nominal temperature $T = 100$ K.

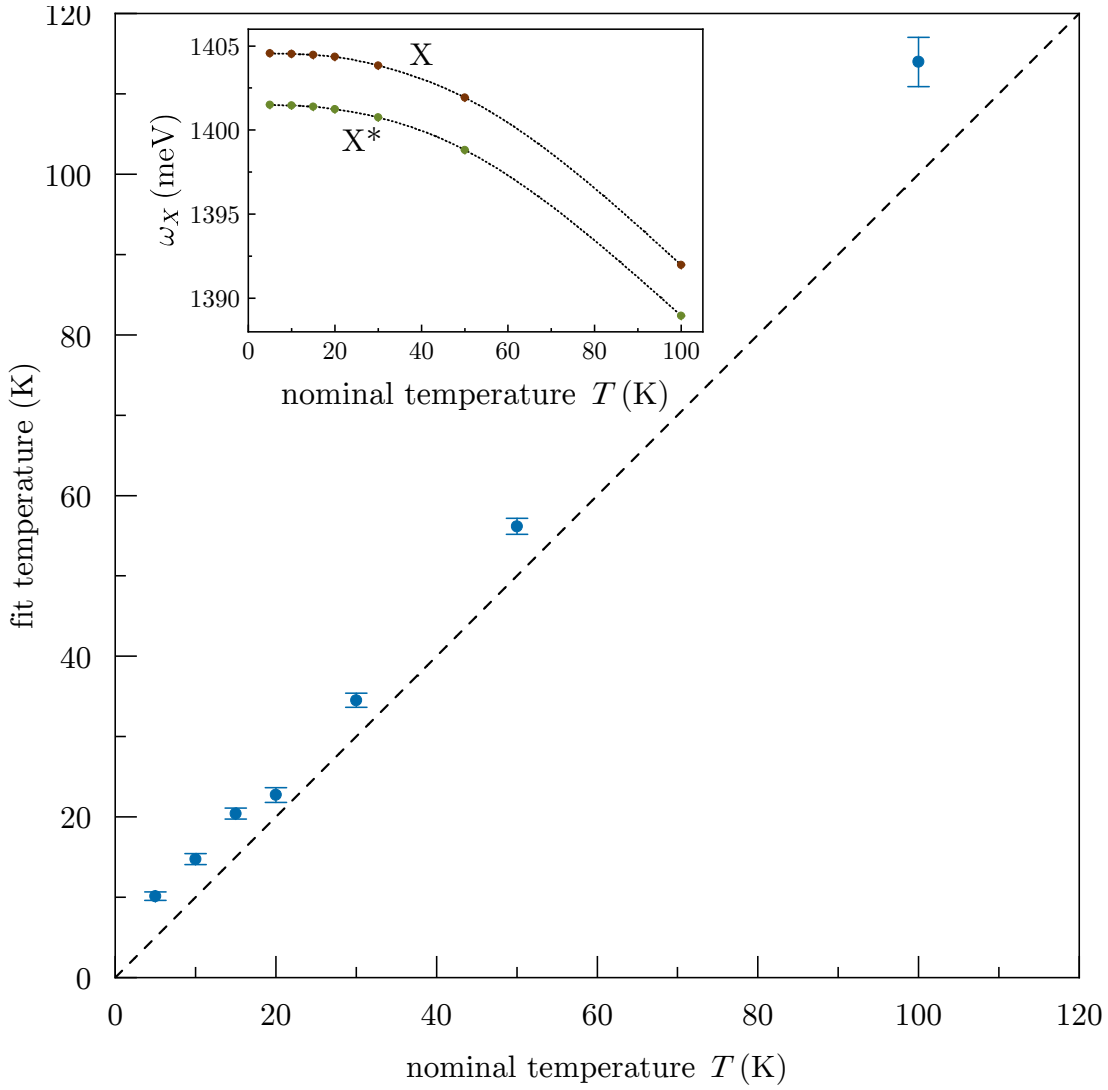

Figure C.13: Fit temperature (with σ error bars) as a function of nominal temperature, shown for double PQD sample (B). Inset: excitation (exciton/trion) transition frequency as a function of nominal temperature, shown for double PQD sample (B).

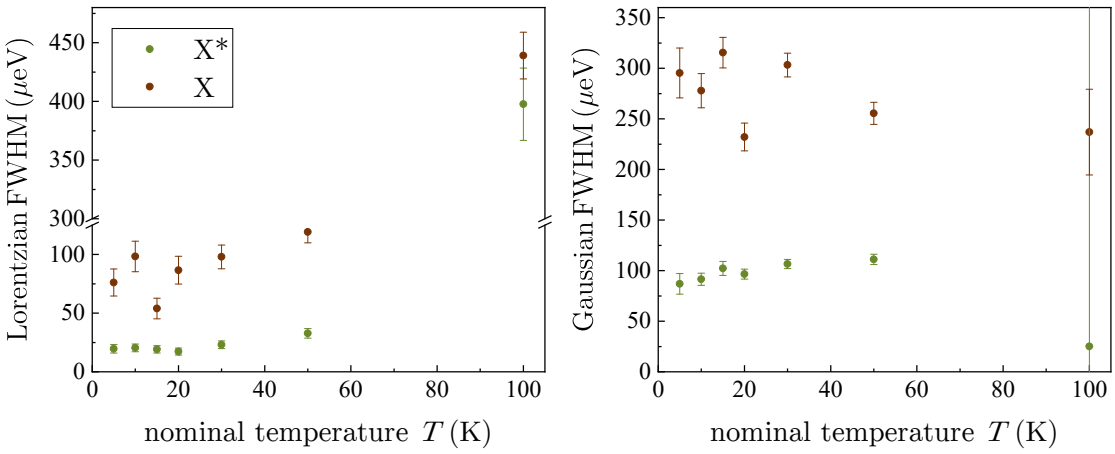

Figure C.14: Lorentzian γ_L and Gaussian γ_G broadening parameters (with σ error bars) as a function of nominal temperature, shown for double PQD sample (B).

C.4 Single PQD sample

Table C.2 provides the deformation potential $|D_c - D_v|$ and QD confinement lengths $a_\parallel$, $a_\perp$ calculated from the first fitting cycle and fixed for the second fitting cycle. Experimental and fit PL spectra are shown in Figs. C.15 to C.19, alongside tabulated fit values and associated σ confidence bounds.

Fig. C.20 shows the relationship between the fit temperature and the nominal temperature, as well as the behaviour of the trion transition frequency with temperature. Finally, Fig. C.21 illustrates the temperature-dependence of the Gaussian and Lorentzian broadening parameters.

Parameter	Fit Value (with σ confidence bound)
$\lvert D_c - D_v \rvert$ (eV)	7.48 (0.07)
$a_\perp$ (nm)	3.11 (0.53)
$a_\parallel$ (nm)	5.28 (0.46)

Table C.2: $1/\sigma^2$ weighted average of deformation potential $|D_c - D_v|$ and trion (X*) confinement lengths $a_\perp$, $a_\parallel$ for single PQD sample.

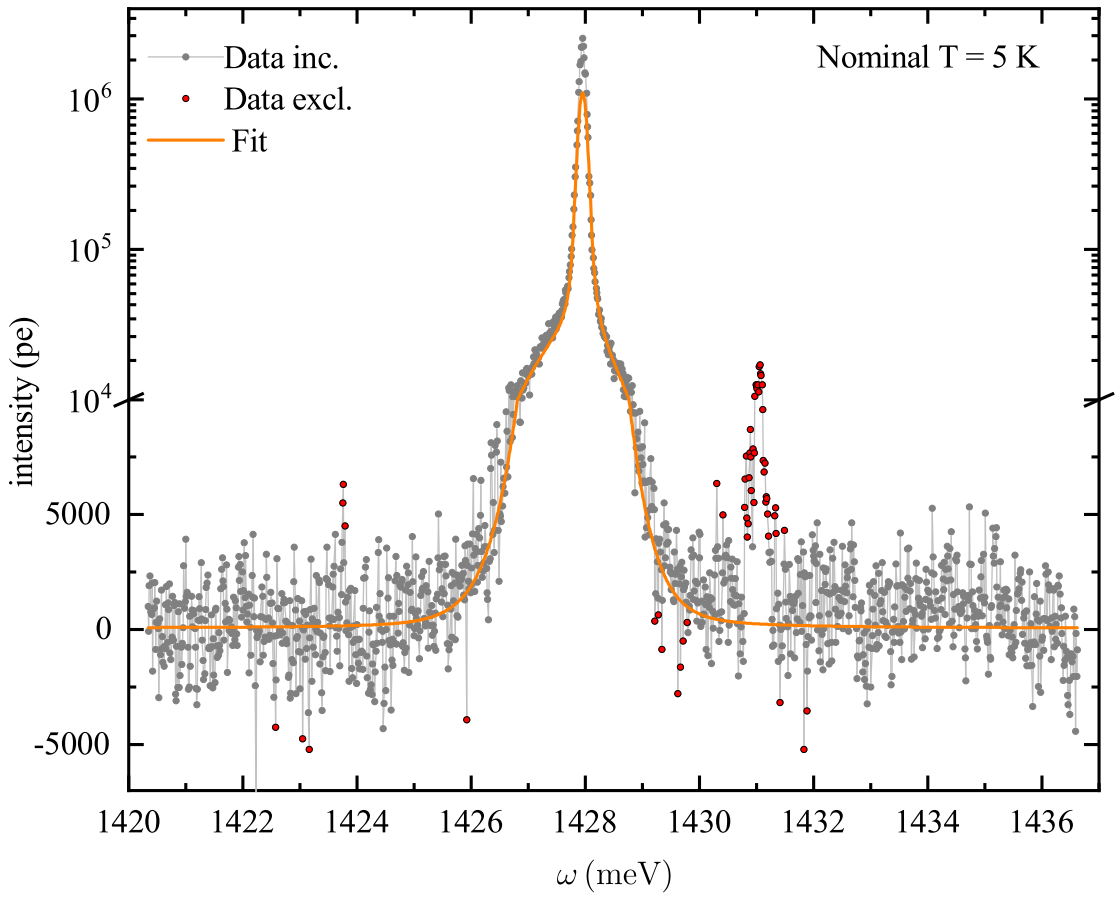

(a) Experimental and fitted PL emission spectra, showing data manually excluded from fit in red.

Parameter		Fit Value (with σ confidence bound)
T	(K)	13.81 (1.90)
γ_L	(μeV)	42.98 (32.51)
γ_G	(μeV)	141.47 (20.81)
$\omega_X - \omega_{\text{ref}}$	(meV)	0.33 (7.89E-03)
α		1.11E+06 (2.23E+05)

(b) Tabulated fit values, with deformation potential and QD confinement lengths fixed to the values detailed in Table C.2. Reference frequency $\omega_{\text{ref}} = 1,427.6$ meV

Figure C.15: PL spectrum and fit for single PQD sample with nominal temperature $T = 5$ K.

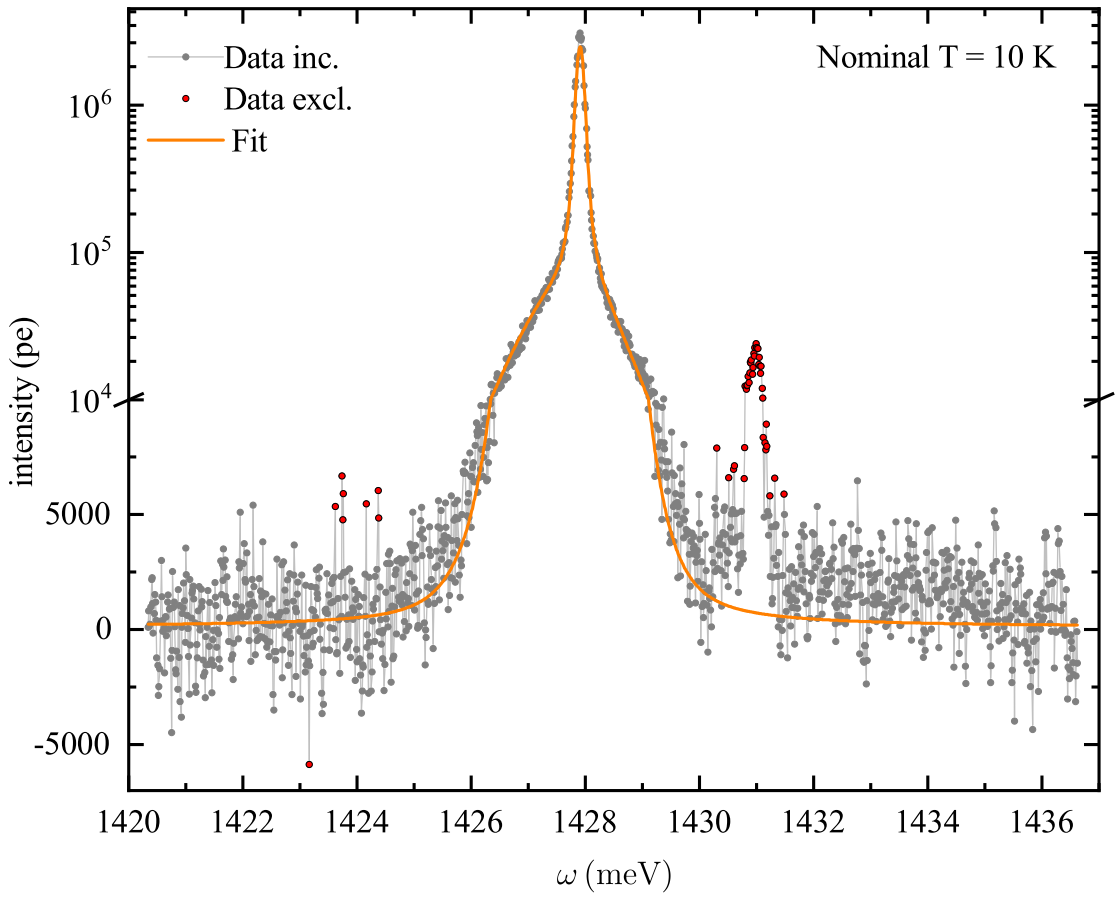

(a) Experimental and fitted PL emission spectra, showing data manually excluded from fit in red.

Parameter		Fit Value (with σ confidence bound)
T	(K)	13.64 (1.50)
γ_L	(μeV)	63.28 (54.66)
γ_G	(μeV)	113.65 (21.53)
$\omega_X - \omega_{\text{ref}}$	(meV)	0.28 (7.04E-03)
α		2.49E+06 (4.40E+05)

(b) Tabulated fit values, with deformation potential and QD confinement lengths fixed to the values detailed in Table C.2. Reference frequency $\omega_{\text{ref}} = 1,427.6$ meV

Figure C.16: PL spectrum and fit for single PQD sample with nominal temperature $T = 10$ K.

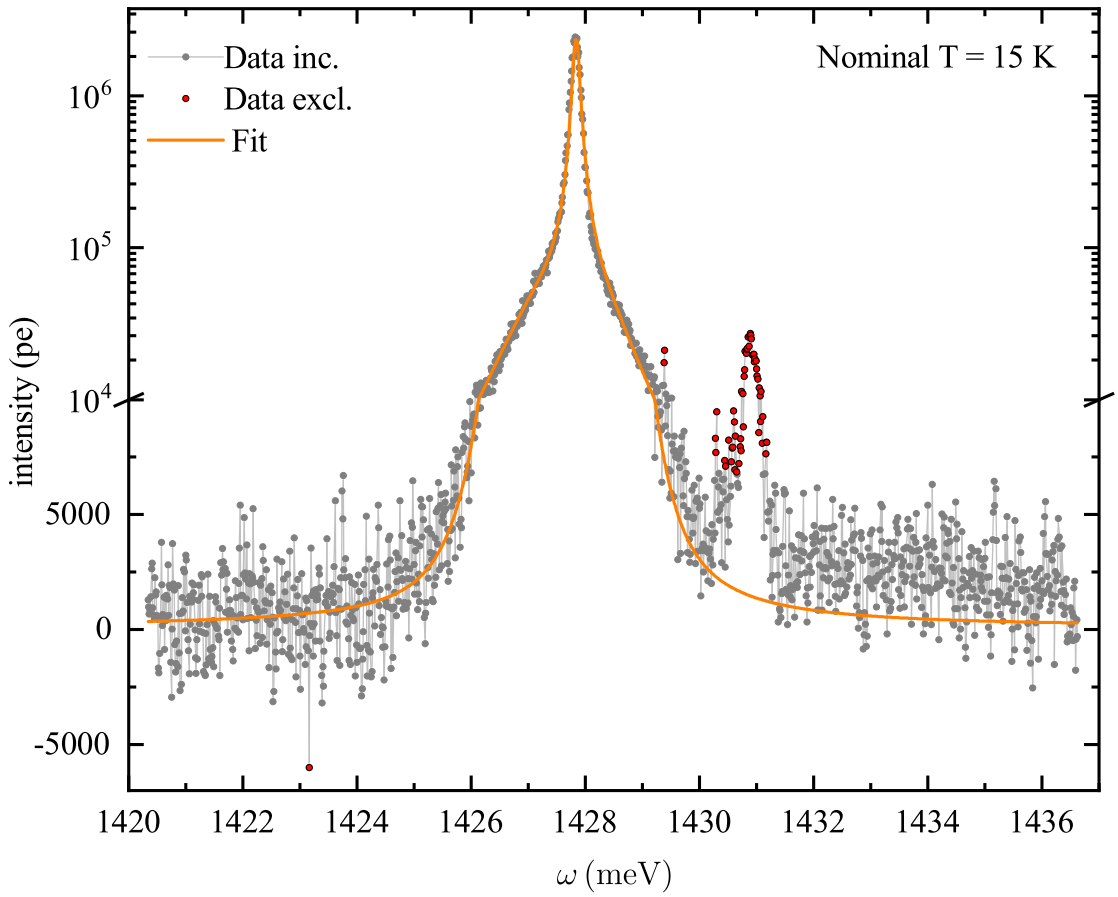

(a) Experimental and fitted PL emission spectra, showing data manually excluded from fit in red.

Parameter		Fit Value (with σ confidence bound)
T	(K)	12.87 (1.66)
γ_L	(μeV)	132.78 (119.33)
γ_G	(μeV)	14.63 (199.21)
$\omega_X - \omega_{\text{ref}}$	(meV)	0.21 (7.32E-03)
α		2.38E+06 (6.06E+05)

(b) Tabulated fit values, with deformation potential and QD confinement lengths fixed to the values detailed in Table C.2. Reference frequency $\omega_{\text{ref}} = 1,427.6$ meV

Figure C.17: PL spectrum and fit for single PQD sample with nominal temperature $T = 15$ K.

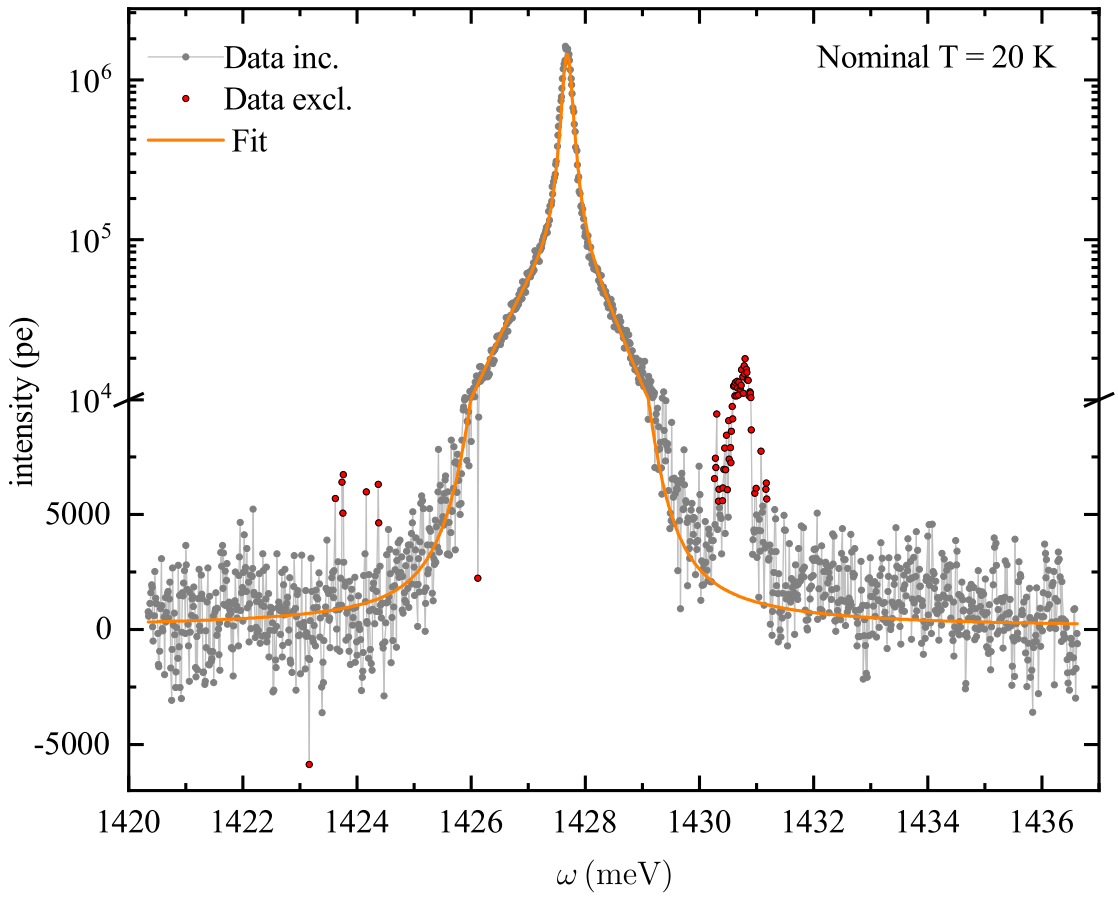

(a) Experimental and fitted PL emission spectra, showing data manually excluded from fit in red.

Parameter		Fit Value (with σ confidence bound)
T	(K)	17.68 (1.70)
γ_L	(μeV)	155.39 (143.31)
γ_G	(μeV)	66.84 (49.28)
$\omega_X - \omega_{\text{ref}}$	(meV)	0.06 (6.21E-03)
α		1.45E+06 (2.27E+05)

(b) Tabulated fit values, with deformation potential and QD confinement lengths fixed to the values detailed in Table C.2. Reference frequency $\omega_{\text{ref}} = 1,427.6$ meV

Figure C.18: PL spectrum and fit for single PQD sample with nominal temperature $T = 20$ K.

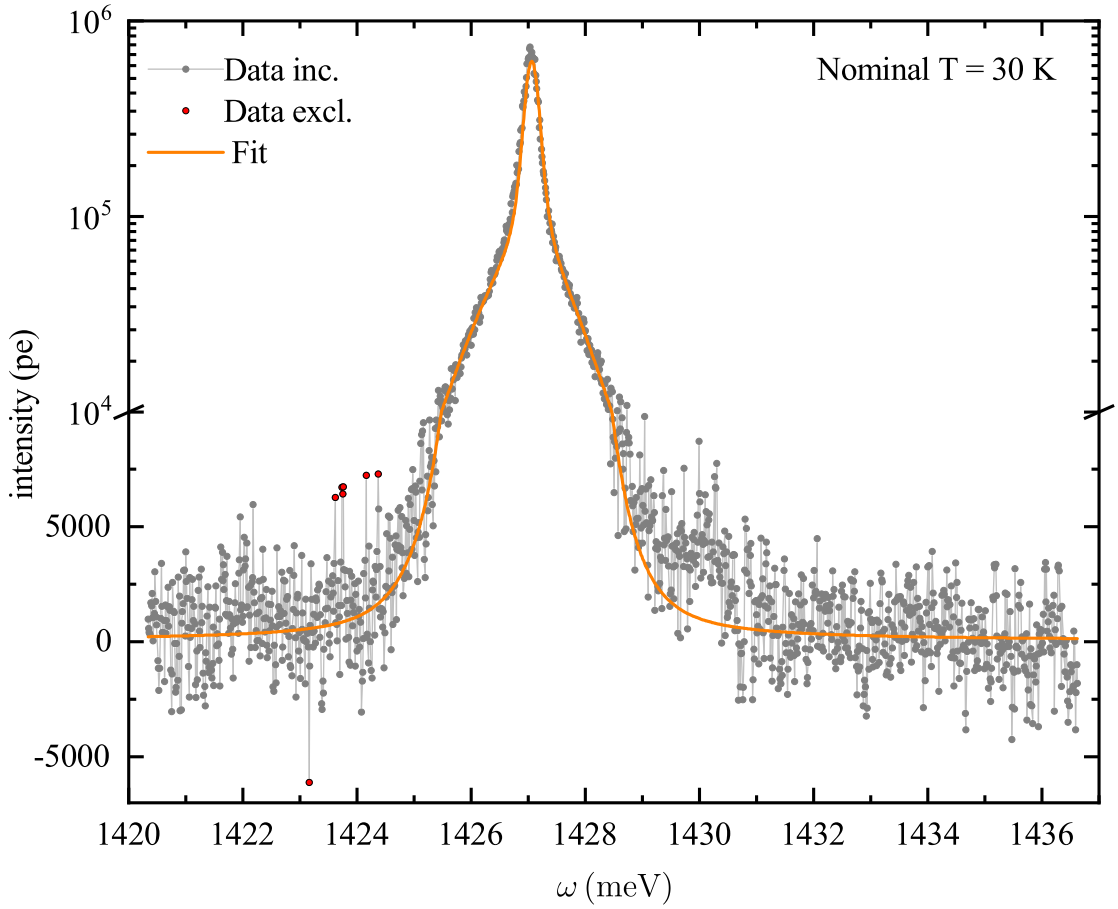

(a) Experimental and fitted PL emission spectra, showing data manually excluded from fit in red.

Parameter		Fit Value (with σ confidence bound)
T	(K)	32.82 (3.21)
γ_L	(μeV)	141.93 (126.18)
γ_G	(μeV)	179.78 (41.15)
$\omega_X - \omega_{\text{ref}}$	(meV)	-0.57 (9.84E-03)
α		6.21E+05 (9.46E+04)

(b) Tabulated fit values, with deformation potential and QD confinement lengths fixed to the values detailed in Table C.2. Reference frequency $\omega_{\text{ref}} = 1,427.6$ meV

Figure C.19: PL spectrum and fit for single PQD sample with nominal temperature $T = 30$ K.

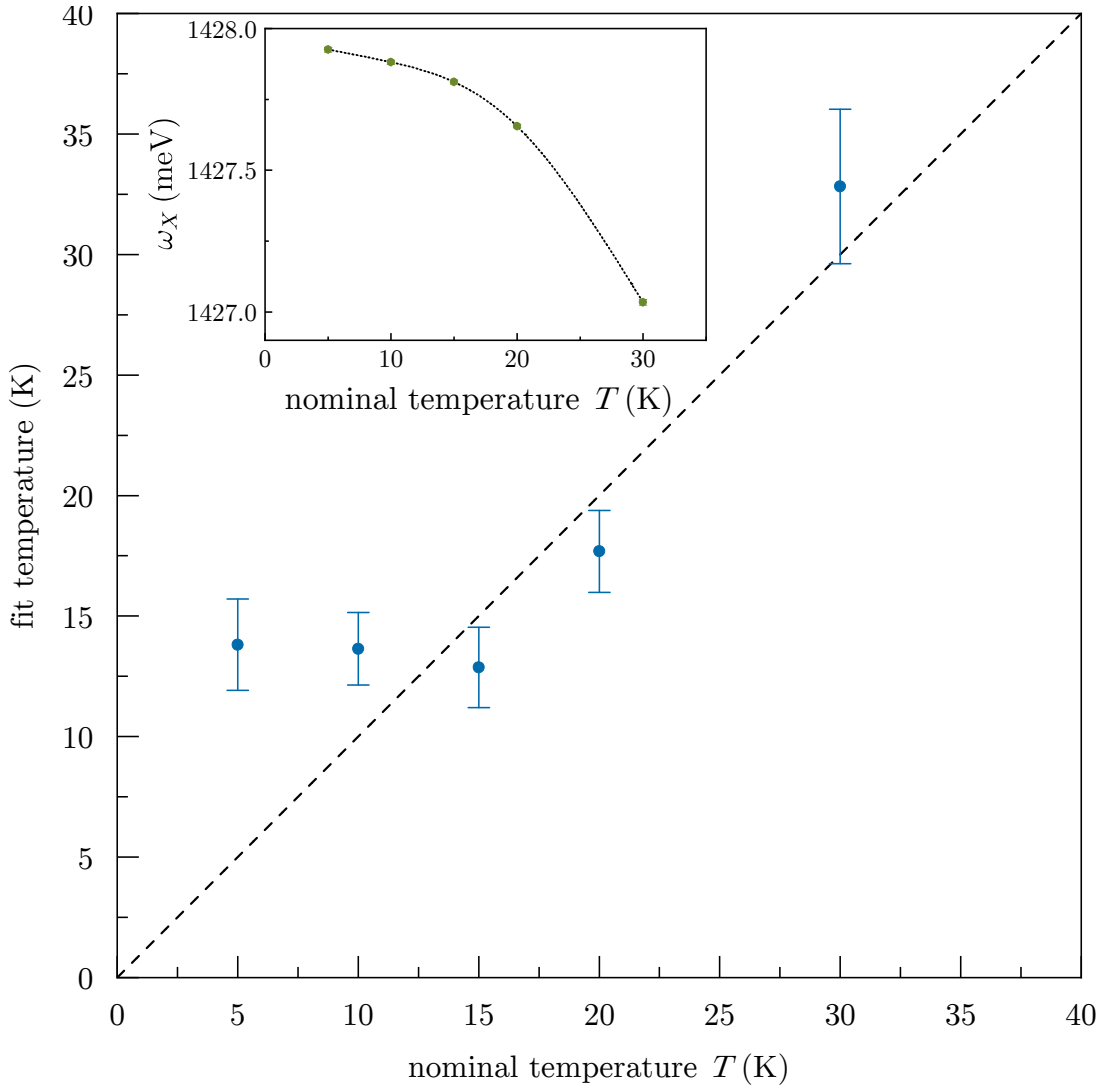

Figure C.20: Fit temperature (with σ error bars) as a function of nominal temperature, shown for single QD sample. Inset: trion transition frequency as a function of nominal temperature, shown for single PQD sample.

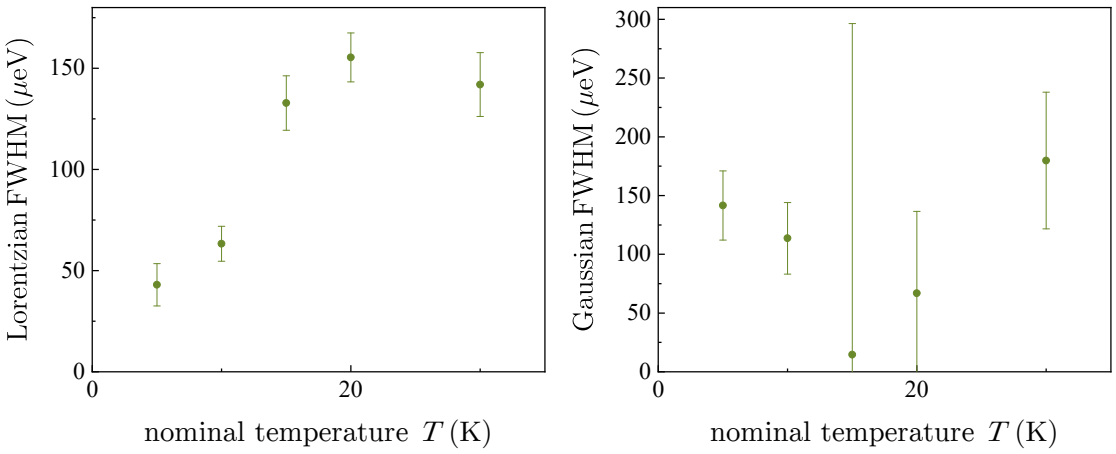

Figure C.21: Lorentzian γ_L and Gaussian γ_G broadening parameters (with σ error bars) as a function of nominal temperature, shown for single PQD sample.

D

Trotter decomposition method

D.1 Derivation of Eq. (3.10) for the linear polarisation

We take Eq. (3.8) as a starting point and note that

$$[\mathcal{H}, \rho] = H\rho - \rho H^* + i\gamma_X(d^\dagger d\rho + \rho d^\dagger d) + i\gamma_C(a^\dagger a\rho + \rho a^\dagger a)\,, \tag{D.1}$$

where H is the full *complex* Hamiltonian defined in Eq. (3.4) and H^* is its complex conjugate. We may therefore re-express the Lindblad master equation (Eq. (3.8)) as

$$i\dot{\rho} = H\rho - \rho H^* + 2i\gamma_X d\rho d^\dagger + 2i\gamma_C a\rho a^\dagger\,. \tag{D.2}$$

In the linear polarisation, we keep in the full polarisation only the terms which are linear in α. Looking closer, this implies keeping only $|X\rangle\langle 0|$ and $|C\rangle\langle 0|$ elements of the density matrix. When the density matrix is reduced to only $|X\rangle\langle 0|$ and $|C\rangle\langle 0|$ elements, the last two terms in Eq. (D.2) vanish, which yields an explicit solution:

$$\rho(t) = e^{-iHt}\rho(0_+)e^{iH^*t}\,, \tag{D.3}$$

The linear polarisation then takes the form

$$P_L(t) = -i\alpha \mathrm{Tr}\left\{e^{-iHt}\tilde{c}^\dagger\,|0\rangle\langle 0|\,\rho_0 e^{iH_{\mathrm{ph}}t}c\right\}\,, \tag{D.4}$$

where we have replaced H^* with $H_{\rm ph}$ since it acts on the $|0\rangle$ associated with annihilation operator c and hence retains only the $H_{\rm ph}$ term.

Now, dropping the unimportant constant factor $-i\alpha$ and introducing indices $j,k = X,C$ to replace the operators $\tilde{c}^\dagger$ and c, we arrive at Eq. (3.10).

D.2 Trotter decomposition of the evolution operator

Using the Trotter decomposition, the evolution operator is presented in Eq. (3.12) as $\hat{U}(t) = \lim_{N\to\infty}\hat{U}_N(t)$, where

$$\begin{aligned}
\hat{U}_N(t) &= e^{iH_{\rm ph}t}e^{-iH_{\rm IB}(t-t_{N-1})}e^{-iH_{\rm JC}(t-t_{N-1})}\dots e^{-iH_{\rm IB}(t_n-t_{n-1})}e^{-iH_{\rm JC}(t_n-t_{n-1})} \\
&\quad \times \dots e^{-iH_{\rm IB}t_1}e^{-iH_{\rm JC}t_1} \\
&= e^{iH_{\rm ph}t}e^{-iH_{\rm IB}(t-t_{N-1})}e^{-iH_{\rm ph}t_{N-1}}e^{-iH_{\rm JC}(t-t_{N-1})}\dots \\
&\quad \times e^{iH_{\rm ph}t_n}e^{-iH_{\rm IB}(t_n-t_{n-1})}e^{-iH_{\rm ph}t_{n-1}}e^{-iH_{\rm JC}(t_n-t_{n-1})}\dots e^{iH_{\rm ph}t_1}e^{-iH_{\rm IB}t_1}e^{-iH_{\rm JC}t_1} \\
&= \hat{W}(t,t_{N-1})\hat{M}(t-t_{N-1})\dots\hat{W}(t_n,t_{n-1})\hat{M}(t_n-t_{n-1})\dots\hat{W}(t_1,0)\hat{M}(t_1)\,,
\end{aligned} \tag{D.5}$$

where we have used the fact that the operators $H_{\rm ph}$ and $H_{\rm JC}$ commute. From the definition of $H_{\rm IB}$ we note that

$$\hat{W}(t_n,t_{n-1}) = e^{iH_{\rm ph}t_n}e^{-iH_{\rm IB}(t_n-t_{n-1})}e^{-iH_{\rm ph}t_{n-1}} \tag{D.6}$$

is a diagonal operator in the 2-basis state matrix representation in terms of $|X\rangle$ and $|C\rangle$:

$$\hat{W}(t_n,t_{n-1}) = \begin{pmatrix} W_X(t_n,t_{n-1}) & 0 \\ 0 & W_C(t_n,t_{n-1}) \end{pmatrix} \tag{D.7}$$

with

$$W_X(t_n,t_{n-1}) = e^{iH_{\rm ph}t_n}e^{-i(H_{\rm ph}+V)(t_n-t_{n-1})}e^{-iH_{\rm ph}t_{n-1}}, \tag{D.8}$$

$$W_C(t_n,t_{n-1}) = 1. \tag{D.9}$$

Using the time ordering operator $\mathcal{T}$, Eq. (D.8) for $W_X(t_n,t_{n-1})$ can be written as

$$W_X(t_n,t_{n-1}) = \mathcal{T}\exp\left\{-i\int_{t_{n-1}}^{t_n}V(\tau)d\tau\right\}, \tag{D.10}$$

where $V(\tau) = e^{iH_{\rm ph}\tau}Ve^{-iH_{\rm ph}\tau}$ is the interaction representation of the exciton-phonon coupling V.

Substituting the evolution operator Eq. (D.5) into Eq. (3.10) for the polarization $P_{jk}(t)$ and explicitly expressing the matrix products gives

$$P_{jk}(t) = \sum_{i_{N-1}=X,C} \dots \sum_{i_1=X,C} \langle W_{i_N} M_{i_N i_{N-1}} W_{i_{N-1}} M_{i_{N-1} i_{N-2}} \dots M_{i_{n+1} i_n} W_{i_n} M_{i_n i_{n-1}} \dots W_{i_1} M_{i_1 i_0} \rangle_{\rm ph} \tag{D.11}$$

with $i_N = j$ and $i_0 = k$. From here, we note that only W elements contain the phonon interaction and through a simple rearrangement of Eq. (D.11) we arrive at Eq. (3.16).

D.3 Linear polarisation in the NN approximation

The single summation in the cumulant Eq. (3.29) allows us to express, for each realisation, the expectation value in Eq. (3.16) as a product

$$\begin{aligned} &\langle W_{i_N}(t, t_{N-1}) \dots W_{i_n}(t_n, t_{n-1}) \dots W_{i_2}(t_2, t_1) W_{i_1}(t_1, 0) \rangle_{ph} \\ &= e^{\delta_{i_N X} K_0} e^{\delta_{i_{N-1} X} \left(K_0 + 2\delta_{i_N X} K_1\right)} \dots e^{\delta_{i_{n-1} X} (K_0 + 2\delta_{i_n X} K_1)} \dots e^{\delta_{i_1 X} \left(K_0 + 2\delta_{i_2 X} K_1\right)}. \end{aligned} \tag{D.12}$$

It is convenient to introduce

$$R_{i_n i_{n-1}} = e^{\delta_{i_{n-1} X} (K_0 + 2\delta_{i_n X} K_1)}, \tag{D.13}$$

enabling us to express the expectation values of the product of W-operators for a given realisation as

$$\langle W_{i_N}(t, t_{N-1}) \dots W_{i_2}(t_2, t_1) W_{i_1}(t_1, 0) \rangle_{ph} = e^{\delta_{i_N X} K_0} R_{i_N i_{N-1}} \dots R_{i_2 i_1} \,. \tag{D.14}$$

Substituting Eq. (D.14) into Eq. (3.16) for P_{jk}, we find

$$P_{jk}(t) = e^{\delta_{i_N X} K_0} \sum_{i_{N-1}=X,C} \dots \sum_{i_1=X,C} \left(M_{i_N i_{N-1}} \dots M_{i_2 i_1} M_{i_1 i_0} \right) \left(R_{i_N i_{N-1}} \dots R_{i_2 i_1} \right). \tag{D.15}$$

We then join together corresponding $M_{i_n i_{n-1}}$ and $R_{i_n i_{n-1}}$ elements through the definition of a matrix

$$G_{i_n i_{n-1}} = M_{i_n i_{n-1}} R_{i_n i_{n-1}} \,, \tag{D.16}$$

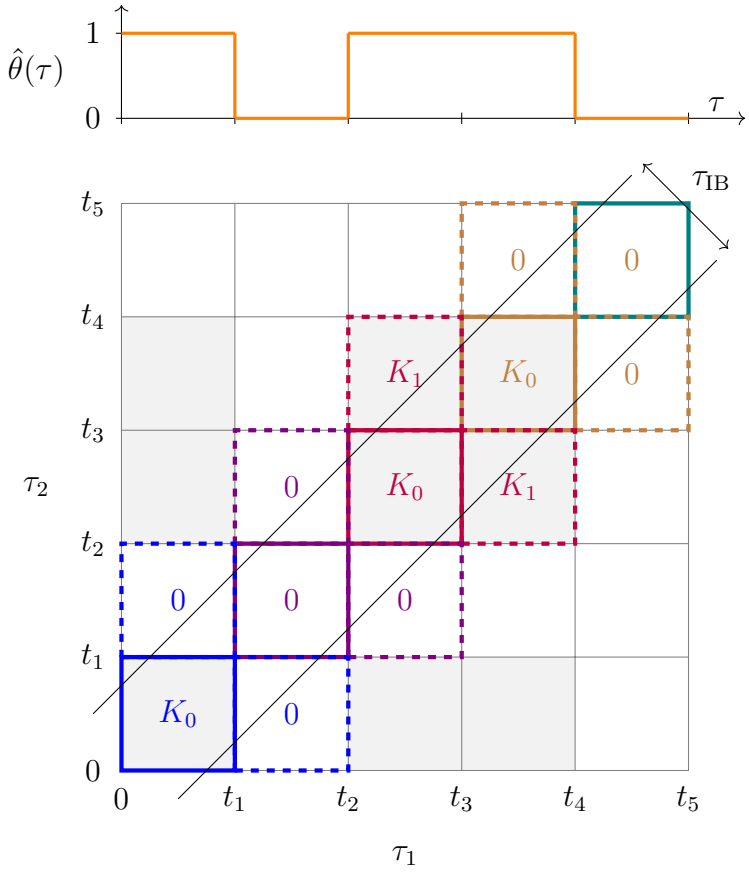

Figure D.1: Example realisation for the NN implementation with $N = 5$. We use the same realisation as shown in Fig. 3.1: $i_1 = X$, $i_2 = C$, $i_3 = X$, $i_4 = X$, $i_5 = C$, as is clear from the step function $\hat{\theta}(t)$ shown an the top of the figure.

which transforms Eq. (D.15) to

$$P_{jk}(t) = e^{\delta_{i_N X} K_0} \sum_{i_{N-1}=X,C} \cdots \sum_{i_{n-1}=X,C} \cdots \sum_{i_1=X,C} G_{i_N i_{N-1}} \ldots G_{i_n i_{n-1}} \ldots G_{i_2 i_1} M_{i_1 i_0} \,. \tag{D.17}$$

Using the fact that $i_N = j$ and $i_0 = k$, we arrive at Eq. (3.30) which is compactly represented in Eq. (3.32) as a product of matrices.

To illustrate this idea by way of an example, we return to the example realisation shown in Fig. 3.1. Fig. D.1 illustrates the time grid associated with the calculation of the cumulant for this particular realisation. Each exponential $e^{\delta_{i_{n-1} X}(K_0 + 2\delta_{i_n X} K_1)}$ in Eq. (D.12) can be visualised as an L-shaped portion of the time grid (colour coded in the figure). In the illustrated realisation we have $i_1 = X$, $i_2 = C$,

$i_3 = X$, $i_4 = X$, $i_5 = C$, giving

$$\begin{aligned} R_{i_2 i_1} &= e^{\delta_{i_1 X}\left(K_0 + 2\delta_{i_2 X} K_1\right)} = e^{K_0}\,, \\ R_{i_3 i_2} &= e^{\delta_{i_2 X}\left(K_0 + 2\delta_{i_3 X} K_1\right)} = e^{0} = 1\,, \\ R_{i_4 i_3} &= e^{\delta_{i_3 X}\left(K_0 + 2\delta_{i_4 X} K_1\right)} = e^{K_0 + 2K_1}\,, \\ R_{i_5 i_4} &= e^{\delta_{i_4 X}\left(K_0 + 2\delta_{i_5 X} K_1\right)} = e^{K_0}\,, \\ e^{\delta_{i_5 X} K_0} &= e^{0} = 1\,. \end{aligned}$$

We then find

$$\begin{aligned} G_{i_2 i_1} &= G_{CX} = M_{CX} e^{K_0}\,, \\ G_{i_3 i_2} &= G_{XC} = M_{XC}\,, \\ G_{i_4 i_3} &= G_{XX} = M_{XX} e^{K_0 + 2K_1}\,, \\ G_{i_5 i_4} &= G_{CX} = M_{CX} e^{K_0}\,, \end{aligned}$$

which contributes to the total polarisation Eq. (D.17).

Note that the condition for the NN approximation to be valid is also illustrated in Fig. D.1: All the time moments of integration for which $|\tau_2 - \tau_1| < \tau_{\mathrm{IB}}$ should be located within the coloured squares, which are taken into account in the NN calculation of the cumulant.

D.4 Analytic approximation from NN result

In this section, we derive the approximate analytic result Eqs. (3.38) and (3.39) for the linear polarisation $\hat{P}(t)$ in the long-time limit. This approximation is valid for small values of the exciton-cavity coupling strength g, which guarantees that the polariton timescale is much longer than the phonon memory time, $\tau_{\mathrm{JC}} \gg \tau_{\mathrm{IB}}$. As a starting point, we take the result for $\hat{P}(t)$ in the NN approach, Eqs. (3.32) and (3.33), and use it for $\Delta t \gtrsim \tau_{\mathrm{IB}}$. This condition implies that we can take both K_0 and K_1 in the long-time limit, using the asymptotic formula Eq. (3.37):

$$K_0 = K(\Delta t) \approx -i\Omega_p \Delta t - S, \tag{D.18}$$

$$K_1 = \frac{1}{2}\left(K(2\Delta t) - 2K(\Delta t)\right) \approx \frac{S}{2}\,. \tag{D.19}$$

We would now like to replace the product of N matrices in Eq. (3.32) by an approximate analytic expression, taking the Trotter limit $N \to \infty$. To do so, we initially derive explicit expressions for $\hat{M}$ and $\hat{G}$ in the two-state basis of $|X\rangle$ and $|C\rangle$. From Eq. (3.13) we obtain

$$\begin{aligned}\begin{pmatrix} M_{XX} & M_{XC} \\ M_{CX} & M_{CC} \end{pmatrix} &= e^{-iH_{\mathrm{JC}}\Delta t} \\ &= \begin{pmatrix} \alpha & \beta \\ -\beta & \alpha \end{pmatrix} \begin{pmatrix} e^{-i\omega_1\Delta t} & 0 \\ 0 & e^{-i\omega_2\Delta t} \end{pmatrix} \begin{pmatrix} \alpha & -\beta \\ \beta & \alpha \end{pmatrix} \\ &= e^{-i\omega_1\Delta t} \begin{pmatrix} 1-\beta^2\delta & -\alpha\beta\delta \\ -\alpha\beta\delta & 1-\alpha^2\delta \end{pmatrix}, \end{aligned} \tag{D.20}$$

where $\omega_{1,2}$ are the eigenvalues of the Jaynes-Cummings Hamiltonian H_{JC} (given by Eq. (1.27)), $\delta = 1 - e^{-i(\omega_2-\omega_1)\Delta t}$, and α and β make up the unitary matrices that diagonalise H_{JC} (given by Eqs. (1.25) and (1.26)).

$$H_{\mathrm{JC}} = \begin{pmatrix} \omega_X & g \\ g & \omega_C \end{pmatrix} = \begin{pmatrix} \alpha & \beta \\ -\beta & \alpha \end{pmatrix} \begin{pmatrix} \omega_1 & 0 \\ 0 & \omega_2 \end{pmatrix} \begin{pmatrix} \alpha & -\beta \\ \beta & \alpha \end{pmatrix}. \tag{D.21}$$

Substituting the expression for $\hat{M}$ given by Eq. (D.20) into Eq. (3.33), and using Eqs. (D.18) and (D.19), we find

$$\hat{G} = \begin{pmatrix} M_{XX}e^{K_0+2K_1} & M_{XC} \\ M_{CX}e^{K_0} & M_{CC} \end{pmatrix} \approx e^{-i\omega_1\Delta t} \begin{pmatrix} e^{-i\Omega_p\Delta t}(1-\beta^2\delta) & -\alpha\beta\delta \\ -e^{-i\Omega_p\Delta t - S}\alpha\beta\delta & 1-\alpha^2\delta \end{pmatrix}. \tag{D.22}$$

Now we use the fact that $\Delta t \ll \tau_{\mathrm{JC}}$ (which is equivalent to $|\omega_2 - \omega_1|\Delta t \ll 1$). We also assume that the polaron shift Ω_p is small, so that $|\Omega_p|\Delta t \ll 1$. Working within these limits is equivalent to taking the Trotter limit $\Delta t = t/N \to 0$. Keeping only the terms linear in Δt in the matrix elements, we obtain

$$\hat{G} \approx e^{-i\omega_1\Delta t} \begin{pmatrix} 1 - i\Delta t(\Omega_p + \beta^2(\omega_2-\omega_1)) & -i\Delta t\,\alpha\beta(\omega_2-\omega_1) \\ -i\Delta t\,\alpha\beta(\omega_2-\omega_1)e^{-S} & 1 - i\Delta t\,\alpha^2(\omega_2-\omega_1) \end{pmatrix}. \tag{D.23}$$

From Eq. (D.21) and the fact that $\alpha^2 + \beta^2 = 1$ we find

$$\beta^2(\omega_2 - \omega_1) = \omega_X - \omega_1, \tag{D.24}$$

$$\alpha^2(\omega_2 - \omega_1) = \omega_C - \omega_1, \tag{D.25}$$

$$\alpha\beta(\omega_2 - \omega_1) = g. \tag{D.26}$$

This allows us to re-write Eq. (D.23) in the following way

$$\hat{G} = e^{-i\omega_1 \Delta t} \left[\mathbb{1}(1 + i\omega_1 \Delta t) - i\Delta t \begin{pmatrix} \omega_X + \Omega_p & g \\ g e^{-S} & \omega_C \end{pmatrix} \right], \tag{D.27}$$

where $\mathbb{1}$ is a 2×2 identity matrix. Now, we diagonalise $\hat{G}$:

$$\hat{G} = \hat{Y} \hat{\Lambda} \hat{Y}^{-1}, \tag{D.28}$$

where the transformation matrix has the form

$$\hat{Y} = \begin{pmatrix} e^{S/2} & 0 \\ 0 & 1 \end{pmatrix} \begin{pmatrix} \tilde{\alpha} & \tilde{\beta} \\ -\tilde{\beta} & \tilde{\alpha} \end{pmatrix}, \tag{D.29}$$

in which the second matrix diagonalises a phonon-renormalised JC Hamiltonian $\tilde{H}$ [see Eq. (3.39)]:

$$\tilde{H} = \begin{pmatrix} \omega_X + \Omega_p & g e^{-S/2} \\ g e^{-S/2} & \omega_C \end{pmatrix} = \begin{pmatrix} \tilde{\alpha} & \tilde{\beta} \\ -\tilde{\beta} & \tilde{\alpha} \end{pmatrix} \begin{pmatrix} \tilde{\omega}_1 & 0 \\ 0 & \tilde{\omega}_2 \end{pmatrix} \begin{pmatrix} \tilde{\alpha} & -\tilde{\beta} \\ \tilde{\beta} & \tilde{\alpha} \end{pmatrix}. \tag{D.30}$$

The matrix of the eigenvalues $\hat{\Lambda}$ in Eq. (D.28) then takes the form

$$\hat{\Lambda} = e^{-i\omega_1 \Delta t} \begin{pmatrix} 1 - i\Delta t(\tilde{\omega}_1 - \omega_1) & 0 \\ 0 & 1 - i\Delta t(\tilde{\omega}_2 - \omega_1) \end{pmatrix}. \tag{D.31}$$

Coming back to the NN expression for the polarisation Eq. (3.32),

$$\hat{P}(t) = \begin{pmatrix} e^{K_0} & 0 \\ 0 & 1 \end{pmatrix} \hat{G}^N \hat{G}^{-1} \hat{M}, \tag{D.32}$$

we note that $\hat{G}^{-1} \approx \mathbb{1}$ and $\hat{M} \approx \mathbb{1}$ in the limit $\Delta t \to 0$, and also $e^{K_0} \approx e^{-S}$ (still keeping the condition $\Delta t \gtrsim \tau_{\mathrm{IB}}$). We then obtain in the long-time limit $t \gtrsim \tau_{\mathrm{IB}}$:

$$\hat{P}(t) = e^{-i\omega_1 t} \begin{pmatrix} e^{-S} & 0 \\ 0 & 1 \end{pmatrix} \hat{Y} \hat{\Lambda}^N \hat{Y}^{-1}. \tag{D.33}$$

Finally, we take the limit $N \to \infty$ in the expression $\hat{\Lambda}^N$, using an algebraic formula

$$\lim_{N \to \infty} \left(1 + \frac{x}{N}\right)^N = e^x. \tag{D.34}$$

Introducing

$$x = -i(\tilde{\omega}_1 - \omega_1)t, \tag{D.35}$$

$$y = -i(\tilde{\omega}_2 - \omega_1)t, \tag{D.36}$$

we find

$$\lim_{N\to\infty}\hat{\Lambda}^N = \lim_{N\to\infty}\begin{pmatrix}1+\frac{x}{N} & 0\\ 0 & 1+\frac{y}{N}\end{pmatrix}^N = e^{i\omega_1 t}\begin{pmatrix}e^{-i\tilde{\omega}_1 t} & 0\\ 0 & e^{-i\tilde{\omega}_2 t}\end{pmatrix}. \tag{D.37}$$

So finally,

$$\hat{P}(t) = \begin{pmatrix}e^{-S} & 0\\ 0 & 1\end{pmatrix}\begin{pmatrix}e^{S/2} & 0\\ 0 & 1\end{pmatrix}\begin{pmatrix}\tilde{\alpha} & \tilde{\beta}\\ -\tilde{\beta} & \tilde{\alpha}\end{pmatrix}\begin{pmatrix}e^{-i\tilde{\omega}_1 t} & 0\\ 0 & e^{-i\tilde{\omega}_2 t}\end{pmatrix}\begin{pmatrix}\tilde{\alpha} & -\tilde{\beta}\\ \tilde{\beta} & \tilde{\alpha}\end{pmatrix}\begin{pmatrix}e^{-S/2} & 0\\ 0 & 1\end{pmatrix} \tag{D.38}$$

$$= \begin{pmatrix}e^{-S/2} & 0\\ 0 & 1\end{pmatrix} e^{-i\tilde{H}t}\begin{pmatrix}e^{-S/2} & 0\\ 0 & 1\end{pmatrix}, \tag{D.39}$$

which is Eq. (3.38).

D.5 Refined analytic approximation

D.5.1 Derivation of Eq. (3.40)

We take as our starting point Eq. (3.10) for the linear polarisation, writing it in a matrix form using the two basis states $|X\rangle$ and $|C\rangle$:

$$\hat{P}(t) = \langle \hat{U}(t)\rangle_{\rm ph}\,, \tag{D.40}$$

where $\langle\ldots\rangle_{\rm ph}$ indicates the trace over all phonon states. The 2×2 evolution matrix operator $\hat{U}(t)$ has the form

$$\hat{U}(t) = e^{iH_{\rm ph}t}e^{-iHt} = e^{-iH_{\rm JC}t}e^{iH_1 t}e^{-iHt}\,, \tag{D.41}$$

where $H_{\rm JC}$ is the JC Hamiltonian defined in Eq. (**??**), and H and H_1 have the following forms:

$$H_1 = H_{\rm JC} + H_{\rm ph}\mathbb{1}, \quad H = H_1 + \begin{pmatrix}1 & 0\\ 0 & 0\end{pmatrix}V\,, \tag{D.42}$$

with $H_{\rm ph}$ and V being defined in Eqs. (3.2) and (3.3) respectively. We now take Eq. (D.41) and express $H_{\rm JC}$ as its diagonalised form $H_{\rm JC} = \hat{Y}\hat{\lambda}_{\rm JC}\hat{Y}^{-1}$ (with matrix $\hat{\lambda}_{\rm JC}$ being the diagonal matrix of JC eigenfrequencies $\omega_{1,2}$), to give

$$\hat{U}(t) = \hat{Y}e^{-iH_0 t}e^{i\bar{H}_1 t}e^{-i\bar{H}t}\hat{Y}^{-1} \tag{D.43}$$

where

$$\bar{H}_1 = \hat{Y}^{-1} H_1 \hat{Y} = \hat{\lambda}_{\rm JC} + H_{\rm ph}\mathbb{1}\,, \tag{D.44}$$

$$\bar{H} = \hat{Y}^{-1} H \hat{Y} = \hat{\lambda}_{\rm JC} + H_{\rm ph}\mathbb{1} + \hat{Q}V\,, \tag{D.45}$$

with $\hat{Q}$ being the polariton operator,

$$\hat{Q} = \hat{Y}^{-1} \begin{pmatrix} 1 & 0 \\ 0 & 0 \end{pmatrix} \hat{Y} = \begin{pmatrix} \alpha^2 & \alpha\beta \\ \alpha\beta & \beta^2 \end{pmatrix}. \tag{D.46}$$

We now introduce a reduced evolution operator $\bar{U}(t)$, which we define such that Eq. (D.43) becomes

$$\hat{U}(t) = \hat{Y} e^{-i\hat{\lambda}_{\rm JC} t} \bar{U}(t) \hat{Y}^{-1}\,. \tag{D.47}$$

The reduced evolution operator $\bar{U}(t)$ can then be written as an exponential series

$$\bar{U}(t) = e^{i\bar{H}_1 t} e^{-i\bar{H}t} = \mathcal{T} \exp\left\{ -i \int_0^t H_{int}(t')dt' \right\}\,, \tag{D.48}$$

where

$$H_{int}(t) = e^{i\bar{H}_1 t}(\bar{H} - \bar{H}_1) e^{-i\bar{H}_1 t} = \hat{Q}(t)V(t)\,, \tag{D.49}$$

with individual interaction representations of the polariton and phonon operators: $\hat{Q}(t) = e^{i\hat{\lambda}_{\rm JC} t}\hat{Q}e^{-i\hat{\lambda}_{\rm JC} t}$ and $V(t) = e^{iH_{\rm ph}t} V e^{-iH_{\rm ph}t}$. The expectation value of $\bar{U}(t)$ becomes an infinite perturbation series:

$$\begin{aligned} \langle \bar{U}(t) \rangle = {} & \mathbb{1} + (-i)^2 \int_0^t dt_1 \int_0^{t_1} dt_2 \hat{Q}(t_1)\hat{Q}(t_2) \langle V(t_1)V(t_2)\rangle \\ & + (-i)^4 \int_0^t dt_1 \int_0^{t_1} dt_2 \int_0^{t_2} dt_3 \int_0^{t_3} dt_4 \hat{Q}(t_1)\hat{Q}(t_2)\hat{Q}(t_3)\hat{Q}(t_4) \\ & \times \langle V(t_1)V(t_2)V(t_3)V(t_4)\rangle \ldots \end{aligned} \tag{D.50}$$

We apply Wick's theorem in an analogous manner to the linked cluster expansion (Sec. B.2.2). For example,

$$\begin{aligned} \langle V(t_1)V(t_2)V(t_3)V(t_4)\rangle = {} & \langle V(t_1)V(t_2)\rangle\langle V(t_3)V(t_4)\rangle + \langle V(t_1)V(t_3)\rangle\langle V(t_2)V(t_4)\rangle \\ & + \langle V(t_1)V(t_4)\rangle\langle V(t_2)V(t_3)\rangle \\ = {} & D(t_1 - t_2)D(t_3 - t_4) + D(t_1 - t_3)D(t_2 - t_4) \\ & + D(t_1 - t_4)D(t_2 - t_3)\,, \end{aligned} \tag{D.51}$$

where

$$D(t-t') = \langle V(t)V(t')\rangle = \sum_q |\lambda_q|^2 i D_q(t-t') \tag{D.52}$$

is the full phonon propagator, from which the IB model cumulant $K(t)$ may be defined ($K(t) = -\frac{i}{2}\int_0^t d\tau_1 \int_0^t d\tau_2 \sum_q |\lambda_q|^2 D_q(\tau_1-\tau_2)$). It is convenient to now introduce Dyson's equation – Eq. (3.41) – which is equivalent to the perturbation series Eq. (D.50) multiplied by $e^{-i\hat{\lambda}_{\rm JC}t}$. Accordingly, from Eqs. (D.40) and (D.47), we arrive at Eq. (3.40).

D.5.2 Derivation of Eq. (3.43)

As mentioned in the main text, the self energy $\hat{\Sigma}$ is represented by all possible connected diagrams such as the second and fourth order diagrams sketched in Fig. 3.4, which are given by the following expressions:

$$\begin{aligned}\hat{\Sigma}(t-t') \;=\; & \hat{Q}\,\hat{G}^{(0)}(t-t')\hat{Q}D(t-t') + \\ & \int_{-\infty}^{\infty} dt_1 \int_{-\infty}^{\infty} dt_2 \hat{Q}\hat{G}^{(0)}(t-t_1)\hat{Q}\hat{G}^{(0)}(t_1-t_2)\hat{Q}\hat{G}^{(0)}(t_2-t')\hat{Q} \\ & \times[D(t-t_2)D(t_1-t') + D(t-t')D(t_1-t_2)] + \ldots \end{aligned} \tag{D.53}$$

Eq. (D.53) are Dyson's equation (3.41) are *exact* provided that all the connected diagrams are included in the self energy. No approximations have been used thus far.

In the case of isolated (phonon-decoupled) polariton states, all of the matrices are diagonal and the problem reduces to the IB model for each polariton level, having an exact analytic solution which we exploit in our approximation. For the two phonon-coupled polariton states treated here, the exact solvability is hindered by the fact that the matrices $\hat{Q}$ and $\hat{G}^{(0)}(t)$ do not commute for any finite time t. However, in the timescale $|\omega_1-\omega_2|t \ll 1$, Eq. (3.42) may be approximated as $\hat{G}^{(0)}(t) \approx \theta(t)e^{-i\omega_1 t}\mathbb{1}$ and thus $\hat{G}^{(0)}(t)$ approximately commutes with $\hat{Q}$, so for example,

$$\hat{Q}\hat{G}^{(0)}(t-t_1)\hat{Q}\hat{G}^{(0)}(t_1-t_2)\hat{Q}\hat{G}^{(0)}(t_2-t')\hat{Q} \approx \hat{Q}\hat{G}^{(0)}(t-t')\theta(t-t_1)\theta(t_1-t_2)\theta(t_2-t')\,, \tag{D.54}$$

using $\hat{Q}^2 = \hat{Q}$. Clearly, this approximation is valid if $\tau_{\rm JC} \gg \tau_{\rm IB}$. In this case we obtain Eq. (3.43).

E
Master equation

E.1 Polaron transformation

The following elements of the Hermitian Hamiltonian $\bar{H}$ are unchanged following the polaron transformation defined in Eqs. (4.3) and (E.1):

$$\omega_X d^\dagger d \to \omega_X d^\dagger d\,, \tag{E.1}$$

$$\omega_C a^\dagger a \to \omega_C a^\dagger a\,, \tag{E.2}$$

The other elements of the Hermitian Hamiltonian $\bar{H}$ transform as follows:

1) $d^\dagger dV$

Splitting V into $\sum_q \lambda_q^* b_q$ and $\sum_q \lambda_q b_q^\dagger$ and using the Baker-Hausdorff identity (Eq. (A.7)) gives

$$e^S \left(d^\dagger d \sum_q \lambda_q^* b_q \right) e^{-S} = d^\dagger d \sum_q \lambda_q^* b_q + \left[d^\dagger d \sum_{q'} \left(\frac{\lambda_{q'}}{\omega_{q'}} b_{q'}^\dagger - \frac{\lambda_{q'}^*}{\omega_{q'}} b_{q'} \right), d^\dagger d \sum_q \lambda_q^* b_q \right] + \dots . \tag{E.3}$$

Using $(d^\dagger d)^n = d^\dagger d$ for integer n and the phonon commutation relations Eq. (A.4) and Eq. (A.5),

$$e^S \left(d^\dagger d \sum_q \lambda_q^* b_q \right) e^{-S} = d^\dagger d \sum_q \lambda_q^* b_q - d^\dagger d \sum_q \frac{|\lambda_q|^2}{\omega_q}\,. \tag{E.4}$$

Note that the third term in the Taylor series expansion of $e^S B e^{-S}$ is given by $\frac{1}{2!}[S,[S,B]]$, which for the present case is $\frac{1}{2!}[d^\dagger d \sum_{q'} \left(\frac{\lambda_{q'}}{\omega_{q'}} b_{q'}^\dagger - \frac{\lambda_{q'}^*}{\omega_{q'}} b_{q'} \right), -d^\dagger d \sum_q \frac{|\lambda_q|^2}{\omega_q}] =$

0. The series therefore terminates after the second term i.e. Eq. (E.4) is exact.

Looking now at $d^\dagger d \sum_q \lambda_q b_q^\dagger$,

$$e^S \left(d^\dagger d \sum_q \lambda_q b_q^\dagger \right) e^{-S} = d^\dagger d \sum_q \lambda_q^* b_q^\dagger + \left[d^\dagger d \sum_{q'} \left(\frac{\lambda_{q'}}{\omega_{q'}} b_{q'}^\dagger - \frac{\lambda_{q'}^*}{\omega_{q'}} b_{q'} \right), d^\dagger d \sum_q \lambda_q b_q^\dagger \right] + \dots \tag{E.5}$$

$$= d^\dagger d \sum_q \lambda_q b_q^\dagger - d^\dagger d \sum_q \frac{|\lambda_q|^2}{\omega_q} \,. \tag{E.6}$$

Again, the series terminates after the second term, rendering Eq. (E.6) exact. Thus,

$$e^S \left(d^\dagger d \sum_q \left(\lambda_q^* b_q + \lambda_q b_q^\dagger \right) \right) e^{-S} = d^\dagger d \sum_q \left(\lambda_q^* b_q + \lambda_q b_q^\dagger \right) - 2 d^\dagger d \sum_q \frac{|\lambda_q|^2}{\omega_q} \,. \tag{E.7}$$

3) $\sum_q \omega_q b_q^\dagger b_q$

$$e^S \left(\sum_q \omega_q b_q^\dagger b_q \right) e^{-S} = \sum_q \omega_q b_q^\dagger b_q + \left[d^\dagger d \sum_{q'} \left(\frac{\lambda_{q'}}{\omega_{q'}} b_{q'}^\dagger - \frac{\lambda_{q'}^*}{\omega_{q'}} b_{q'} \right), \sum_q \omega_q b_q^\dagger b_q \right] + \dots \tag{E.8}$$

Looking at the individual parts:

$$\left[d^\dagger d \sum_{q'} \frac{\lambda_{q'}}{\omega_{q'}} b_{q'}^\dagger, \sum_q \omega_q b_q^\dagger b_q \right] = d^\dagger d \sum_q \lambda_q [b_q^\dagger, b_q^\dagger b_q] \tag{E.9}$$

$$= d^\dagger d \sum_q \lambda_q b_q^\dagger [b_q^\dagger, b_q] \tag{E.10}$$

$$= -d^\dagger d \sum_q \lambda_q b_q^\dagger \,, \tag{E.11}$$

and,

$$\left[-d^\dagger d \sum_{q'} \frac{\lambda_{q'}^*}{\omega_{q'}} b_{q'}, \sum_q \omega_q b_q^\dagger b_q \right] = -d^\dagger d \sum_q \lambda_q^* [b_q, b_q^\dagger b_q] \tag{E.12}$$

$$= d^\dagger d \sum_q \lambda_q^* [b_q, b_q^\dagger] b_q \tag{E.13}$$

$$= -d^\dagger d \sum_q \lambda_q^* b_q \,. \tag{E.14}$$

Thus,

$$e^S \left(\sum_q \omega_q b_q^\dagger b_q \right) e^{-S} = \sum_q \omega_q b_q^\dagger b_q - d^\dagger d \sum_q \left(\lambda_q^* b_q + \lambda_q b_q^\dagger \right) + \dots \tag{E.15}$$

The third term of the Taylor expansion of $e^S B e^{-S}$ is given by $\frac{1}{2!}[S,[S,B]]$, which for the present case is $\frac{1}{2!}[d^\dagger d\sum_{q'}\left(\frac{\lambda_{q'}}{\omega_{q'}}b^\dagger_{q'}-\frac{\lambda^*_{q'}}{\omega_{q'}}b_{q'}\right), -d^\dagger d\sum_q\left(\lambda^*_q b_q+\lambda_q b^\dagger_q\right)]$. We note that this commutator $[d^\dagger d\sum_{q'}\left(\frac{\lambda_{q'}}{\omega_{q'}}b^\dagger_{q'}-\frac{\lambda^*_{q'}}{\omega_{q'}}b_{q'}\right), d^\dagger d\sum_q\left(\lambda^*_q b_q+\lambda_q b^\dagger_q\right)]$ was previously calculated when evaluating the second term of Eq. (E.7). Exploiting this result yields

$$e^S\left(\sum_q \omega_q b^\dagger_q b_q\right)e^{-S}=\sum_q\omega_q b^\dagger_q b_q - d^\dagger d\sum_q\left(\lambda^*_q b_q+\lambda_q b^\dagger_q\right)+d^\dagger d\sum_q\frac{|\lambda_q|^2}{\omega_q}\,. \tag{E.16}$$

4) $ga^\dagger d$

Express the exponential $e^{\pm S}$ as a Taylor series,

$$e^{\pm S}=\mathbb{1}\pm S+\frac{S^2}{2!}+\ldots \tag{E.17}$$

Substituting for S from Eq. (4.3) and using $(d^\dagger d)^n=d^\dagger d$ for integer n,

$$e^{\pm S}=\mathbb{1}+d^\dagger d\left(A_\pm+\frac{A^2_\pm}{2!}+\frac{A^3_\pm}{3!}+\ldots\right) \tag{E.18}$$

$$=\mathbb{1}+d^\dagger d\left(e^{A_\pm}-\mathbb{1}\right), \tag{E.19}$$

where $A_\pm=\pm\sum_q\left(\frac{\lambda_q}{\omega_q}b^\dagger_q-\frac{\lambda^*_q}{\omega_q}b_q\right)$. Using Eq. (E.19) in the transformation of $ga^\dagger d$ gives

$$e^S ga^\dagger d e^{-S}=g\left(\mathbb{1}+d^\dagger d\left(e^{A_+}-\mathbb{1}\right)\right)a^\dagger d\left(\mathbb{1}+d^\dagger d\left(e^{A_-}-\mathbb{1}\right)\right) \tag{E.20}$$

$$\begin{aligned}=ga^\dagger d+ga^\dagger\Big(&d^\dagger dd\{e^{A_+}-\mathbb{1}\}+dd^\dagger d\{e^{A_-}-\mathbb{1}\}\\&+d^\dagger ddd^\dagger d\{e^{A_+}-\mathbb{1}\}\{e^{A_-}-\mathbb{1}\}\Big)\,.\end{aligned} \tag{E.21}$$

Using $d^\dagger dd=0$ and $dd^\dagger d=d$,

$$e^S\left(ga^\dagger d\right)e^{-S}=ga^\dagger d\;e^{A_-}\,. \tag{E.22}$$

5) $gd^\dagger a$

Employing an analogous method to step (4) above gives,

$$e^S\left(gd^\dagger a\right)e^{-S}=gd^\dagger a\;e^{A_+}\,. \tag{E.23}$$

Drawing together Eqns Eqs. (E.1), (E.2), (E.7), (E.16), (E.22) and (E.23), we arrive at the following expression for the transformed Hamiltonian H':

$$H' = (\omega_X + \Omega_p)\, d^\dagger d + \omega_C a^\dagger a + g\left(a^\dagger d B_- + d^\dagger a B_+\right) + \sum_q \omega_q b_q^\dagger b_q\,, \tag{E.24}$$

where we have defined,

$$\Omega_p = -\sum_q \frac{|\lambda_q|^2}{\omega_q}\,, \tag{E.25}$$

$$B_\pm = e^{A_\pm} = e^{\pm\sum_q\left(\frac{\lambda_q}{\omega_q} b_q^\dagger - \frac{\lambda_q^*}{\omega_q} b_q\right)}\,. \tag{E.26}$$

The transformed Hamiltonian H' described by Eq. (E.24) contains non-Hermitian operators $B_\pm$. Following [83], we separate the average of $B_\pm$ from the fluctuations. We denote the average as follows,

$$\langle B\rangle = \langle B_+\rangle = \langle B_-\rangle\,. \tag{E.27}$$

We then choose Hermitian combinations of the fluctuations,

$$B_g = \frac{1}{2}\left(B_+ + B_- - 2\langle B\rangle\right)\,, \tag{E.28}$$

$$B_u = \frac{i}{2}\left(B_- - B_+\right)\,, \tag{E.29}$$

from which we arrive at Eqns Eqs. (4.4) to (4.7).

To find an explicit expression for the average $\langle B\rangle$, we consider a single q within the expression for $B_\pm$,

$$B_{\pm,q} = e^{\pm\left(\frac{\lambda_q}{\omega_q} b_q^\dagger - \frac{\lambda_q^*}{\omega_q} b_q\right)}\,. \tag{E.30}$$

Using the commutation relation $[b_q^\dagger, b_q] = 1$, we note that $[[b_q^\dagger, b_q], b_q] = [[b_q^\dagger, b_q], b_q^\dagger] = 0$. We may therefore apply the identity $e^{A+B} = e^A e^B e^{-\frac{1}{2}[A,B]}$, giving

$$B_{\pm,q} = e^{-\frac{1}{2}\left|\frac{\lambda_q}{\omega_q}\right|^2} e^{\pm\frac{\lambda_q}{\omega_q} b_q^\dagger} e^{\mp\frac{\lambda_q^*}{\omega_q} b_q}\,. \tag{E.31}$$

Taking the expectation value,

$$\langle B_{\pm,q}\rangle = e^{-\frac{1}{2}\left|\frac{\lambda_q}{\omega_q}\right|^2}\left\langle e^{\pm\frac{\lambda_q}{\omega_q}b_q^\dagger}e^{\mp\frac{\lambda_q^*}{\omega_q}b_q}\right\rangle \tag{E.32}$$

$$= e^{-\frac{1}{2}\left|\frac{\lambda_q}{\omega_q}\right|^2}\left\langle\left(1\pm\frac{\lambda_q}{\omega_q}b_q^\dagger+\ldots\right)\left(1\mp\frac{\lambda_q^*}{\omega_q}b_q+\ldots\right)\right\rangle \tag{E.33}$$

$$= e^{-\frac{1}{2}\left|\frac{\lambda_q}{\omega_q}\right|^2}\left(1-\left|\frac{\lambda_q}{\omega_q}\right|^2\left\langle b_q^\dagger b_q\right\rangle+\ldots\right). \tag{E.34}$$

Noting that $\langle b_q^\dagger b_q\rangle = N_q = \frac{1}{e^{\beta\omega_q}-1}$ where β is the inverse temperature $(k_BT)^{-1}$, Eq. (E.34) may be expressed as

$$\langle B_{\pm,q}\rangle = \exp\left\{-\left|\frac{\lambda_q}{\omega_q}\right|^2\left(N_q+\frac{1}{2}\right)\right\} \tag{E.35}$$

$$= \exp\left\{-\frac{1}{2}\left|\frac{\lambda_q}{\omega_q}\right|^2\coth\left(\frac{\beta\omega_q}{2}\right)\right\}. \tag{E.36}$$

Returning now to the full expression for $B_\pm$,

$$B_\pm = e^{\pm\sum_q\left(\frac{\lambda_q}{\omega_q}b_q^\dagger-\frac{\lambda_q^*}{\omega_q}b_q\right)} \tag{E.37}$$

$$= \prod_q B_\pm(q)\,. \tag{E.38}$$

Hence,

$$\langle B_\pm\rangle = \exp\left\{-\frac{1}{2}\sum_q\left|\frac{\lambda_q}{\omega_q}\right|^2\coth\left(\frac{\beta\omega_q}{2}\right)\right\}. \tag{E.39}$$

Finally, converting the summation over q to an integration over ω: $\sum_q \to \frac{V}{(2\pi)^3v_s^3}\int d^3\omega$, Eq. (E.39) becomes,

$$\langle B_\pm\rangle = \exp\left\{-\frac{1}{2}\int_0^\infty \mathrm{d}\omega\frac{J(\omega)}{\omega^2}\coth\left(\frac{\beta\omega}{2}\right)\right\}. \tag{E.40}$$

E.2 Levels of approximation

Factorisation of initial density matrix

Factorisation of the initial density matrix $\tilde\rho(0)$ as $\tilde\rho(0)=\tilde\rho_S(0)\otimes\tilde\rho_B(0)$ allows us to express the first term of Eq. (4.25) as,

$$\mathrm{tr}_B\left\{-i[\tilde H_{\mathrm{int}}(t),\tilde\rho(0)]\right\} = \mathrm{tr}_B\left\{-i\left[\sum_{\alpha=g,u}\tilde X_\alpha(t)\otimes\tilde B_\alpha(t),\,\rho_S(0)\otimes\rho_B(0)\right]\right\}, \tag{E.41}$$

where we have replaced H_{int} with the expression given in used Eq. (4.7). We note that $\tilde{X}_\alpha(t) = e^{iH_0 t} X_\alpha e^{iH_0 t} = e^{iH_{\text{sys}}t}, X_\alpha\, e^{iH_{\text{sys}}t}$ due to the commutivity of H_{bath} and X_α. Similarly, $\tilde{B}_\alpha(t) = e^{iH_{\text{bath}}t}\, B_\alpha\, e^{iH_{\text{bath}}t}$. Given that $\tilde{X}_\alpha(t)$ and ρ_S act only on the system Hilbert space $\mathcal{H}^{(\text{sys})}$, whilst $\tilde{B}_\alpha(t)$ and ρ_B act only on the bath Hilbert space $\mathcal{H}^{(\text{bath})}$, we may separate the commutator of Eq. (E.41) as follows,

$$\begin{aligned}\text{tr}_B\left\{-i[\tilde{H}_{\text{int}}(t), \tilde{\rho}(0)]\right\} &= \text{tr}_B\left\{-i \sum_{\alpha=g,u}\left([\tilde{X}_\alpha(t), \rho_S(0)] \otimes [\tilde{B}_\alpha(t), \rho_B(0)]\right)\right\} \\ &= -i \sum_{\alpha=g,u} [\tilde{X}_\alpha(t), \rho_S(0)] \otimes \text{tr}_B\left\{\left[\tilde{B}_\alpha(t), \rho_B(0)\right]\right\}. \quad \text{(E.42)}\end{aligned}$$

All operators within the partial trace are now solely operative within the bath Hilbert space $\mathcal{H}^{(\text{bath})}$, thereby allowing us to replace the partial trace over bath states with a full trace. Exploiting the cyclic properties of the trace operation, we note that $\text{tr}\left\{\tilde{B}_\alpha(t)\rho_B(0)\right\} = \text{tr}\left\{\rho_B(0)\tilde{B}_\alpha(t)\right\}$ and therefore $\text{tr}\left\{[\tilde{B}_\alpha, \rho_B(0)]\right\} = 0$. The first term of Eq. (4.25) accordingly vanishes.

Factorisation of density matrix at all times

Applying the density matrix factorisation $\tilde{\rho}(t) = \tilde{\rho}_S(t) \otimes \tilde{\rho}_B$ and treating the second term of Eq. (4.25) analogously to the first term,

$$\begin{aligned}&\text{tr}_B\left\{i\left[\tilde{H}'_{\text{int}}(t), \int_0^t d\tau\ \tilde{\mathcal{D}}(\tau)\right]\right\} = \\ &i\int_0^t d\tau\, \text{tr}_B\left\{\left[\sum_{\alpha=g,u} \tilde{X}_\alpha(t) \otimes \tilde{B}_\alpha(t),\ \gamma_C\, 2\tilde{a}(\tau)\tilde{\rho}_S(\tau) \otimes \tilde{\rho}_B(\tau)\tilde{a}^\dagger(\tau) + \ldots\right]\right\}, \quad \text{(E.43)}\end{aligned}$$

where we have explicitly included only the first term of the Lindblad dissipator $\tilde{\mathcal{D}}(\tau)$ for clarity. We note that $\tilde{\rho}_S(\tau) = e^{iH_{\text{sys}}t}\, \rho_S\, e^{-iH_{\text{sys}}t}$ due to the commutivity of ρ_S and H_{bath}. Similarly, $\tilde{\rho}_B(\tau) = e^{iH_{\text{bath}}t}\, \rho_B\, e^{-iH_{\text{bath}}t}$ due to the commutivity of ρ_B and H_{sys}. Accordingly, as for the first term of Eq. (4.25), we may separate the commutator and obtain terms such as $i\int_0^t d\tau \sum_\alpha 2\gamma_C[\tilde{X}_\alpha(t), \tilde{a}(\tau)\tilde{\rho}_S(\tau)\tilde{a}^\dagger(\tau)] \otimes \text{tr}_B\{[\tilde{B}_\alpha(t), \tilde{\rho}_B(\tau)]\}$. All terms within Eq. (E.43) include a direct product ($\otimes$) with $\text{tr}_B\{[\tilde{B}_\alpha(t), \tilde{\rho}_B(\tau)]\}$ and therefore equate to zero for the reasons outlined above.

E.2.1 Markov approximation in the interaction representation

Expressing the interaction picture density matrix $\tilde{\rho_S}(t)$ in terms of the Schrödinger picture system density matrix $\rho_S(t)$, we have

$$\frac{d\tilde{\rho_S}(t)}{dt} = \frac{d}{dt}\left(e^{iH_0t}\rho_S(t)e^{-iH_0t}\right) = e^{iH_0t}\frac{d\rho_S(t)}{dt}e^{-iH_0t} + i[H_0, \tilde{\rho}_S(t)]\,. \tag{E.44}$$

Replacing the LHS of Eq. (4.27) with Eq. (E.44) and noting that $e^{-iH_0t}H_0e^{iH_0t} = H_0$,

$$\frac{d\rho_S(t)}{dt} = -i[H_0, \rho_S(t)] - \int_0^t d\tau\ \ \mathrm{tr}_B[H_{\mathrm{int}}(t), [\tilde{H}_{\mathrm{int}}(\tau - t), \rho_S(t)\otimes\rho_B]] + \mathcal{D}_S(t)\,. \tag{E.45}$$

We note that $H_0 = H_{\mathrm{sys}} + H_{\mathrm{bath}}$ and that $[H_{\mathrm{bath}}, \rho_S(t)] = 0$. Making a change of variables $t' = t - \tau$, we can write

$$\frac{d\rho_S(t)}{dt} = -i[H_{\mathrm{sys}}, \rho_S(t)] - \underbrace{\int_0^t dt'\ \ \mathrm{tr}_B[H_{\mathrm{int}}(t), [\tilde{H}_{\mathrm{int}}(-t'), \rho_S(t)\otimes\rho_B]]}_{(\star)} + \mathcal{D}_S(t)\,. \tag{E.46}$$

As a final step, we consider term $(\star)$ in isolation. Substituting for H_{int} from Eq. (4.7) yields

$$\begin{aligned}\int_0^t dt'\ \ &\mathrm{tr}_B[H_{\mathrm{int}}(t), [\tilde{H}_{\mathrm{int}}(-t'), \rho_S(t)\rho_B]] \\ &= \int_0^t dt'\ \ \mathrm{tr}_B\left[\sum_{\alpha=g,u} X_\alpha\otimes B_\alpha, \left[\sum_{\alpha'=g,u}\tilde{X}_{\alpha'}(-t')\otimes\tilde{B}_{\alpha'}(-t'), \rho_S(t)\otimes\rho_B\right]\right].\end{aligned} \tag{E.47}$$

Looking initially at the $\alpha = \alpha' = g$ term within Eq. (E.47),

$$\begin{aligned}\int_0^t dt'\ \ &\mathrm{tr}_B[X_g\otimes B_g, [\tilde{X}_g(-t')\otimes\tilde{B}_g(-t'), \rho_S(t)\otimes\rho_B]] \\ &= \int_0^t dt'\langle B_g\tilde{B}_g(-t')\rangle\left([X_g, \tilde{X}_g(-t')\rho_S(t)] - [X_g, \rho_S(t)\tilde{X}_g(-t')]\right),\end{aligned} \tag{E.48}$$

where $\langle\ldots\rangle$ represents the expectation value over the phonon bath. Applying the same procedure to the $\alpha = \alpha' = u$ term within Eq. (E.47), noting that the second term in Eq. (E.48) is the Hermitian conjugate (H.c) of the first, and further noting that $\langle B_\alpha\tilde{B}_{\alpha'}(-t')\rangle = 0$ for $\alpha \neq \alpha'$ (see Eqs. (E.54) and (E.55)), we arrive at Eq. (4.29).

Equations of motion

We consider each term in Eq. (4.29) in isolation, noting that in analogy to the case without phonons, the only matrix elements of interest are the $|X\rangle\langle 0|$ and $|C\rangle\langle 0|$ elements.

$\underline{-i[H_{\rm sys}, \rho_S(t)]}$

Substituting for $H'_{\rm sys}$ from Eq. (4.5) gives the following,

$$\begin{aligned} -i[H_{\rm sys}, \rho_S(t)] = &\Big(-i(\Omega_p + \Omega_X)\rho_{X0} - ig\langle B\rangle\rho_{C0}\Big)|X\rangle\langle 0| \\ &+ \Big(-i\Omega_C\rho_{C0} - ig\langle B\rangle\rho_{X0}\Big)|C\rangle\langle 0| + \text{o.t.} \end{aligned} \tag{E.49}$$

where o.t. denotes matrix elements other than $|X\rangle\langle 0|$ and $|C\rangle\langle 0|$.

$\underline{\mathcal{D}_S(t)}$

Substituting for $\mathcal{D}_S(t)$ from Eq. (4.21) gives,

$$\mathcal{D}_S(t) = -\gamma_X\rho_{X0}|X\rangle\langle 0| - \gamma_C\rho_{C0}|C\rangle\langle 0| + \text{o.t.} \tag{E.50}$$

Combining Eq. (E.49) and Eq. (E.50), we find

$$-i[H_{\rm sys}, \rho_S(t)] + \mathcal{D}_S(t) = -i\begin{pmatrix} \omega_X + \Omega_p & g\langle B\rangle \\ g\langle B\rangle & \omega_c \end{pmatrix}\begin{pmatrix} \rho_{X0} \\ \rho_{C0} \end{pmatrix}, \tag{E.51}$$

where $\omega_{X,C} = \omega_{X,C} - i\gamma_{X,C}$, as defined in Eq. (1.20).

$\underline{\langle B_g\tilde{B}_g(-t')\rangle}$

Substituting for B_g from Eq. (4.12),

$$\langle B_g\tilde{B}_g(-t')\rangle = \frac{1}{4}\Big\langle (B_+ + B_- - 2\langle B\rangle)\Big(\tilde{B}_+(-t') + \tilde{B}_-(-t') - 2\langle B\rangle\Big)\Big\rangle \tag{E.52}$$

$$\begin{aligned} &= \frac{1}{4}\Big(\langle B_+\tilde{B}_+(-t')\rangle + \langle B_-\tilde{B}_-(-t')\rangle \\ &+\langle B_+\tilde{B}_-(-t')\rangle + \langle B_-\tilde{B}_+(-t')\rangle - 4\langle B\rangle^2\Big), \end{aligned} \tag{E.53}$$

where we have used the fact that $\langle\tilde{B}_\pm(-t')\rangle = \langle B_\pm\rangle = \langle B\rangle$. Evaluating each term, we find,

$$\langle B_\pm\tilde{B}_\pm(-t')\rangle = \langle B\rangle^2 e^{-\phi(t')}, \tag{E.54}$$

$$\langle B_\pm\tilde{B}_\mp(-t')\rangle = \langle B\rangle^2 e^{\phi(t')}, \tag{E.55}$$

where $\phi(t')$ is the phonon propagator evaluated at time t',

$$\phi(t') = \int_0^\infty d\omega \frac{J(\omega)}{\omega^2} \left(\coth\left(\frac{\beta\omega}{2}\right) \cos(\omega t') - i \sin(\omega t') \right) . \tag{E.56}$$

(Note that $\phi(t)$ may be related to the IB cumulant $K(t)$: $\phi(t) = K(t) + i\Omega_p t + S$.) Thus,

$$\langle B_g \tilde{B}_g(-t') \rangle = \frac{\langle B \rangle^2}{2} \left(e^{\phi(t')} + e^{-\phi(t')} - 2 \right) \tag{E.57}$$

$$= \langle B \rangle^2 \left(\cosh(\phi(t')) - 1 \right) . \tag{E.58}$$

Herein, we will denote this term by G_g:

$$G_g(t) = \langle B_g \tilde{B}_g(-t) \rangle = \langle B \rangle^2 \left(\cosh(\phi(t)) - 1 \right) . \tag{E.59}$$

$\underline{\langle B_u \tilde{B}_u(-t') \rangle}$

Substituting for B_u from Eq. (4.13) and in analogy with the above step,

$$\langle B_u \tilde{B}_u(-t') \rangle = \frac{1}{4} \Big(-\langle B_+ \tilde{B}_+(-t') \rangle - \langle B_- \tilde{B}_-(-t') \rangle + \langle B_+ \tilde{B}_-(-t') \rangle + \langle B_- \tilde{B}_+(-t') \rangle \Big) \tag{E.60}$$

$$= \frac{\langle B \rangle^2}{2} \left(e^{\phi(t')} - e^{-\phi(t')} \right) \tag{E.61}$$

$$= \langle B \rangle^2 \sinh(\phi(t')) . \tag{E.62}$$

Herein, we will denote this term by G_u:

$$G_u(t) = \langle B_u \tilde{B}_u(-t) \rangle = \langle B \rangle^2 \sinh(\phi(t)) . \tag{E.63}$$

$\underline{[X_g, \tilde{X}_g(-t')\rho_S(t)]}$

In evaluating this term, we use the Baker-Hausdorff identity [Eq. (A.7)] to express $\tilde{X}_g(-t')$ as,

$$\tilde{X}_g(-t') = X + [H_{\rm sys}, X_g] + \frac{1}{2}[H_{\rm sys}, [[H_{\rm sys}, X_g]] + \dots , \tag{E.64}$$

where we have made use of the commutivity of $H_{\rm bath}$ and X_g. Owing to the form of $H_{\rm sys}$ and X_g, Eq. (E.64) is, in general, an infinite series that cannot be reduced to a compact analytic form. We therefore take the limiting case of zero effective

detuning i.e. $\Omega_C = \Omega_X + \Omega_p$. In this case, $[H_{\text{sys}}, X_g] = 0$ and thus $\tilde{X}_g(-t') = X_g$. Substituting for X_g from Eq. (4.10),

$$[X_g, \tilde{X}_g(-t')\rho_S(t)] = [X_g, X_g\rho_S(t)] \tag{E.65}$$

$$= g^2\rho_{X0}\left|X\right\rangle\left\langle 0\right| + g^2\rho_{C0}\left|C\right\rangle\left\langle 0\right| + \text{o.t.} \tag{E.66}$$

Note that whilst we have chosen the case of zero effective detuning, one may equally evaluate this term for non-zero detuning $\Omega_C \neq \Omega_X + \Omega_p$ by calculating the $\tilde{X}_g(-t')$ as a matrix product in the $\{\left|X\right\rangle, \left|C\right\rangle\}$ basis,

$$\tilde{X}_g(-t') = W \begin{pmatrix} e^{-i\Omega_1 t'} & 0 \\ 0 & e^{-i\Omega_2 t'} \end{pmatrix} W^{-1} \begin{pmatrix} 0 & g \\ g & 0 \end{pmatrix} W \begin{pmatrix} e^{i\Omega_1 t'} & 0 \\ 0 & e^{i\Omega_2 t'} \end{pmatrix} W^{-1}, \tag{E.67}$$

where $\Omega_{1,2}$ are the eigenvalues of H_{sys} and W is a matrix composed of the right eigenvectors of H_{sys}. Having calculated $\tilde{X}_g(-t')$, one may proceed to calculate the commutator $[X_g, \tilde{X}_g(-t')\rho_S(t)]$ through matrix algebra.

$\underline{[X_u, \tilde{X}_u(-t')\rho_S(t)]}$

Again, we make use of the Baker-Hausdorff identity [Eq. (A.7)], noting that,

$$X_u = ig\left(\left|X\right\rangle\left\langle C\right| - \left|C\right\rangle\left\langle X\right|\right), \tag{E.68}$$

$$[H_{\text{sys}}, X_u] = ig(-2g\langle B\rangle it')\left(\left|C\right\rangle\left\langle C\right| - \left|X\right\rangle\left\langle X\right|\right), \tag{E.69}$$

$$[H_{\text{sys}}, [H_{\text{sys}}, X_u]] = ig(-2g\langle B\rangle it')^2\left(\left|X\right\rangle\left\langle C\right| - \left|C\right\rangle\left\langle X\right|\right), \tag{E.70}$$

where we have again taken the limiting case of $\Omega_C = \Omega_X + \Omega_p$. Continuing in this vein, we arrive at the following expression for $\tilde{X}_u(-t')$

$$\begin{aligned}\tilde{X}_u(-t') &= ig\left(1 - \frac{1}{2}(2g\langle B\rangle t')^2 + \ldots\right)\left(\left|X\right\rangle\left\langle C\right| - \left|C\right\rangle\left\langle X\right|\right) \\ &\quad + g\left((2g\langle B\rangle t') - \frac{1}{3!}(2g\langle B\rangle t')^3 + \ldots\right)\left(\left|C\right\rangle\left\langle C\right| - \left|X\right\rangle\left\langle X\right|\right) \qquad \text{(E.71)} \\ &= ig\cos(2g\langle B\rangle t')\left(\left|X\right\rangle\left\langle C\right| - \left|C\right\rangle\left\langle X\right|\right) \\ &\quad + g\sin(2g\langle B\rangle t')\left(\left|C\right\rangle\left\langle C\right| - \left|X\right\rangle\left\langle X\right|\right). \qquad \text{(E.72)}\end{aligned}$$

Thus,

$$\begin{aligned}[X_u, \tilde{X}_u(-t')\rho_S(t)] = &\left(g^2\cos(2g\langle B\rangle t')\rho_{X0} + ig^2\sin(2g\langle B\rangle t')\rho_{C0}\right)|X\rangle\langle 0| \\ &+ \left(g^2\cos(2g\langle B\rangle t')\rho_{C0} + ig^2\sin(2g\langle B\rangle t')\rho_{X0}\right)|C\rangle\langle 0| \\ &+ \text{o.t.}\end{aligned} \tag{E.73}$$

Again, whilst we focus on the case of zero effective detuning, one may equally evaluate this term for $\Omega_C \neq \Omega_X + \Omega_p$ in a manner analogous to that described for the term $[X_g, \tilde{X}_g(-t')\rho_S(t)]$.

Combining all of the above and noting that the Hermitian conjugate of $[X_\alpha, \tilde{X}_\alpha(-t')\rho_S(t)]$ for $\alpha = g, u$ does not contribute any $|X\rangle\langle 0|$ or $|C\rangle\langle 0|$ terms, we arrive at Eq. (4.30).

E.2.2 Non-Markov

Taking Eq. (4.27) as our starting point and converting from the interaction representation to the Schrödinger representation yields,

$$\begin{aligned}\frac{d\rho_S(t)}{dt} = &-i[H_0, \rho_S(t)] + \mathcal{D}_S(t) \\ &- \underbrace{\int_0^t d\tau\; e^{-iH_0t}\,\mathrm{tr}_B\left\{[\tilde{H}_{\text{int}}(t), [\tilde{H}_{\text{int}}(\tau), \tilde{\rho}_S(\tau)\otimes\tilde{\rho}_B]]\right\}e^{iH_0t}}_{(\star)}\,.\end{aligned} \tag{E.74}$$

We note that the difference between Eq. (E.46) and Eq. (E.74) is contained within term $(\star)$ of both equations. Considering term $(\star)$ in isolation and substituting for H_{int} from Eq. (4.7) yields

$$\begin{aligned}&\int_0^t d\tau\; e^{-iH_0t}\,\mathrm{tr}_B\left\{[\tilde{H}_{\text{int}}(t), [\tilde{H}_{\text{int}}(\tau), \tilde{\rho}_S(\tau)\otimes\rho_B]]\right\}e^{iH_0t} \\ &= \int_0^t d\tau\;\; \mathrm{tr}_B\left[\sum_{\alpha=g,u} X_\alpha(t)\otimes B_\alpha(t), e^{-iH_0t}\left[\sum_{\alpha'=g,u}\tilde{X}_{\alpha'}(\tau)\otimes\tilde{B}_{\alpha'}(\tau), \tilde{\rho}_S(\tau)\otimes\tilde{\rho}_B\right]e^{-iH_0t}\right].\end{aligned} \tag{E.75}$$

Looking initially at the $\alpha = \alpha' = g$ term within Eq. (E.75) and separating the system and bath Hilbert spaces,

$$\begin{aligned}
&\int_0^t d\tau \;\; \mathrm{tr}_B[X_g \otimes B_g, e^{-iH_0 t}[\tilde{X}_g(\tau) \otimes \tilde{B}_g(\tau), \tilde{\rho}_S(\tau) \otimes \tilde{\rho}_B]e^{iH_0 t}] \\
&\quad = \int_0^t d\tau \, \mathrm{tr}_B \left\{ \left[B_g, e^{-iH_{\mathrm{bath}} t}[\tilde{B}_g(\tau), \tilde{\rho}_B]e^{iH_{\mathrm{bath}} t} \right] \right\} \otimes \left[X_g, e^{-iH_{\mathrm{sys}} t}[\tilde{X}_g(\tau), \tilde{\rho}_S(\tau)]e^{iH_{\mathrm{sys}} t} \right] \qquad \text{(E.76)} \\
&\quad = \int_0^t d\tau \Big(\langle B_g \tilde{B}_g(\tau - t) \rangle \left[X_g, e^{-iH_{\mathrm{sys}} t} \tilde{X}_g(\tau) \, \tilde{\rho}_S(\tau) e^{iH_{\mathrm{sys}} t} \right] \\
&\qquad + \langle \tilde{B}_g(\tau - t) B_g \rangle \left[X_g, e^{-iH_{\mathrm{sys}} t} \tilde{\rho}_S(\tau) \tilde{X}_g(\tau) e^{iH_{\mathrm{sys}} t} \right] \Big) \qquad \text{(E.77)}
\end{aligned}$$

where $\langle \ldots \rangle$ represents the expectation value over the phonon bath. Noting that $\tilde{\rho}_S(\tau) = e^{iH_{\mathrm{sys}}\tau} \rho_S(\tau) e^{-iH_{\mathrm{sys}}\tau}$ and $\tilde{X}_g(\tau) = e^{iH_{\mathrm{sys}}\tau} X_g e^{-iH_{\mathrm{sys}}\tau}$ (converting from the interaction representation to the Schrödinger representation), we may express Eq. (E.77) as

$$\begin{aligned}
&\int_0^t d\tau \;\; \mathrm{tr}_B[X_g \otimes B_g, e^{-iH_0 t}[\tilde{X}_g(\tau) \otimes \tilde{B}_g(\tau), \tilde{\rho}_S(\tau) \otimes \tilde{\rho}_B]e^{iH_0 t}] \\
&\qquad = \int_0^t d\tau \langle B_g \tilde{B}_g(\tau - t) \rangle \left[X_g, e^{iH_{\mathrm{sys}}(\tau - t)}[X_g, \rho_S(\tau)]e^{-iH_{\mathrm{sys}}(\tau - t)} \right] . \qquad \text{(E.78)}
\end{aligned}$$

Expanding the inner commutator, we arrive at Eq. (4.41).

List of Figures

References

[1] R. Knox. *Theory of Excitons*. Academic Press Inc., 1972.

[2] P. Borri, W. Langbein, S. Schneider, U. Woggon, R. L. Sellin, D. Ouyang, and D. Bimberg. Ultralong Dephasing Time in InGaAs Quantum Dots. *Phys. Rev. Lett.* **87** (2001), 157401.

[3] B. Krummheuer, V. M. Axt, and T. Kuhn. Theory of pure dephasing and the resulting absorption line shape in semiconductor quantum dots. *Phys. Rev. B* **65** (2002), 195313.

[4] L. Besombes, K. Kheng, L. Marsal, and H. Mariette. Acoustic phonon broadening mechanism in single quantum dot emission. *Phys. Rev. B* **63** (2001), 155307.

[5] E. A. Muljarov and R. Zimmermann. Dephasing in Quantum Dots: Quadratic Coupling to Acoustic Phonons. *Phys. Rev. Lett.* **93** (2004), 237401.

[6] E. A. Muljarov, T. Takagahara, and R. Zimmermann. Phonon-Induced Exciton Dephasing in Quantum Dot Molecules. *Phys. Rev. Lett.* **95** (2005), 177405.

[7] J. Frenkel. On the Transformation of light into Heat in Solids. I. *Phys. Rev.* **37** (1931), 17–44.

[8] L. D. Landau. Electron motion in crystal lattices. *Phys. Z. Sowjet.* **3** (1933), 664.

[9] H. Fröhlich. Electrons in lattice fields. *Advances in Physics* **3** (1954), 325–361.

[10] G. D. Mahan. *Many-Particle Physics*. Springer US, 2000.

[11] J. Kasprzak, S. Reitzenstein, E. A. Muljarov, C. Kistner, C. Schneider, M. Strauss, S. Höfling, A. Forchel, and W. Langbein. Up on the Jaynes-Cummings ladder of a quantum-dot/microcavity system. *Nat. Mat.* **9** (2010), 304.

[12] G. Khitrova, H. M. Gibbs, M. Kira, S. W. Koch, and A. Scherer. Vacuum Rabi splitting in semiconductors. *Nature Physics* **2** (2006), 81–90.

[13] P. Meystre and M. Sargent. *Elements of Quantum Optics*. Springer Berlin Heidelberg, 2013.

[14] J. J. Hopfield. Theory of the Contribution of Excitons to the Complex Dielectric Constant of Crystals. *Phys. Rev.* **112** (1958), 1555–1567.

[15] I. Wilson-Rae and A. Imamoğlu. Quantum dot cavity-QED in the presence of strong electron-phonon interactions. *Phys. Rev. B* **65** (2002), 235311.

[16] P. Kaer, T. R. Nielsen, P. Lodahl, A.-P. Jauho, and J. Mørk. Non-Markovian Model of Photon-Assisted Dephasing by Electron-Phonon Interactions in a Coupled Quantum-Dot–Cavity System. *Phys. Rev. Lett.* **104** (2010), 157401.

[17] U. Hohenester. Cavity quantum electrodynamics with semiconductor quantum dots: Role of phonon-assisted cavity feeding. *Phys. Rev. B* **81** (2010), 155303.

[18] C. Roy and S. Hughes. Phonon-Dressed Mollow Triplet in the Regime of Cavity Quantum Electrodynamics: Excitation-Induced Dephasing and Nonperturbative Cavity Feeding Effects. *Phys. Rev. Lett.* **106** (2011), 247403.

[19] M. Glässl, L. Sörgel, A. Vagov, M. D. Croitoru, T. Kuhn, and V. M. Axt. Interaction of a quantum-dot cavity system with acoustic phonons: Stronger light-matter coupling can reduce the visibility of strong coupling effects. *Phys. Rev. B* **86** (2012), 035319.

[20] A. Nazir and D. P. S. McCutcheon. Modelling exciton phonon interactions in optically driven quantum dots. *J. Phys. Cond. Mat.* **28** (2016), 103002.

[21] D. G. Nahri, F. H. A. Mathkoor, and C. H. R. Ooi. Real-time path-integral approach for dissipative quantum dot-cavity quantum electrodynamics: impure dephasing-induced effects. *J. Phys. Cond. Mat.* **29** (2016), 055701.

[22] G. Hornecker, A. Auffèves, and T. Grange. Influence of phonons on solid-state cavity-QED investigated using nonequilibrium Green's functions. *Phys. Rev. B* **95** (2017), 035404.

[23] U. Hohenester, A. Laucht, M. Kaniber, N. Hauke, A. Neumann, A. Mohtashami, M. Seliger, M. Bichler, and J. J. Finley. Phonon-assisted transitions from quantum dot excitons to cavity photons. *Phys. Rev. B* **80** (2009), 201311.

[24] M. Calic, P. Gallo, M. Felici, K. A. Atlasov, B. Dwir, A. Rudra, G. Biasiol, L. Sorba, G. Tarel, V. Savona, and E. Kapon. Phonon-Mediated Coupling of InGaAs/GaAs Quantum-Dot Excitons to Photonic Crystal Cavities. *Phys. Rev. Lett.* **106** (2011), 227402.

[25] D. Valente, J. Suffczyński, T. Jakubczyk, A. Dousse, A. Lemaître, I. Sagnes, L. Lanco, P. Voisin, A. Auffèves, and P. Senellart. Frequency cavity pulling induced by a single semiconductor quantum dot. *Phys. Rev. B* **89** (2014), 041302.

[26] S. L. Portalupi, G. Hornecker, V. Giesz, T. Grange, A. Lemaître, J. Demory, I. Sagnes, N. D. Lanzillotti-Kimura, L. Lanco, A. Auffèves, and P. Senellart. Bright Phonon-Tuned Single-Photon Source. *Nano Letters* **15** (2015). PMID: 26325603, 6290–6294.

[27] K. Müller, K. A. Fischer, A. Rundquist, C. Dory, K. G. Lagoudakis, T. Sarmiento, Y. A. Kelaita, V. Borish, and J. Vučkovi ć. Ultrafast Polariton-Phonon Dynamics of Strongly Coupled Quantum Dot-Nanocavity Systems. *Phys. Rev. X* **5** (2015), 031006.

[28] D. P. S. McCutcheon and A. Nazir. Quantum dot Rabi rotations beyond the weak exciton–phonon coupling regime. *New Journal of Physics* **12** (2010), 113042.

[29] Y. Ota, S. Iwamoto, N. Kumagai, and Y. Arakawa. Impact of electron-phonon interactions on quantum-dot cavity quantum electrodynamics (Aug. 6, 2009). arXiv: `http://arxiv.org/abs/0908.0788v1 [cond-mat.mes-hall]`.

[30] J. P. Reithmaier, G. Sęk, A. Löffler, C. Hofmann, S. Kuhn, S. Reitzenstein, L. V. Keldysh, V. D. Kulakovskii, T. L. Reinecke, and A. Forchel. Strong coupling in a single quantum dot–semiconductor microcavity system. *Nature* **432** (2004), 197–200.

[31] K. Srinivasan, M. Borselli, O. Painter, A. Stintz, and S. Krishna. Cavity Q, mode volume, and lasing threshold in small diameter AlGaAs microdisks with embedded quantum dots. *Optics Express* **14** (2006), 1094.

[32] X. Yu, Y. Yuan, J. Xu, K.-T. Yong, J. Qu, and J. Song. Strong Coupling in Microcavity Structures: Principle, Design, and Practical Application. *Laser & Photonics Reviews* **13** (2018), 1800219.

[33] F. P. Heinz-Peter Breuer. *The Theory of Open Quantum Systems*. Oxford University Press, Feb. 11, 2007.

[34] R. Zimmermann and E. Muljarov. Dephasing of optical transitions in quantum dots — Where exact solutions meet sophisticated experiments. *12th Int. Symp. "Nanostructures: Physics and Technology" St Petersburg, Russia* (2004).

[35] Y. Sugiyama, Y. Sakuma, S. Muto, and N. Yokoyama. Novel InGaAs/GaAs Quantum Dot Structures Formed in Tetrahedral-Shaped Recesses on (111)B GaAs Substrate Using Metalorganic Vapor Phase Epitaxy. *Japanese Journal of Applied Physics* **34** (1995), 4384.

[36] S. T. Moroni, T. H. Chung, G. Juska, A. Gocalinska, and E. Pelucchi. Statistical study of stacked/coupled site-controlled pyramidal quantum dots and their excitonic properties. *Applied Physics Letters* **111** (2017), 083103.

[37] L. Scarpelli. *Optical spectroscopy of excitons confined in two-dimensional materials and semiconductor heterostructures*. PhD thesis. Cardiff University, Unpublished.

[38] M. H. Baier, E. Pelucchi, E. Kapon, S. Varoutsis, M. Gallart, I. Robert-Philip, and I. Abram. Single photon emission from site-controlled pyramidal quantum dots. *Applied Physics Letters* **84** (2004), 648–650.

[39] B. V. Hattem. *Orientation-dependent magneto-photoluminescence of excitons confined in semiconductor nanostructures*. PhD thesis. Hughes Hall College, University of Cambridge, 2014.

[40] T.-H. Chung. *Arrays of quantum-light-emitting diodes with site-controlled pyramidal quantum dots*. PhD thesis. University College Cork, 2016.

[41] T. Schmidt, K. Lischka, and W. Zulehner. Excitation-power dependence of the near-band-edge photoluminescence of semiconductors. *Physical Review B* **45** (1992), 8989–8994.

[42] D Kaplan, Y Gong, K Mills, V Swaminathan, P. M. Ajayan, S Shirodkar, and E Kaxiras. Excitation intensity dependence of photoluminescence from monolayers of MoS 2 and WS 2 /MoS 2 heterostructures. *2D Materials* **3** (2016), 015005.

[43] D. Sarkar, H. P. van der Meulen, J. M. Calleja, J. M. Becker, R. J. Haug, and K. Pierz. Exciton fine structure and biexciton binding energy in single self-assembled InAsAlAs quantum dots. *Journal of Applied Physics* **100** (2006), 023109.

[44] A. J. Nozik. Spectroscopy and hot electron relaxation dynamics in semiconductor quantum wells and quantum dots. *Annual Review of Physical Chemistry* **52** (2001). PMID: 11326064, 193–231.

[45] W. S. Pelouch, R. J. Ellingson, P. E. Powers, C. L. Tang, D. M. Szmyd, and A. J. Nozik. Comparison of hot-carrier relaxation in quantum wells and bulk GaAs at high carrier densities. *Physical Review B* **45** (1992), 1450–1453.

[46] D. S. Boudreaux, F. Williams, and A. J. Nozik. Hot carrier injection at semiconductor-electrolyte junctions. *Journal of Applied Physics* **51** (1980), 2158.

[47] P. Guyot-Sionnest, M. Shim, C. Matranga, and M. Hines. Intraband relaxation in CdSe quantum dots. *Phys. Rev. B* **60** (1999), R2181–R2184.

[48] P. Wang, C. Sotomayor Torres, H McLelland, S. Thoms, M Holland, and C. Stanley. Photoluminescence intensity and multiple phonon Raman scattering in quantum dots: evidence of the bottleneck effect. *Surface Science* **305** (Mar. 1994), 585–590.

[49] K. Mukai, N. Ohtsuka, and M. Sugawara. High photoluminescence efficiency of InGaAs/GaAs quantum dots self-formed by atomic layer epitaxy technique. *Applied Physics Letters* **70** (1997), 2416–2418.

[50] B. N. Murdin, A. R. Hollingworth, M. Kamal-Saadi, R. T. Kotitschke, C. M. Ciesla, C. R. Pidgeon, P. C. Findlay, H. P. M. Pellemans, C. J. G. M. Langerak, A. C. Rowe, R. A. Stradling, and E. Gornik. Suppression of LO phonon scattering in Landau quantized quantum dots. *Phys. Rev. B* **59** (1999), R7817–R7820.

[51] M. Sugawara, K. Mukai, and H. Shoji. Effect of phonon bottleneck on quantum-dot laser performance. *Applied Physics Letters* **71** (1997), 2791–2793.

[52] R. Heitz, M. Veit, N. N. Ledentsov, A. Hoffmann, D. Bimberg, V. M. Ustinov, P. S. Kop'ev, and Z. I. Alferov. Energy relaxation by multiphonon processes in InAs/GaAs quantum dots. *Phys. Rev. B* **56** (1997), 10435–10445.

[53] R. Heitz, A. Kalburge, Q. Xie, M. Grundmann, P. Chen, A. Hoffmann, A. Madhukar, and D. Bimberg. Excited states and energy relaxation in stacked InAs/GaAs quantum dots. *Phys. Rev. B* **57** (1998), 9050–9060.

[54] K. Brunner, U. Bockelmann, G. Abstreiter, M. Walther, G. Böhm, G. Tränkle, and G. Weimann. Photoluminescence from a single GaAs/AlGaAs quantum dot. *Phys. Rev. Lett.* **69** (1992), 3216–3219.

[55] P. C. Sercel. Multiphonon-assisted tunneling through deep levels: A rapid energy-relaxation mechanism in nonideal quantum-dot heterostructures. *Phys. Rev. B* **51** (1995), 14532–14541.

[56] M. Lowisch, M. Rabe, F. Kreller, and F. Henneberger. Electronic excitations and longitudinal optical phonon modes of self-assembled CdSe quantum dots revealed by microprobe studies. *Applied Physics Letters* **74** (1999), 2489–2491.

[57] K. Král and Z. Khás. Absence of Phonon Bottleneck and Fast Electronic Relaxation in Quantum Dots. *Phys. Status Solidi* **208** (1998), R5–R6.

[58] V. I. Klimov and D. W. McBranch. Femtosecond 1P-to- 1S Electron Relaxation in Strongly Confined Semiconductor Nanocrystals. *Phys. Rev. Lett.* **80** (1998), 4028–4031.

[59] U. Woggon, H. Giessen, F. Gindele, O. Wind, B. Fluegel, and N. Peyghambarian. Ultrafast energy relaxation in quantum dots. *Phys. Rev. B* **54** (1996), 17681–17690.

[60] B. Ohnesorge, M. Albrecht, J. Oshinowo, A. Forchel, and Y. Arakawa. Rapid carrier relaxation in self-assembled $In_xGa_{1-x}As$/GaAs quantum dots. *Phys. Rev. B* **54** (1996), 11532–11538.

[61] G. Wang, S. Fafard, D. Leonard, J. E. Bowers, J. L. Merz, and P. M. Petroff. Time-resolved optical characterization of InGaAs/GaAs quantum dots. *Applied Physics Letters* **64** (1994), 2815–2817.

[62] J. Sandmann, S. Grosse, G. Von Plessen, J. Feldmann, G. Hayes, R. Phillips, H. Lipsanen, M. Sopanen, and J. Ahopelto. Ultrafast relaxation dynamics in strain-induced quantum dots. *Phys. Status Solidi* **204** (1997), 251–254.

[63] M. I. Dyakonov, ed. *Spin Physics in Semiconductors*. Springer Berlin Heidelberg, Aug. 18, 2008.

[64] M. Bayer, G. Ortner, O. Stern, A. Kuther, A. A. Gorbunov, A. Forchel, P. Hawrylak, S. Fafard, K. Hinzer, T. L. Reinecke, S. N. Walck, J. P. Reithmaier, F. Klopf, and F. Schäfer. Fine structure of neutral and charged excitons in self-assembled In(Ga)As/(Al)GaAs quantum dots. *Physical Review B* **65** (2002).

[65] H. W. van Kesteren, E. C. Cosman, W. A. J. A. van der Poel, and C. T. Foxon. Fine structure of excitons in type-II GaAs/AlAs quantum wells. *Phys. Rev. B* **41** (1990), 5283–5292.

[66] E. Blackwood, M. J. Snelling, R. T. Harley, S. R. Andrews, and C. T. B. Foxon. Exchange interaction of excitons in GaAs heterostructures. *Phys. Rev. B* **50** (1994), 14246–14254.

[67] Y. Varshni. Temperature dependence of the energy gap in semiconductors. *Physica* **34** (1967), 149–154.

[68] G. Ortner, M. Schwab, M. Bayer, R. Pässler, S. Fafard, Z. Wasilewski, P. Hawrylak, and A. Forchel. Temperature dependence of the excitonic band gap in In_xGa_{1-x}AsGaAs self-assembled quantum dots. *Phys. Rev. B* **72** (2005), 085328.

[69] R. People, A. Jayaraman, K. W. Wecht, D. L. Sivco, and A. Y. Cho. Measurement of the pressure dependence of the direct band gap of $In_{0.53}Ga_{0.47}As$ using stimulated emission. *Applied Physics Letters* **52** (1988), 2124–2126.

[70] V. A. Wilkinson, A. D. Prins, J. D. Lambkin, E. P. O'Reilly, D. J. Dunstan, L. K. Howard, and M. T. Emeny. Hydrostatic pressure coefficients of the photoluminescence of In_xGa_{1-x}As/GaAs strained-layer quantum wells. *Phys. Rev. B* **42** (1990), 3113–3119.

[71] A. J. Ramsay, T. M. Godden, S. J. Boyle, E. M. Gauger, A. Nazir, B. W. Lovett, A. M. Fox, and M. S. Skolnick. Phonon-Induced Rabi-Frequency Renormalization of Optically Driven Single InGaAs/GaAs Quantum Dots. *Phys. Rev. Lett.* **105** (2010), 177402.

[72] P. Machnikowski and L. Jacak. Resonant nature of phonon-induced damping of Rabi oscillations in quantum dots. *Physical Review B* **69** (2004).

[73] D. Mogilevtsev, A. P. Nisovtsev, S. Kilin, S. B. Cavalcanti, H. S. Brandi, and L. E. Oliveira. Driving-Dependent Damping of Rabi Oscillations in Two-Level Semiconductor Systems. *Physical Review Letters* **100** (2008).

[74] D. E. Makarov and N. Makri. Path integrals for dissipative systems by tensor multiplication. Condensed phase quantum dynamics for arbitrarily long time. *Chem. Phys. Lett.* **221** (1994), 482 –491.

[75] E. Sim. Quantum dynamics for a system coupled to slow baths: On-the-fly filtered propagator method. *J. Chem. Phys.* **115** (2001), 4450–4456.

[76] A. Vagov, M. D. Croitoru, V. M. Axt, T. Kuhn, and F. M. Peeters. Nonmonotonic Field Dependence of Damping and Reappearance of Rabi Oscillations in Quantum Dots. *Phys. Rev. Lett.* **98** (2007), 227403.

[77] A. Vagov, M. Glässl, M. D. Croitoru, V. M. Axt, and T. Kuhn. Competition between pure dephasing and photon losses in the dynamics of a dot-cavity system. *Phys. Rev. B* **90** (2014), 075309.

[78] T. Grange, G. Hornecker, D. Hunger, J.-P. Poizat, J.-M. Gérard, P. Senellart, and A. Auffèves. Cavity-Funneled Generation of Indistinguishable Single Photons from Strongly Dissipative Quantum Emitters. *Phys. Rev. Lett.* **114** (2015), 193601.

[79] J. Iles-Smith, D. P. S. McCutcheon, A. Nazir, and J. Mørk. Phonon scattering inhibits simultaneous near-unity efficiency and indistinguishability in semiconductor single-photon sources. *Nat. Phot.* **11** (2017), 521.

[80] F. Albert, K. Sivalertporn, J. Kasprzak, M. Strauß, C. Schneider, S. Höfling, M. Kamp, A. Forchel, S. Reitzenstein, E. A. Muljarov, and W. Langbein. Microcavity controlled coupling of excitonic qubits. *Nat. Comm.* **4** (2013), 1747.

[81] Y.-J. Wei, Y. He, Y.-M. He, C.-Y. Lu, J.-W. Pan, C. Schneider, M. Kamp, S. Höfling, D. P. S. McCutcheon, and A. Nazir. Temperature-Dependent Mollow Triplet Spectra from a Single Quantum Dot: Rabi Frequency Renormalization and Sideband Linewidth Insensitivity. *Phys. Rev. Lett.* **113** (2014), 097401.

[82] J. Iles-Smith, D. P. S. McCutcheon, J. Mørk, and A. Nazir. Limits to coherent scattering and photon coalescence from solid-state quantum emitters. *Physical Review B* **95** (2017).

[83] A. Würger. Strong-coupling theory for the spin-phonon model. *Phys. Rev. B* **57** (1998), 347–361.